Figure 1.1. Overview map showing the location of the study area in Beaufort Sea.
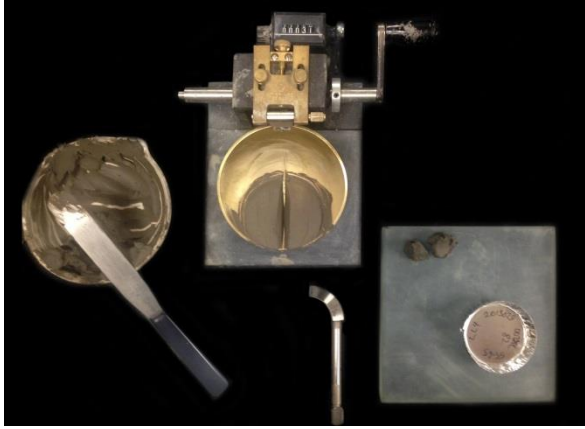
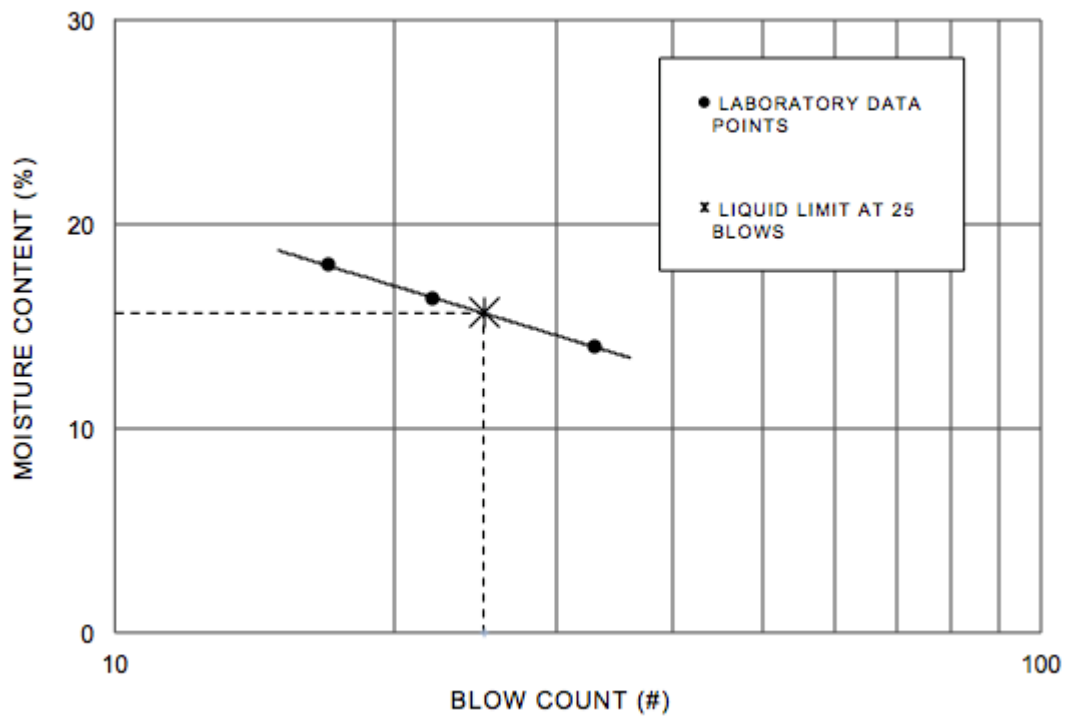Figure 3.1. Liquid limit test apparatus. Photograph by K. MacKillop. NRCan photo 2021-518.

Figure 3.2. Laboratory data for determining the *LL* of the soil.
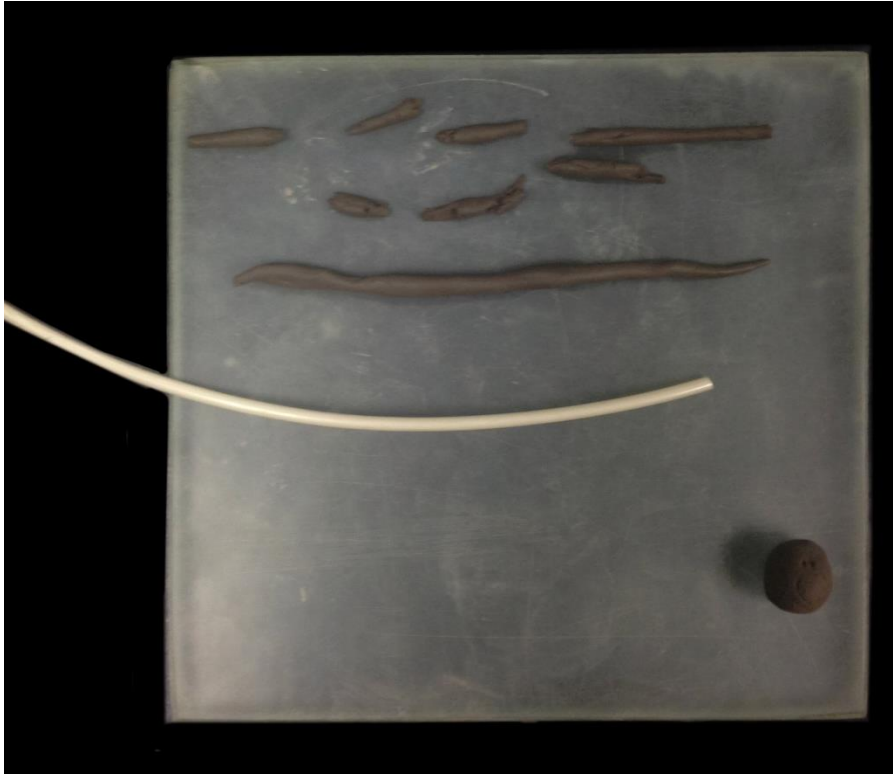
Figure 3.3. Crumbing of the soil threads at the plastic limit. Photograph by K. MacKillop. NRCan photo 2021-519.
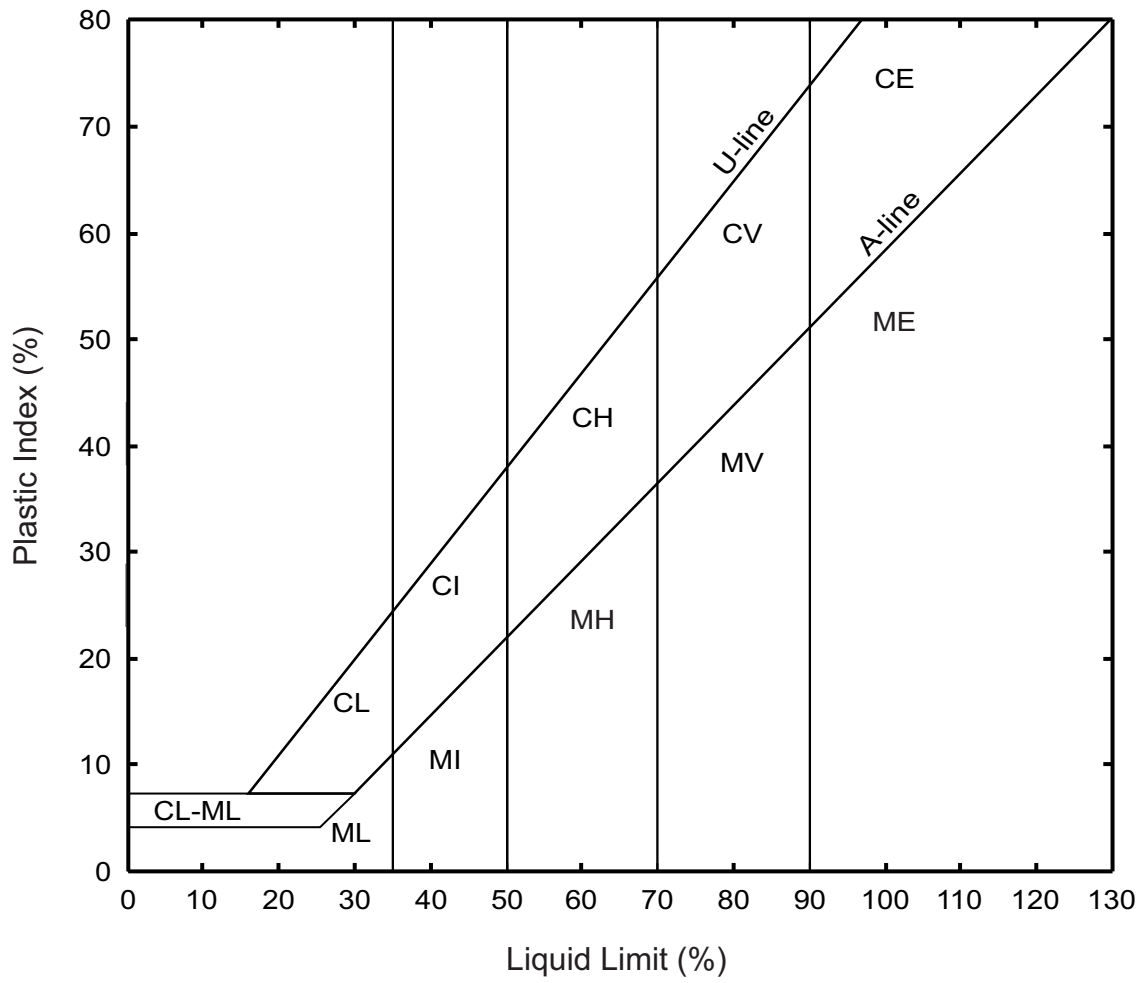
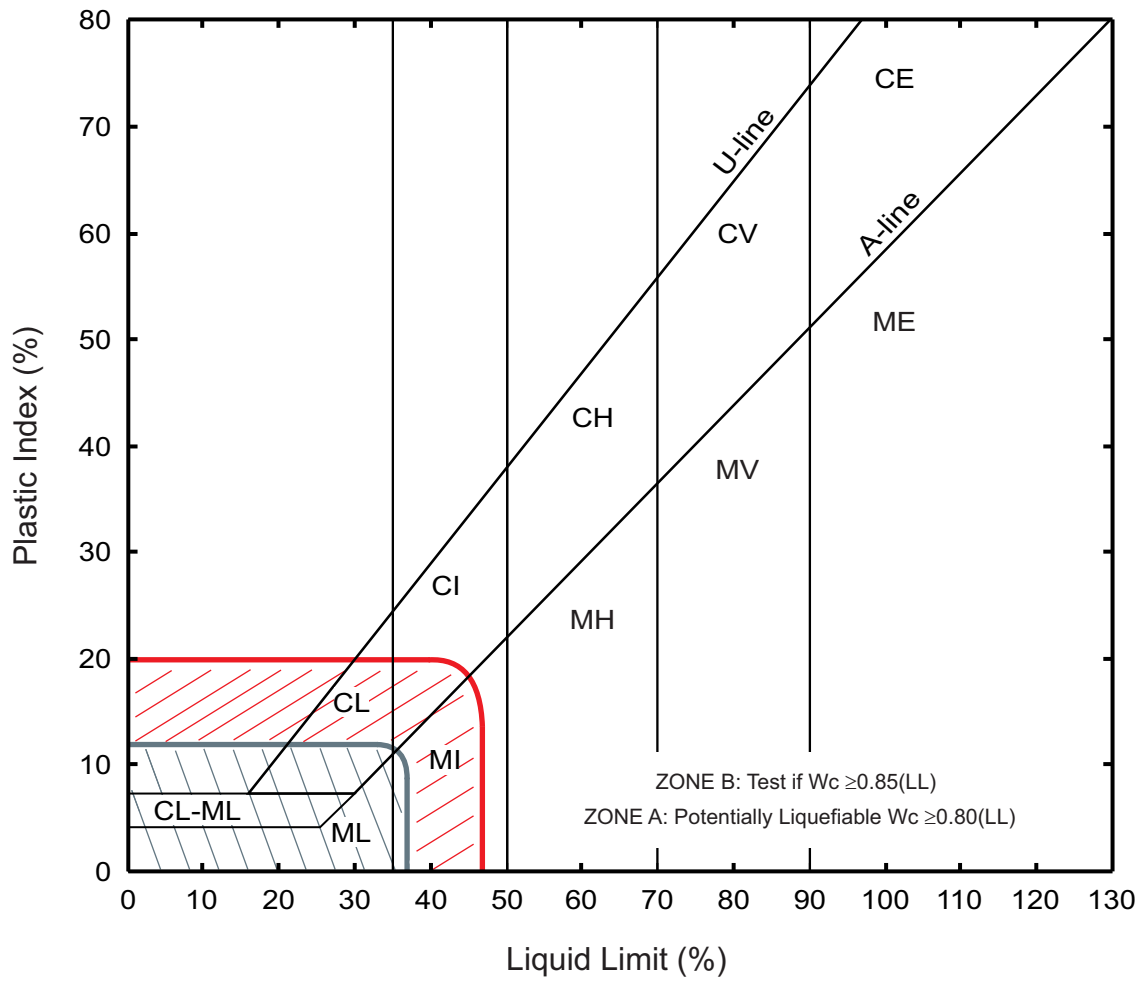Figure 3.4. British Standard plasticity chart with A and U lines defined.

Figure 3.5. Plasticity chart with liquefaction potential zones (Seed et al., 2003).
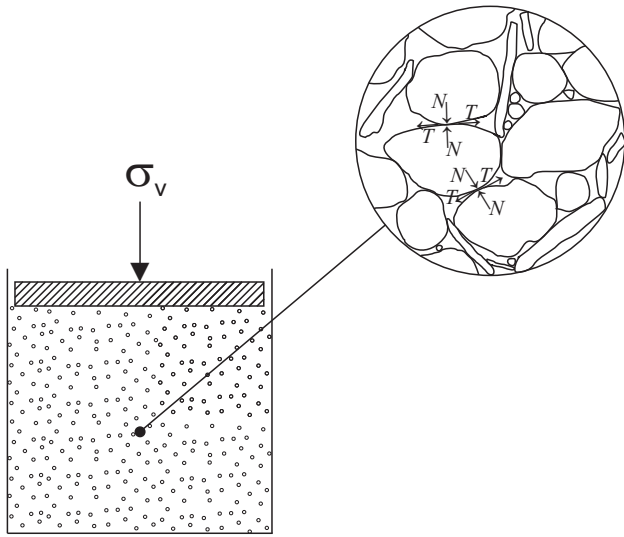
Figure 4.1. Schematic representation of normal (N)
and tangential (T) force transmission through soil under
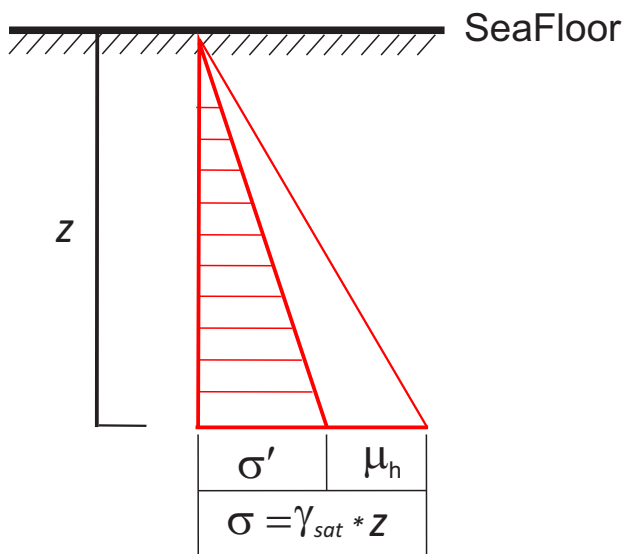an applied vertical load (σ_v) (after Lamb and Whitman, 1969).

Figure 4.2. The total normal stress acting on sediment below the seafloor is a combination of effective stress and pore water pressure.
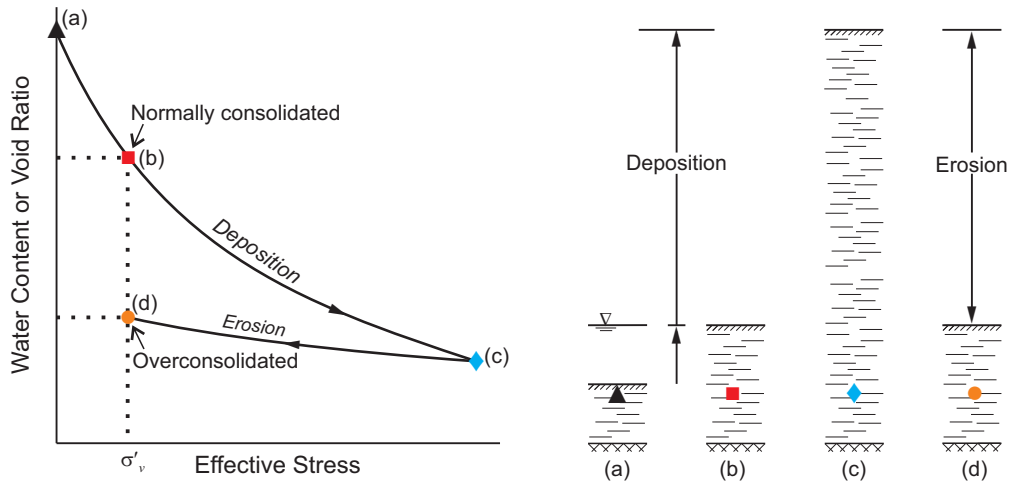
Figure 5.1. Normal and overconsolidated clays by gravitational compaction (Skempton, 1970)
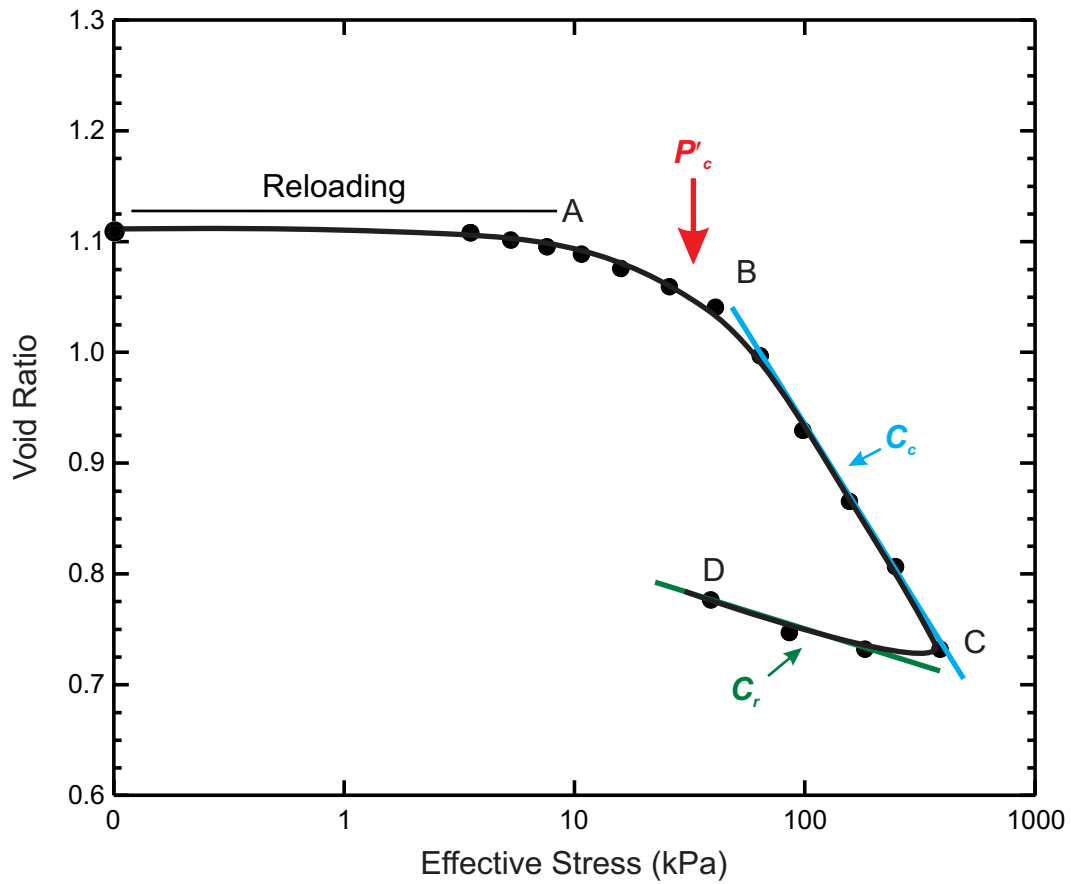
Figure 5.2. Typical consolidation e-log effective stress curve. Point A marks the end of the reloading point A to B marks the transition from reloading to new stresses, point B to C defines the virgin compression line and point C to D defines the expansion index.
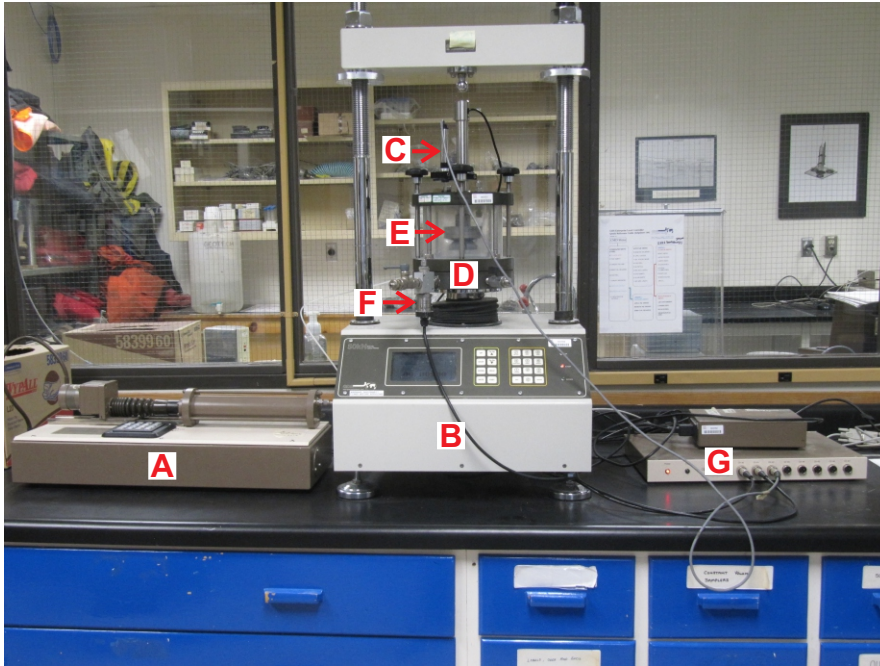
Figure 5.3. The GDS CRS consolidation system includes (A) back pressure controller, (B) 50 kN load frame, (C) axial displacement transducer, (D) CRS consolidation cell, (E) submersible load cell, (F) pore pressure transducer and (G) DAQ system. Photograph by K. MacKillop. NRCan photo 2021-520.
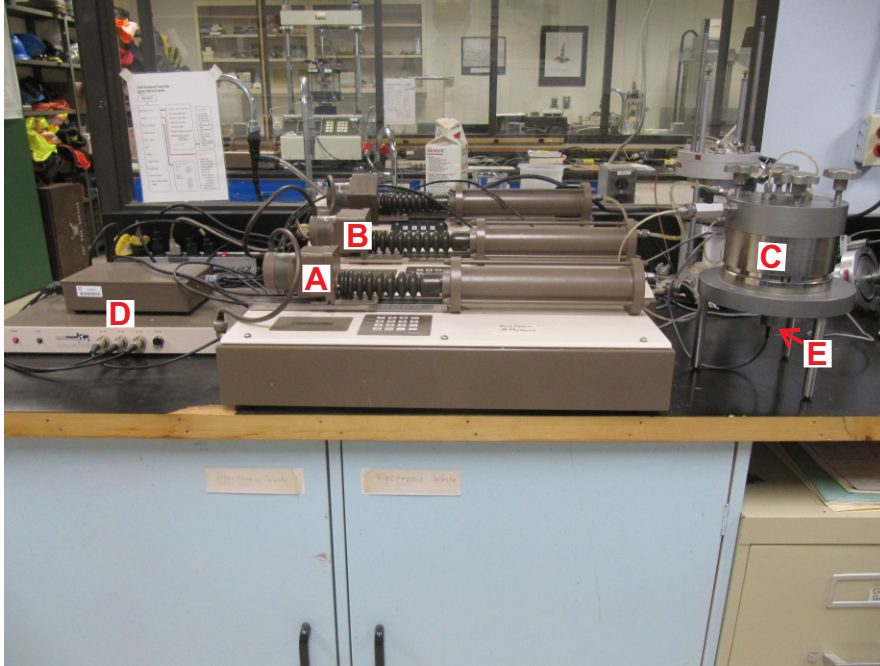
Figure 5.4. The GDS Rowe consolidation system includes (A) back pressure controller, (B) load chamber controller, (C) Rowe consolidation cell, (D) DAQ system and (E) pore pressure transducer. Photograph taken by K. MacKillop. NRCan photo 2021-521.
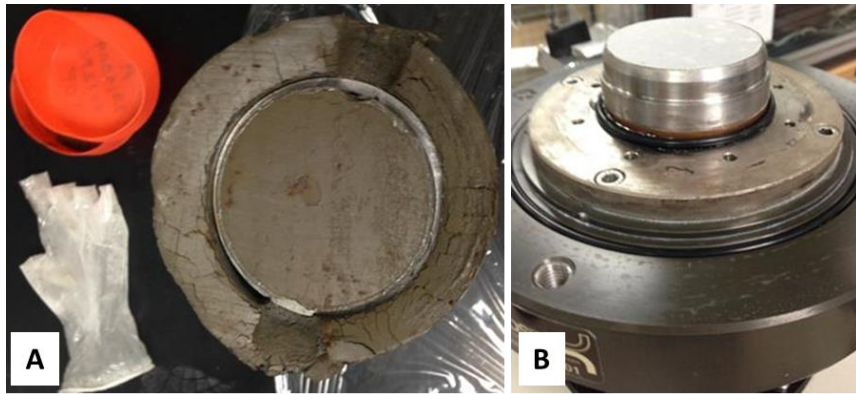
Figure 5.5. Sediment extruded into CRS consolidation ring (A) and a trimmed sample on the CRS cell base (B). Photographs by K. MacKillop. (A) NRCan photo 2021-522. (B) NRCan photo 2021-523.
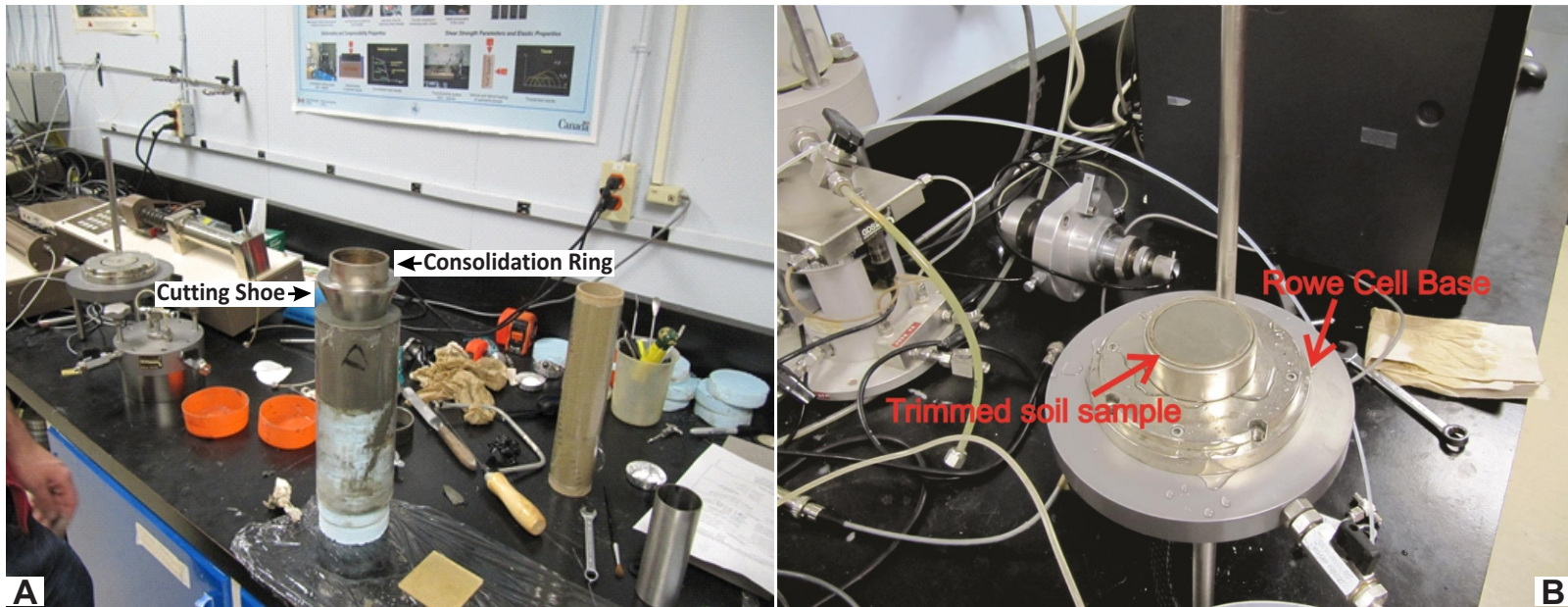
Figure 5.6. Sediment being extruded into the Rowe cell consolidation ring (A) and a trimmed sample on the Rowe cell base (B). Photographs by K. MacKillop. (A) NRCan photo 2021-524. (B) NRCan photo 2021-525.
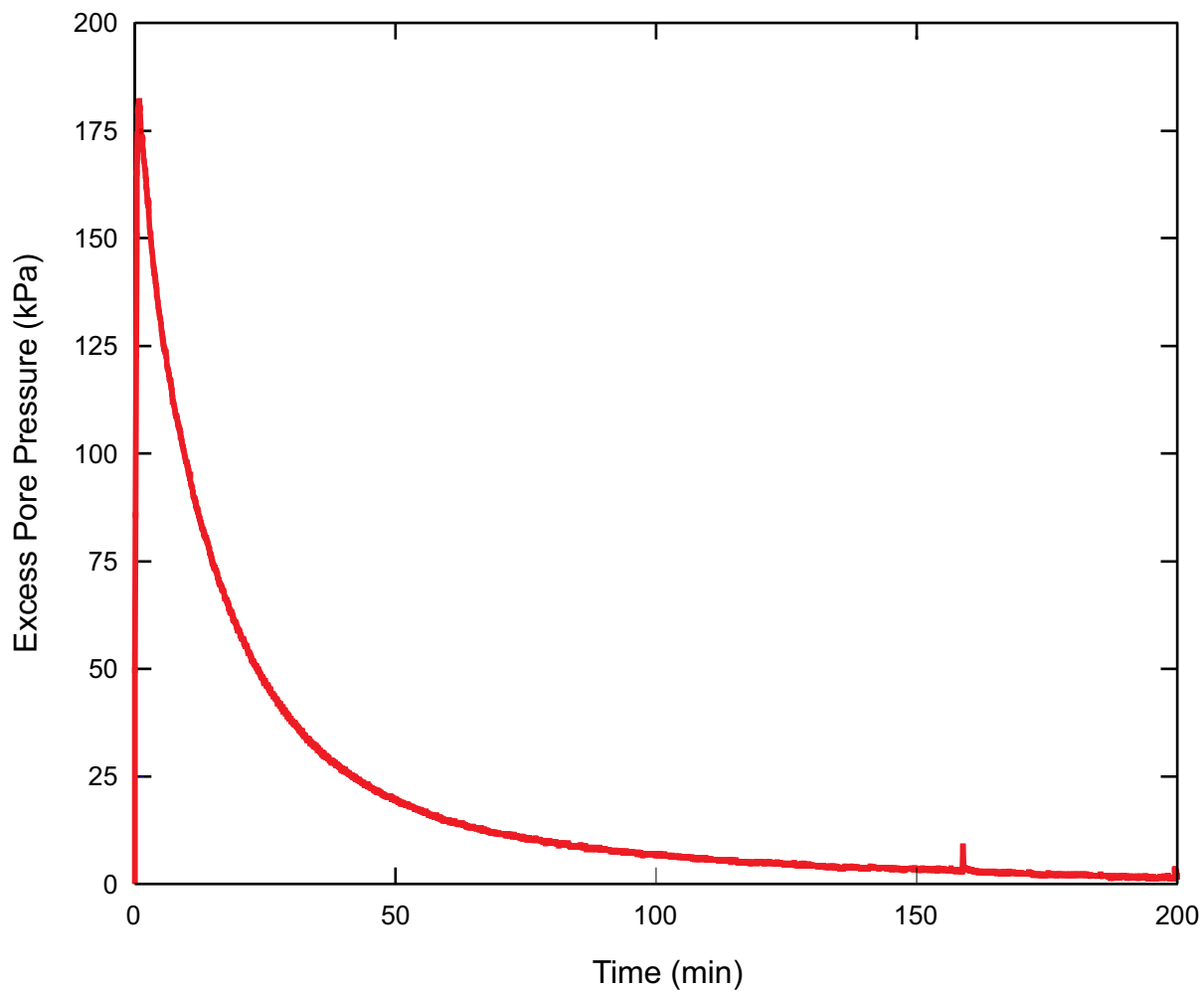
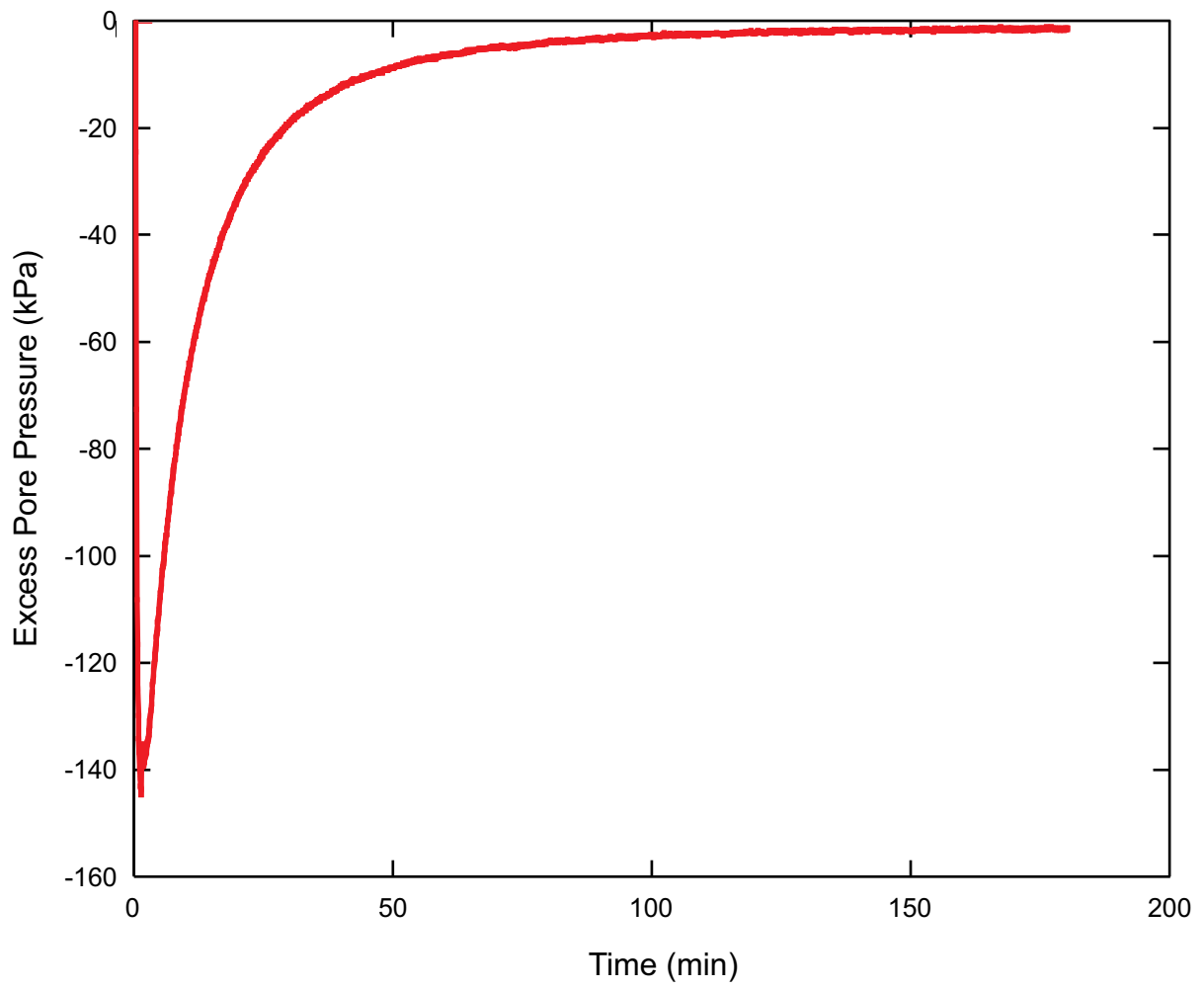Figure 5.7. Sample pore pressure response measured at the base of the sample to a new load increment.

Figure 5.8. Sample pore pressure response measured at the base of the sample to a new unload increment.
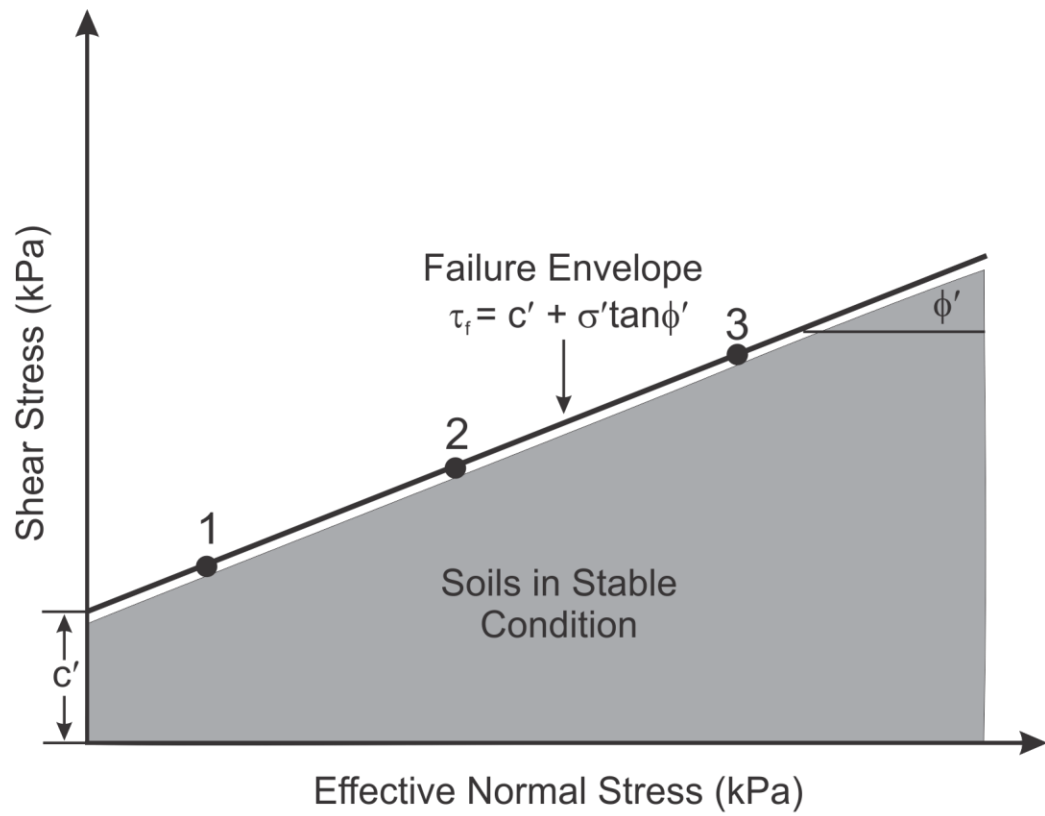
Figure 6.1. Maximum shear strength related to effective normal stress from triaxial tests.
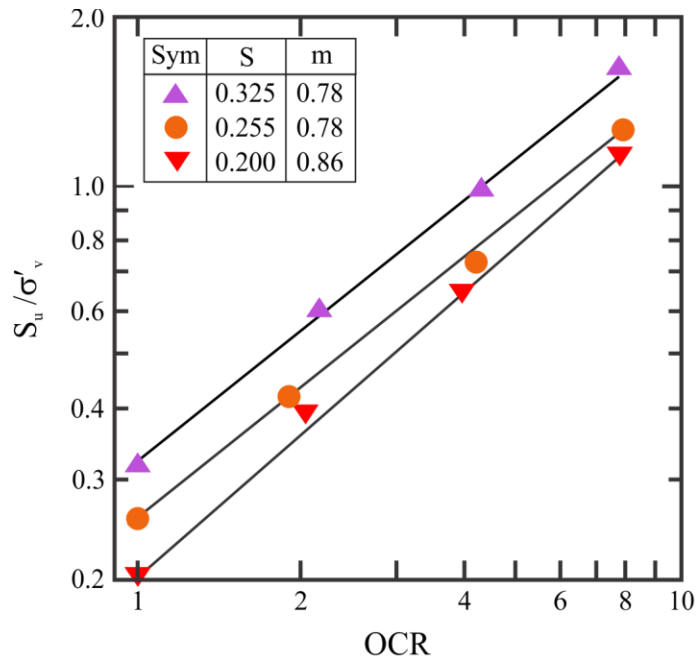
Figure 6.2. Example of a SHANSEP analysis for plastic marine clay showing the OCR vs undrained strength ratio relationship (after Ladd and DeGroot, 2003).
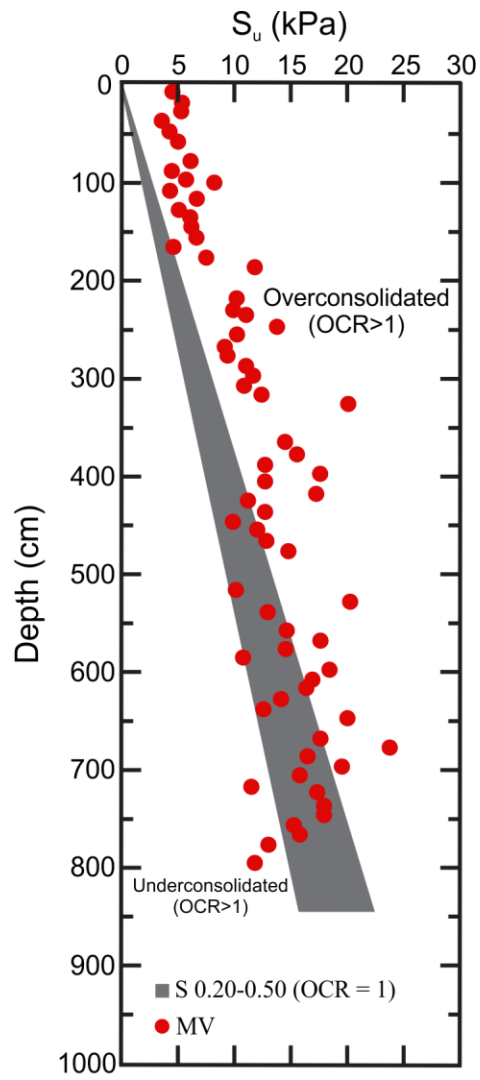
Figure 6.3. A comparison of the undrained shear strength
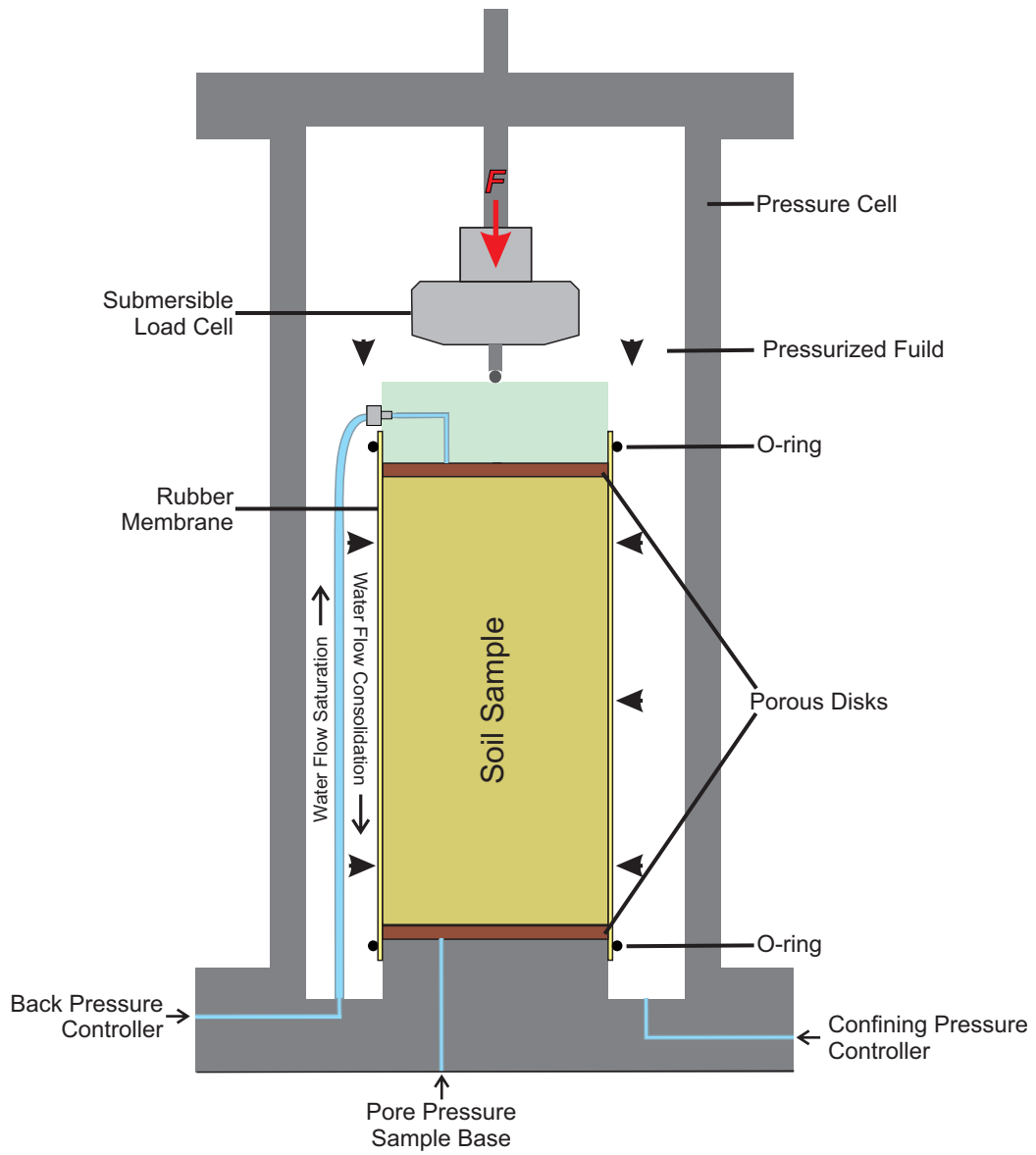calculated using the S ratio and the MV shear strength data

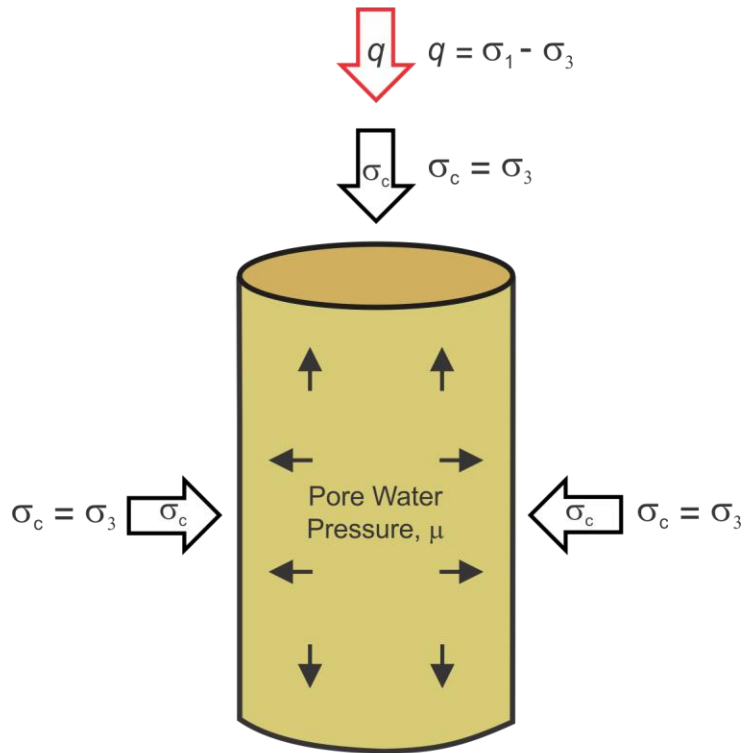Figure 6.4. General set-up of a soil sample in a triaxial cell.

Figure 6.5. Sample stress during the shear stage where σ_c is the confining pressure that remains constant during the shear stage.
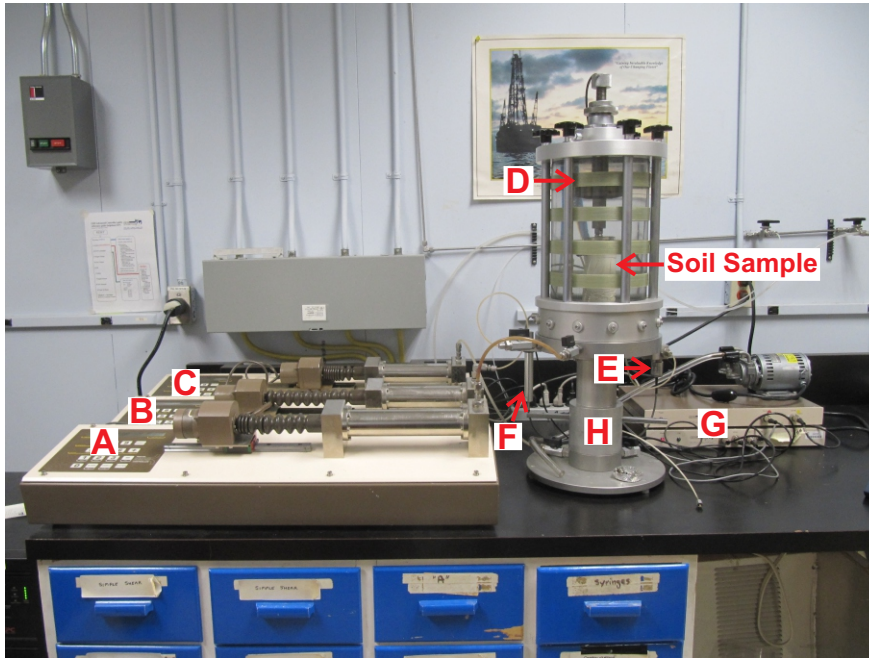
Figure 6.6. The GDS CRS consolidation system includes 3 pressure volume controllers (A, B, C), submersible load cell (D), pore pressure transducer (E), axial displacement transducer (F), DAQ system (G) and Bishop and Wesley triaxial cell (H). Photograph by K. MacKillop. NRCan photo 2021-526.
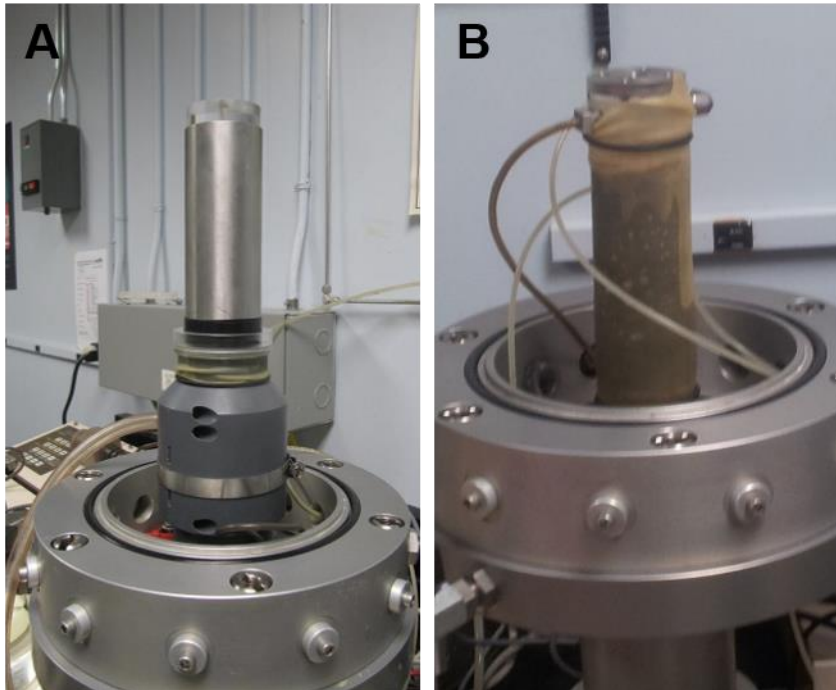
Figure 6.7. Placement of the sample into the rubber membrane in the B&W triaxial cell. A) Sampling ring with sample and split form with rubber membrane. B) Soil sample in the rubber membrane with top cap attached. Photographs taken by K. MacKillop. (A) NRCan photo 2021-527. (B) NRCan photo 2021-528.
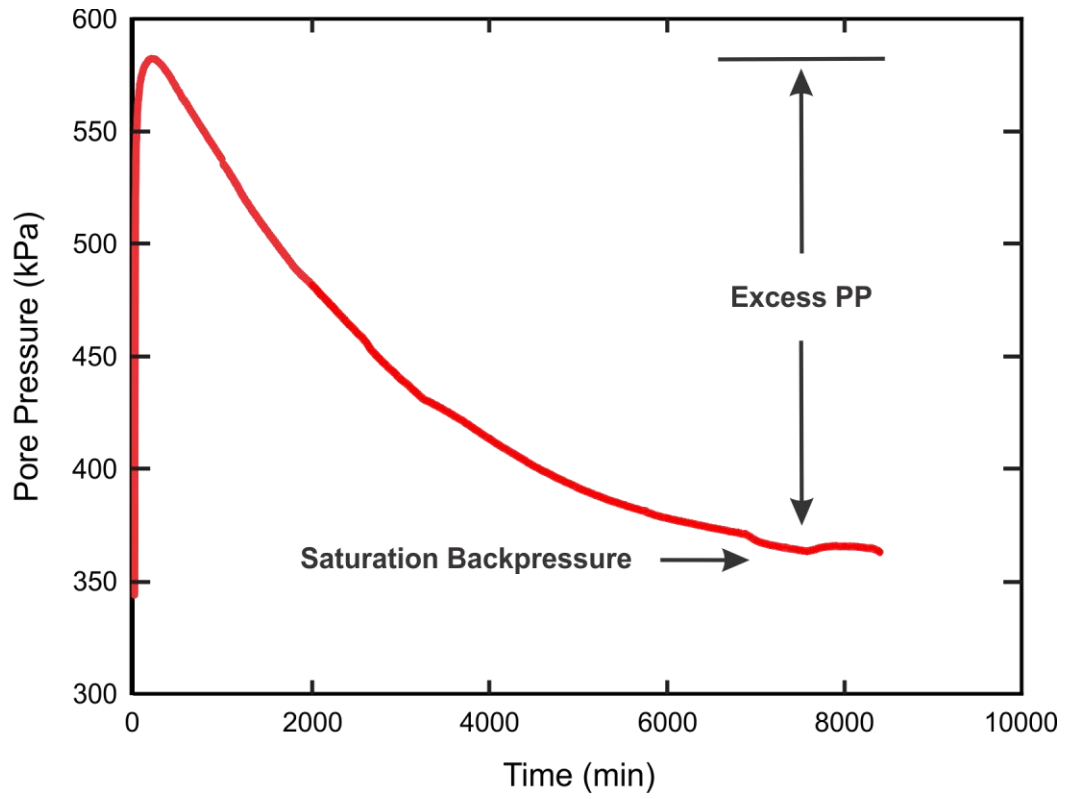
Figure 6.8. Triaxial test data illustrating pore pressure dissipation during the isotropic consolidation stage.
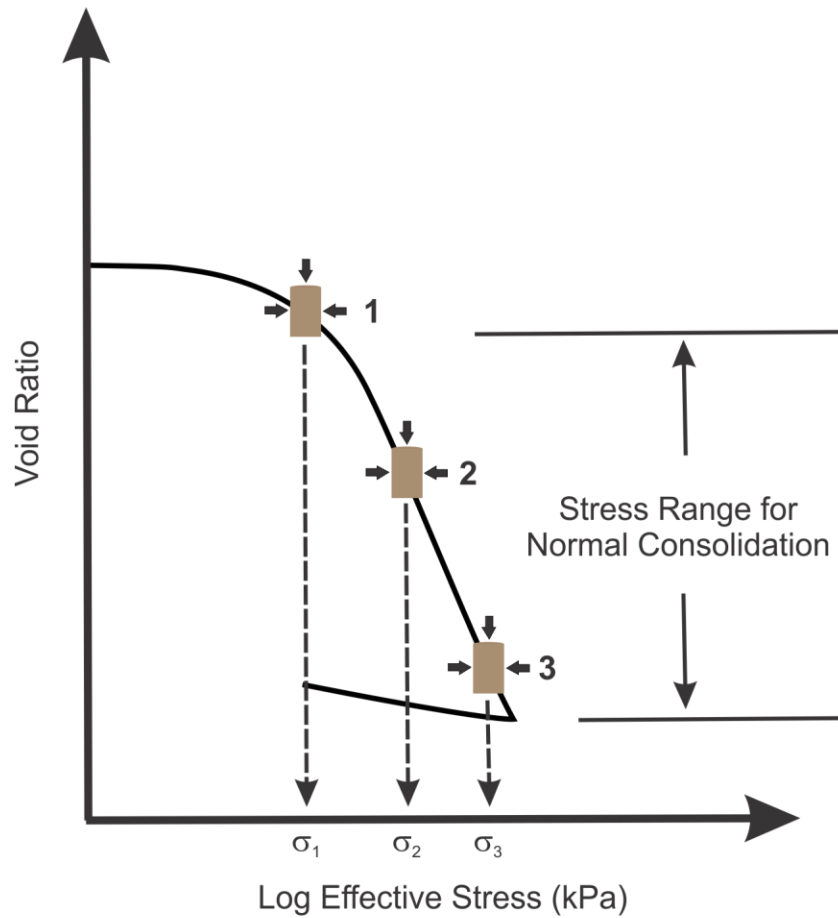
Figure 6.9. Consolidation test data illustrating the procedure for selecting 3 confining pressures for CIU triaxial testing. Note that confining pressures 2 and 3 are in the normal consolidation stress range for the sample.
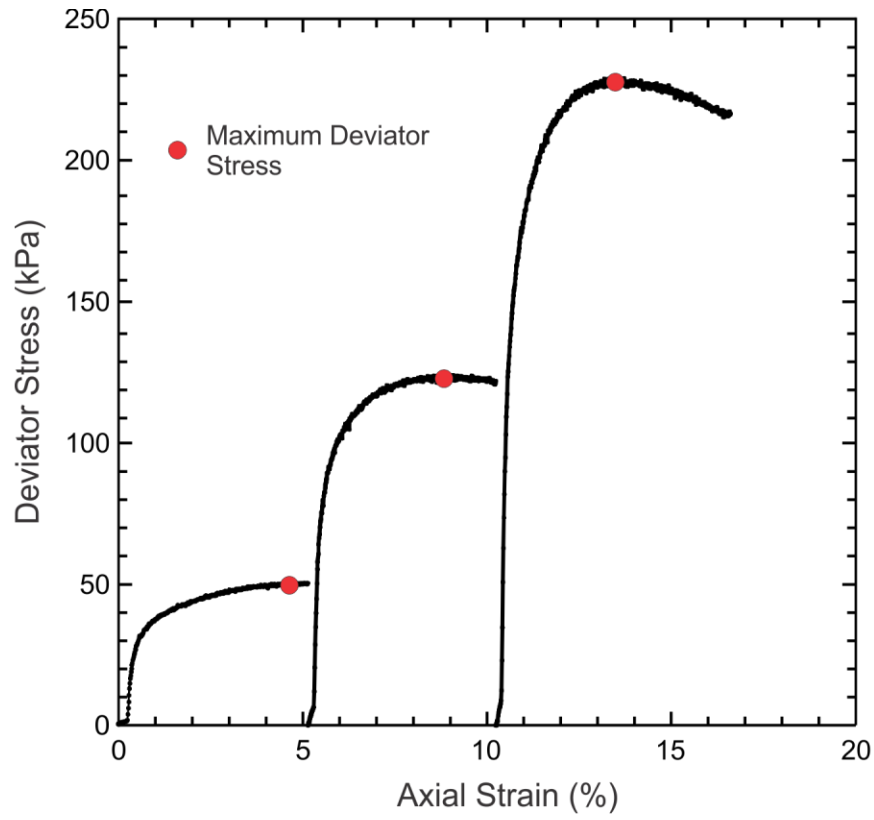
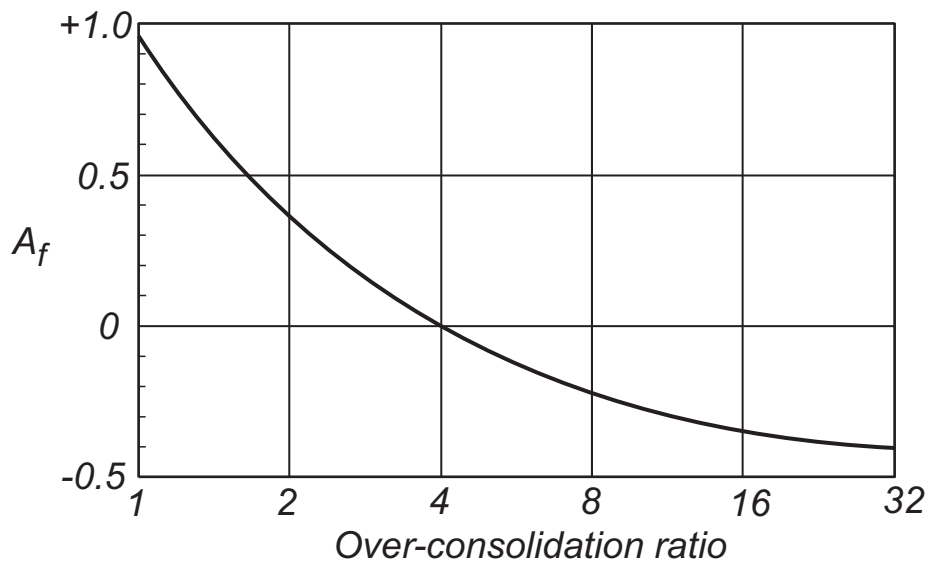Figure 6.10. Triaxial test data illustrating the stress-strain for the 3 shear stages.

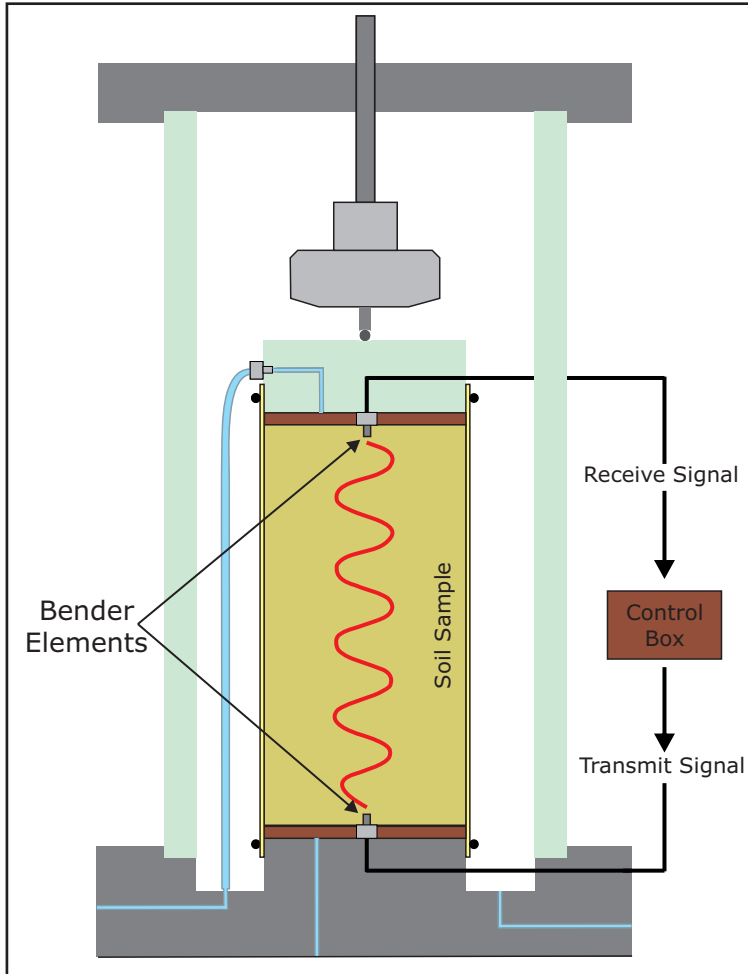Figure 611. Relationship between A_f and OCR values (after Bishop and Henkel 1962) .

Figure 7.1. Schematic detailing the typical configuration of a pair of vertical bender elements set in a triaxial specimen.
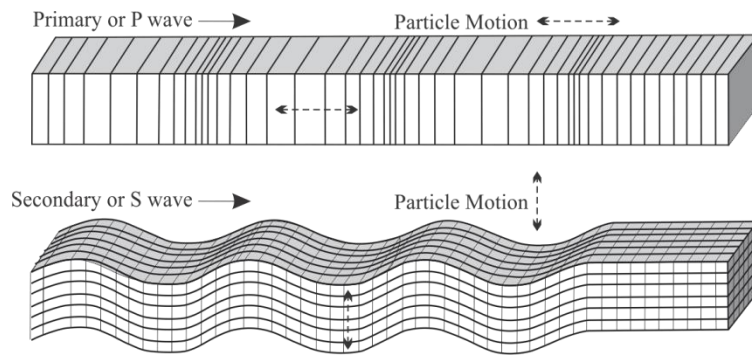
Figure 7.2. Schematic of P & S wave frequencies.
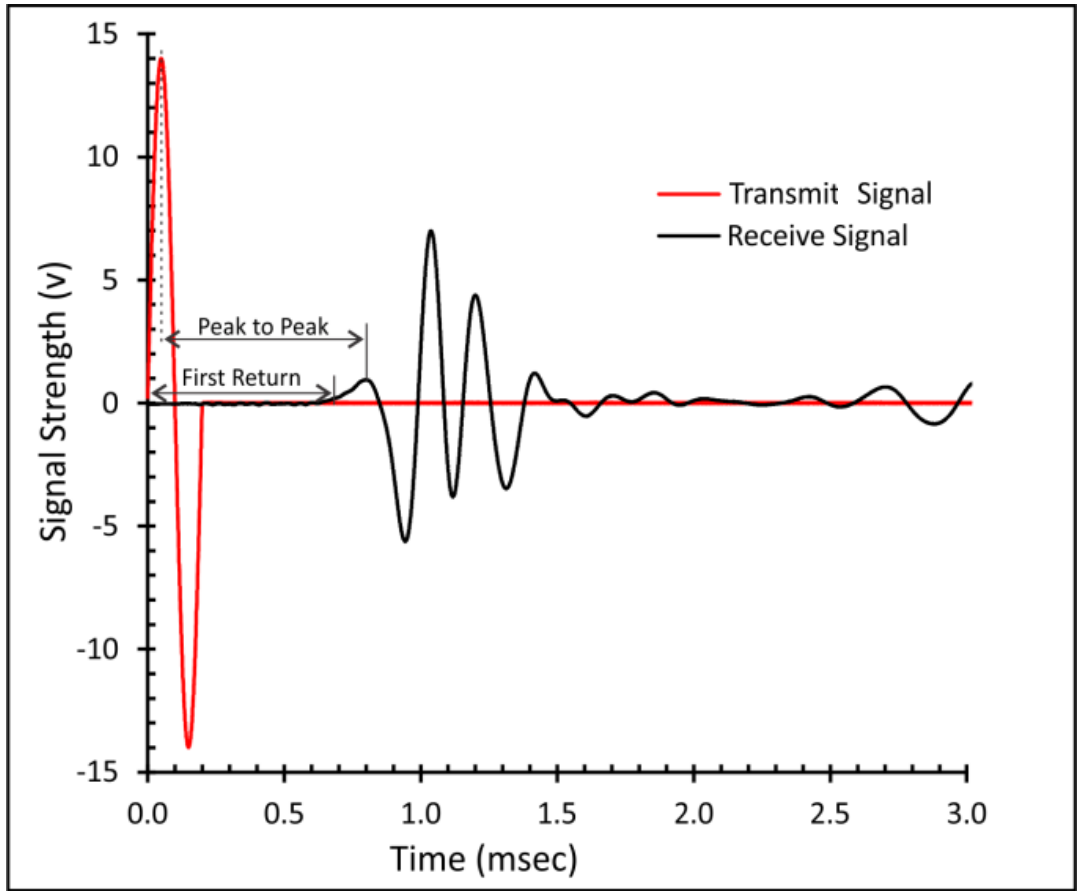
Figure 7.3. Plot of S-wave transmit and receive signals showing peak to peak and first return methods for manually picking S-wave receive signal.

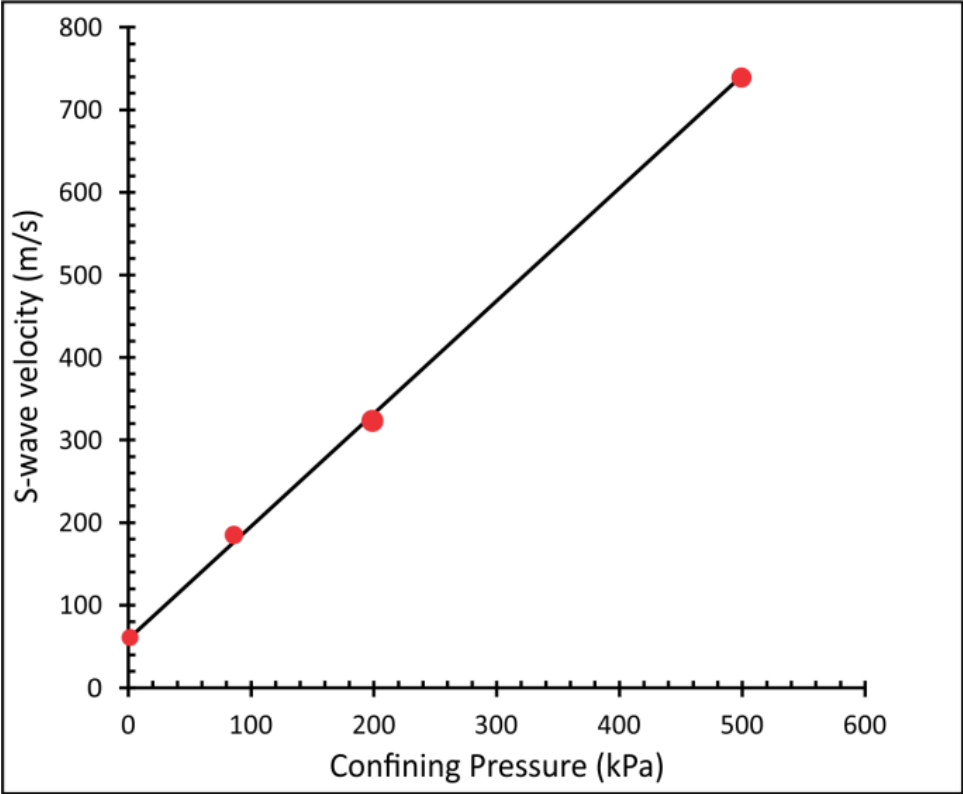Figure 7.4. Example of S-wave data obtained from triaxial sample 20130290048PC_483-494cm. S-wave is measured at different confining pressures during the triaxial test.
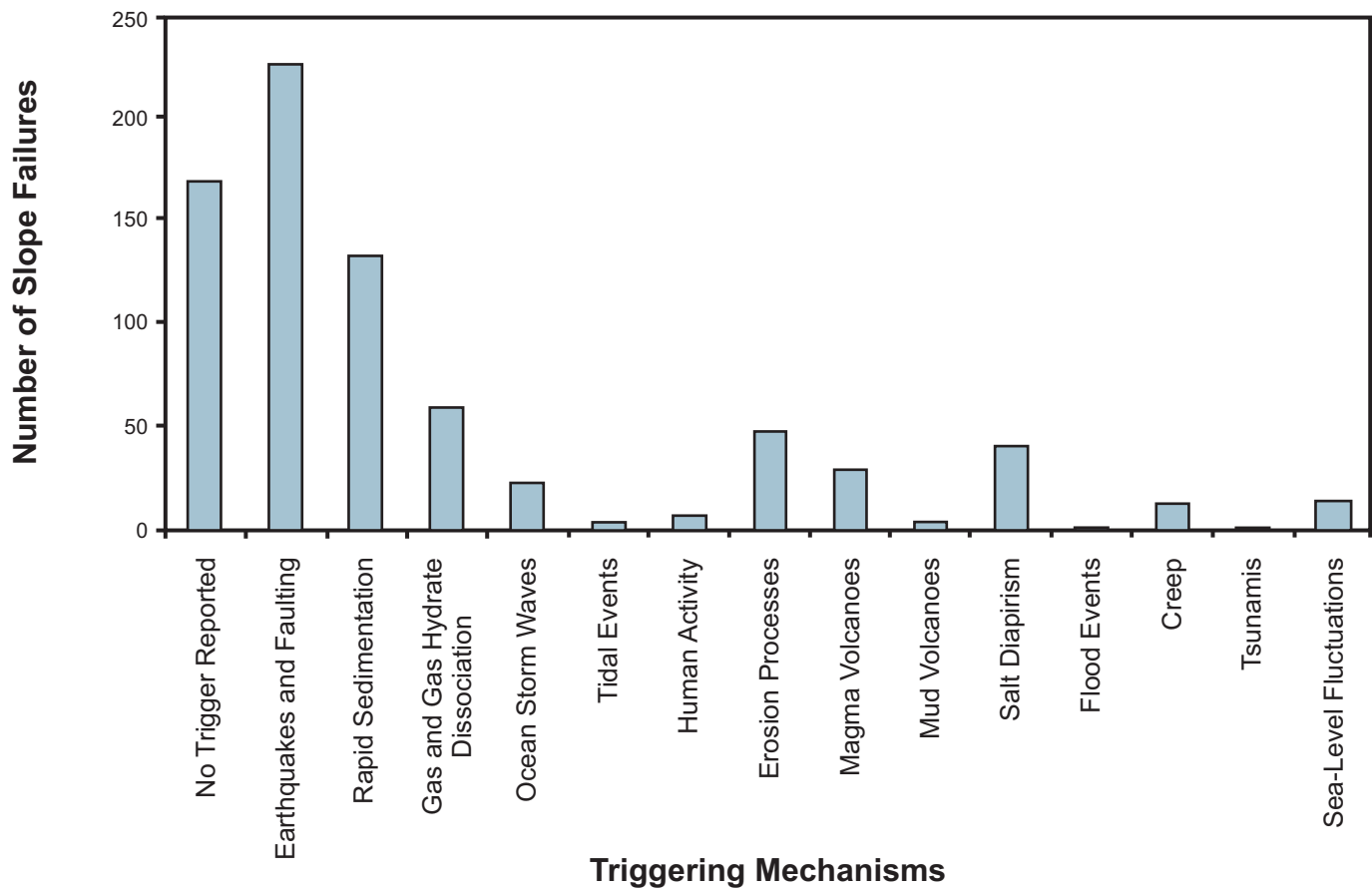
Figure 8.1. Triggering mechanisms for 534 submarine slides (Hance, 2003)

Figure 8.2. The equilibrium of an infinite slope under undrained conditions, with gravity forces, T (after Morgenstren, 1967). Only the forces used in the FS calculation are shown.
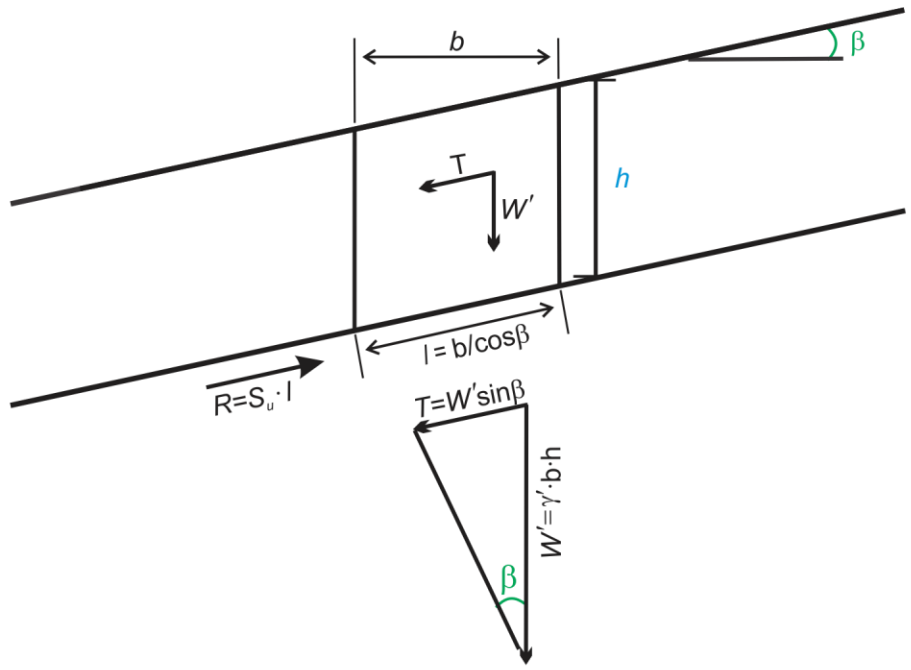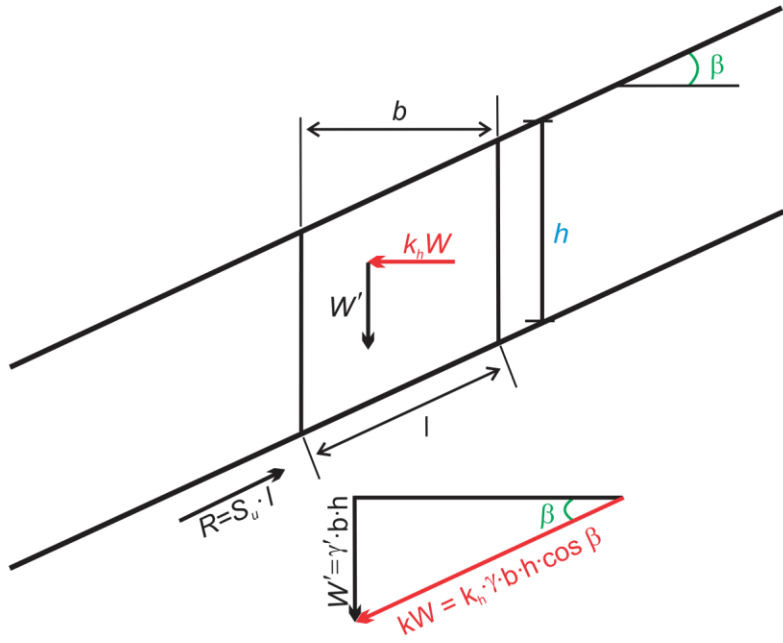
Figure 8.3. The equilibrium of an infinite slope under undrained conditions, with an earthquake force (kW, after Morgenstren, 1967). Only the forces used in the FS calculation are shown.
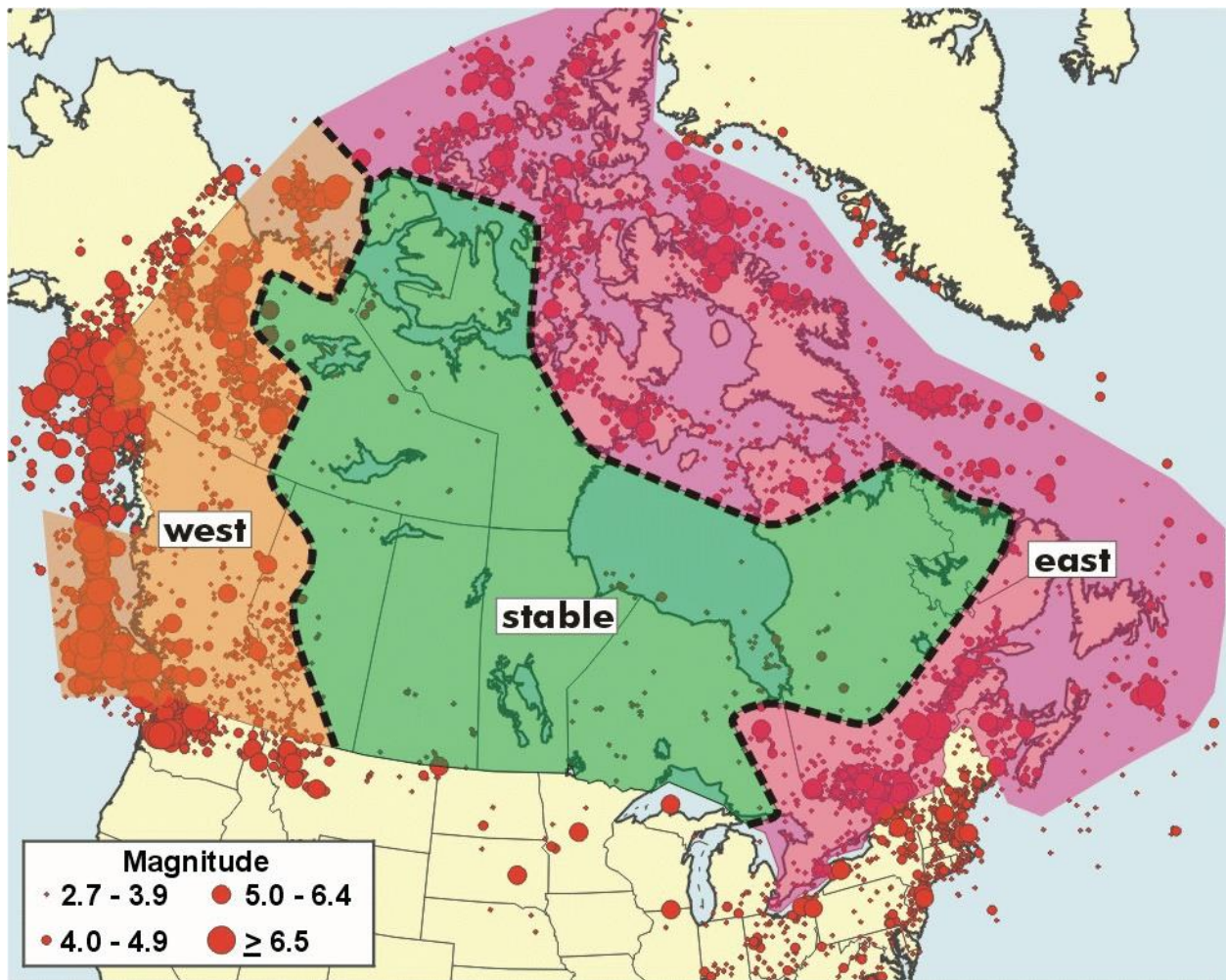
Figure 8.4. Map showing the regional seismicity zones (West, Stable, and East) in Canada as identified by Adams & Halchuk 2004.
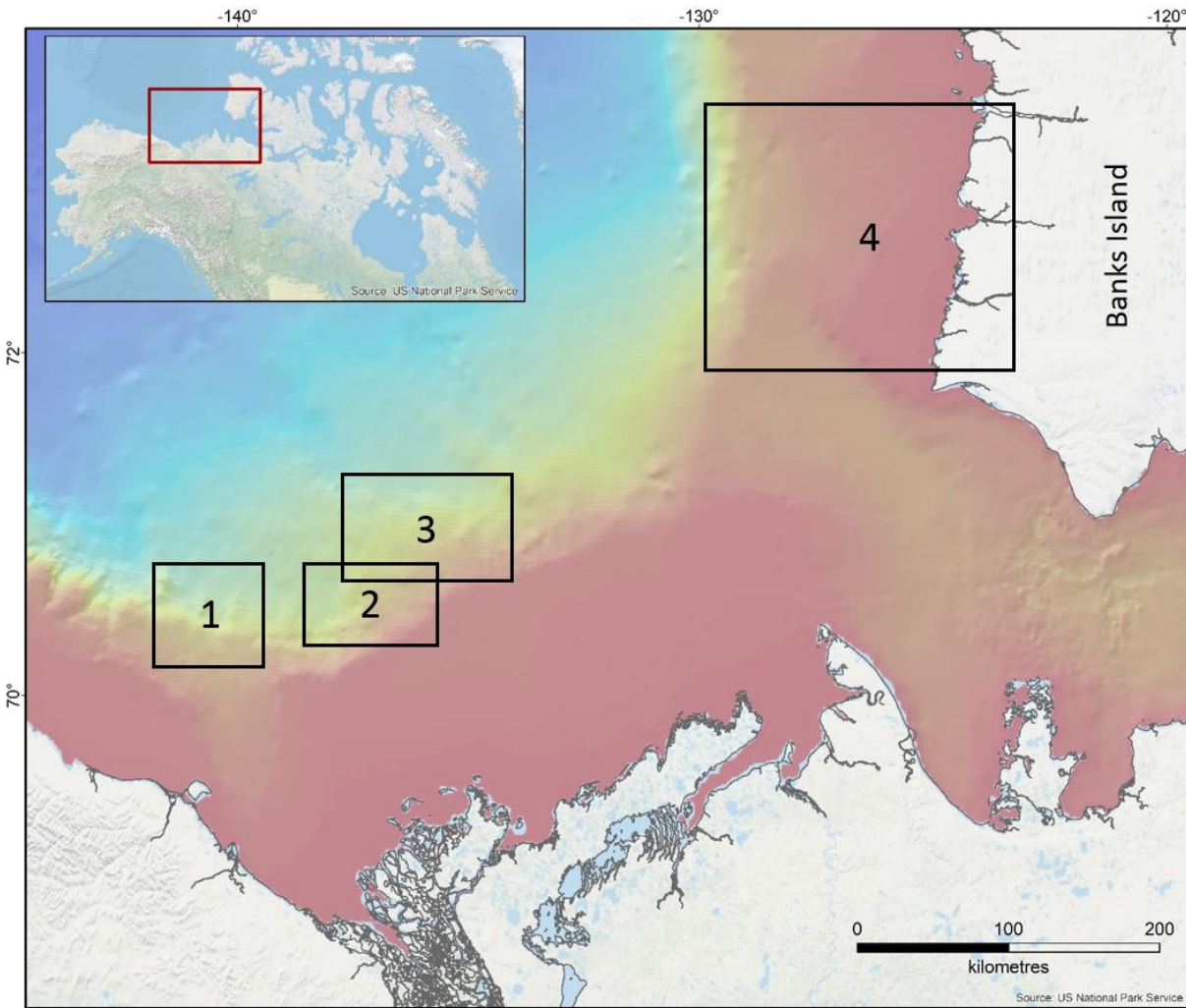
Figure 9.1. Overview map showing location of Beaufort Sea and location of regions within the study area. Region 1 – Western, Region 2 – Central, Region 3 – Eastern, and Region 4 – Banks Island.
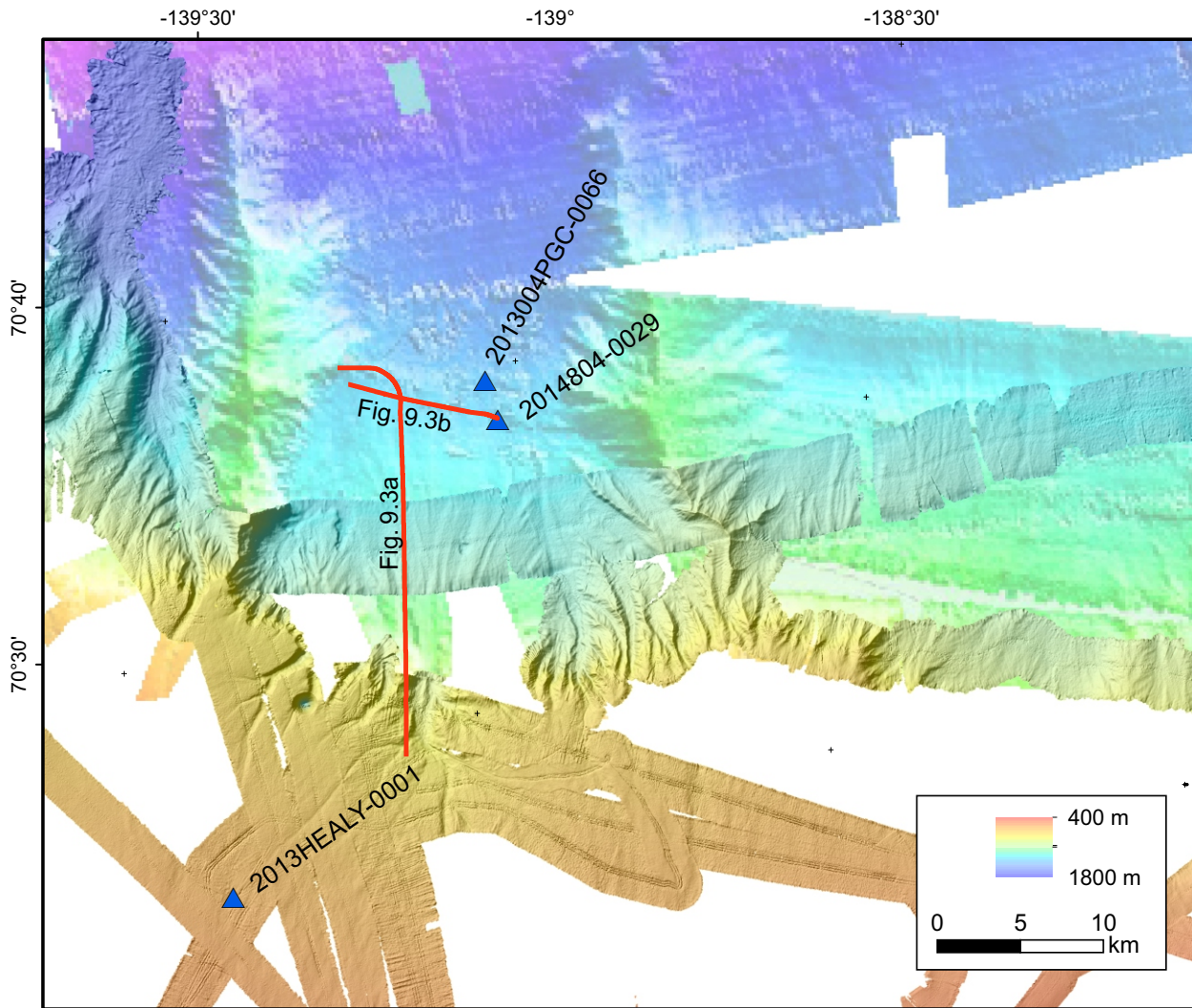
Figure 9.2. Region 1 core locations at the mouth of the Mackenzie Trough on Araon and ArcticNet multibeam bathymetry.

N — **Fig. 9.3a** — **S**

numerous mass failures

profile intersection point

Holocene-age MTD

Healy 2013-0001 (15 km west) lateral equivalent

top section / bottom section

glacimarine mud

buried debris flows

glacial diamict

2013Healy_SEISMIC_3_5KHZ_243_0817_to_243_1246_envelope.jp2

Time, ms / Depth, m @ 1500 m/s

Distance Along Track (km)

WNW — **Fig. 9.3b** — **ESE**

1500m WD / 70m projected

2014804-0029

profile intersection point

Holocene age MTD

glacimarine mud

top section

bottom section

2014804_SEISMIC_KNUDSON_250_0557_to_250_1204_envelope.jp2

E King, Sept. 2019
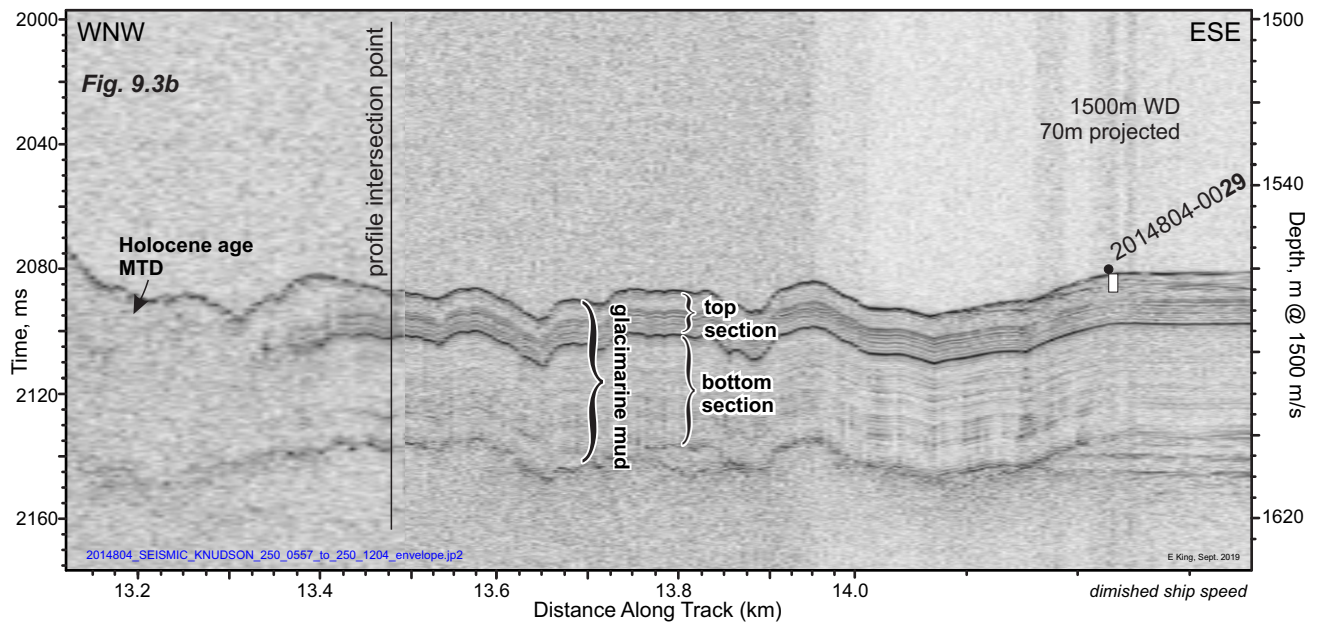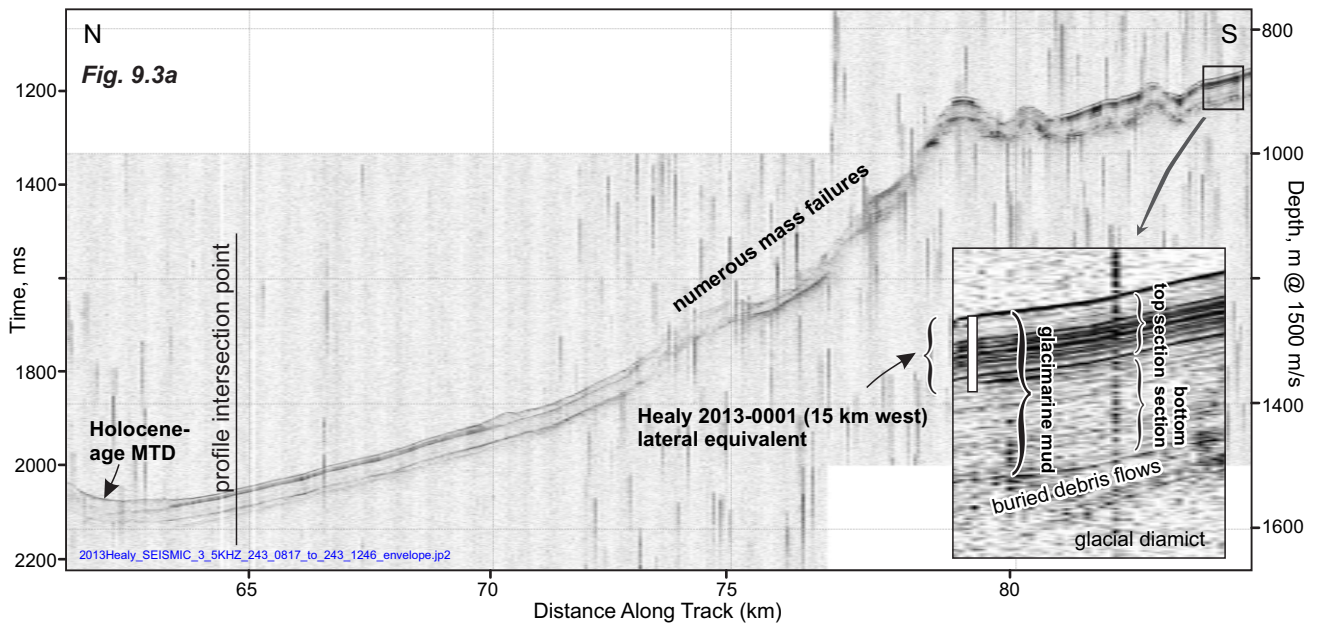
dimished ship speed

Distance Along Track (km)

Figure 9.3. 3.5 kHz sub-bottom profile showing the acoustic stratigraphy and position of piston core sites in Region1. Core Healy20130001pc, Fig. 9.3a, recovered a continuous surficial stratified glacimarine and Holocene mud blanket at the of Mackenzie Trough (shallower than ~1000 m). Core 20148040029pc, Fig 9.3b lies well beyond the shelf break between two large exhumed north-south-oriented ridges (Fig. 9.2) and on a relatively flat-lying area. The glacimarine and Holocene blanket, sampled here, has direct stratigraphic equivalents on the shelf.
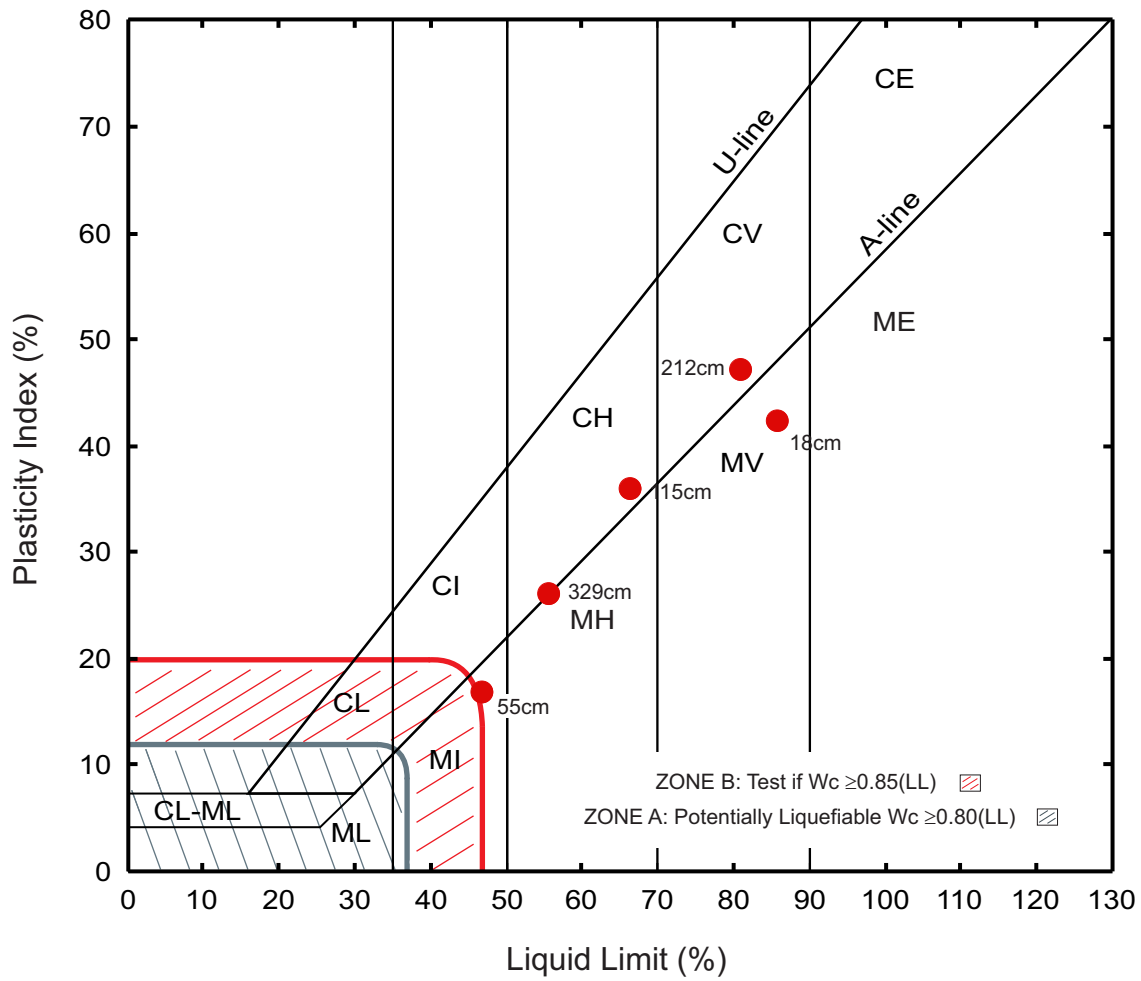
Figure 9.4. Plasticity chart showing Atterberg limit results of piston core 20148040029.
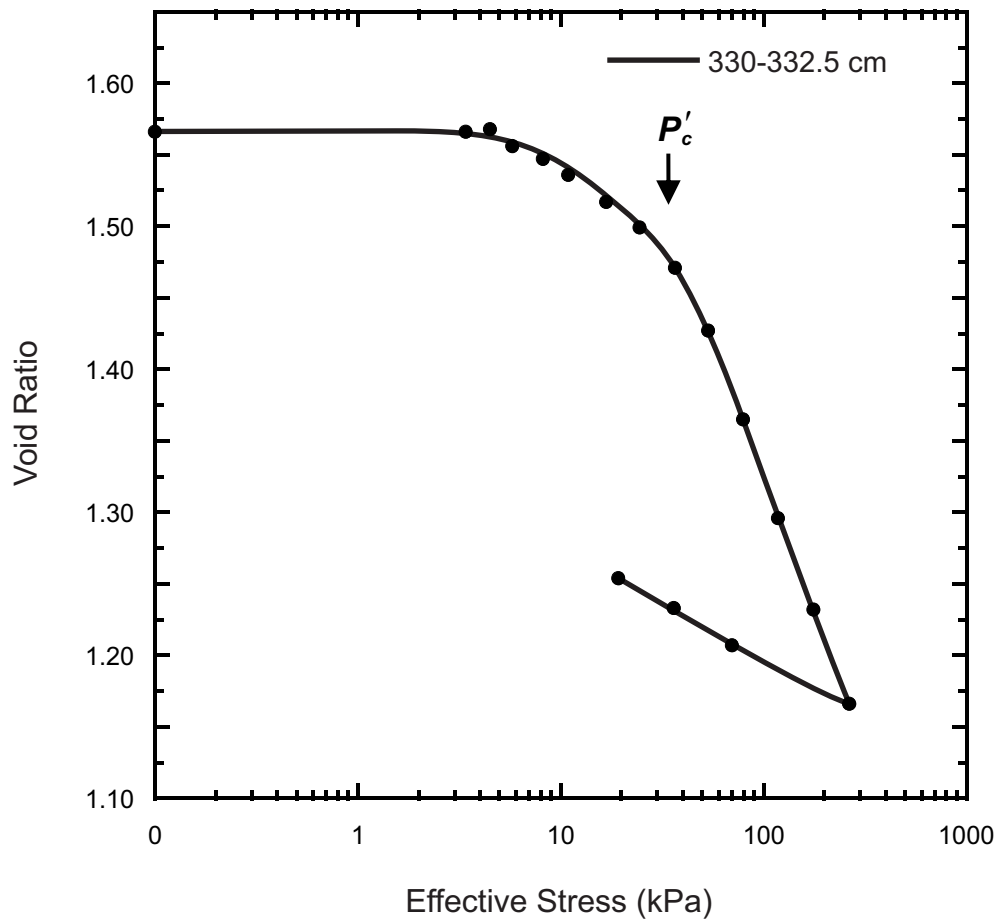
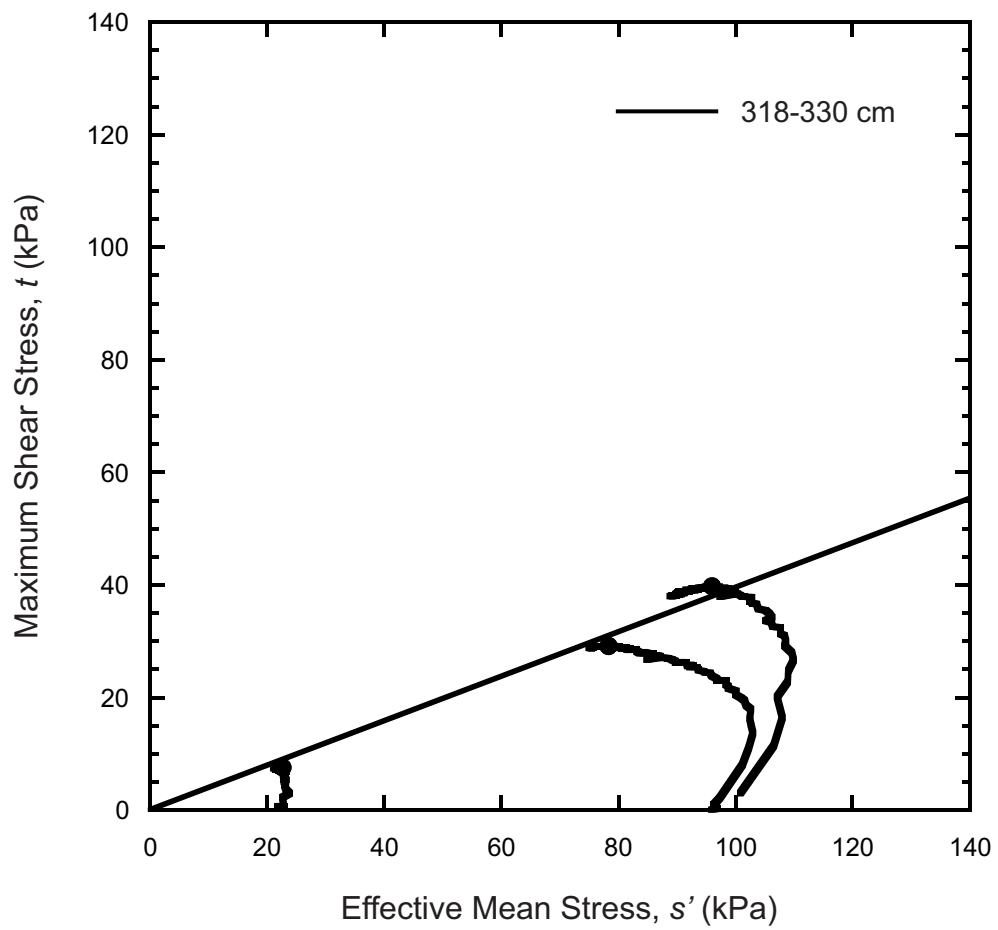Figure 9.5. Consolidation plot for piston core 20148040029.

Figure 9.6. Stress paths and failure envelope from triaxial test results for piston core 20148040029.
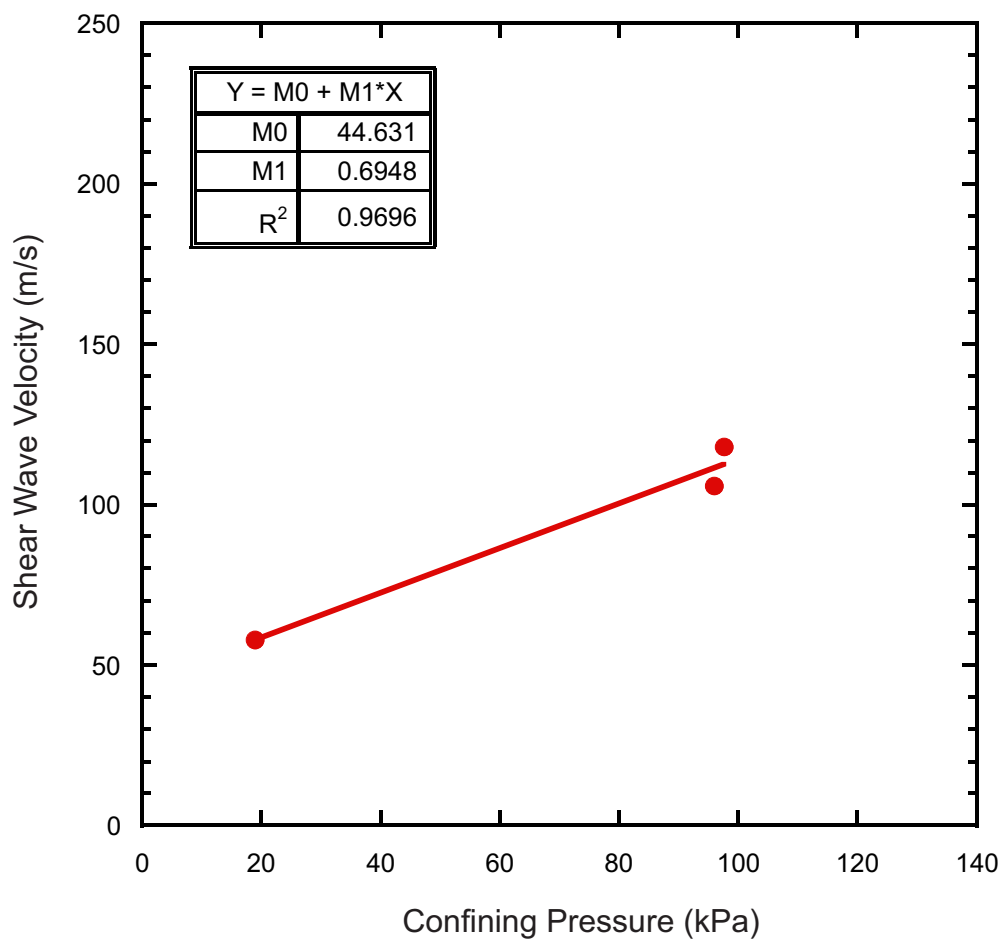
Figure 9.7. Shear wave velocities at various confining pressures for piston core 20148040029.
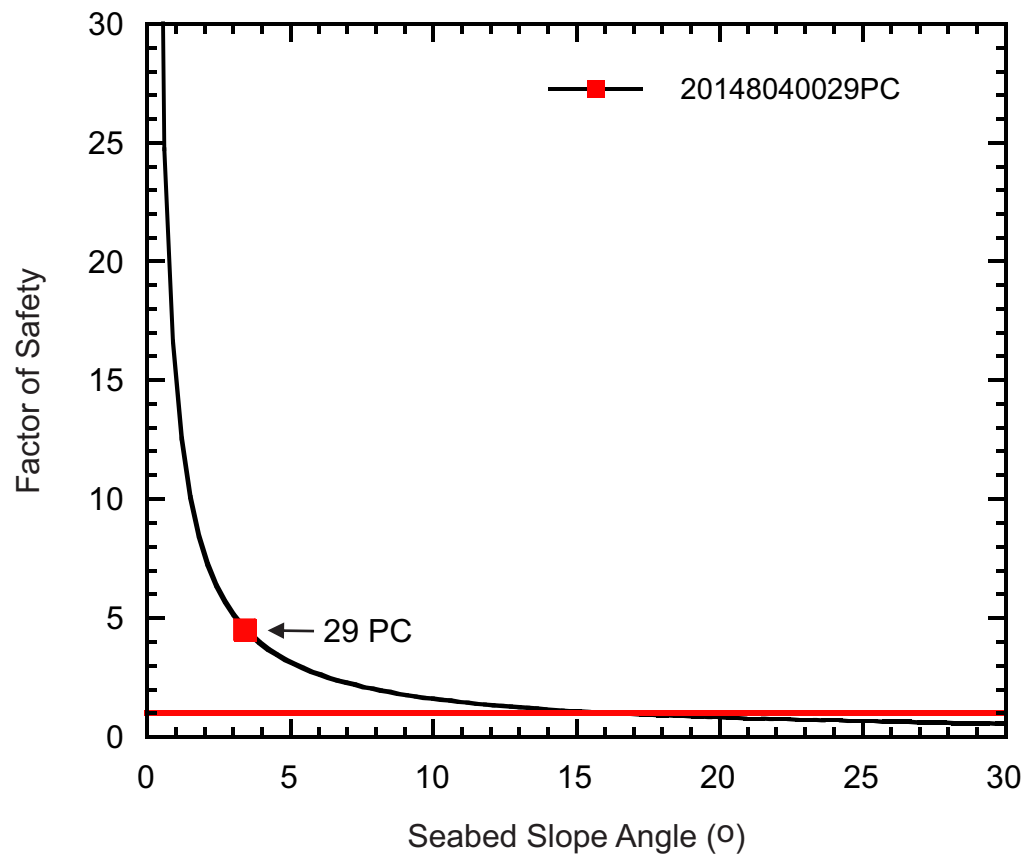
Figure 9.8. FS at various slope angles for piston core 20148040029. The red square identifies the minimum FS for the present-day slope angle of the core site.
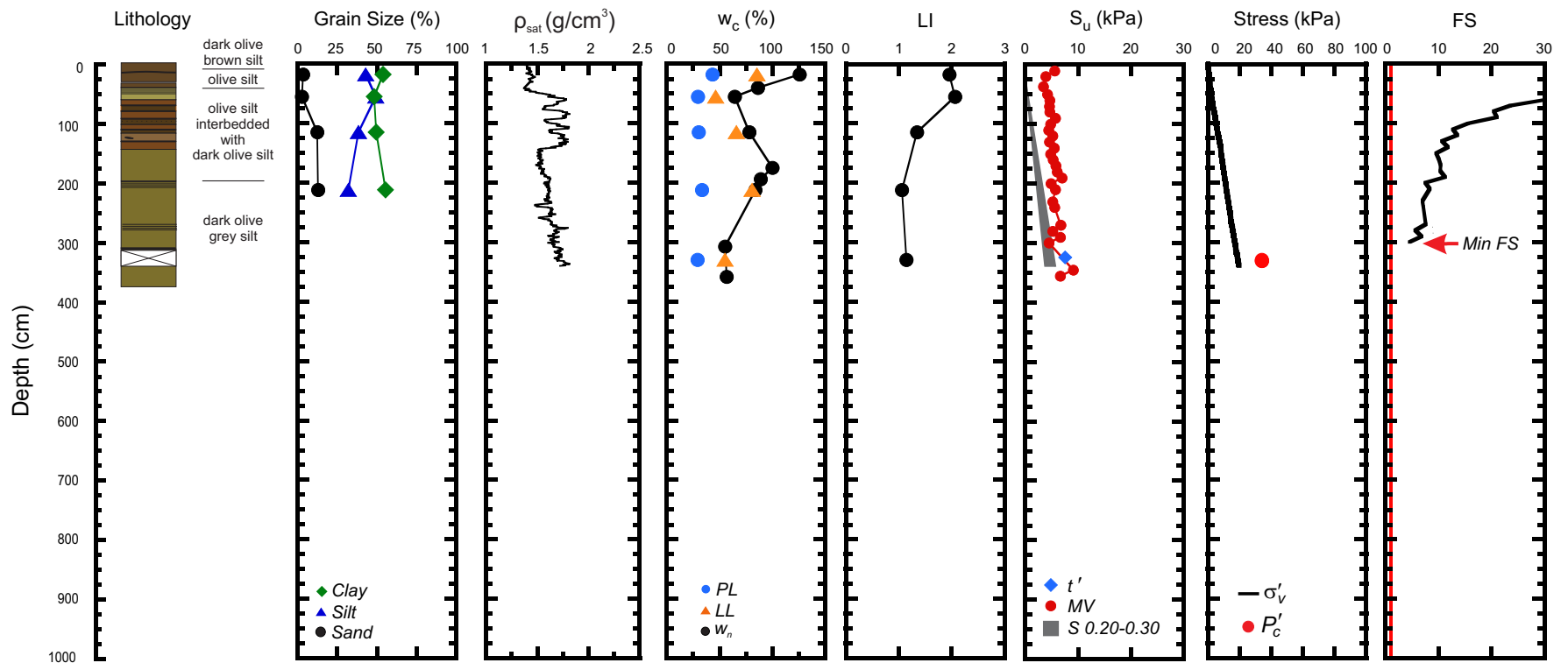
Figure 9.9. Geotechnical profile for core 20148040029 from Region 1. (ρ_{sat}= saturated bulk density, w_c = water content, w_n = natural in-situ water content, PL = plastic limit, LL = liquid limit, LI = liquidity index, S_u = undrained shear strength, MV = laboratory miniature vane shear strength, t' = maximum shear stress, S = shear strength calculated from the normalized strength ratio, σ'_v = effective overburden stress, P'_c = past maximum stress, FS = factor of safety).
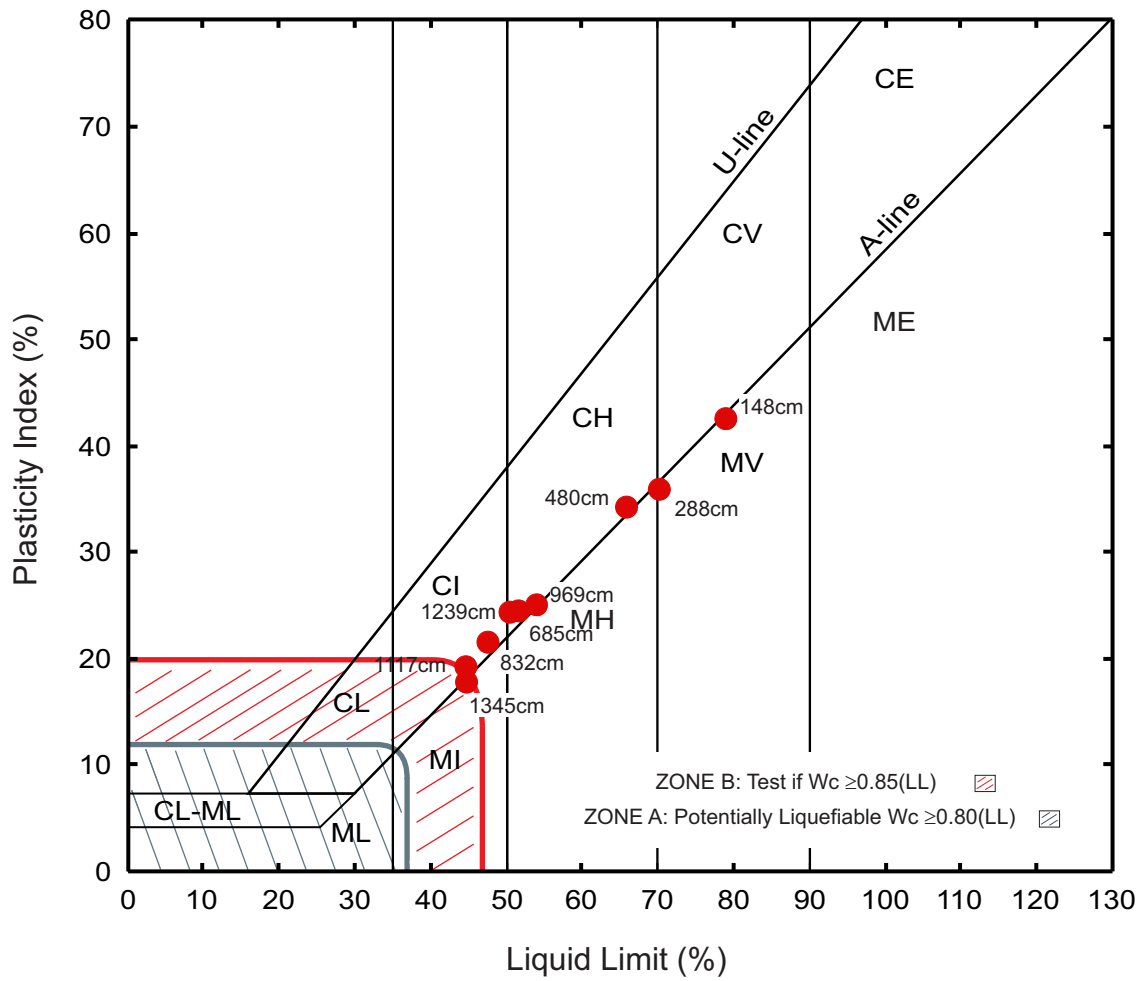
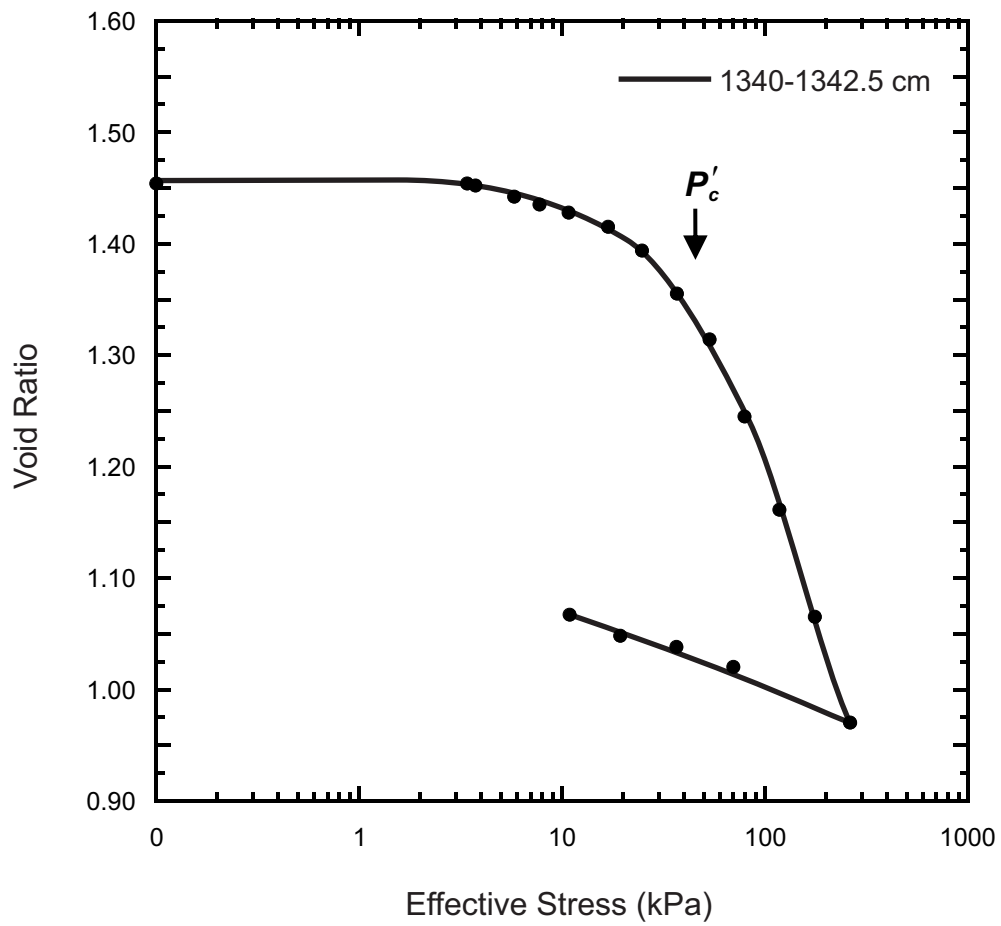Figure 9.10. Plasticity chart showing Atterberg limit results of piston core 2013HEALY0001.

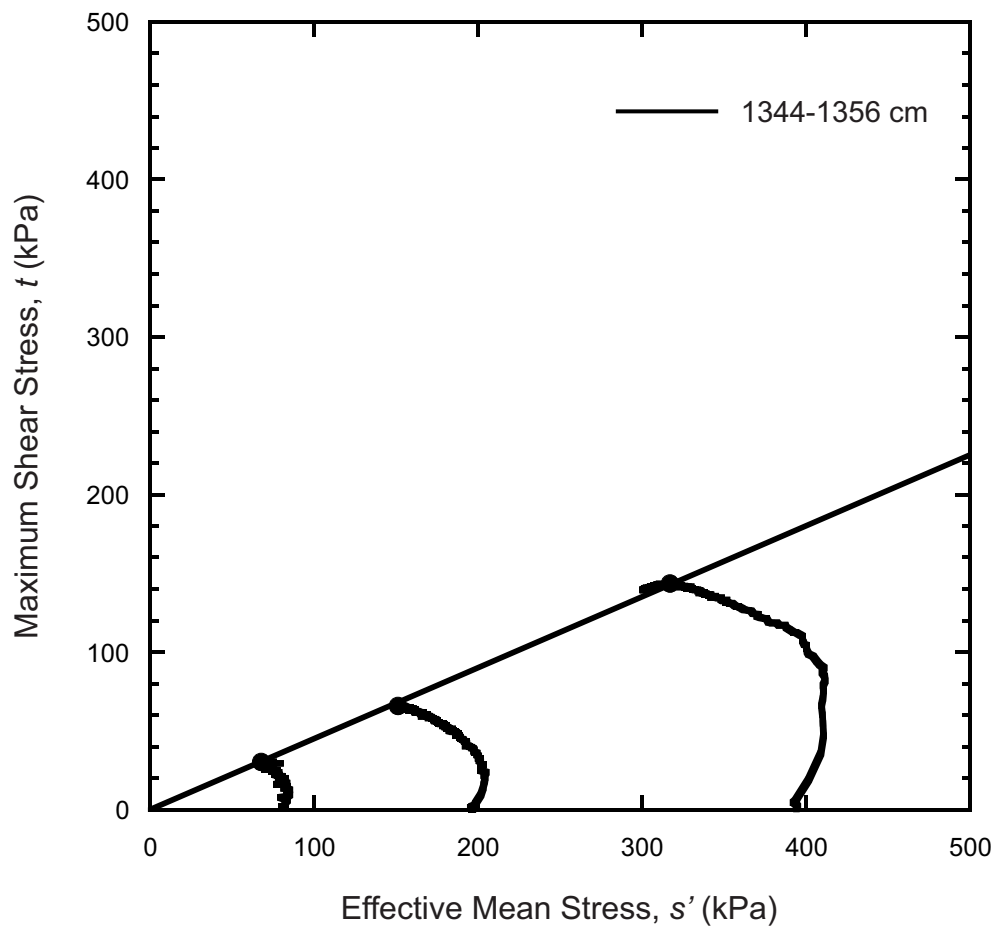Figure 9.11. Consolidation plot for piston core 2013HEALY0001.

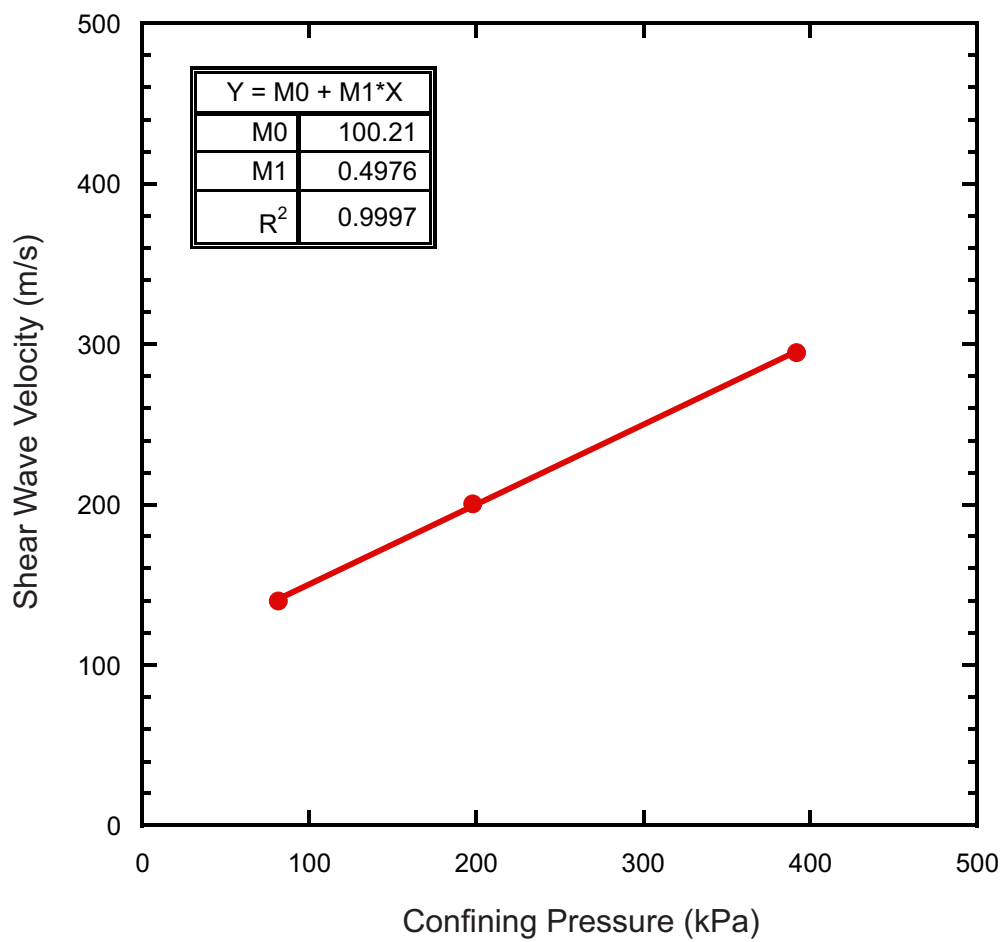Figure 9.12. Stress paths and failure envelopes from triaxial test results for piston core 2013HEALY0001.

Figure 9.13. Shear wave velocities at various confining pressures for piston core 2013HEALY0001.
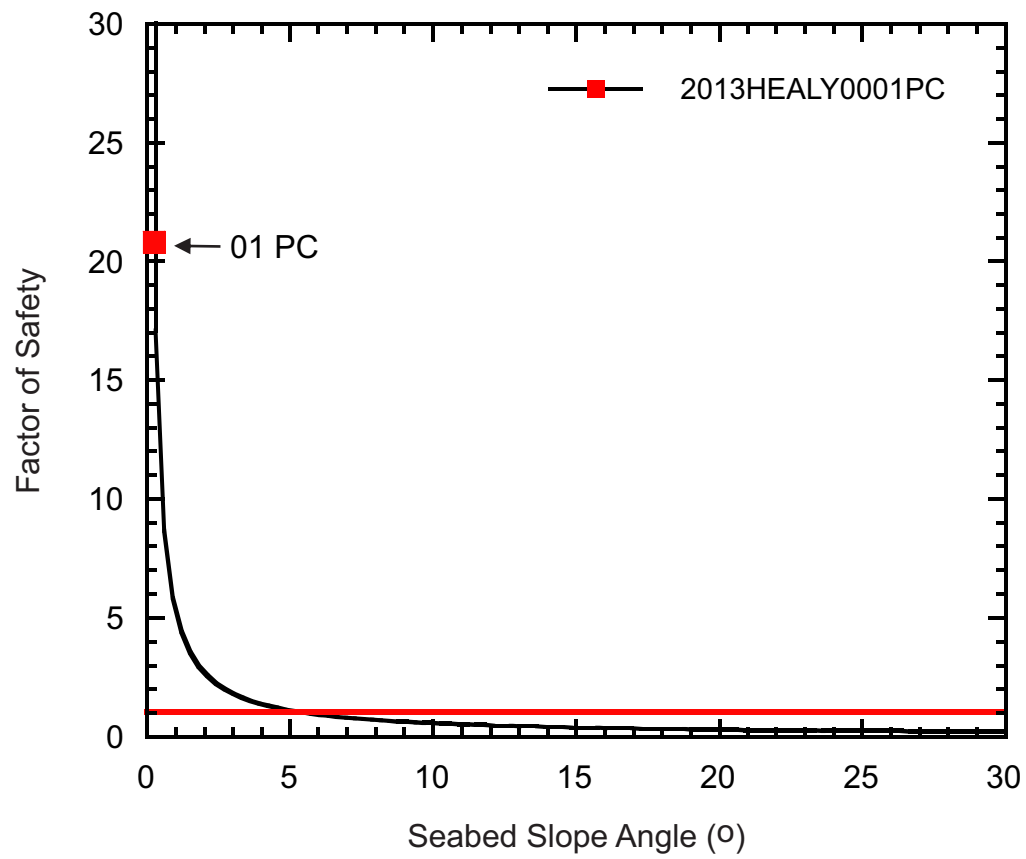
Figure 9.14. FS at various slope angles for piston core 2013HEALY0001. The red square identifies the minimum FS for the present-day slope angle of the core site.
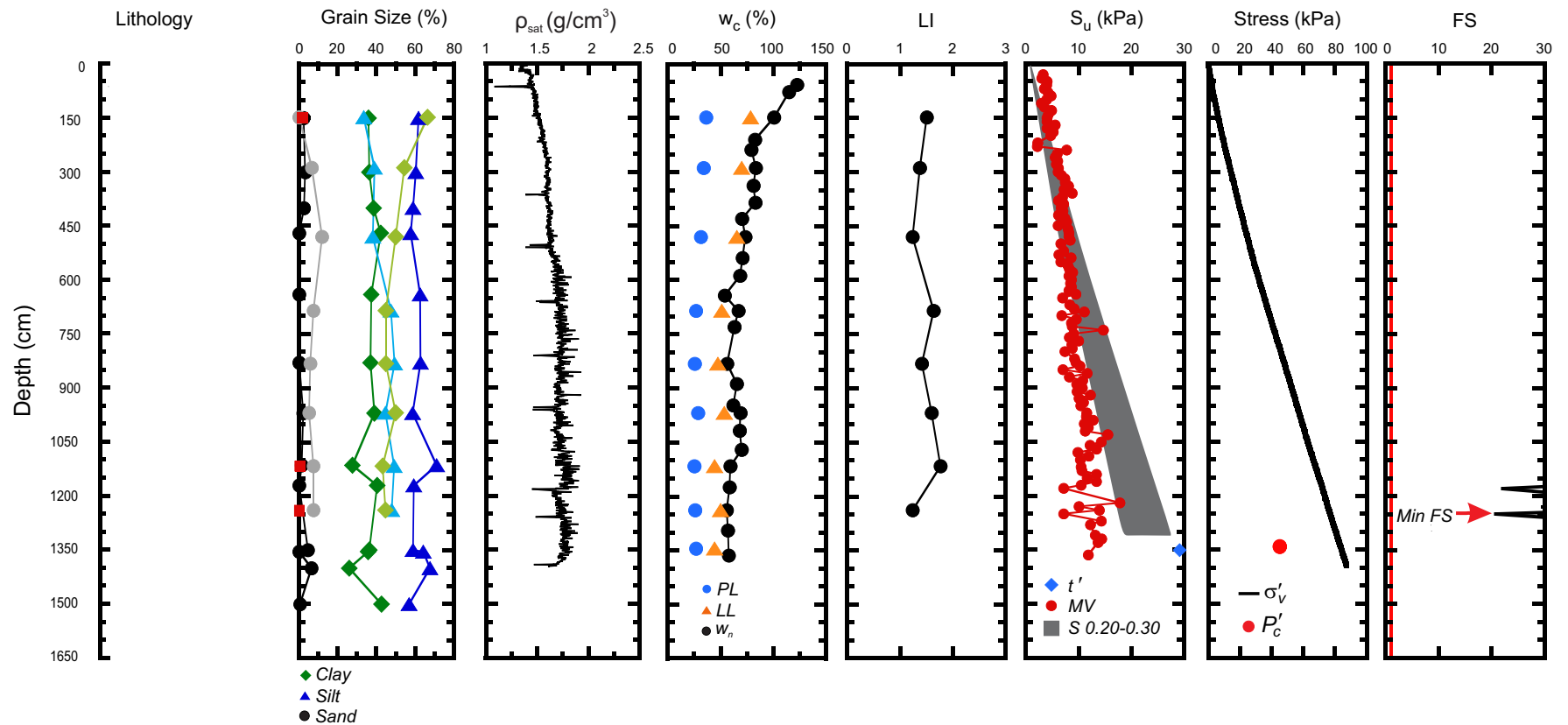
Figure 9.15. Geotechnical profile for core 2013HEALY0001 from the MacKenzie Trough. (ρ_{sat} = saturated bulk density, w_c = water content, w_n = natural in-situ water content, PL = plastic limit, LL = liquid limit, LI = liquidity index, S_u = undrained shear strength, MV = laboratory miniature vane shear strength, t' = maximum shear stress, S = shear strength calculated from the normalized strength ratio, σ'_v = effective overburden stress, P'_c = past maximum stress, FS = factor of safety).
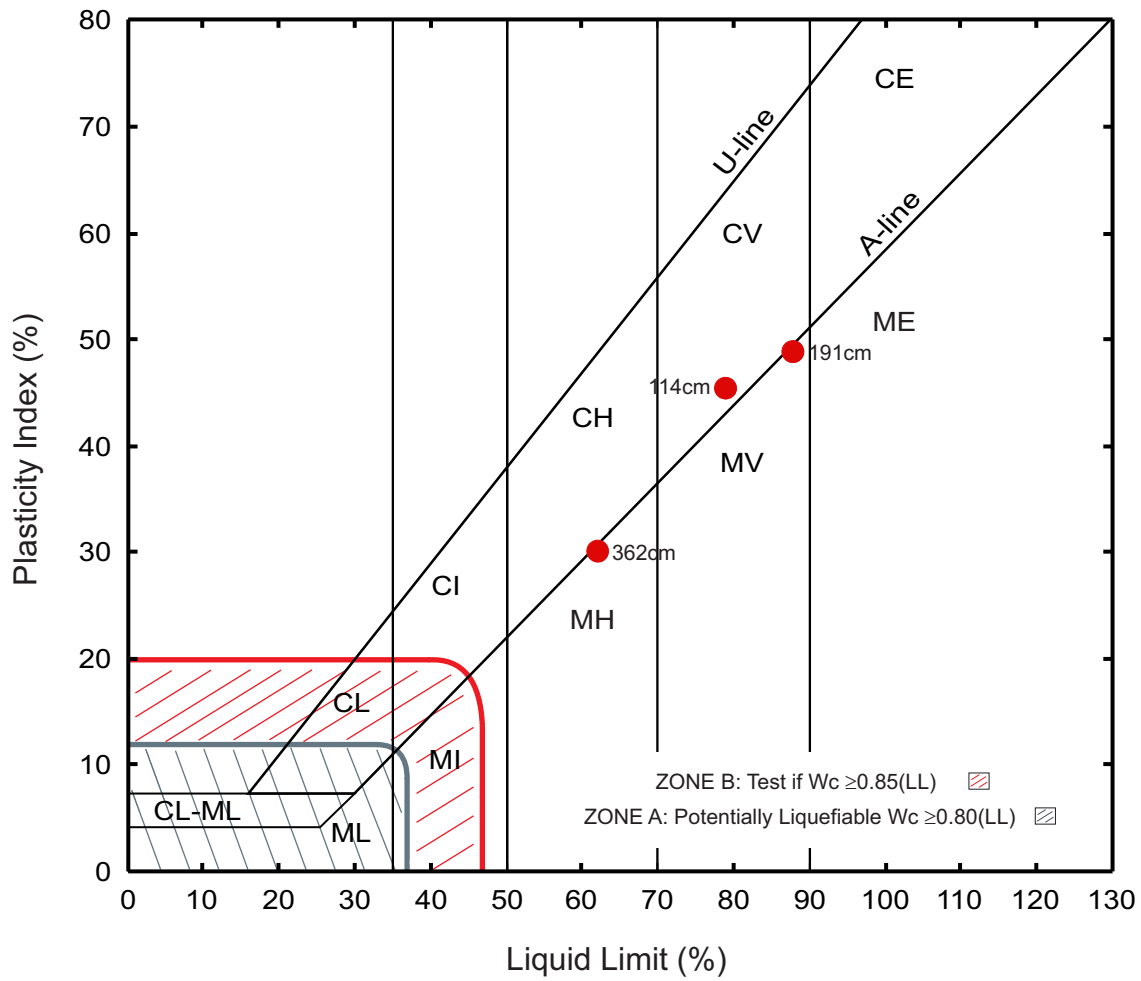
Figure 9.16. Plasticity chart showing Atterberg limit results of gravity core 2013004PGC0066.
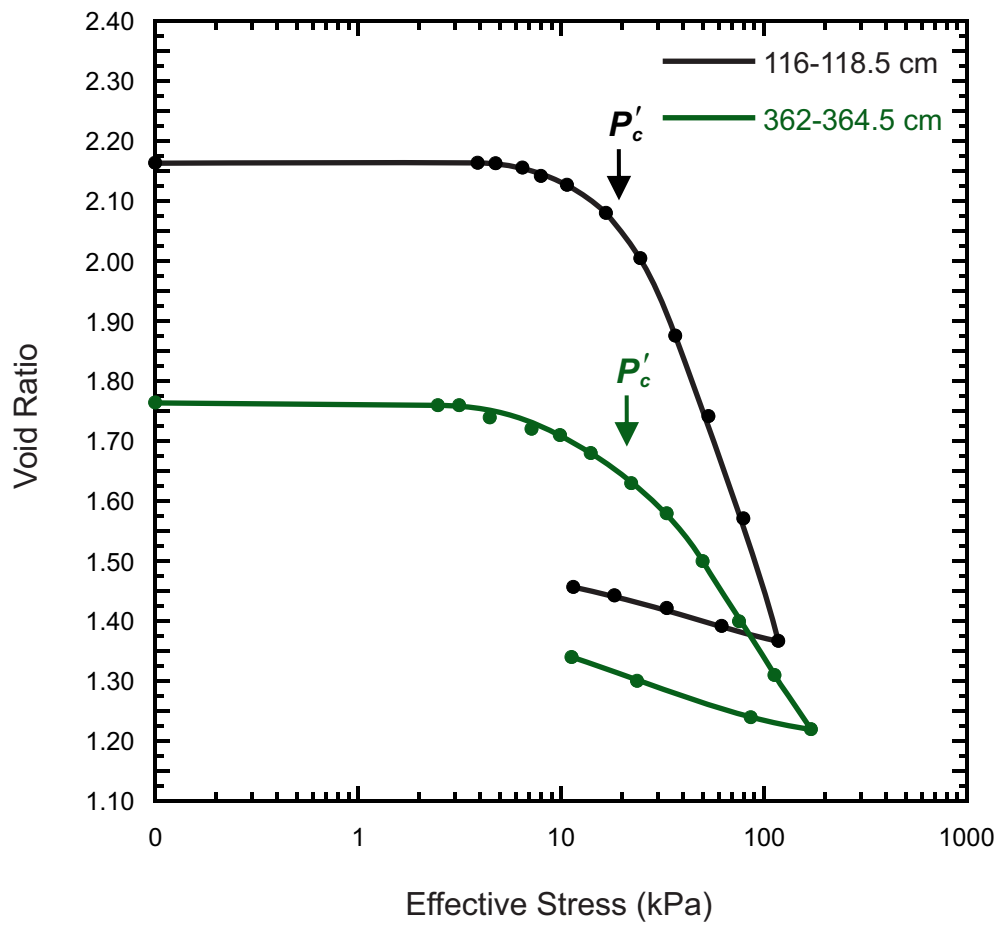
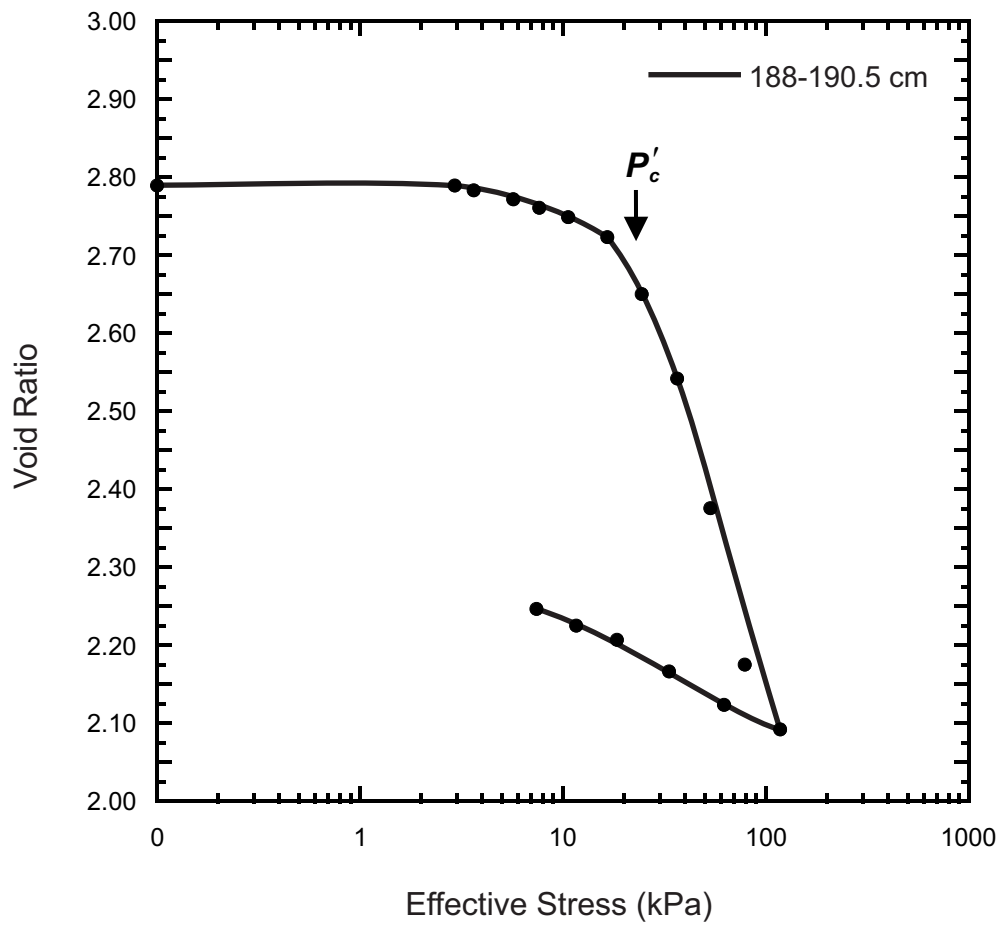Figure 9.17a. Consolidation plots for gravity core 2013004PGC0066.

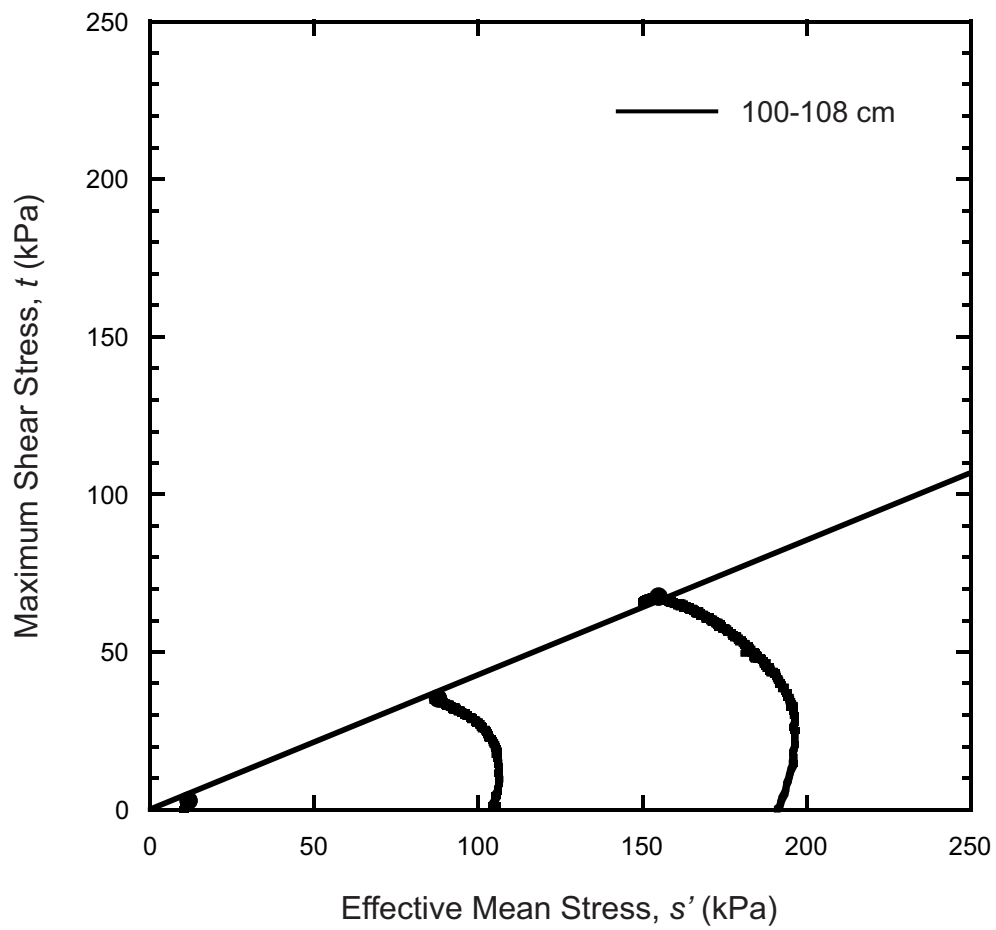Figure 9.17b. Consolidation plot for gravity core 2013004PGC0066.

Figure 9.18a. Stress paths and failure envelope from triaxial test results for gravity core 2013004PGC0066 at core depth 100-108 cm.
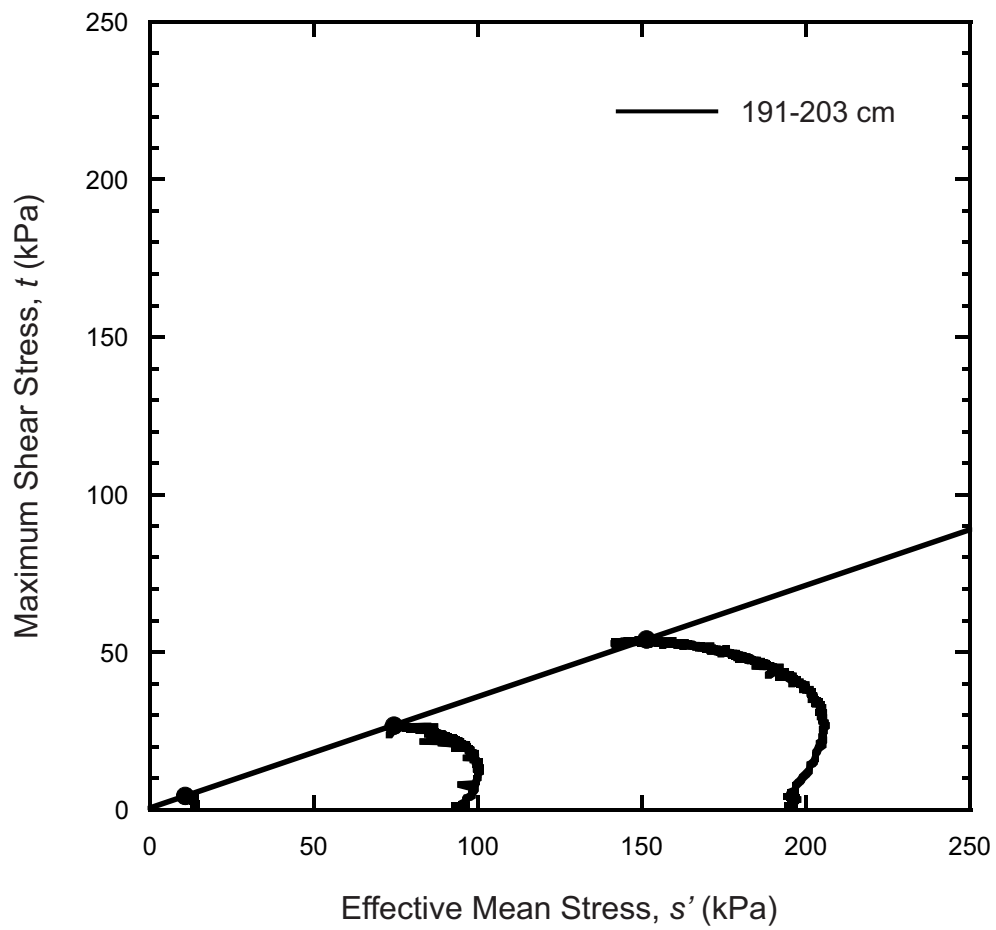
Figure 9.18b. Stress paths and failure envelope from triaxial test results for gravity core 2013004PGC0066 at core depth 191-203 cm.
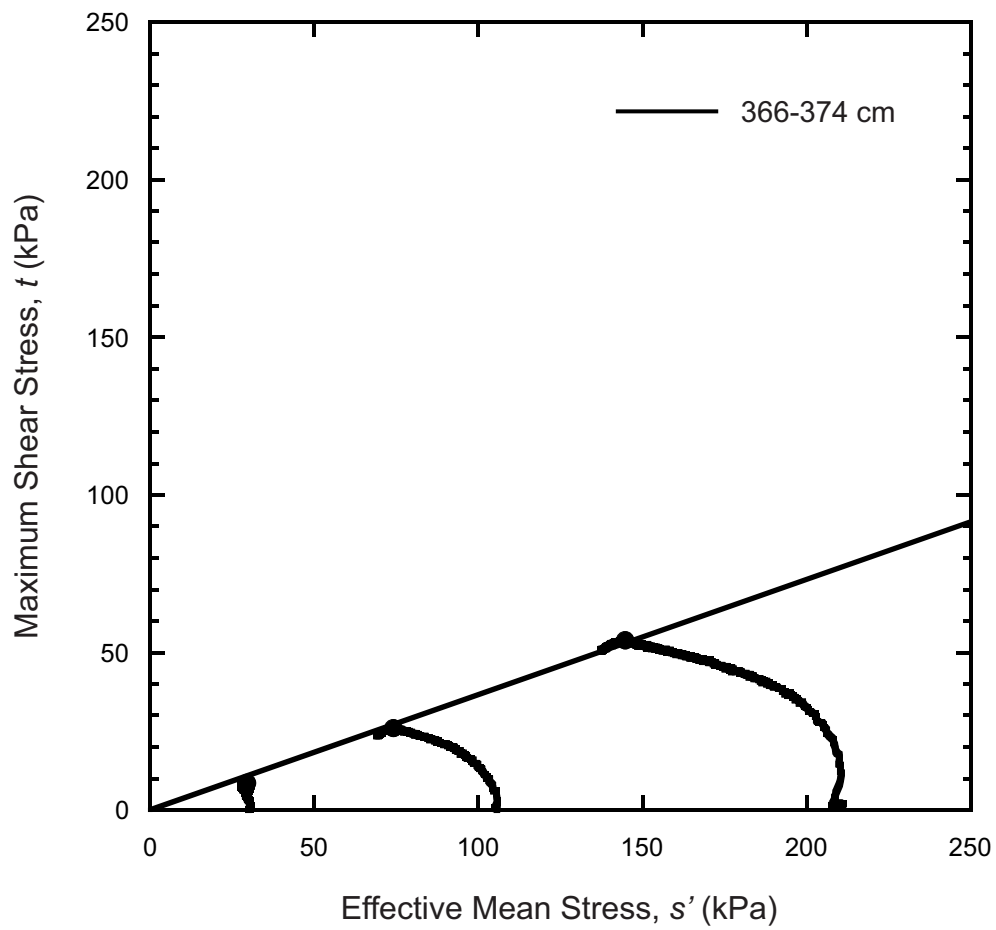
Figure 9.18c. Stress paths and failure envelope from triaxial test results for gravity core 2013004PGC0066 at core depth 366-374 cm.
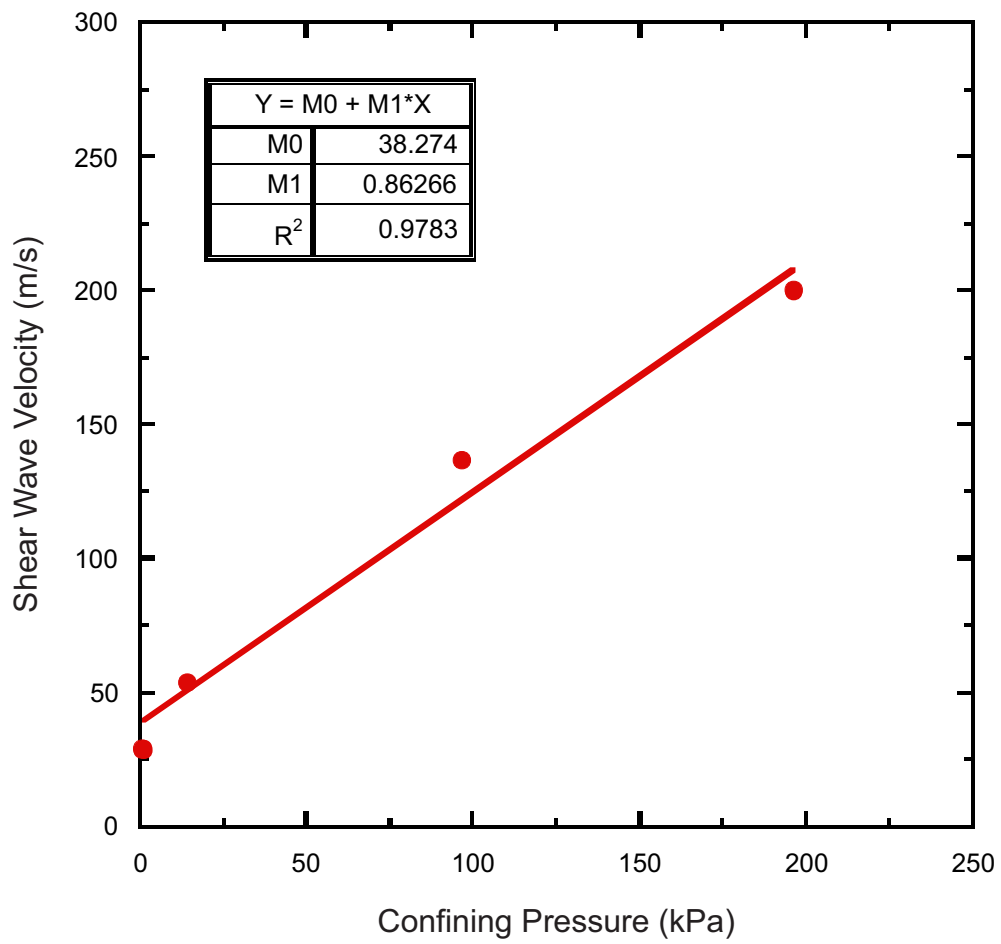
Figure 9.19. Shear wave velocities at various confining pressures for gravity core 2013004PGC0066 at core depth 191-203 cm.
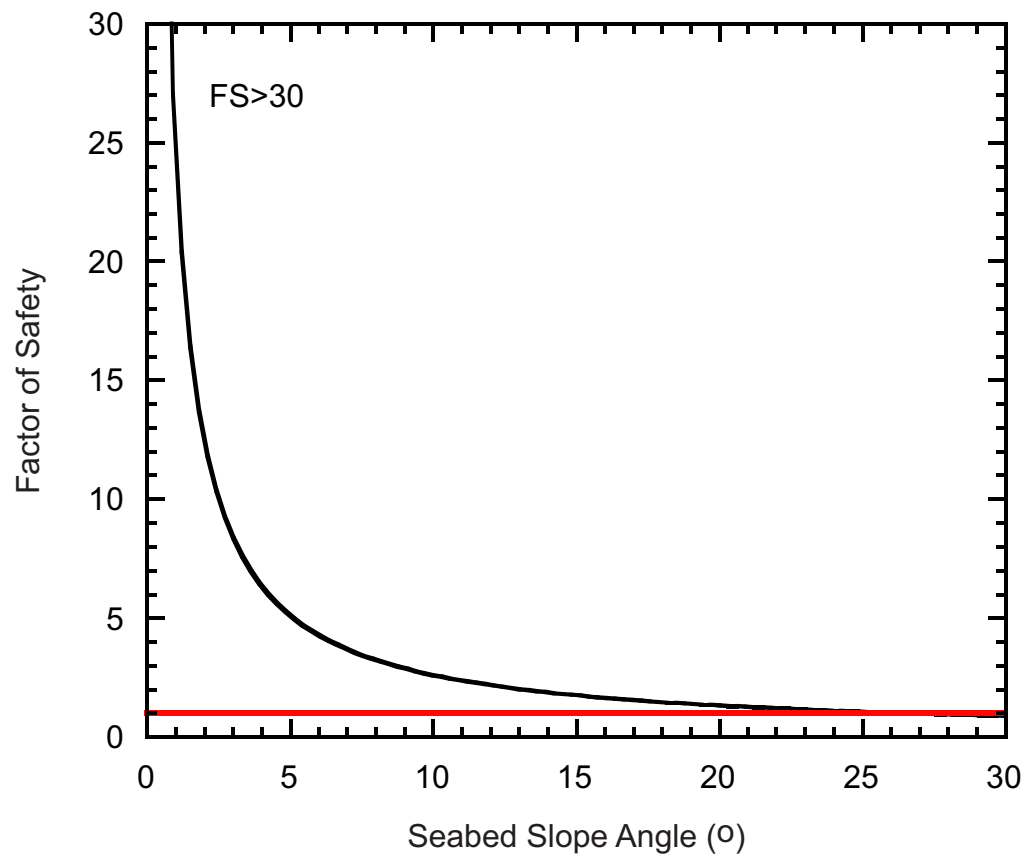
Figure 9.20. FS at various slope angles for gravity core 2013004PGC0066. The minimum FS for the present-day slope angle of the core site is > 30.
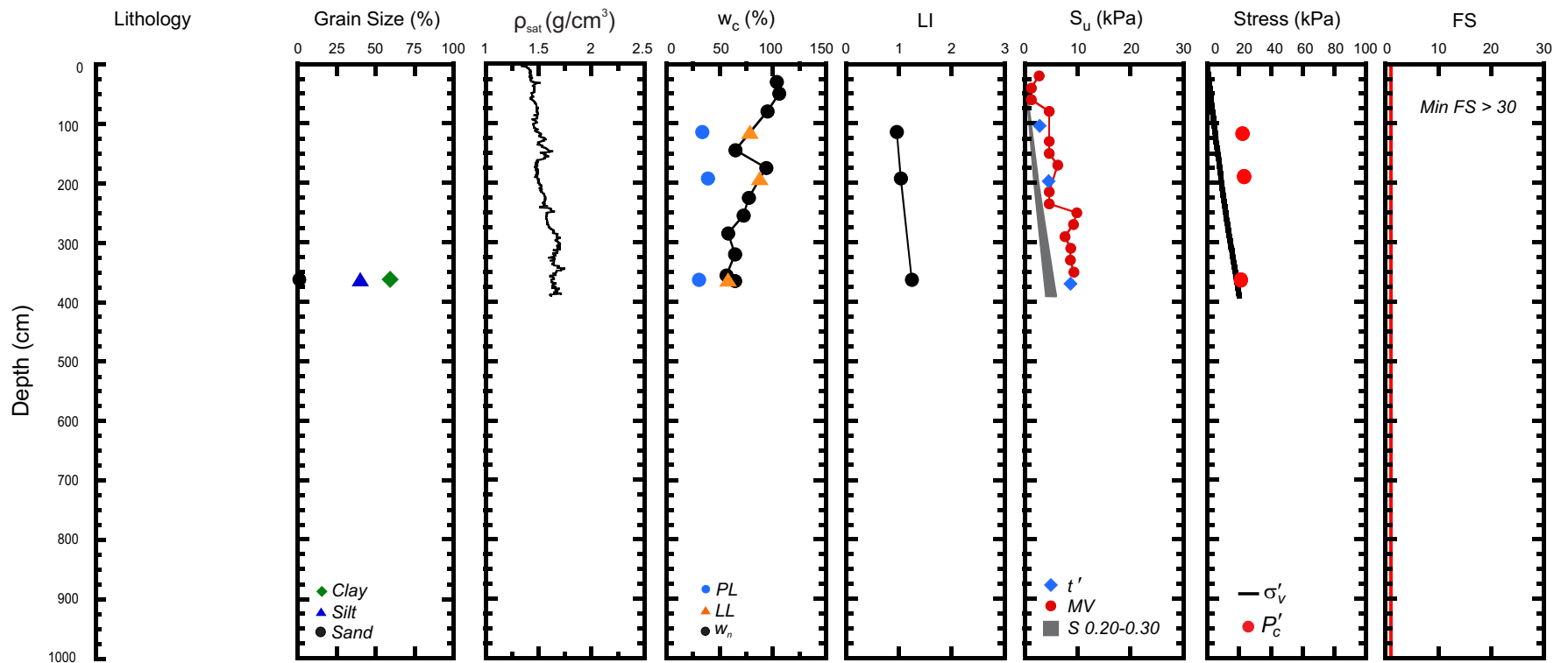
Figure 9.21. Geotechnical profile for core 2013004PGC0066gc from the channel between the two ridges in Region 1.
(ρ_{sat} = saturated bulk density, w_c = water content, w_n = natural in-situ water content, PL = plastic limit, LL = liquid limit, LI = liquidity index, S_u = undrained shear strength, MV = laboratory miniature vane shear strength, S = shear strength calculated from the normalized strength ratio, σ'_v = effective overburden stress, P'_c = past maximum stress, FS = factor of safety).
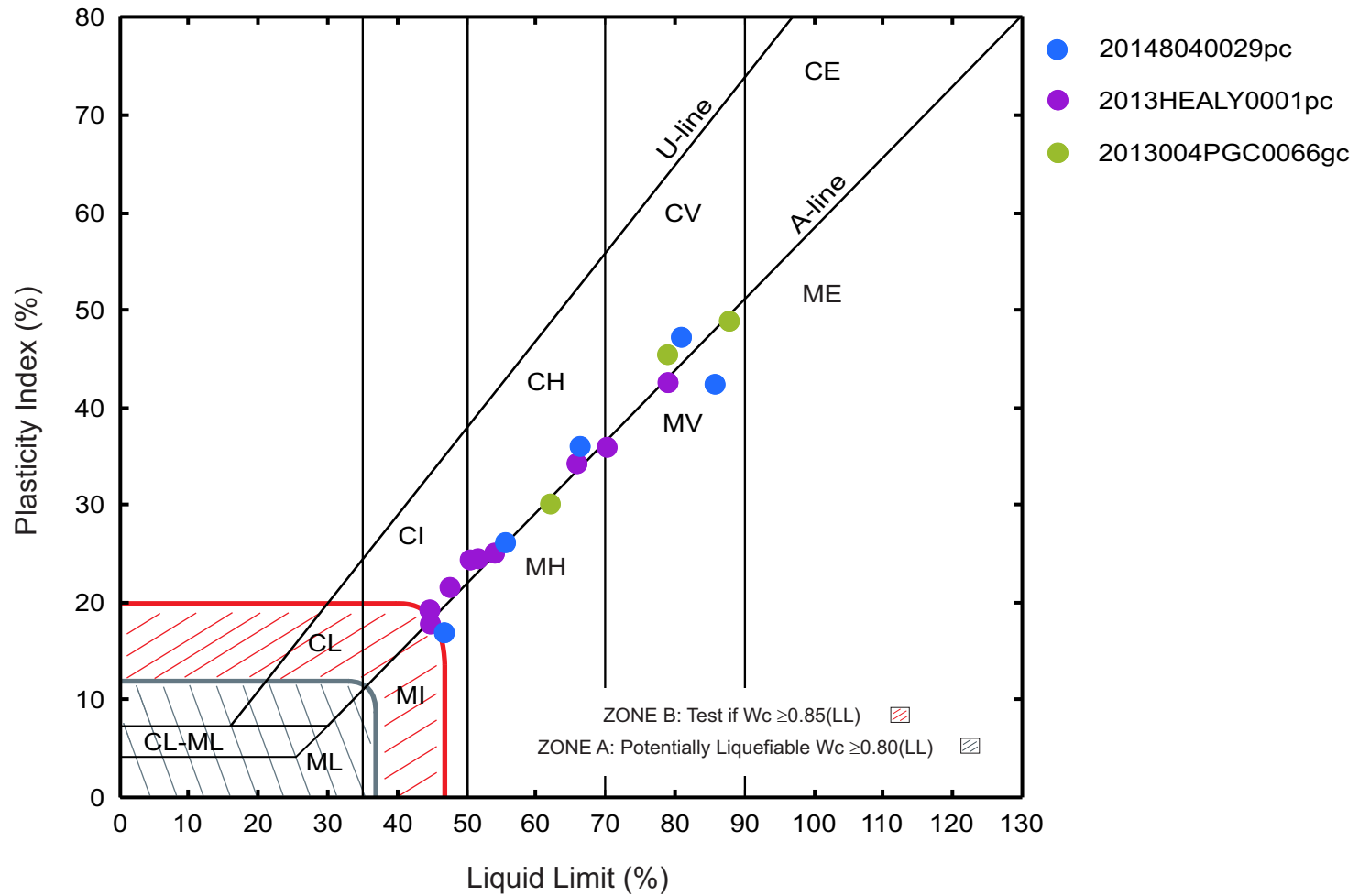
Figure 9.22. Plasticity chart showing Atterberg limit results of cores in Region 1.
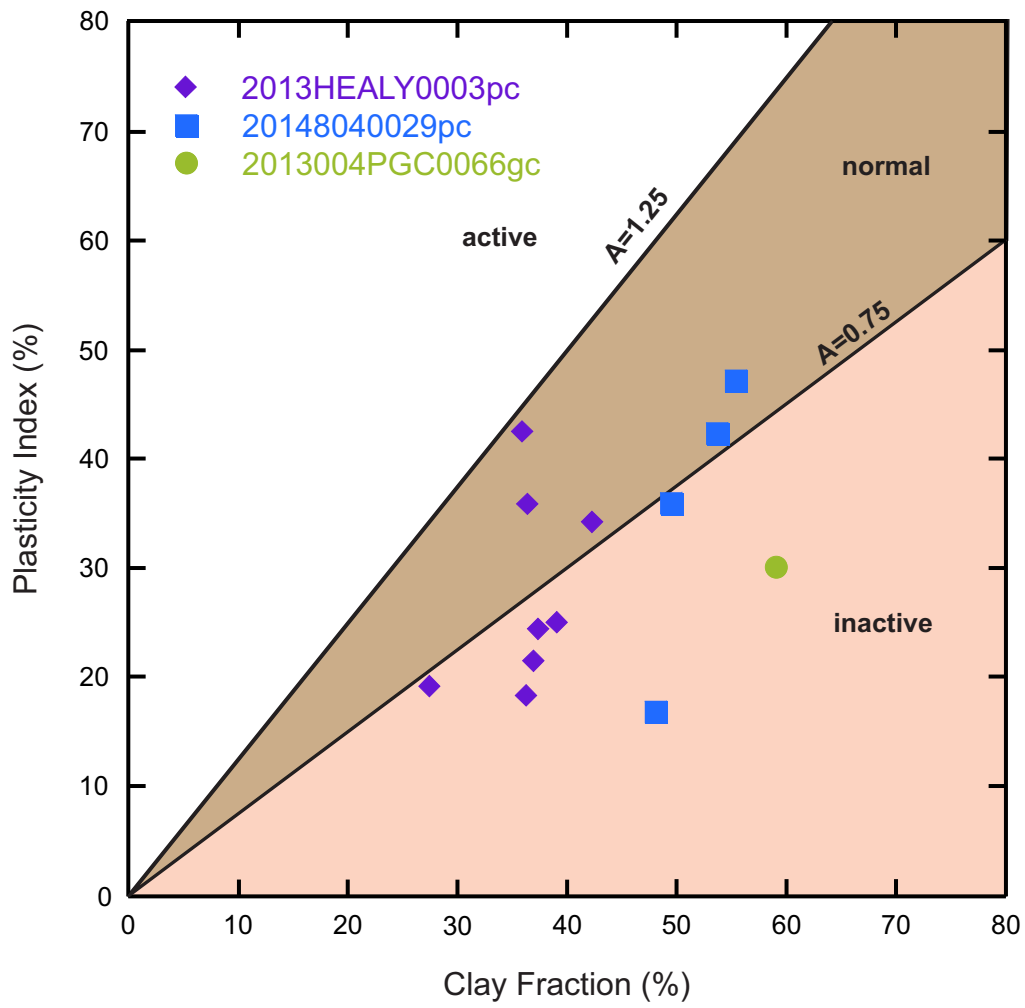
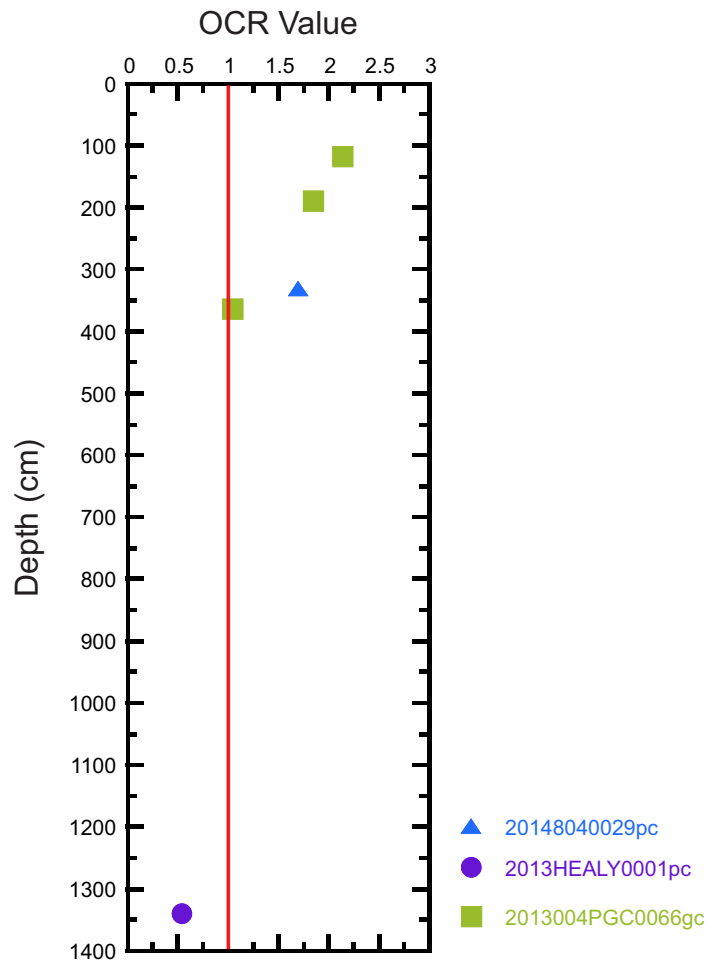Figure 9.23. Region 1 activity chart.

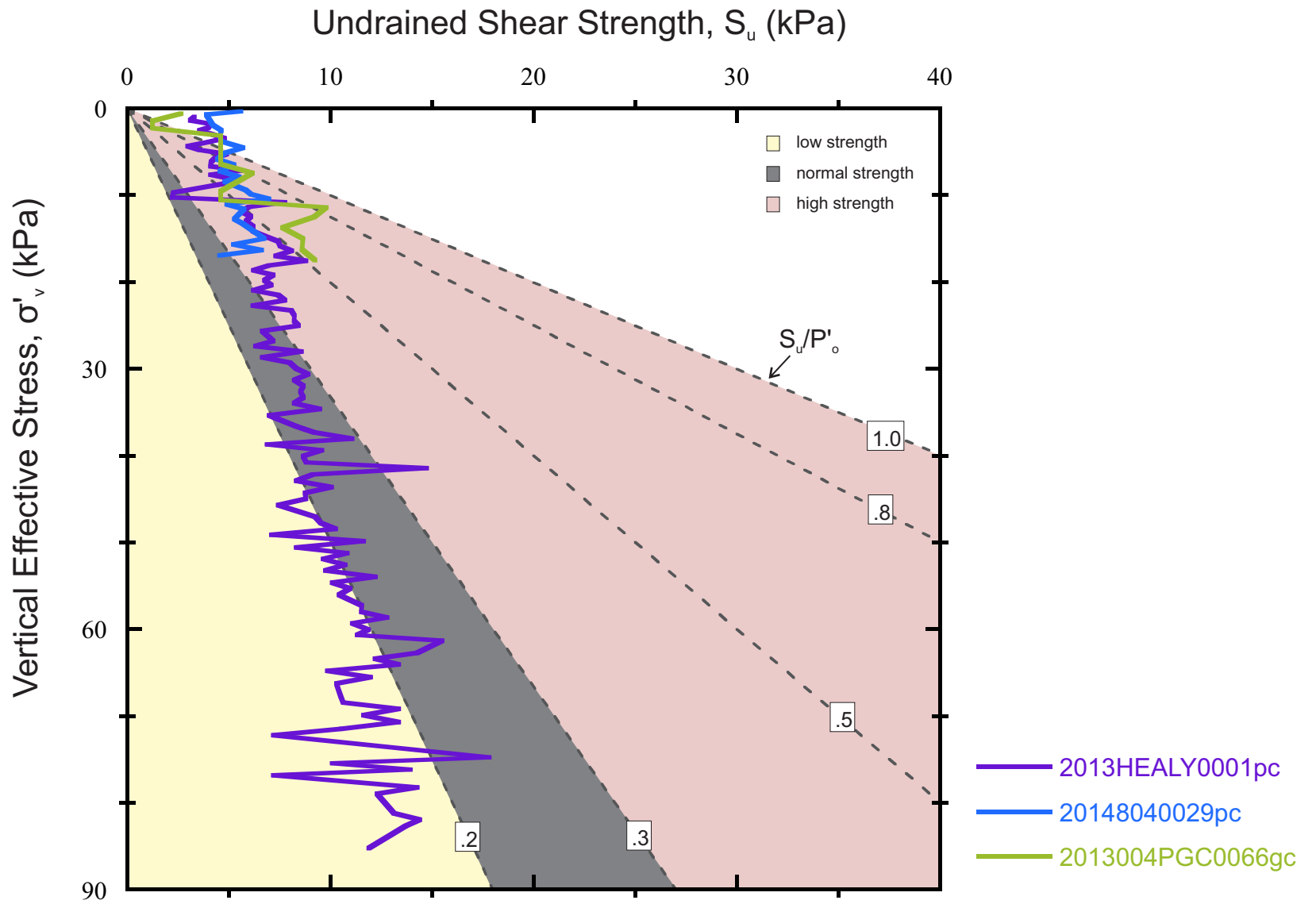Figure 9.24. OCR values with depth for consolidation tests in Region 1.

Figure 9.25. Shear strength profiles with effective overburden pressure from Region 1.
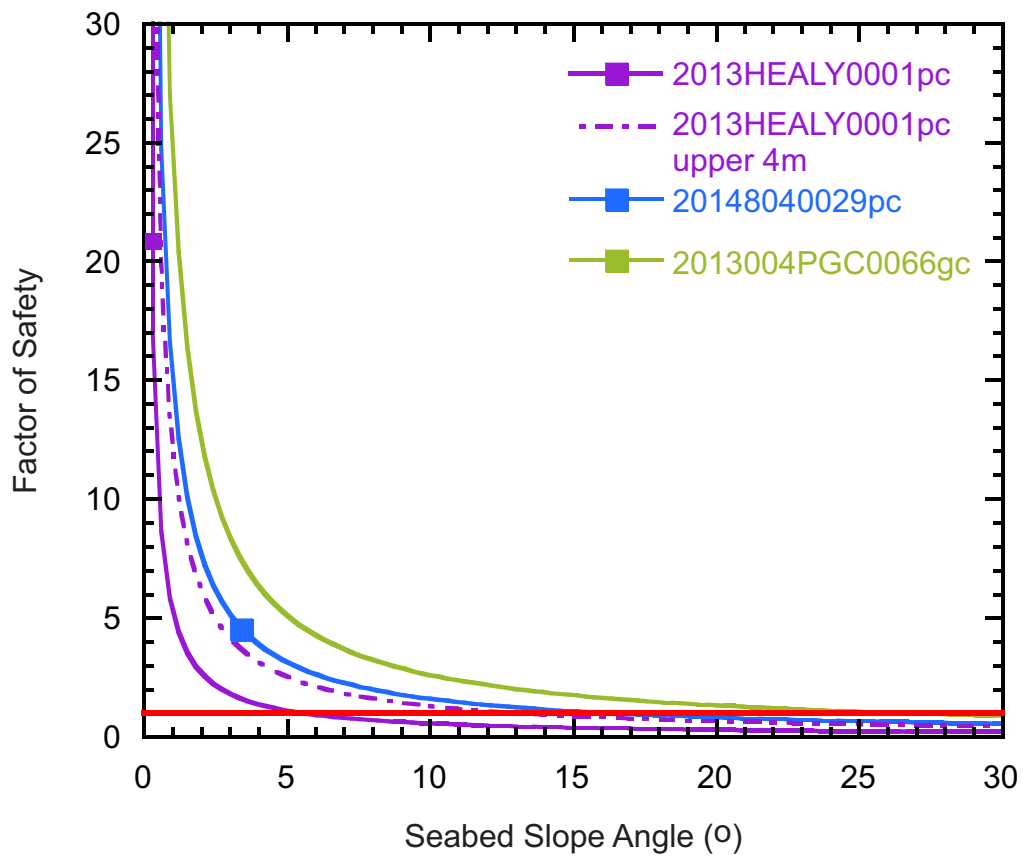
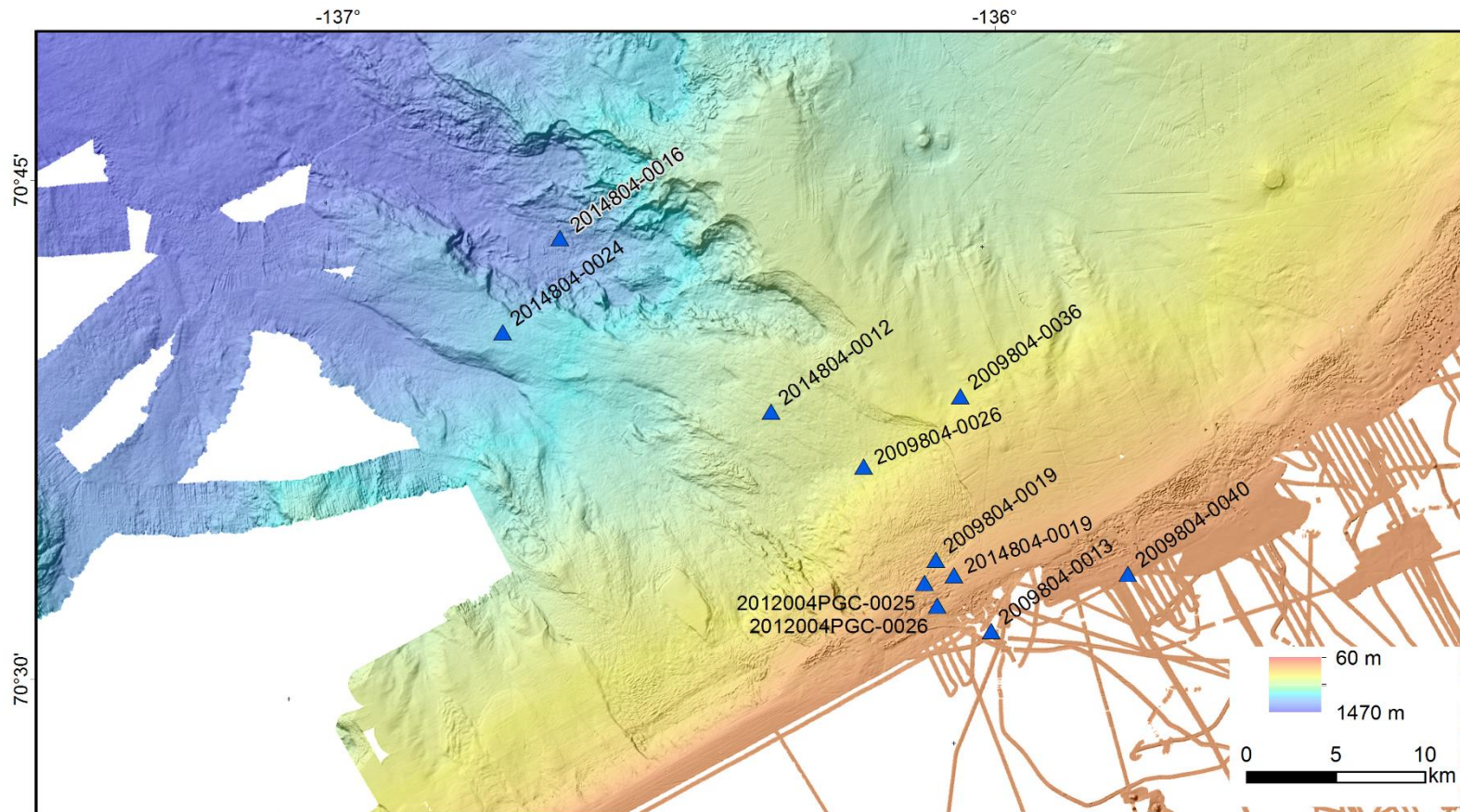Figure 9.26. FS at various slope angles for cores in Region 1.

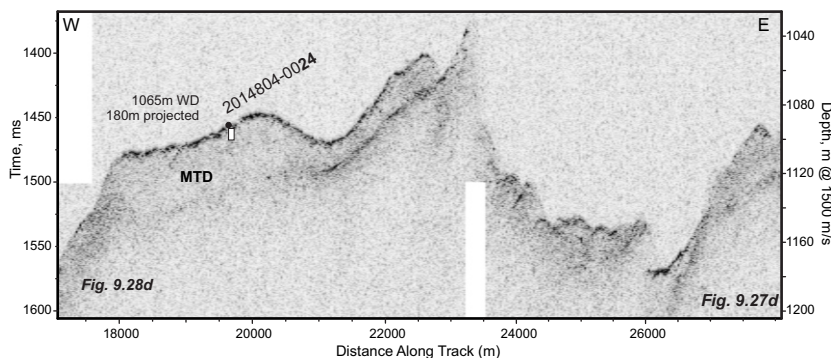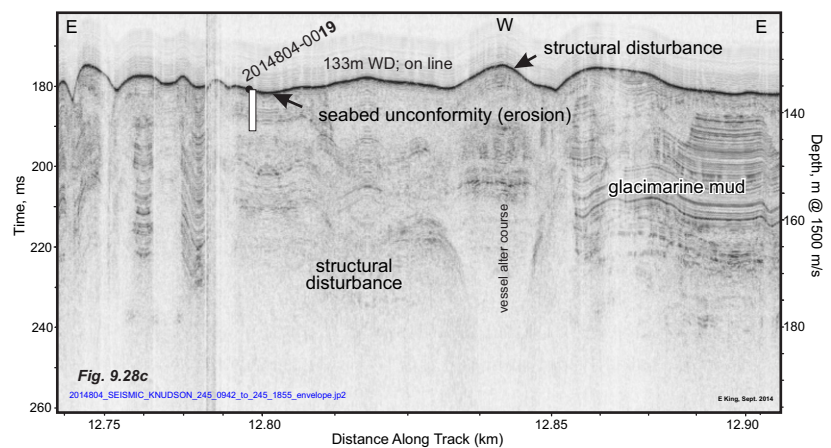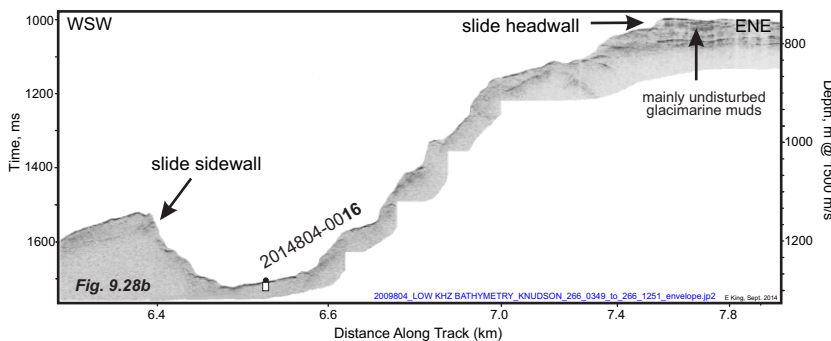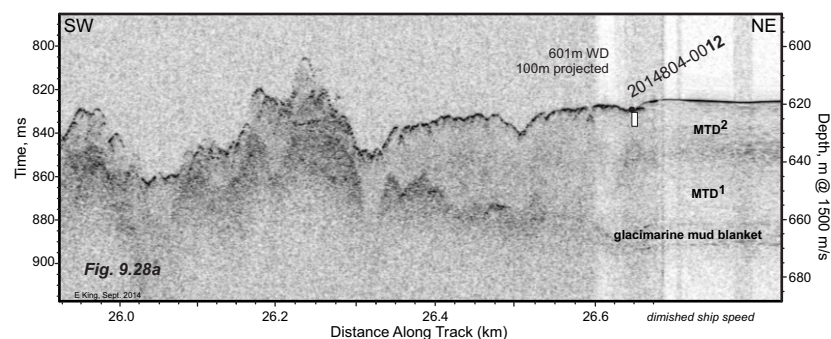Figure 9.27. Region 2 core locations on ArcticNet multibeam bathymetry.

Figure 9.28 3.5 kHz sub-bottom profile showing the acoustic stratigraphy and position of piston core sites in the Ajurak Area (Region 2). Core 20148040012pc, Fig 9.28a, lies on a thick mass transport (debris flow) deposit, MTD Cameron and King (2018). Core 20148040016pc, Fig 9.28b intersected a small but intact, slightly buried block of parent sediment transported from the sidewall. Core 20148040019pc, Fig 9.28c, intersected stratificatied glacimarine muds. Primary stratification is preserved locally, despite the "pingo-like feature" (PLF) disturbance associated with permafrost and fluid and sediment flow. Core 20148040024, Fig 9.28d intersected a mass transport deposit of about 20 m thickness which likely represents the distal (downslope) equivalent to that sampled with PC 20148040012pc (Cameron and King 2018). It is now perched on a broad inter-slide erosional remnant indicating it pre-dates the adjacent MTDs.
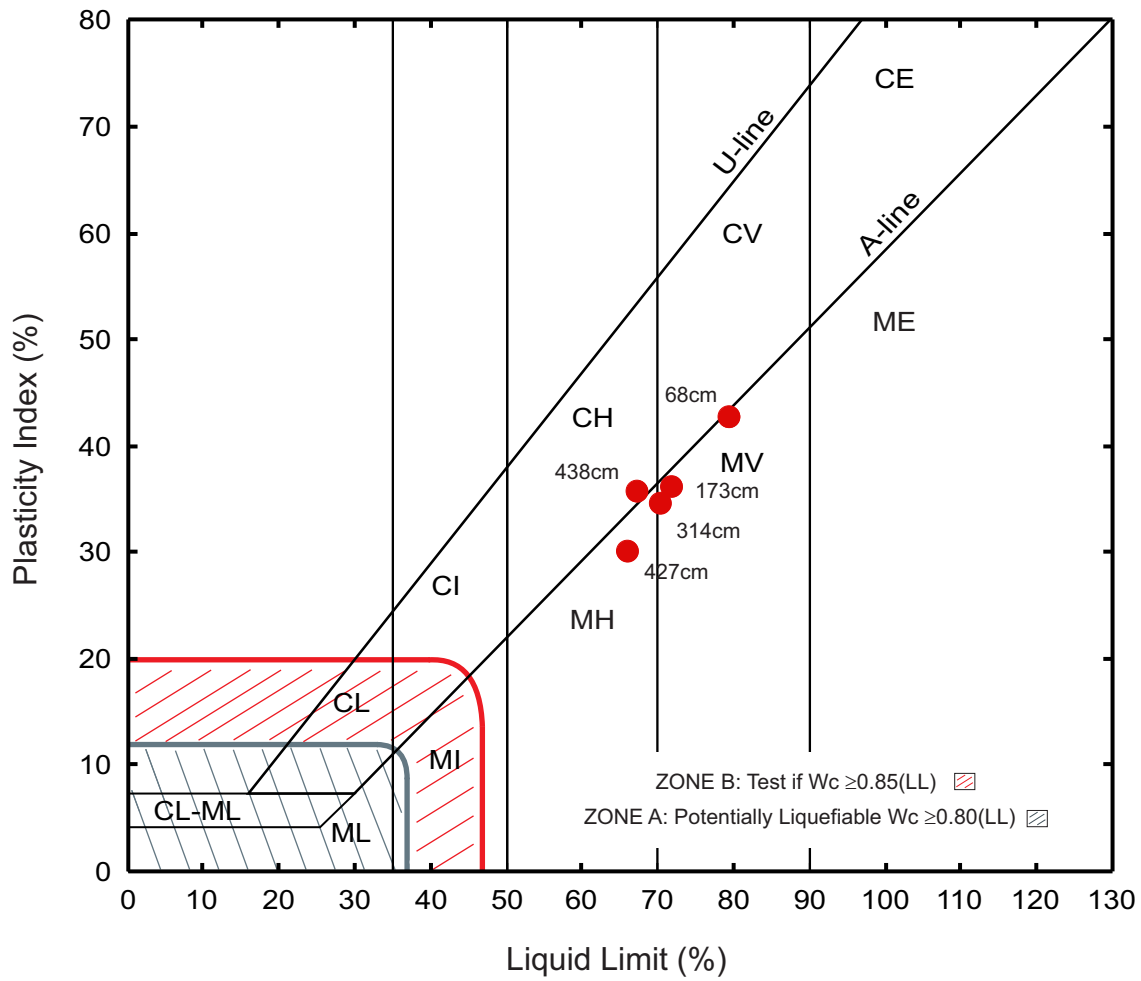
Figure 9.29. Plasticity chart showing Atterberg limit results of piston core 20148040012.
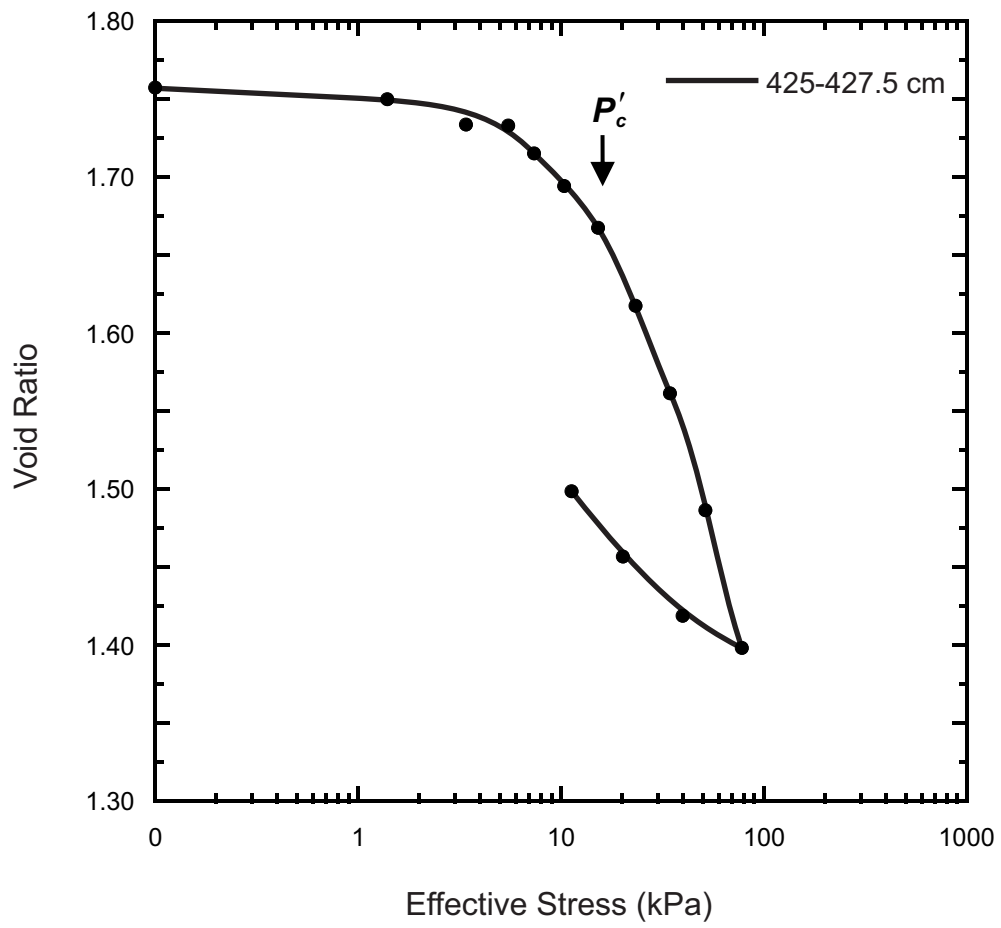
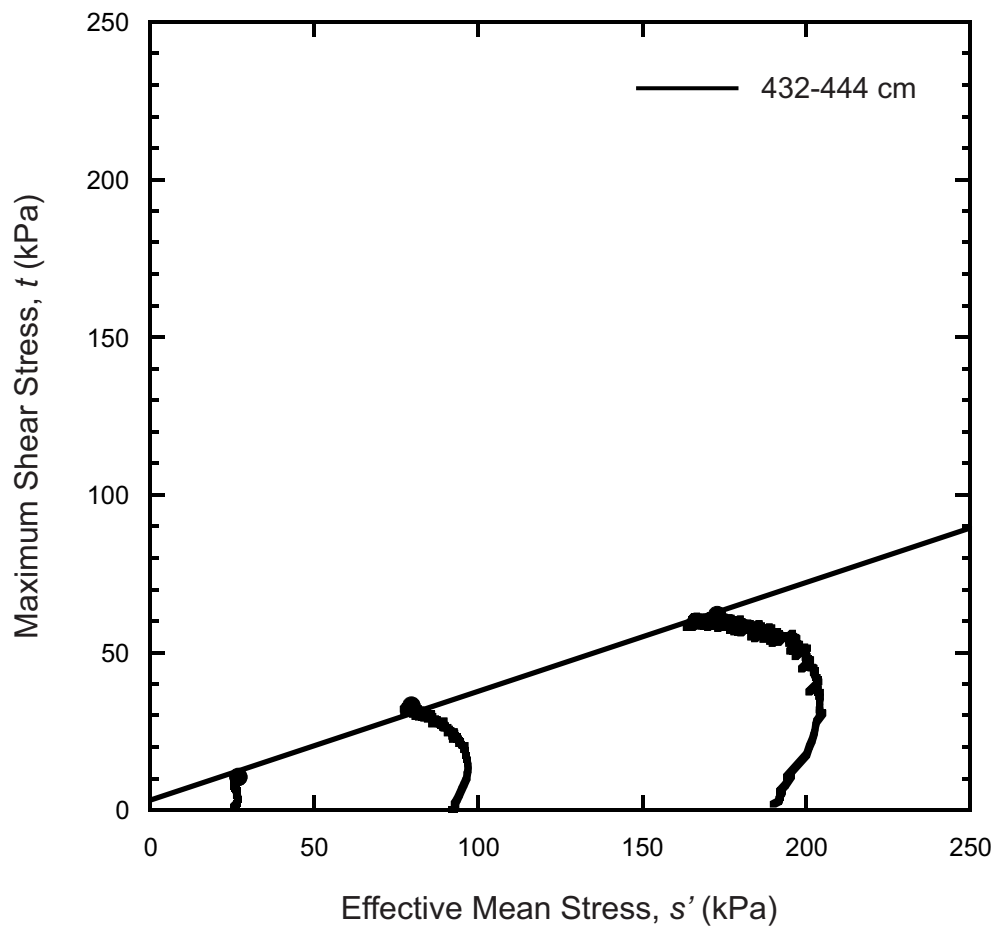Figure 9.30. Consolidation plot for piston core 20148040012.

Figure 9.31. Stress paths and failure envelopes from triaxial test results for piston core 20148040012.

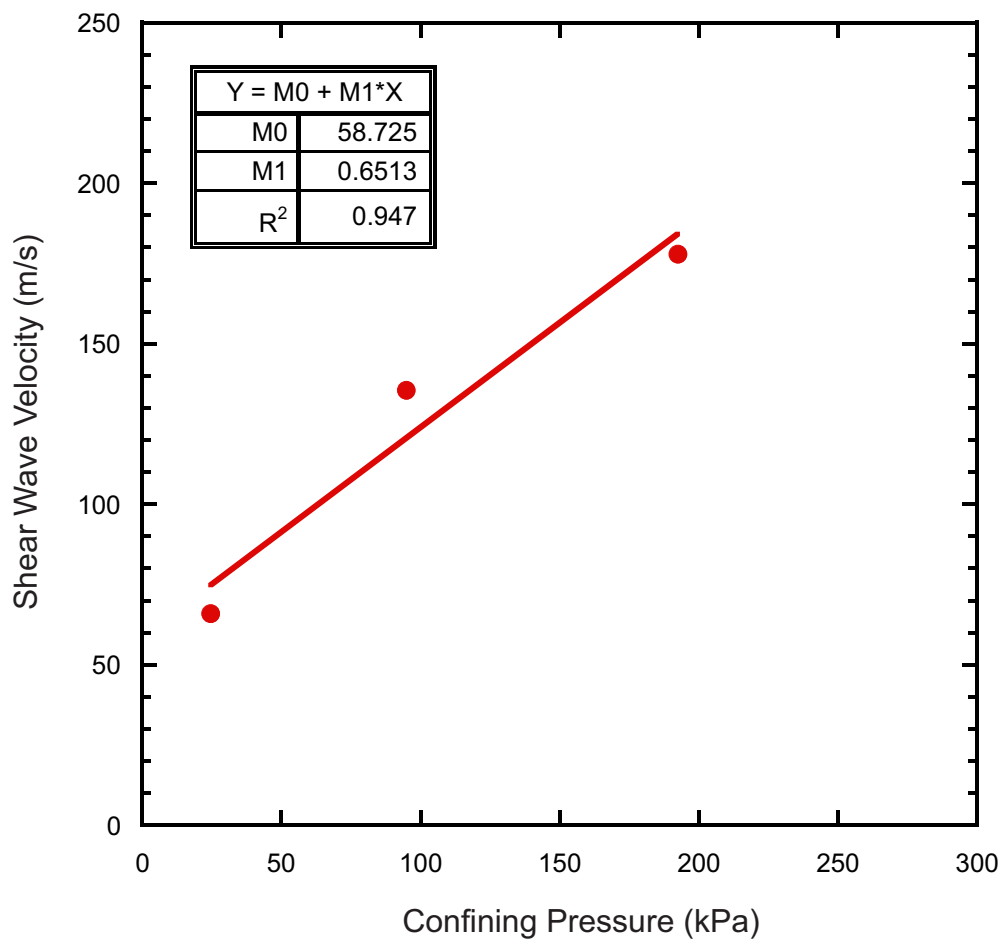| Y = M0 + M1*X	
M0	58.725
M1	0.6513
R^2	0.947

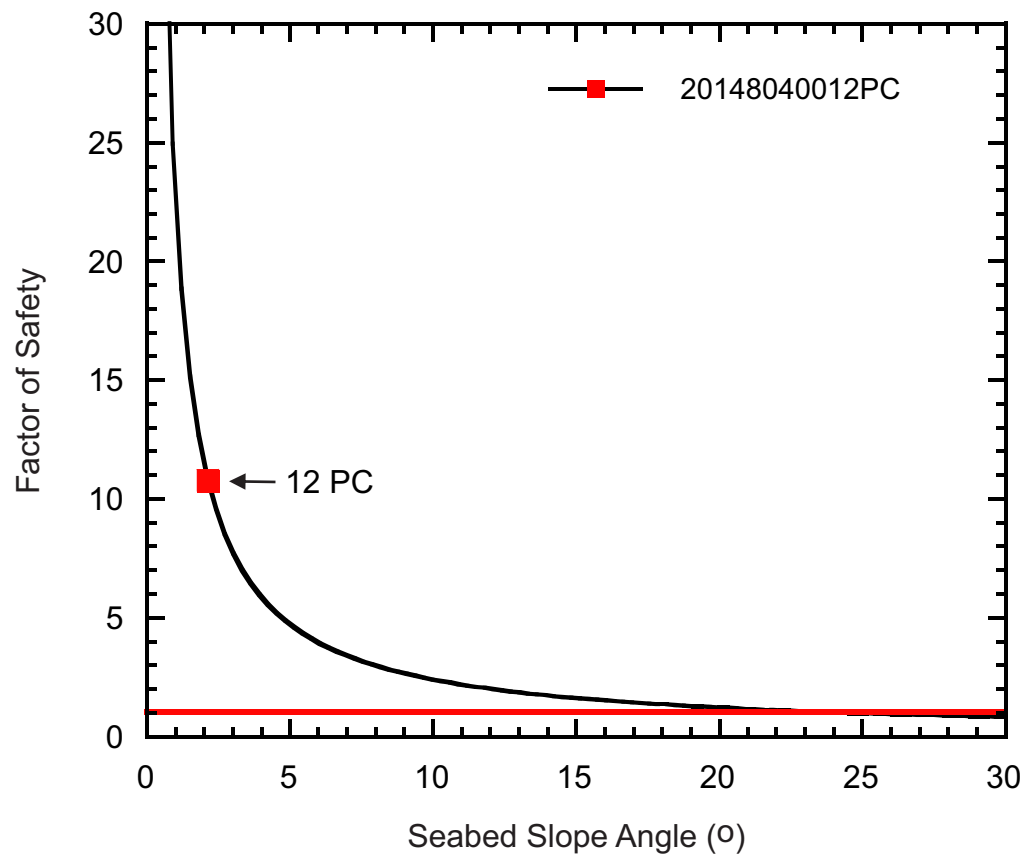Figure 9.32. Shear wave velocities at various confining pressures for piston core 20148040012.

Figure 9.33. FS at various slope angles for piston core 20148040012. The red square identifies the minimum FS for the present-day slope angle of the core site.
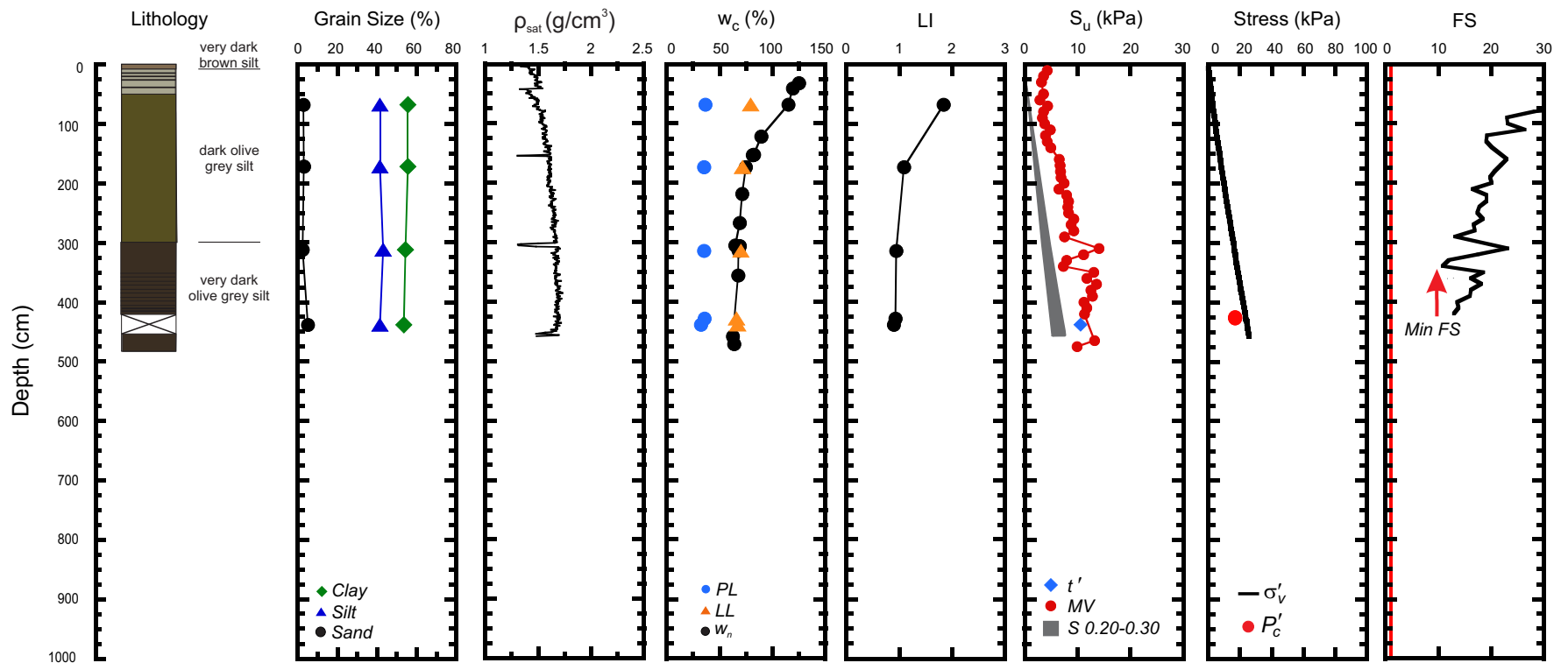
Figure 9.34. Geotechnical profile for core 20148040012 from the Region 2 failure. (ρ_{sat}= saturated bulk density, w_c = water content, w_n = natural in-situ water content, PL = plastic limit, LL = liquid limit, LI = liquidity index, S_u = undrained shear strength, MV = laboratory miniature vane shear strength, t' = maximum shear stress, S = shear strength calculated from the normalized strength ratio, σ'_v = effective overburden stress, P'_c = past maximum stress, FS = factor of safety).
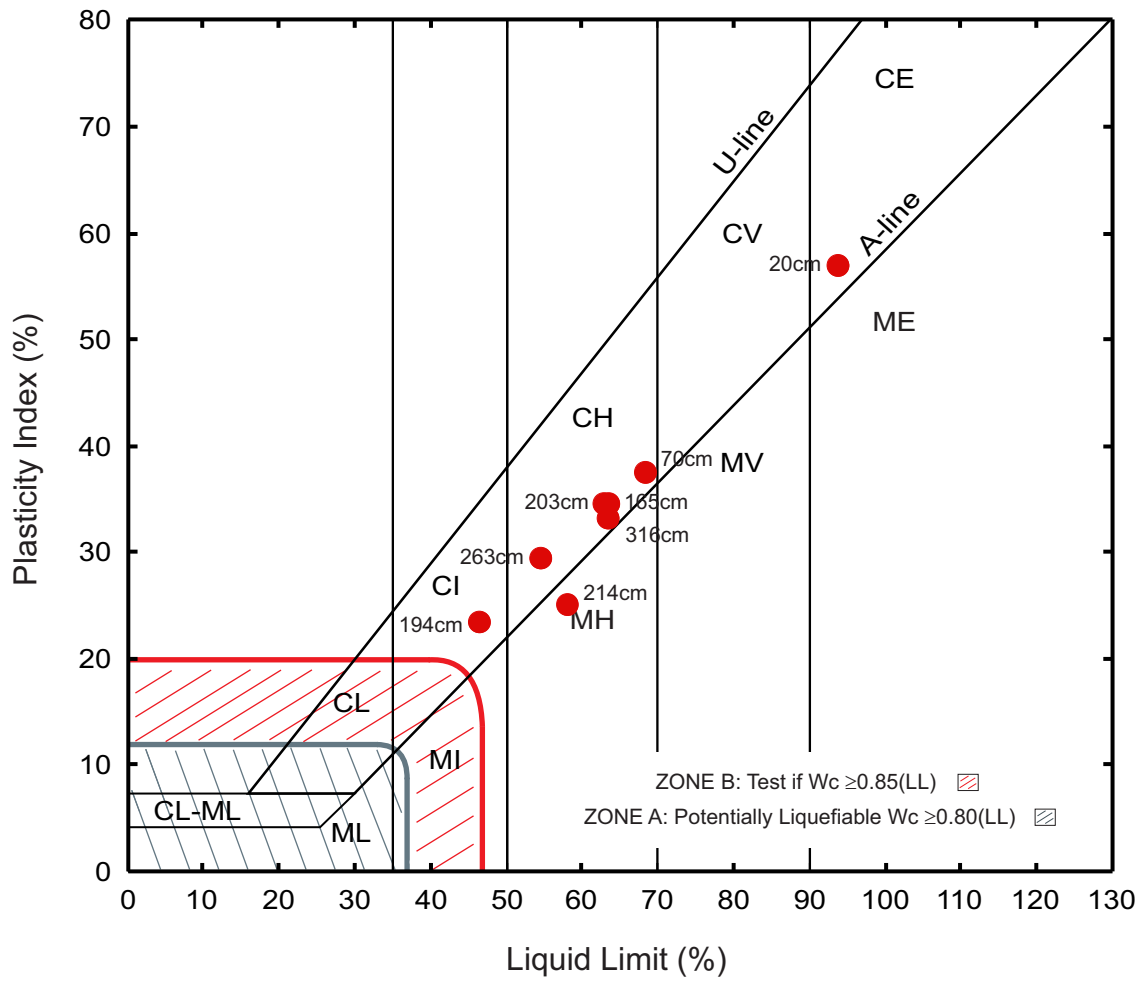
Figure 9.35. Plasticity chart showing Atterberg limit results of piston core 20148040016.
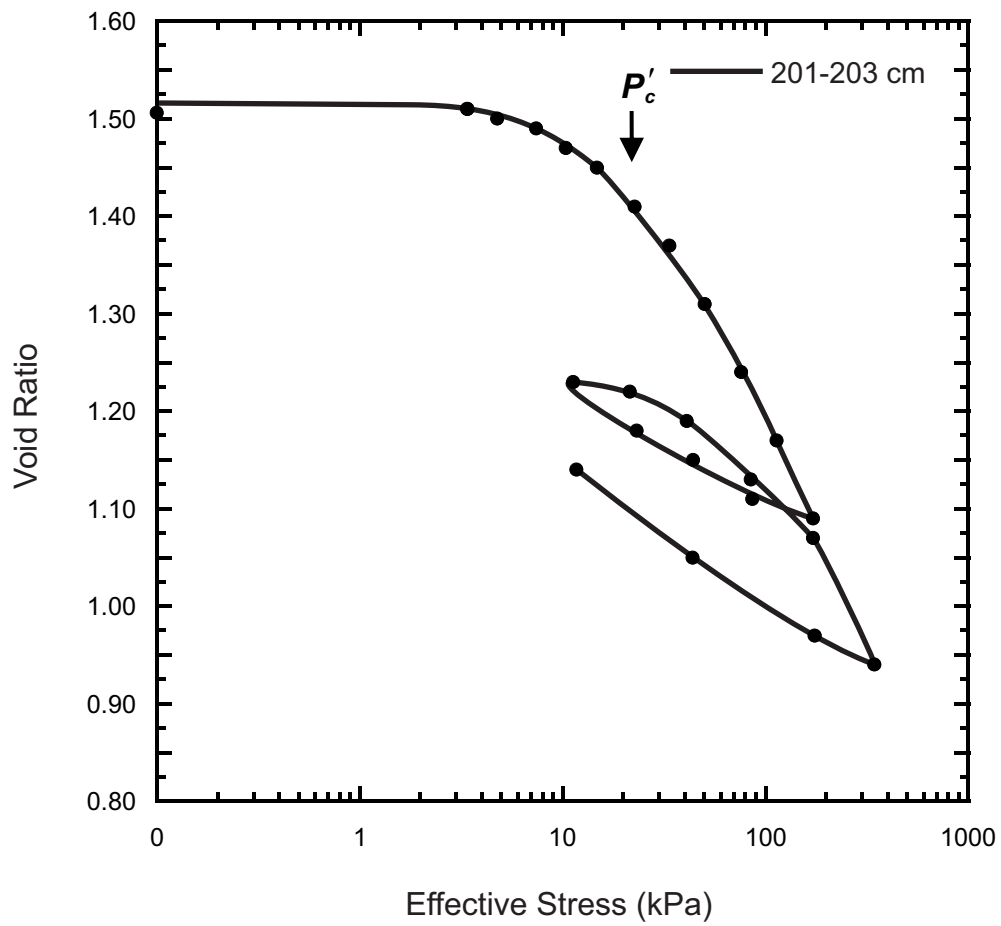
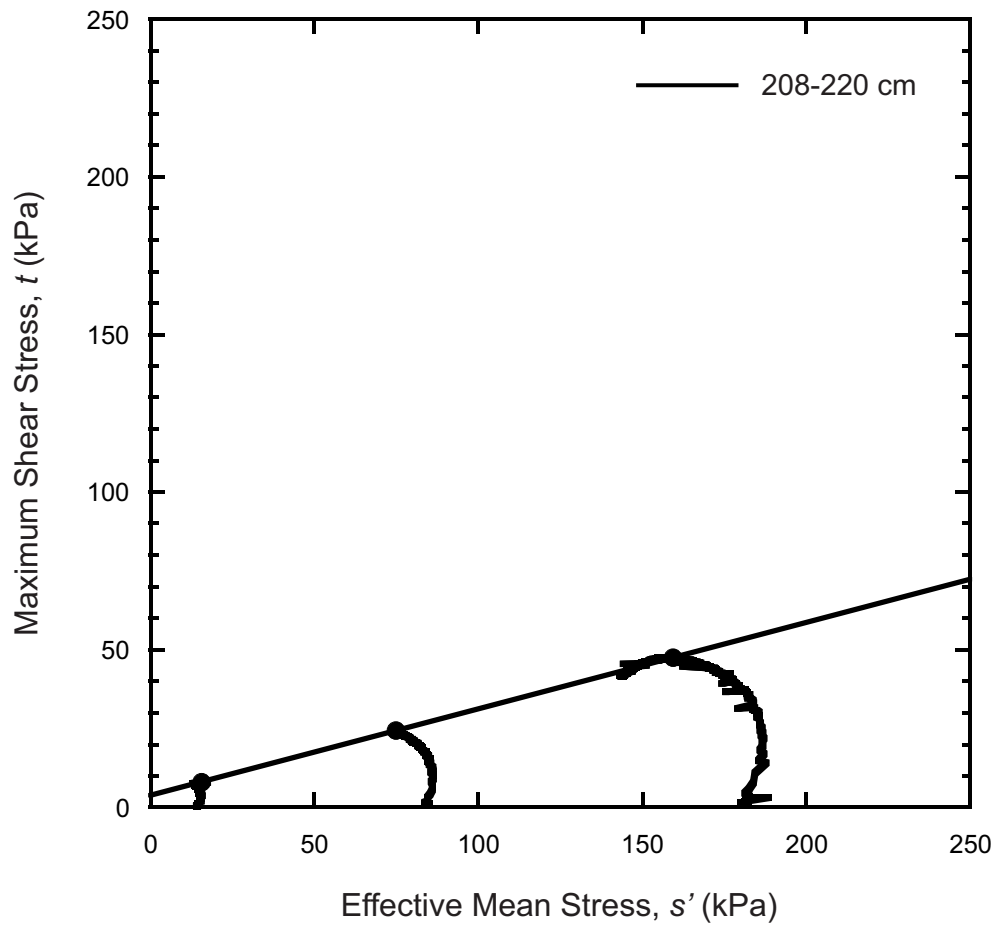Figure 9.36. Consolidation plot for piston core 20148040016.

Figure 9.37. Stress paths and failure envelopes from triaxial test results for piston core 20148040016.
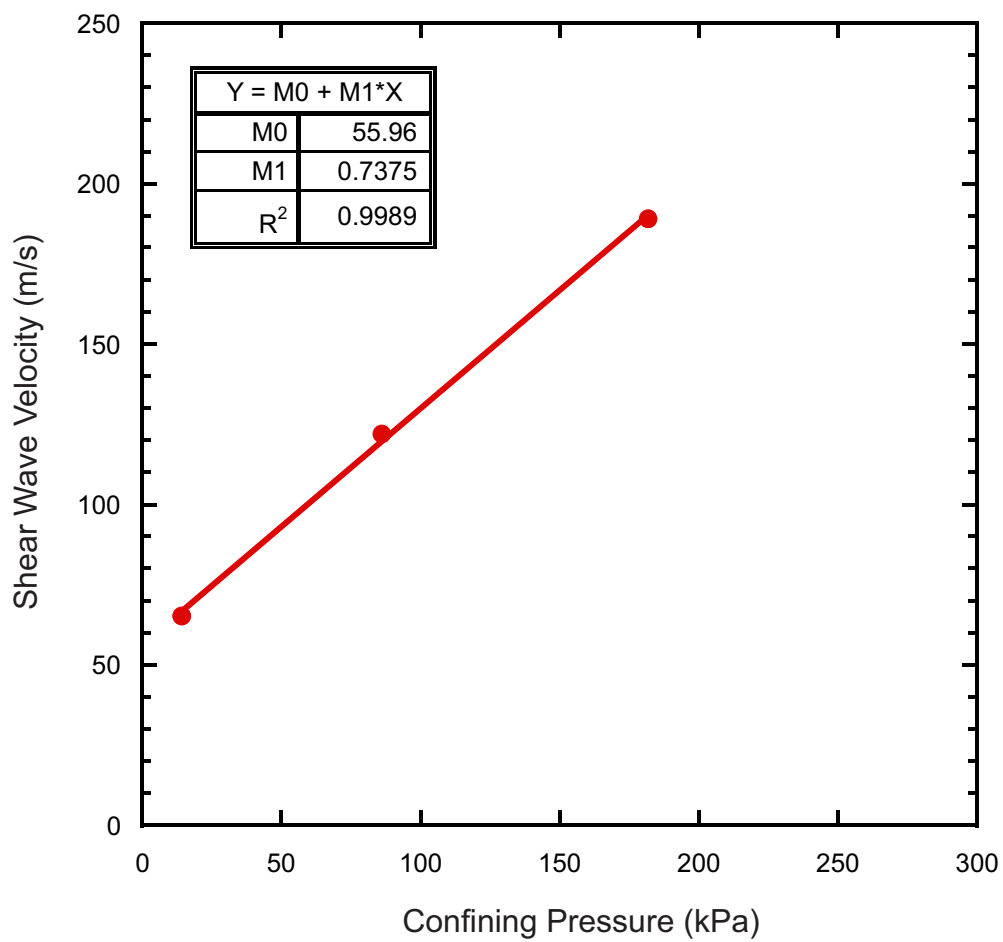
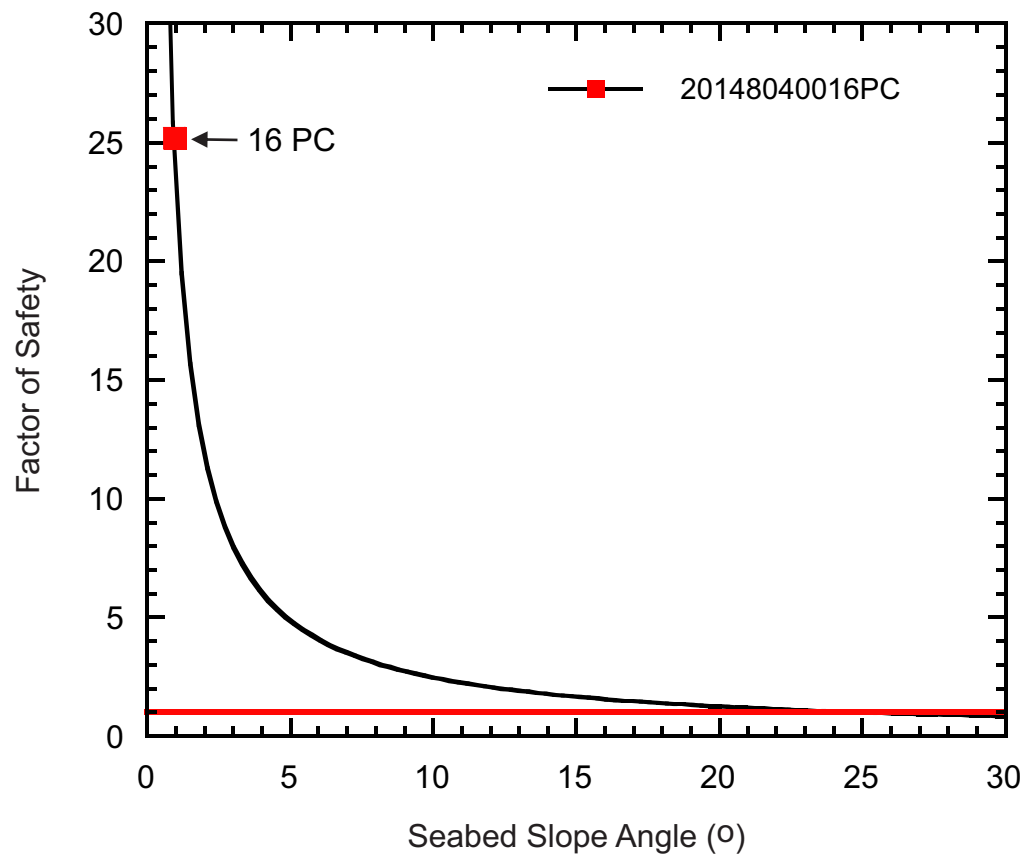Figure 9.38. Shear wave velocities at various confining pressures for piston core 20148040016.

Figure 9.39. FS at various slope angles for piston core 20148040016. The red square identifies the minimum FS for the present-day slope angle of the core site.
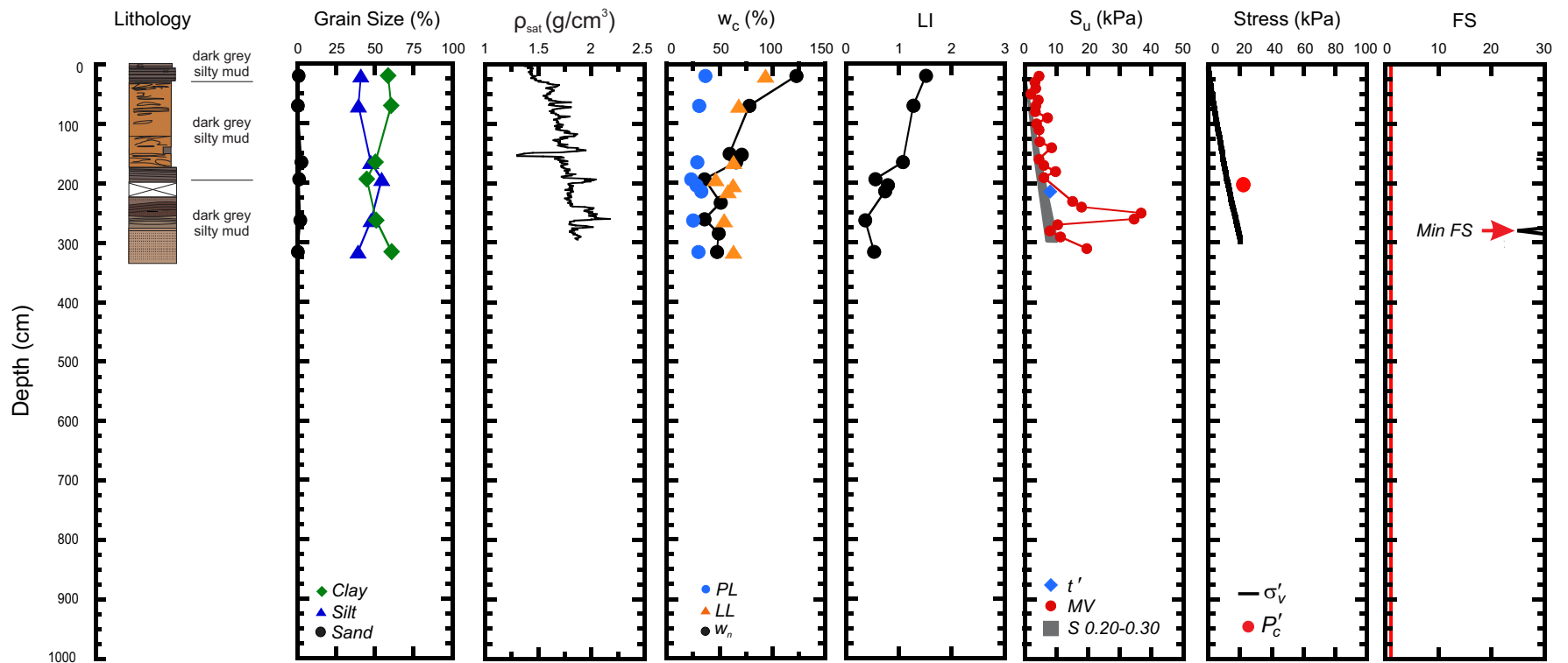
Figure 9.40. Geotechnical profile for core 20148040016 from the deep canyon in Region 2. (ρ_{sat}= saturated bulk density, w_c = water content, w_n = natural in-situ water content, PL = plastic limit, LL = liquid limit, LI = liquidity index, S_u = undrained shear strength, MV = laboratory miniature vane shear strength, t' = maximum shear stress, S = shear strength calculated from the normalized strength ratio, σ'_v = effective overburden stress, P'_c = past maximum stress, FS = factor of safety).
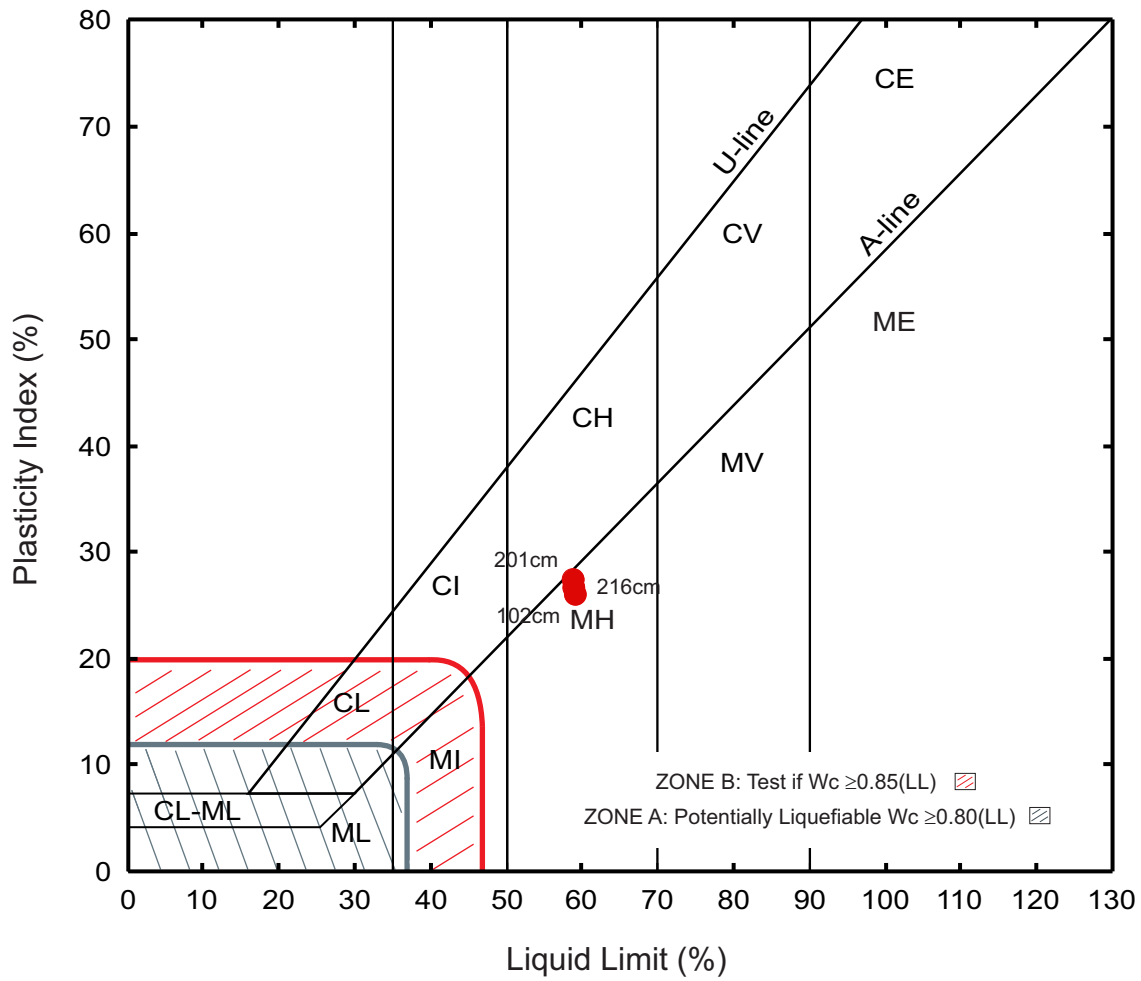
Figure 9.41. Plasticity chart showing Atterberg limit results of piston core 20148040019.
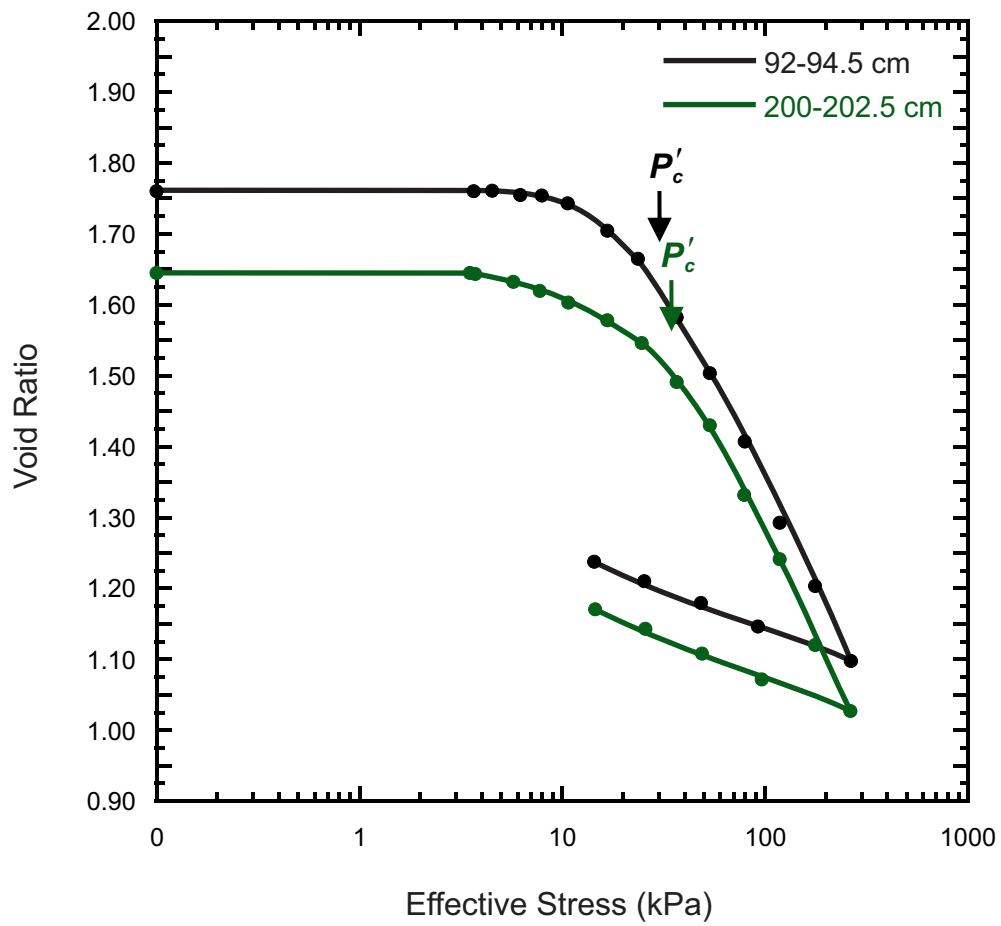
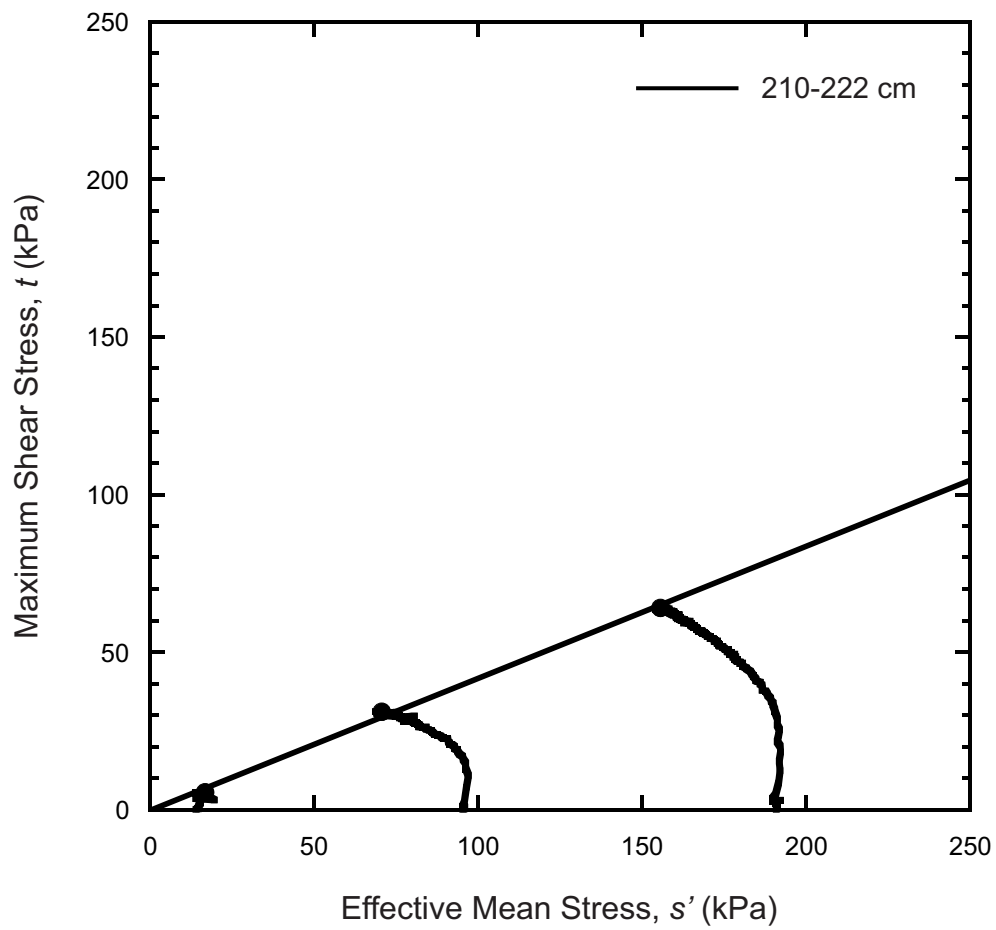Figure 9.42. Consolidation plots for piston core 20148040019.

Figure 9.43. Stress paths and failure envelope from triaxial test results for piston core 20148040019.
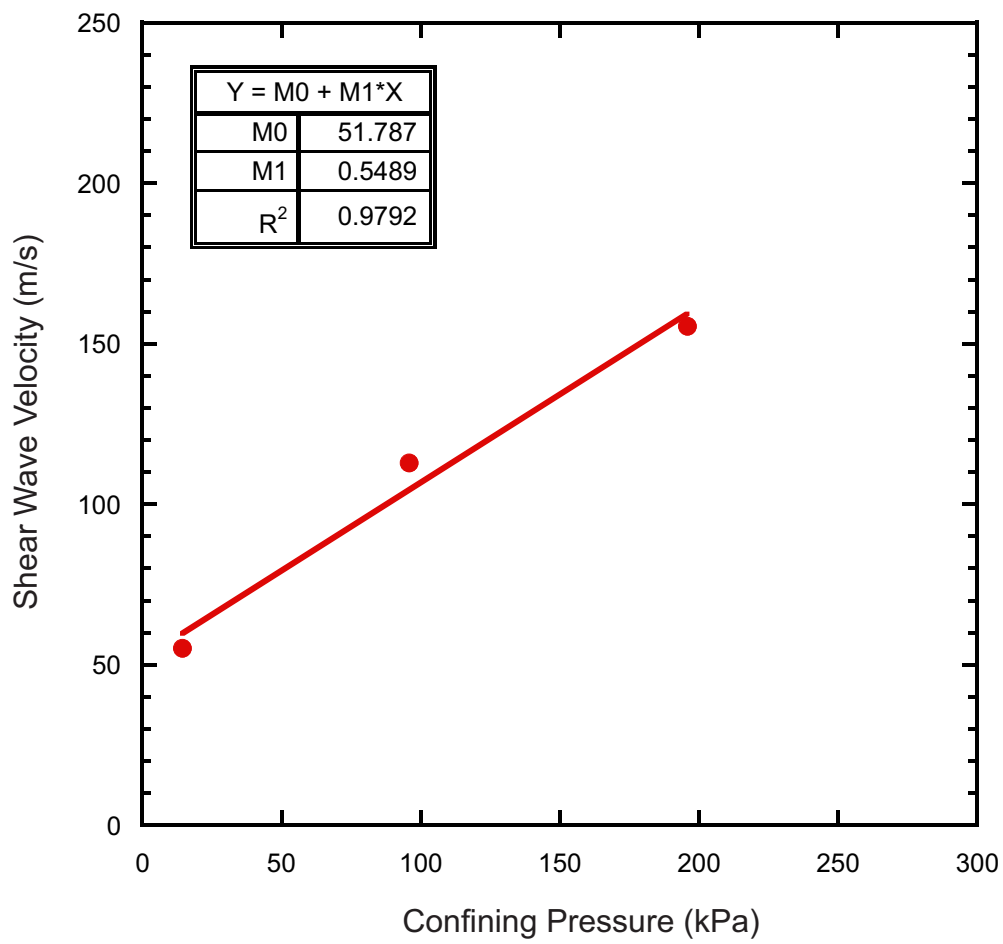
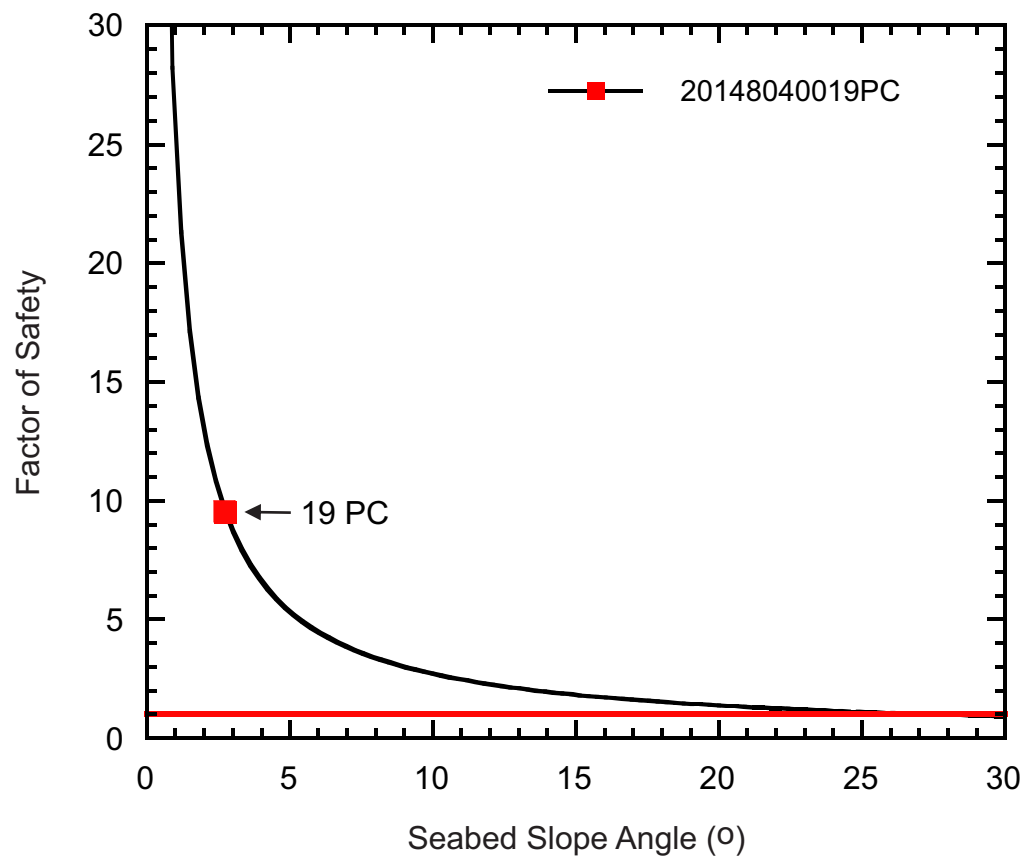Figure 9.44. Shear wave velocities at various confining pressures for piston core 20148040019.

Figure 9.45. FS at various slope angles for piston core 20148040019. The red square identifies the minimum FS for the present-day slope angle of the core site.
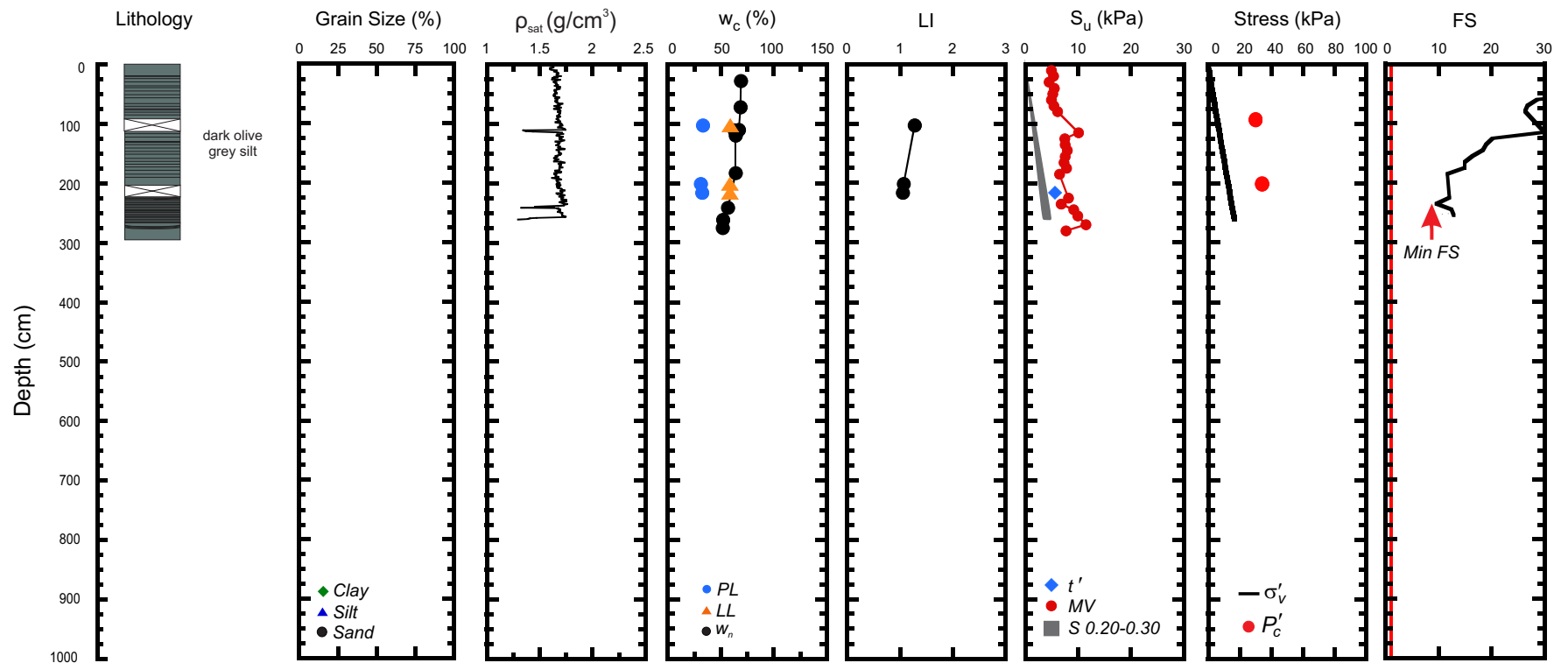
Figure 9.46. Geotechnical profile for core 20148040019 from above the head wall in Region 2. (ρ_{sat}= saturated bulk density, w_c = water content, w_n = natural in-situ water content, PL = plastic limit, LL = liquid limit, LI = liquidity index, S_u = undrained shear strength, MV = laboratory miniature vane shear strength, t' = maximum shear stress, S = shear strength calculated from the normalized strength ratio, σ'_v = effective overburden stress, P'_c = past maximum stress, FS = factor of safety).
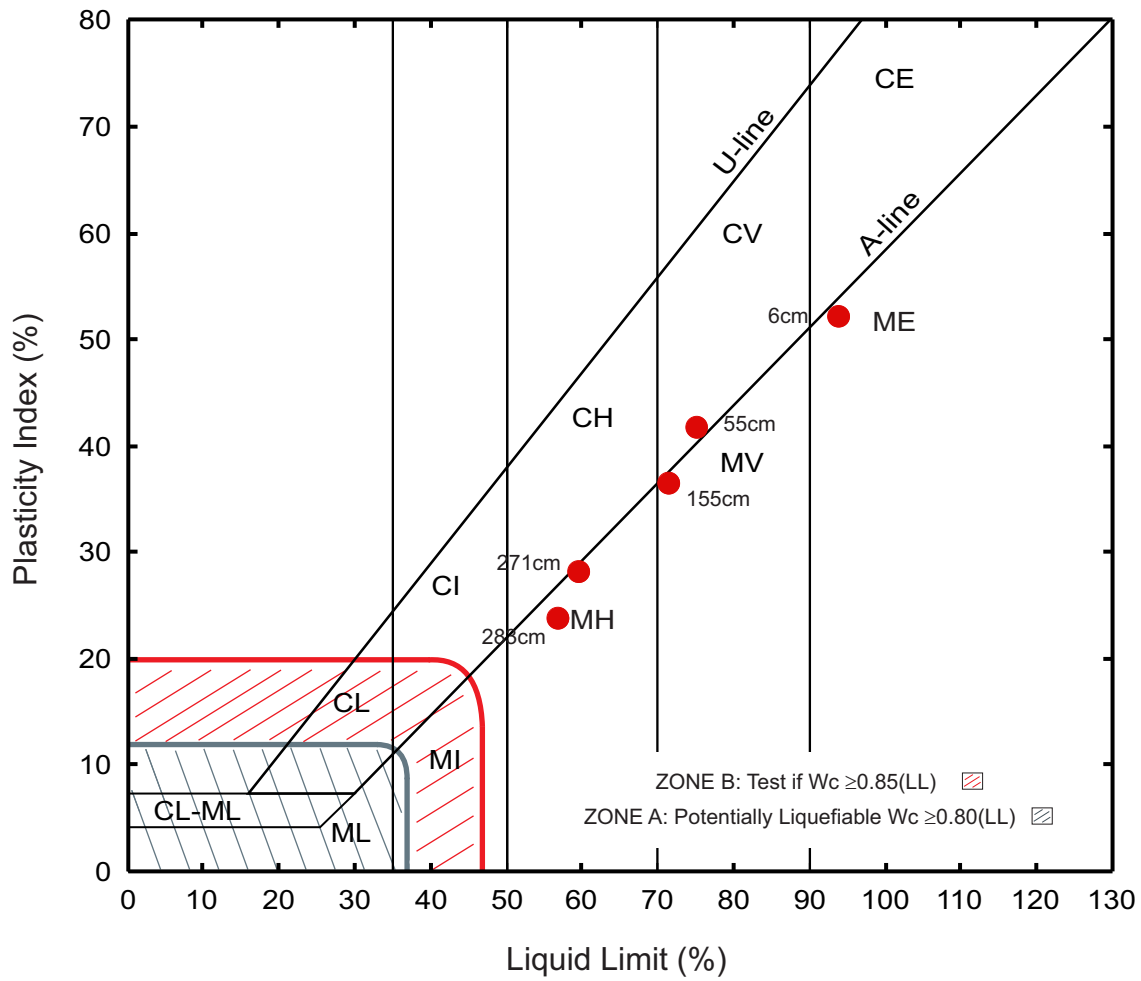
Figure 9.47. Plasticity chart showing Atterberg limit results of piston core 20148040024.
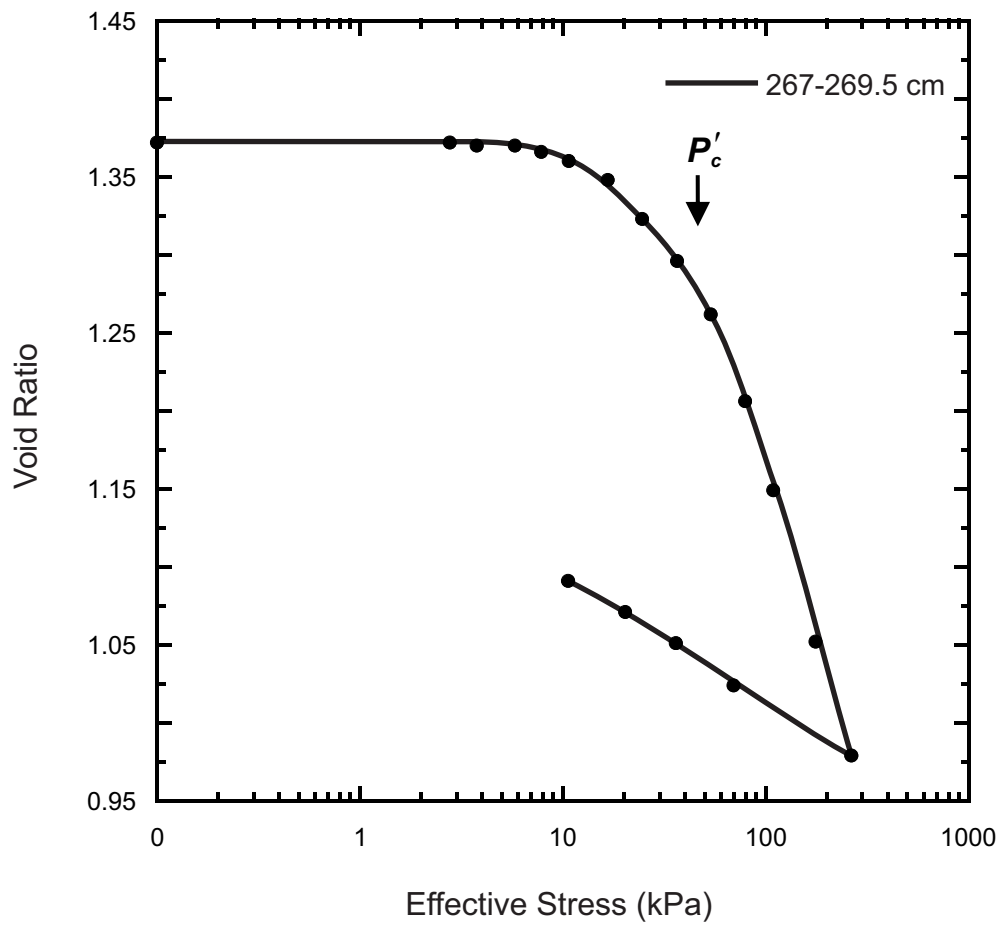
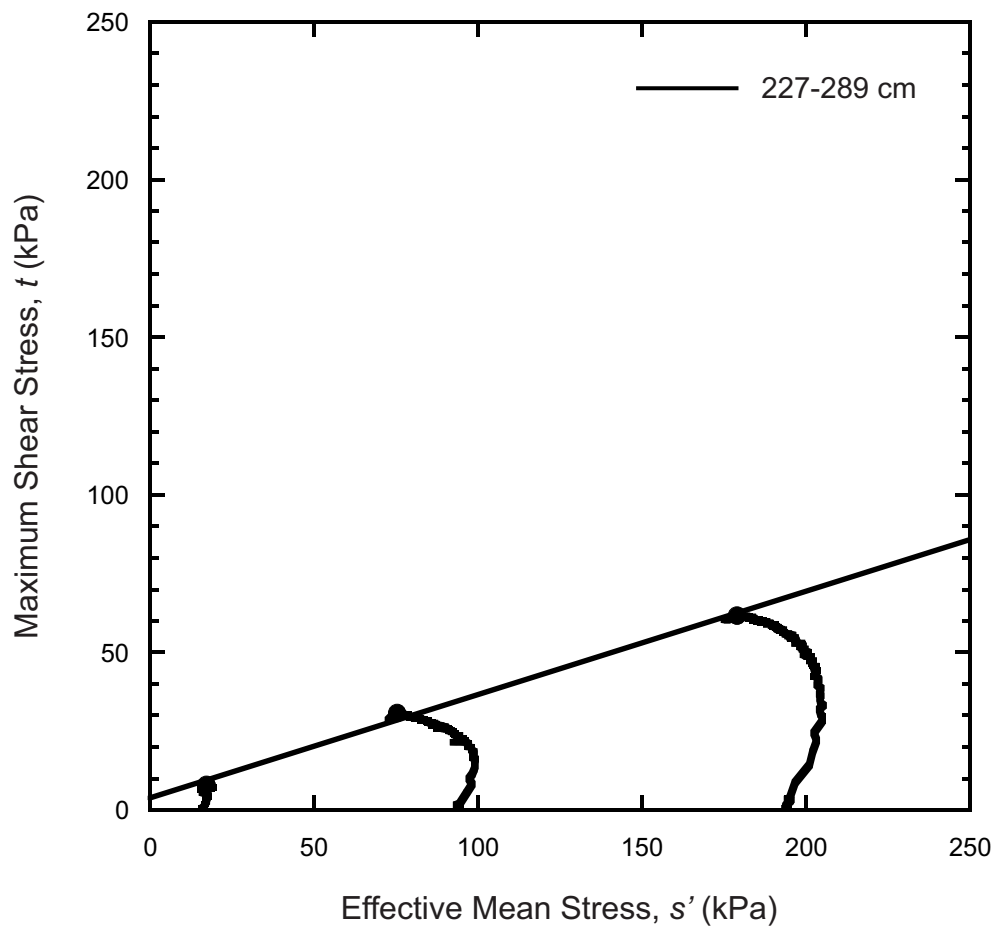Figure 9.48. Consolidation plot for piston core 20148040024.

Figure 9.49. Stress paths and failure envelopes from triaxial test results for piston core 20148040024.
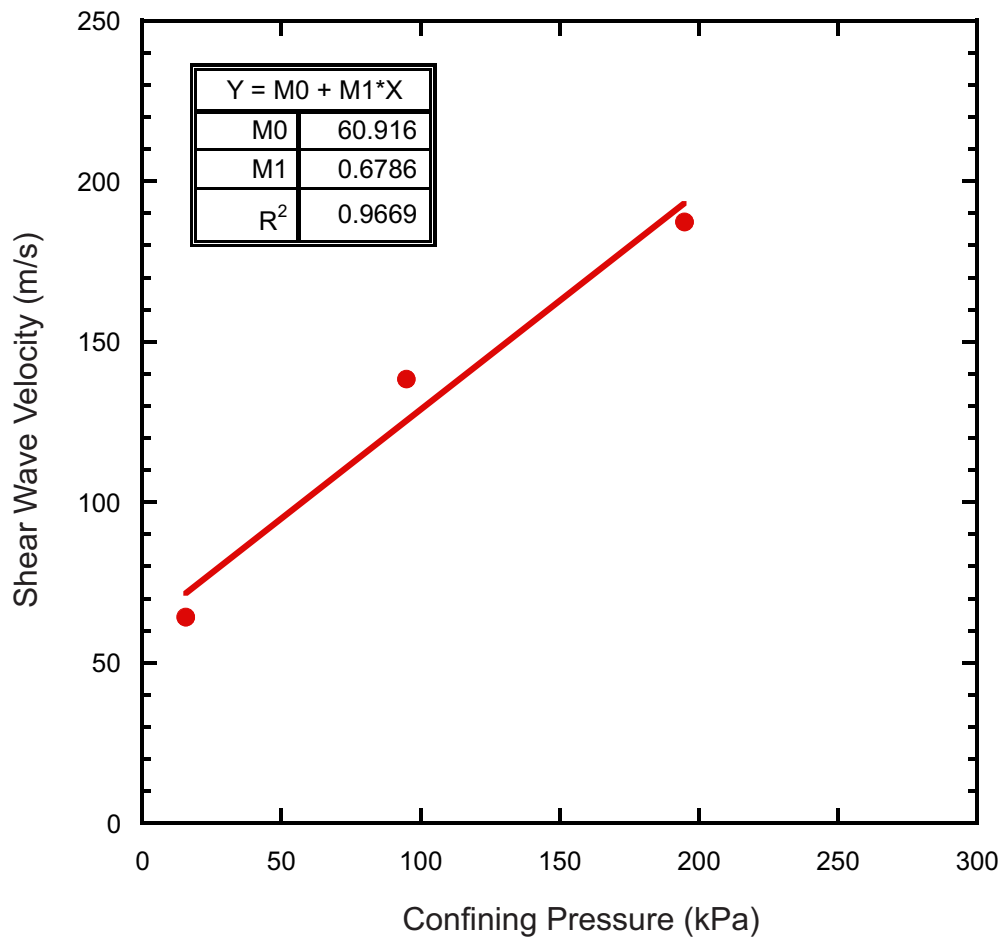
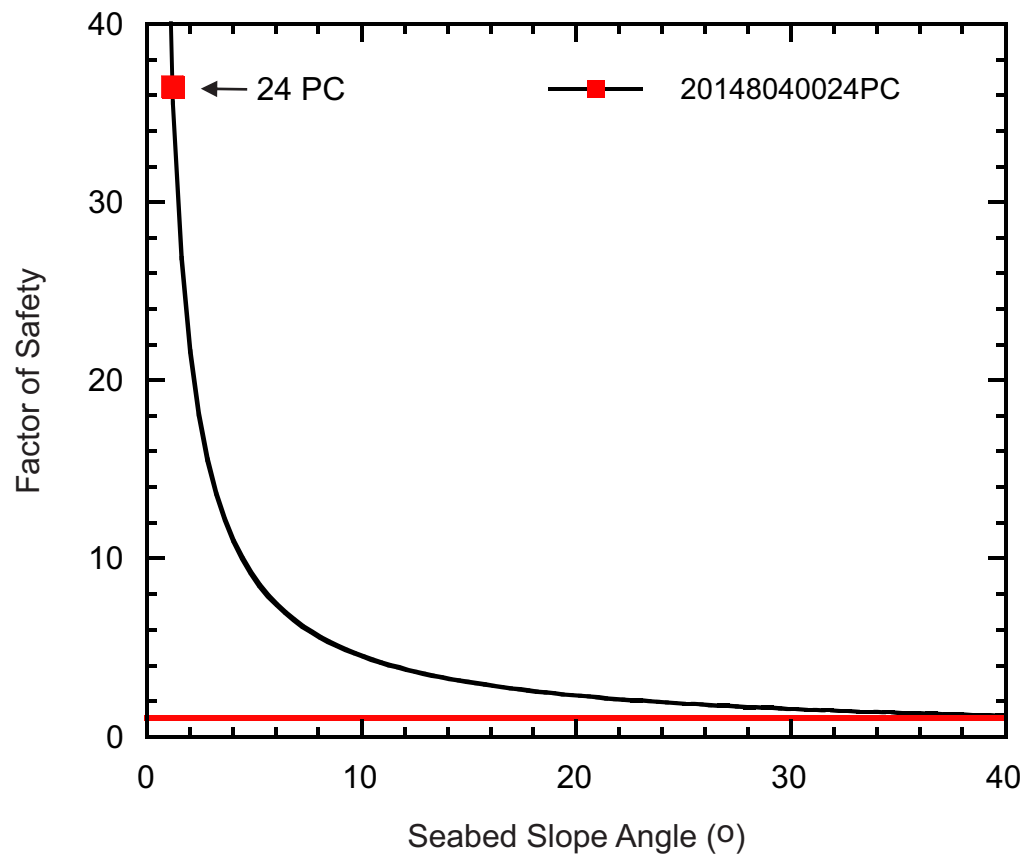Figure 9.50. Shear wave velocities at various confining pressures for piston core 20148040024.

Figure 9.51. FS at various slope angles for piston core 20148040024. The red square identifies the minimum FS for the present-day slope angle of the core site.
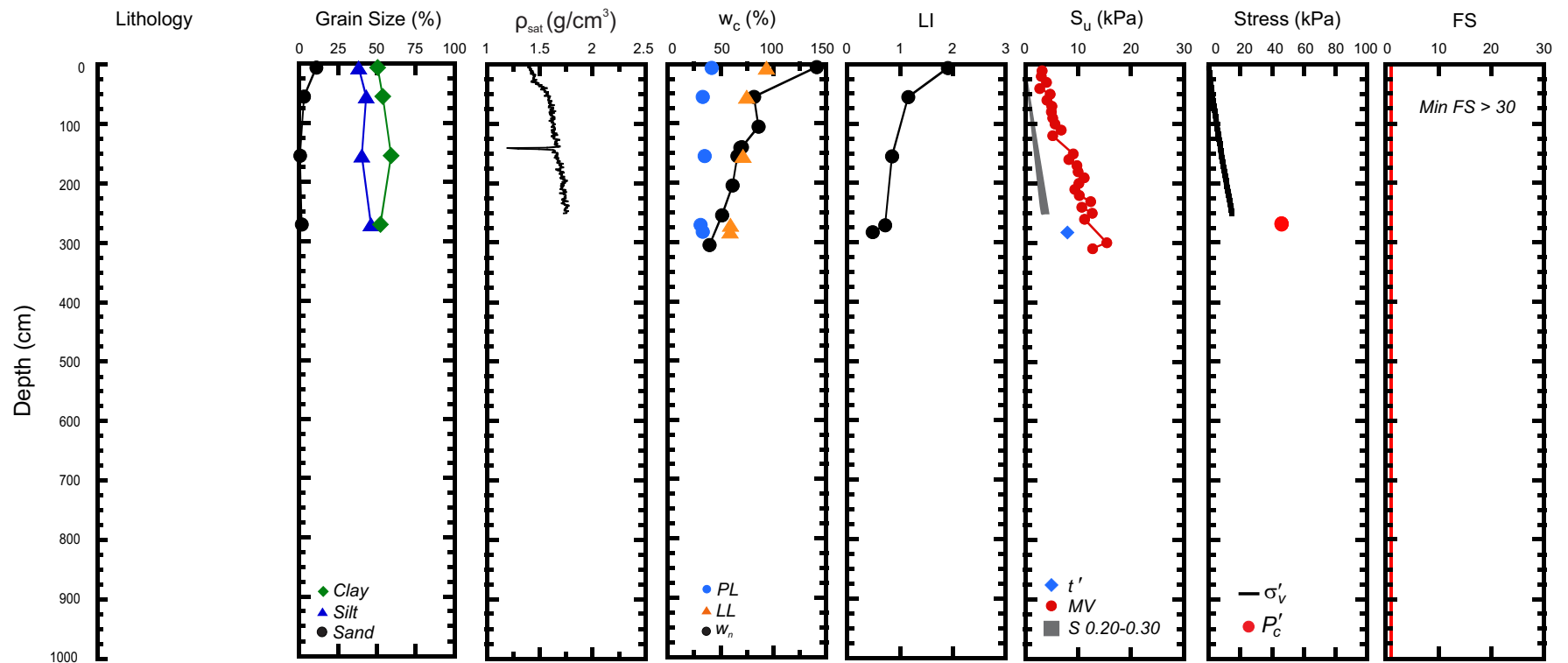
Figure 9.52. Geotechnical profile for core 20148040024 from Region 2. (ρ_{sat} = saturated bulk density, w_c = water content, w_n = natural in-situ water content, PL = plastic limit, LL = liquid limit, LI = liquidity index, S_u = undrained shear strength, MV = laboratory miniature vane shear strength, t' = maximum shear stress, S = shear strength calculated from the normalized strength ratio, σ'_v = effective overburden stress, P'_c = past maximum stress, FS = factor of safety).
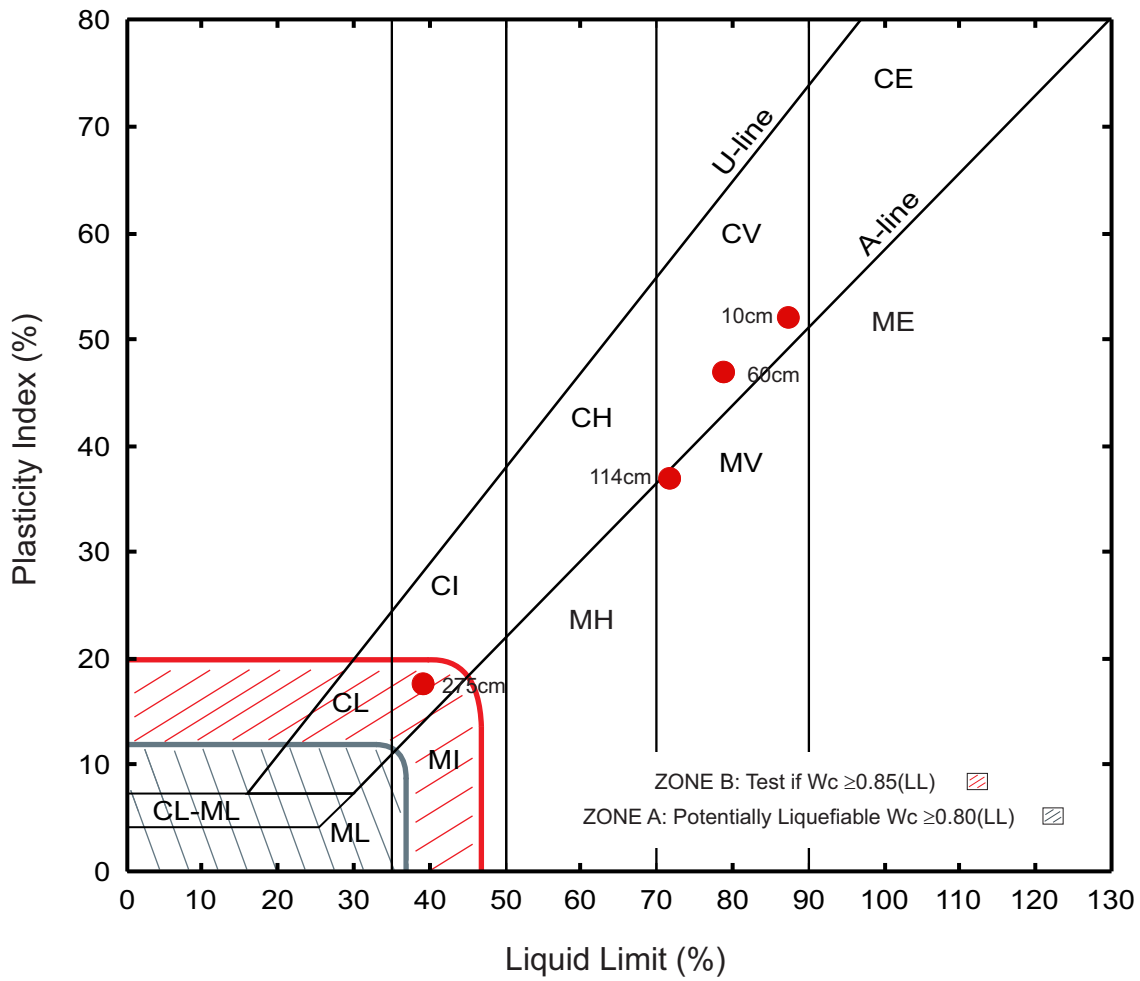
Figure 9.53. Plasticity chart showing Atterberg limit results of piston core 20098040013.
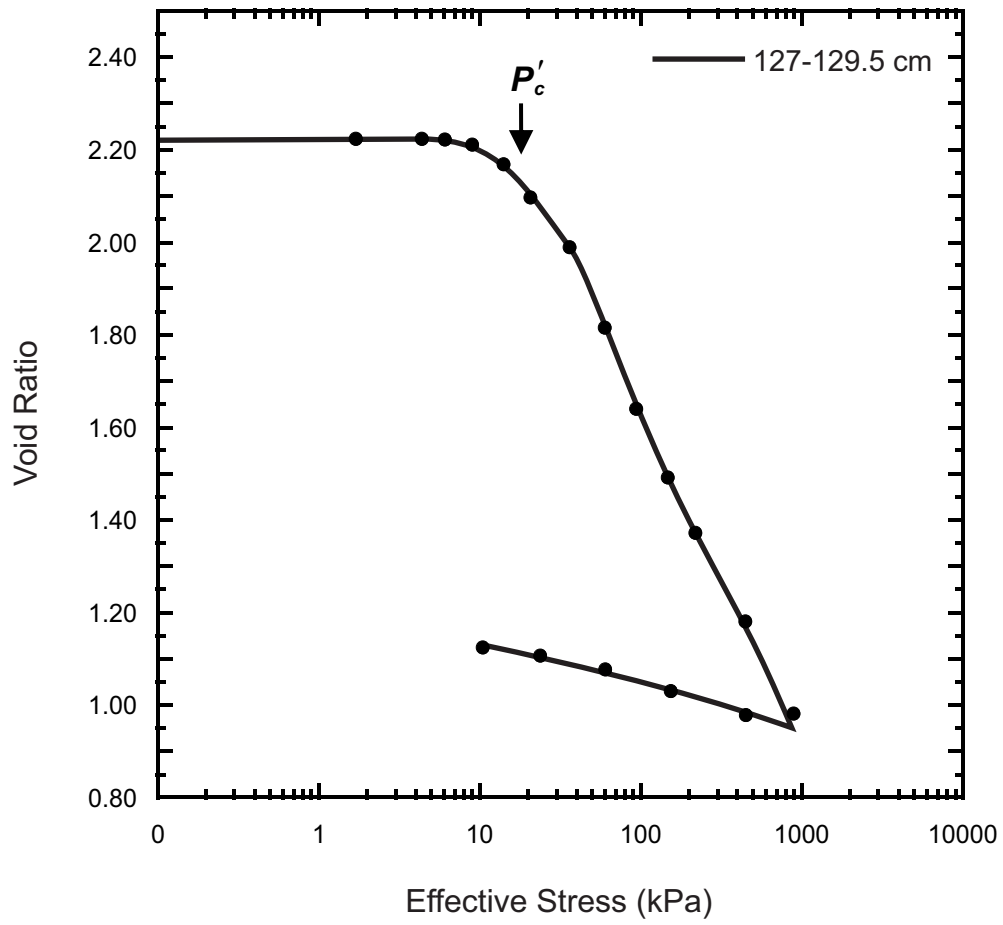
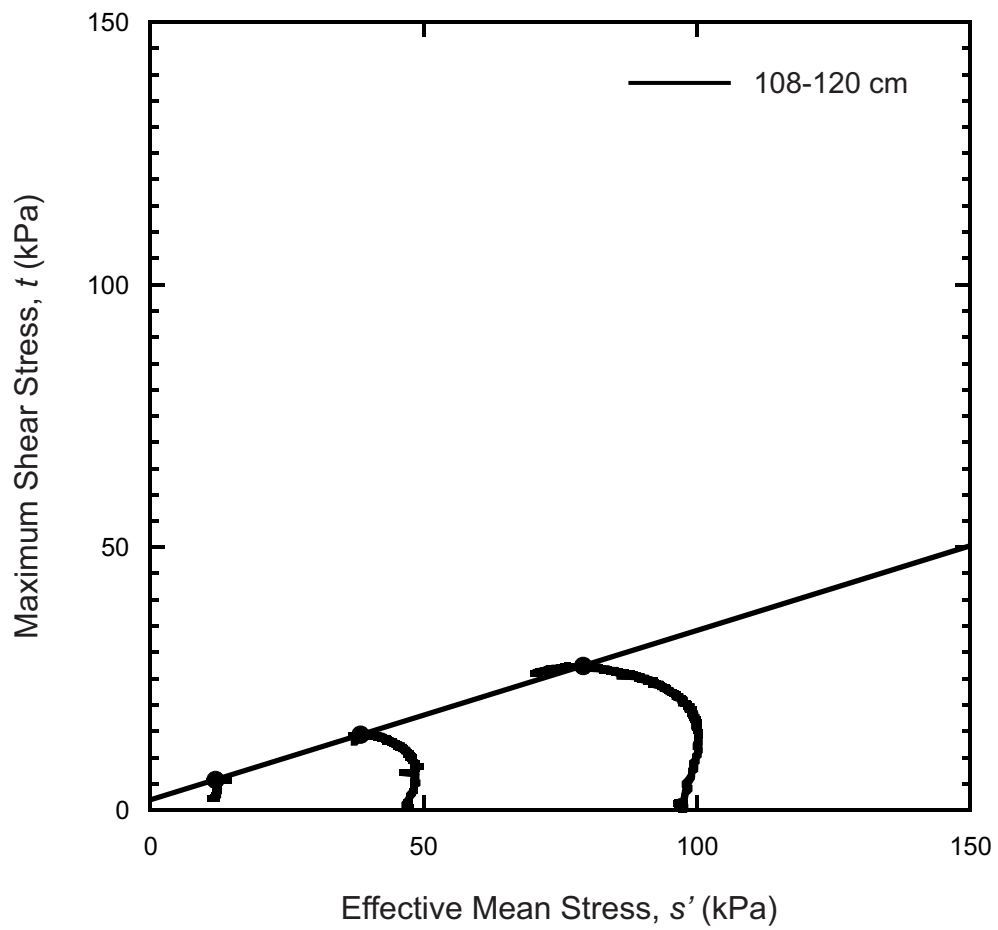Figure 9.54. Consolidation plot for piston core 20098040013.

Figure 9.55. Stress paths and failure envelopes from triaxial test results for piston core 20098040013.
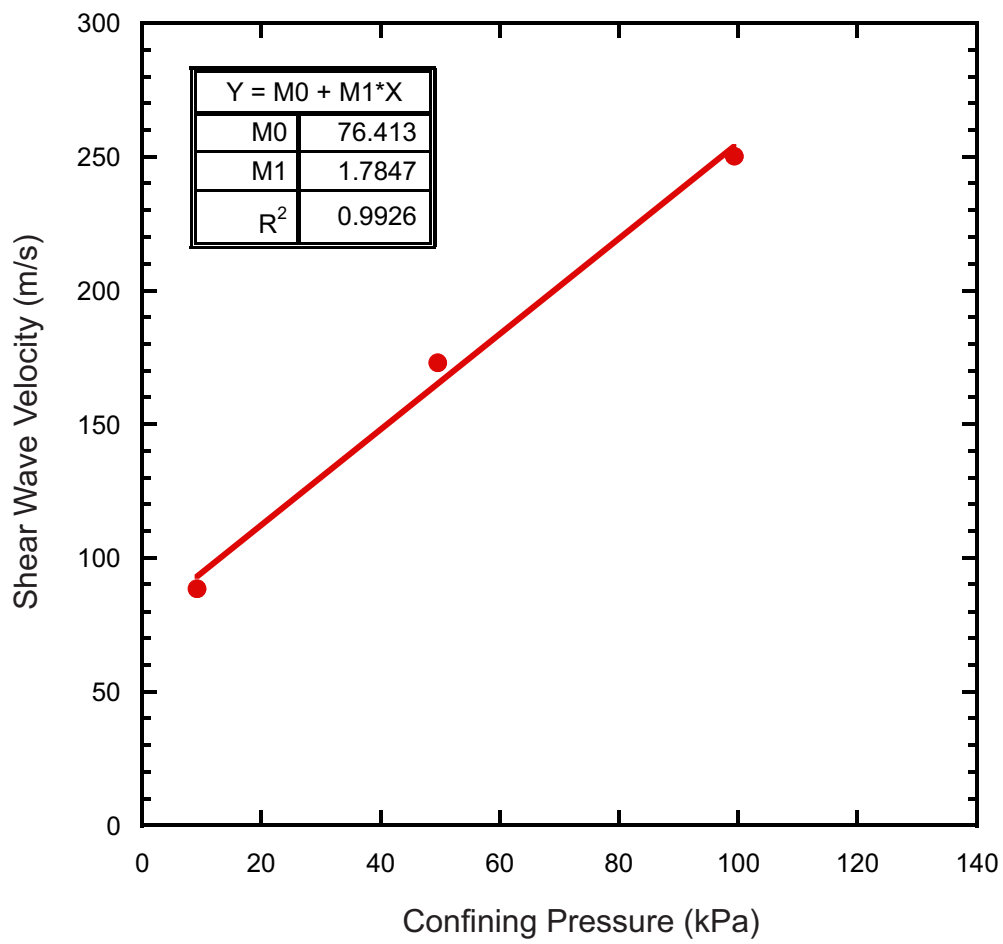
Figure 9.56. Shear wave velocities at various confining pressures for piston core 20098040013.
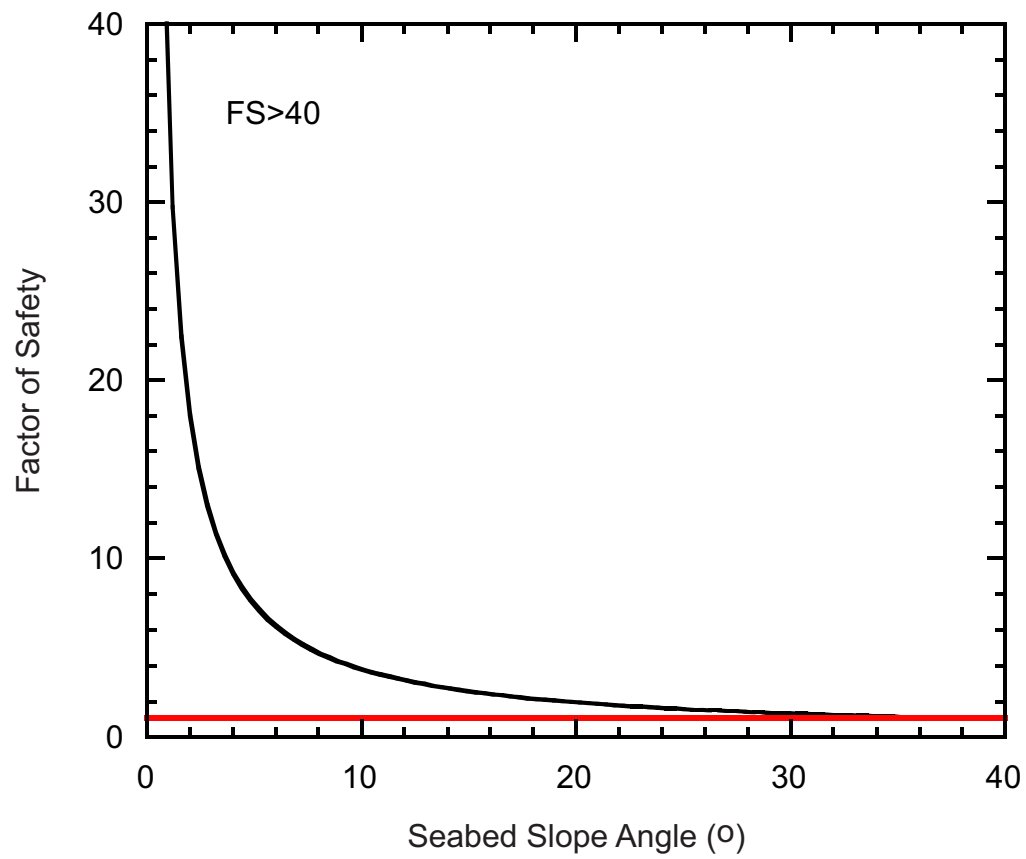
Figure 9.57. FS at various slope angles for piston core 20098040013. The minimum FS for the present-day slope angle of the core site is > 40.
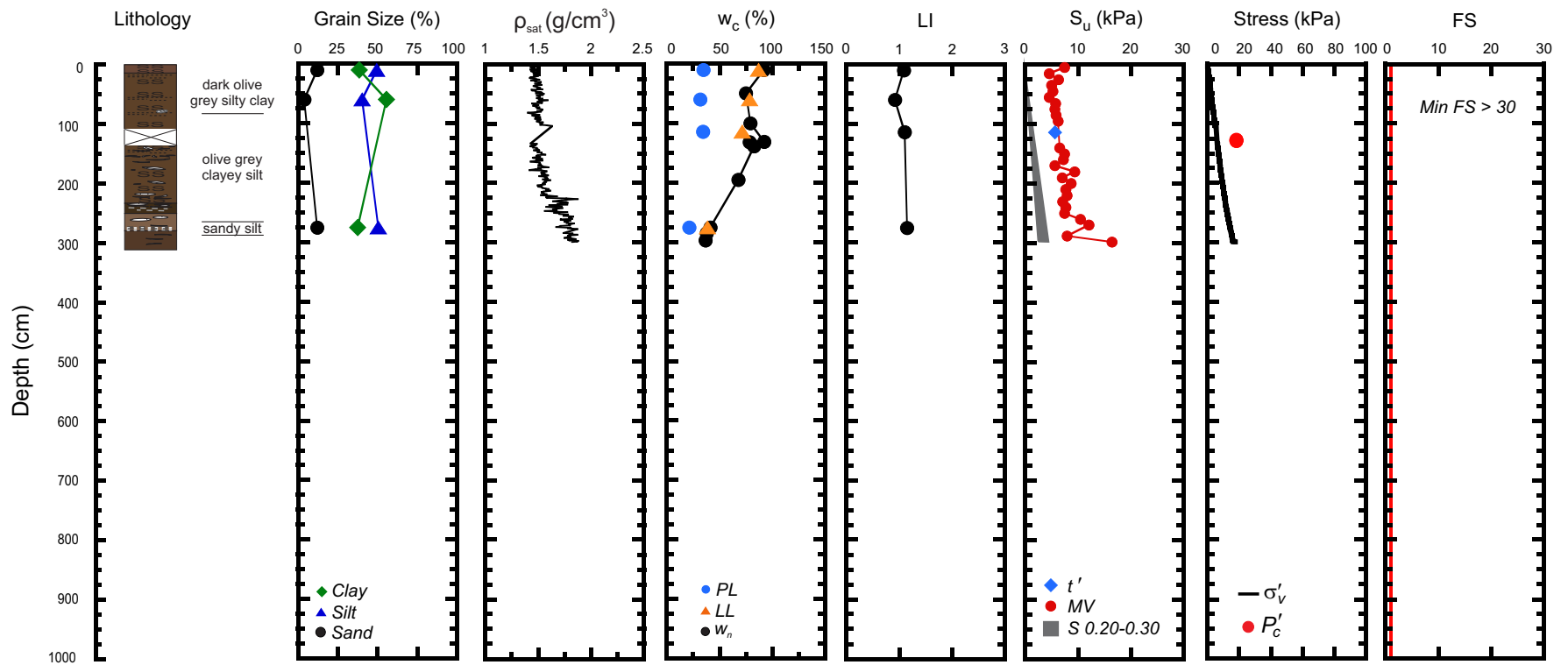
Figure 9.58. Geotechnical profile for core 20098040013 from Region 2. (ρ_{sat}= saturated bulk density, w_c = water content, w_n = natural in-situ water content, PL = plastic limit, LL = liquid limit, LI = liquidity index, S_u = undrained shear strength, MV = laboratory miniature vane shear strength, t' = maximum shear stress, S = shear strength calculated from the normalized strength ratio, σ'_v = effective overburden stress, P'_c = past maximum stress, FS = factor of safety).
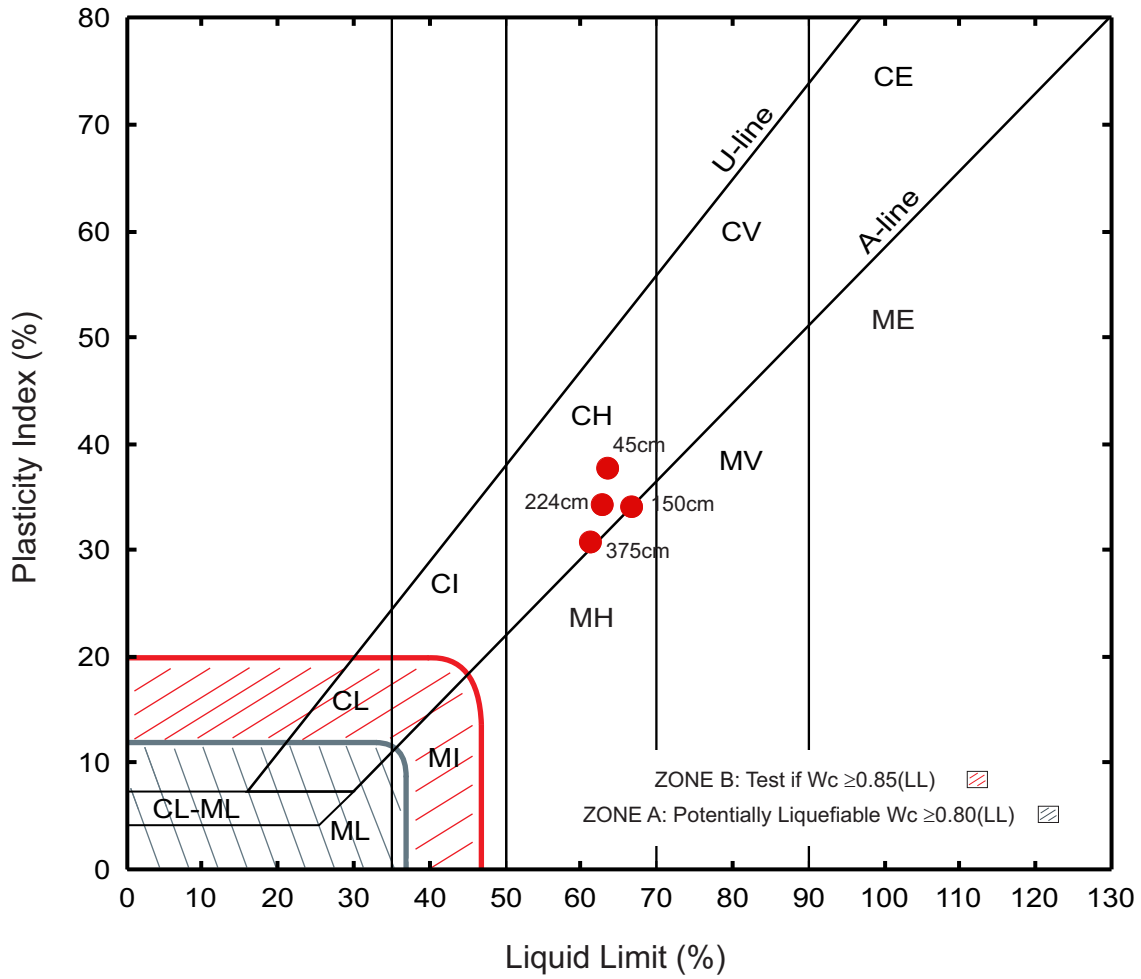
Figure 9.59. Plasticity chart showing Atterberg limit results of piston core 20098040019.
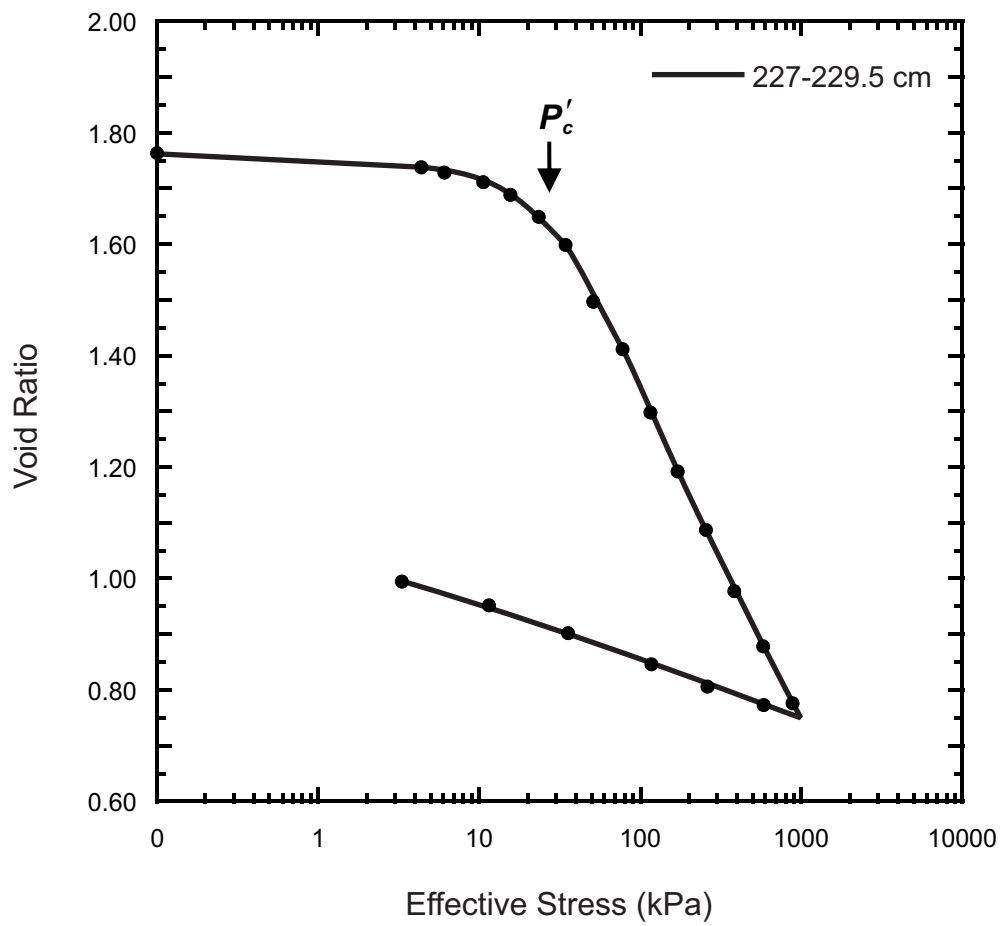
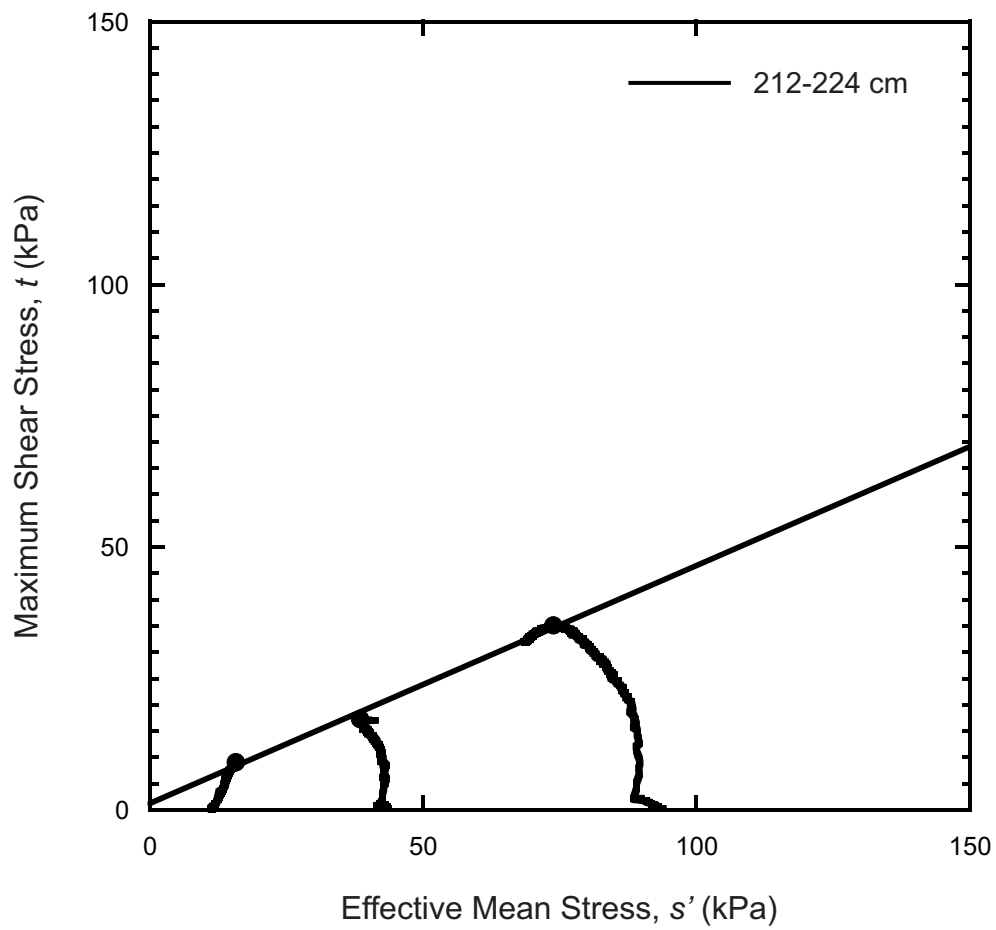Figure 9.60. Consolidation plot for piston core 20098040019.

Figure 9.61. Stress paths and failure envelopes from triaxial test results for piston core 20098040019.
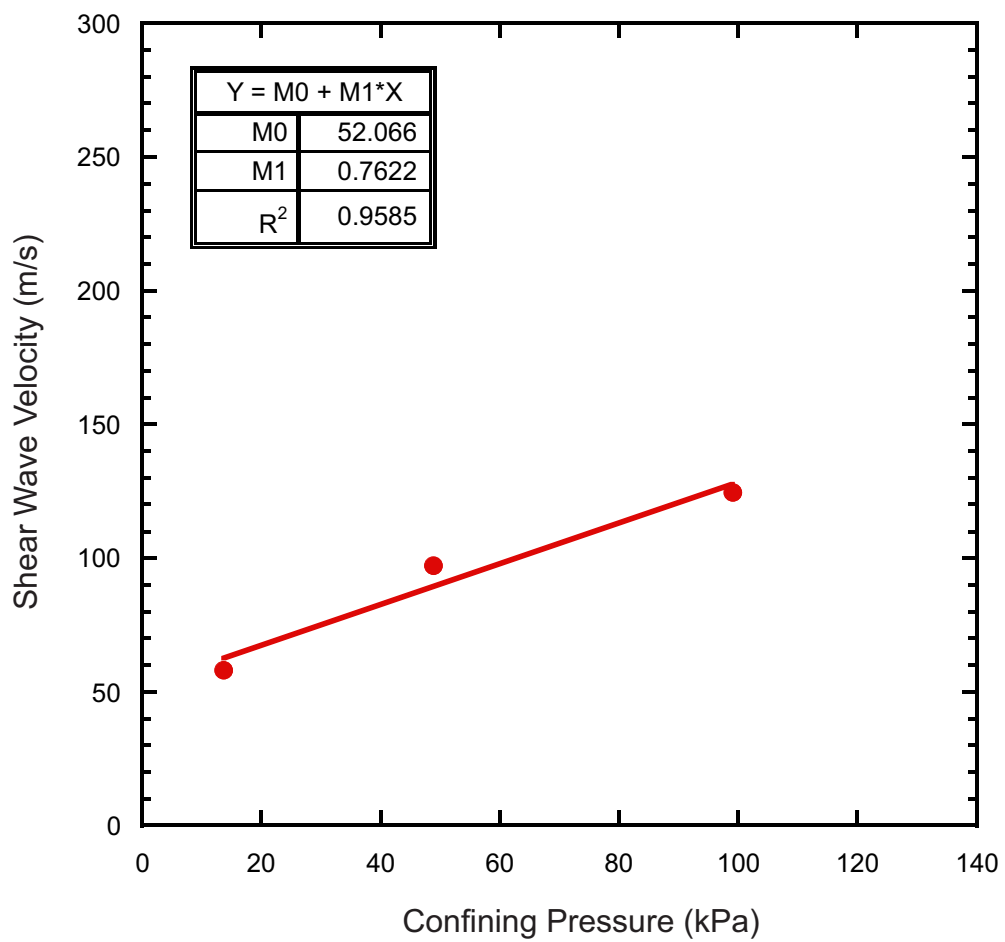
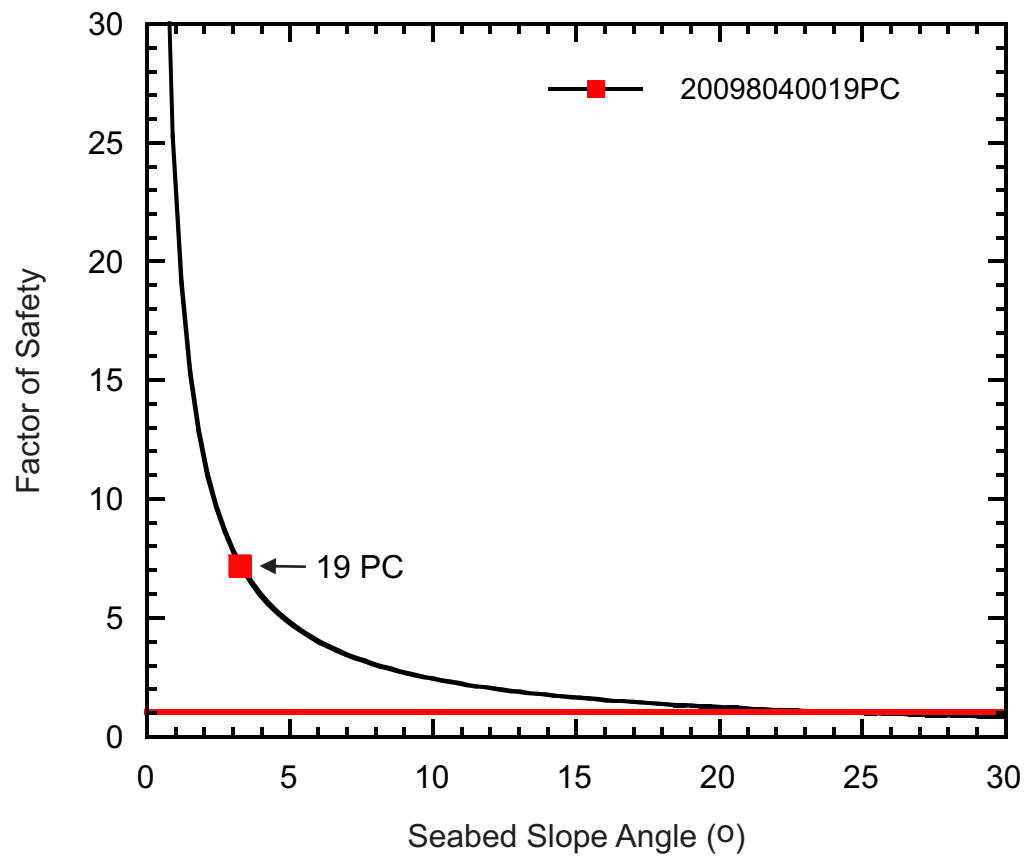Figure 9.62. Shear wave velocities at various confining pressures for piston core 20098040019.

Figure 9.63. FS at various slope angles for piston core 20098040019. The red square identifies the minimum FS for the present-day slope angle of the core site.
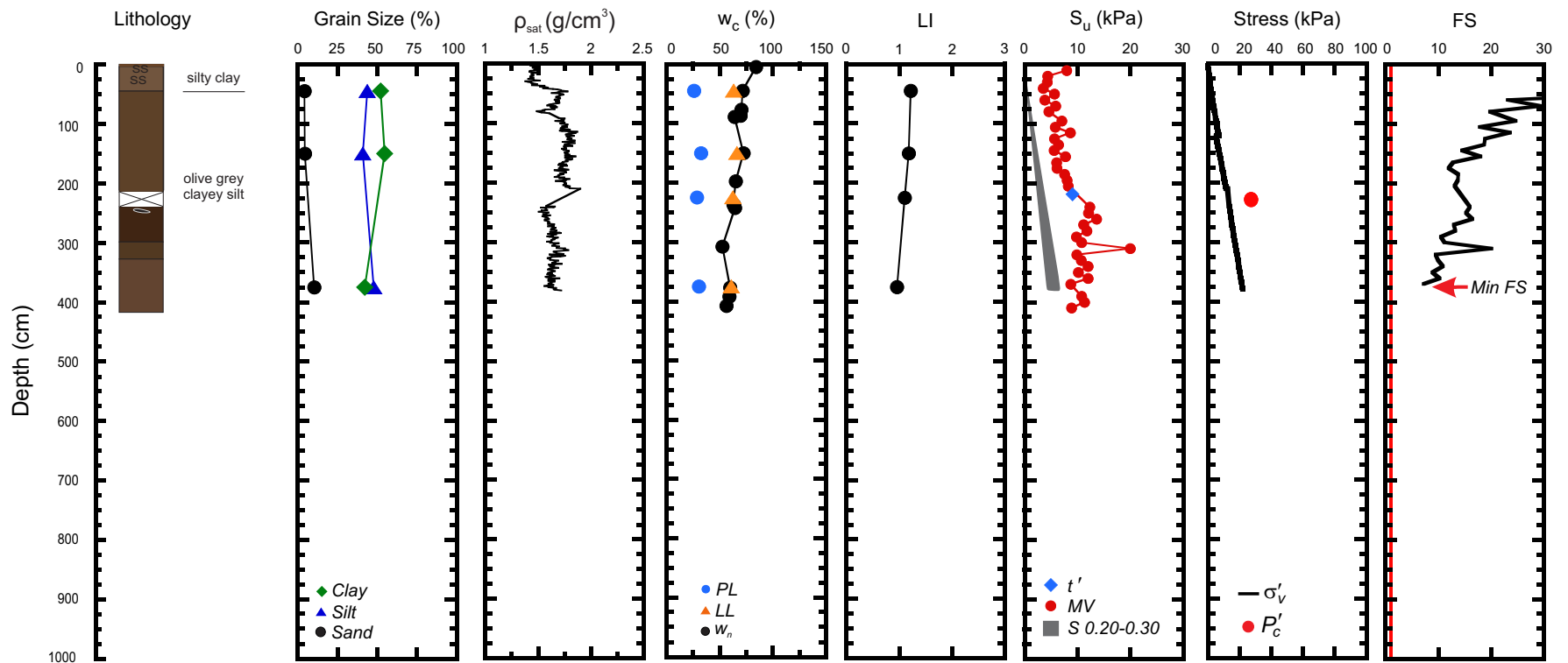
Figure 9.64. Geotechnical profile for core 20098040019 from Region 2. (ρ_{sat}= saturated bulk density, w_c = water content, w_n = natural in-situ water content, PL = plastic limit, LL = liquid limit, LI = liquidity index, S_u = undrained shear strength, MV = laboratory miniature vane shear strength, t' = maximum shear stress, S = shear strength calculated from the normalized strength ratio, σ'_v = effective overburden stress, P'_c = past maximum stress, FS = factor of safety).
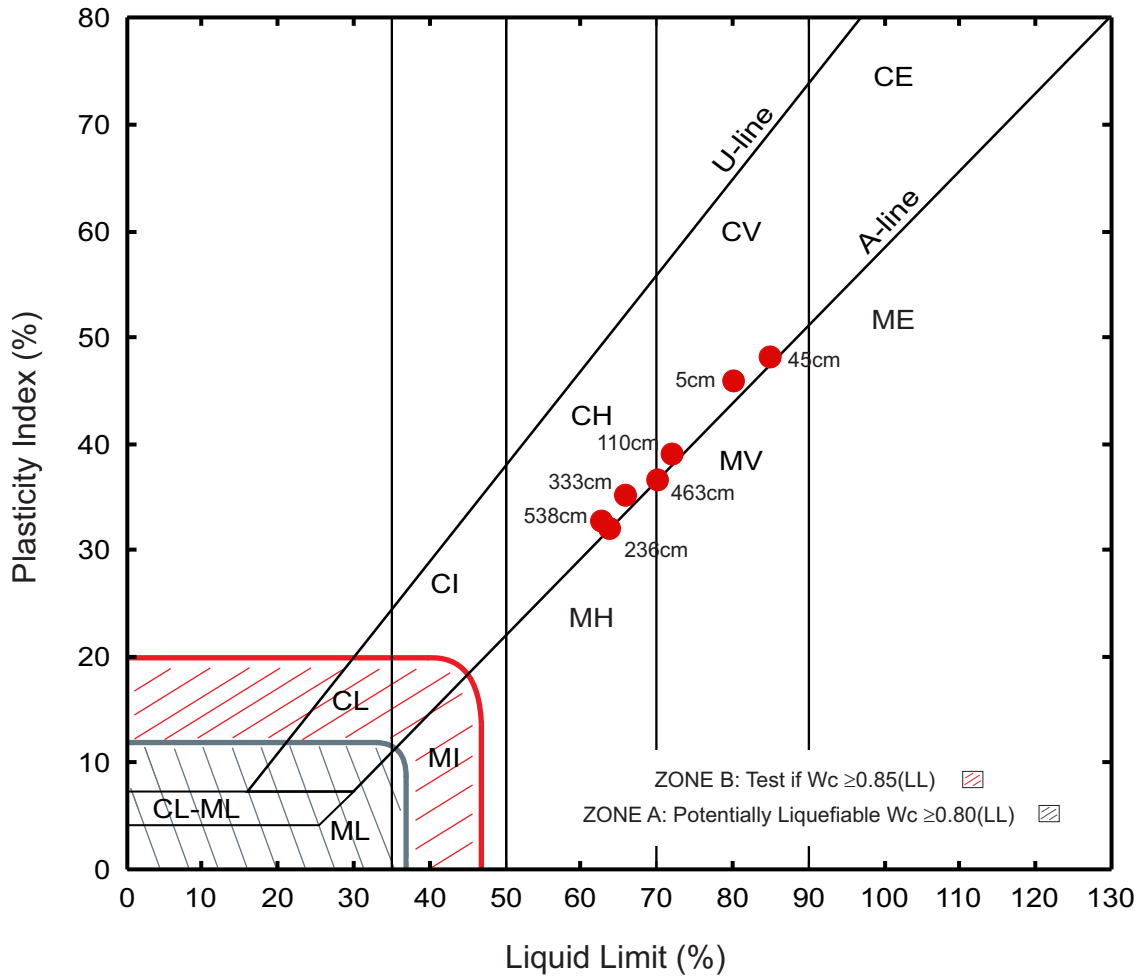
Figure 9.65. Plasticity chart showing Atterberg limit results of piston core 20098040026.
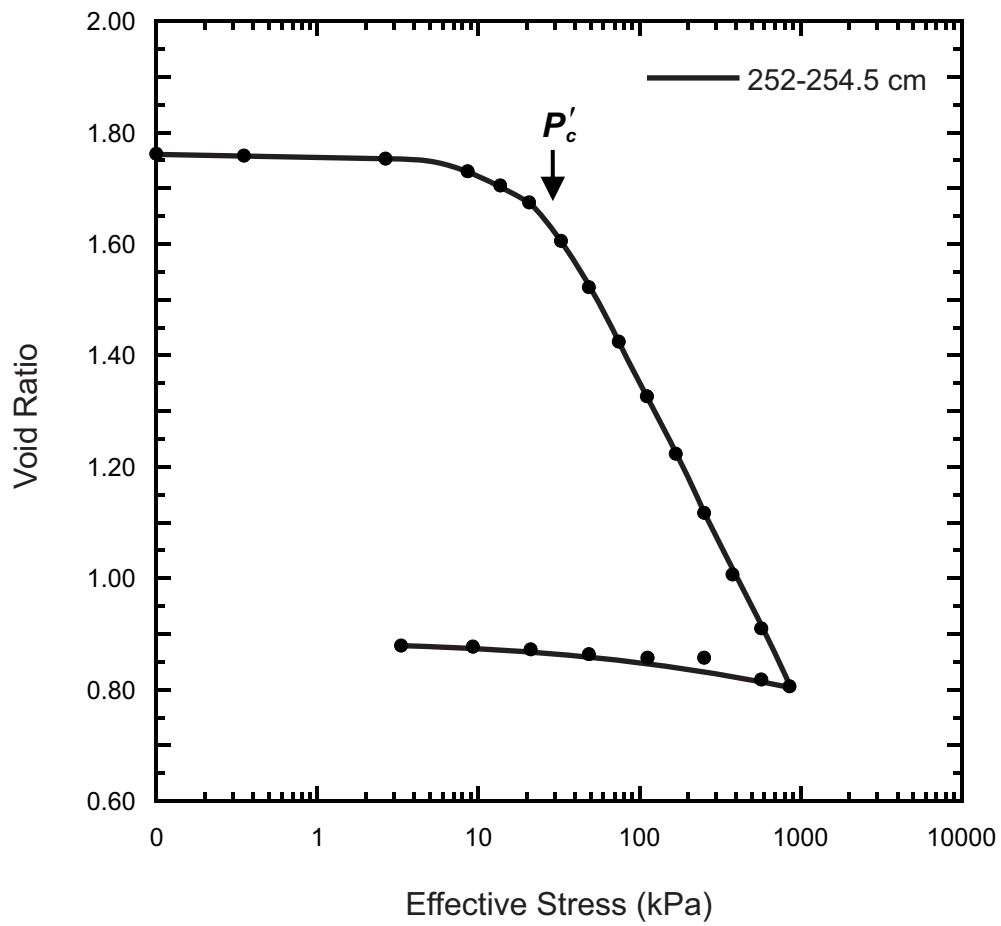
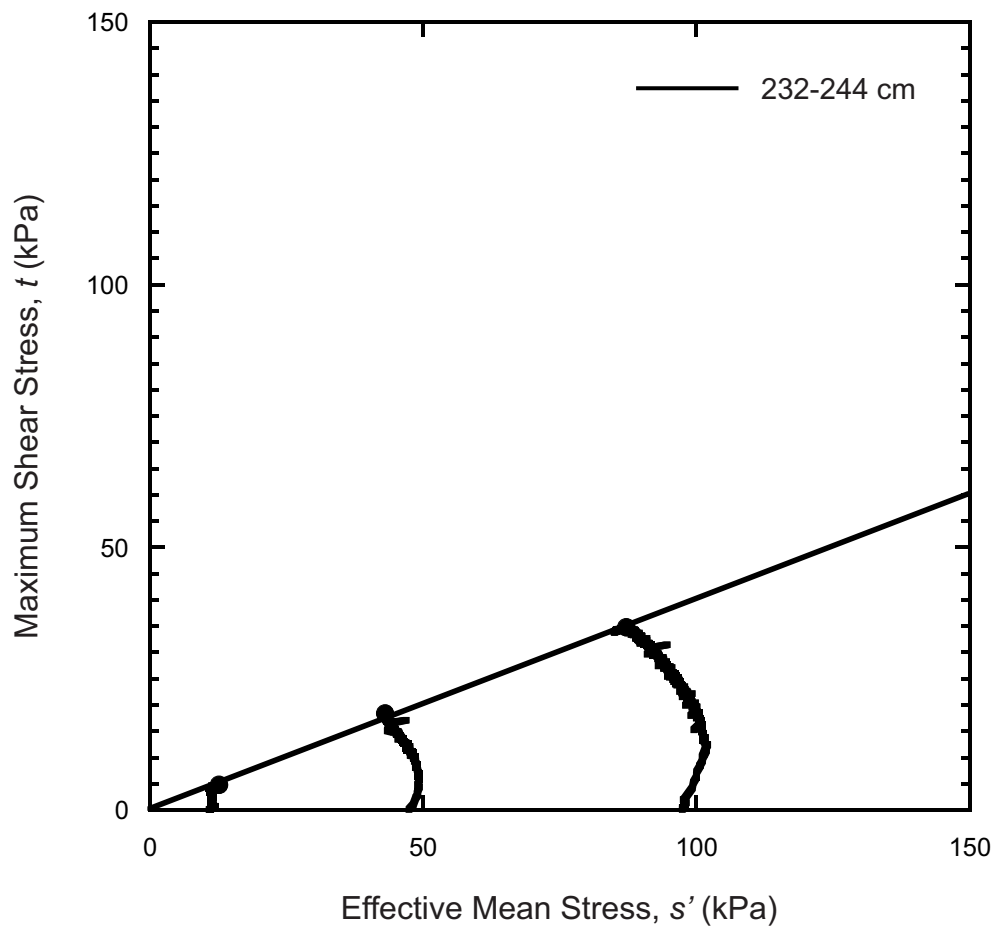Figure 9.66. Consolidation plot for piston core 20098040026.

Figure 9.67. Stress paths and failure envelopes from triaxial test results for piston core 20098040026.

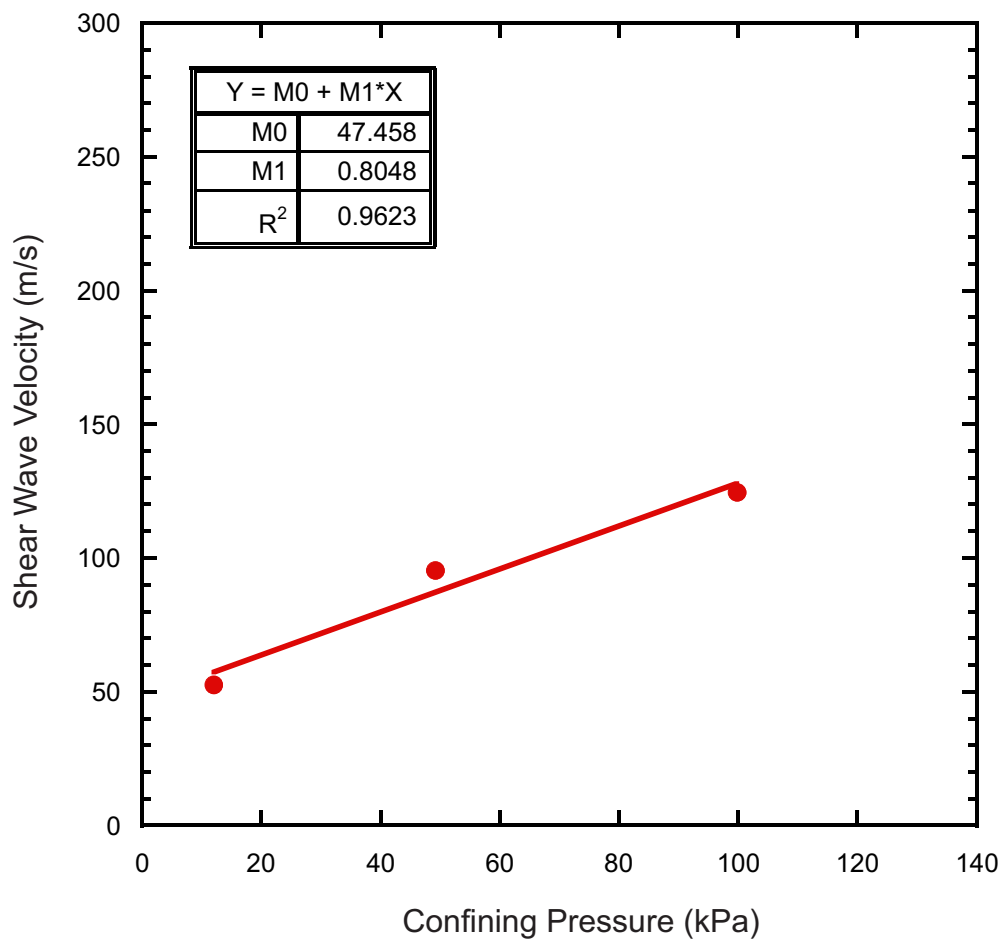| Y = M0 + M1*X	
M0	47.458
M1	0.8048
R^2	0.9623

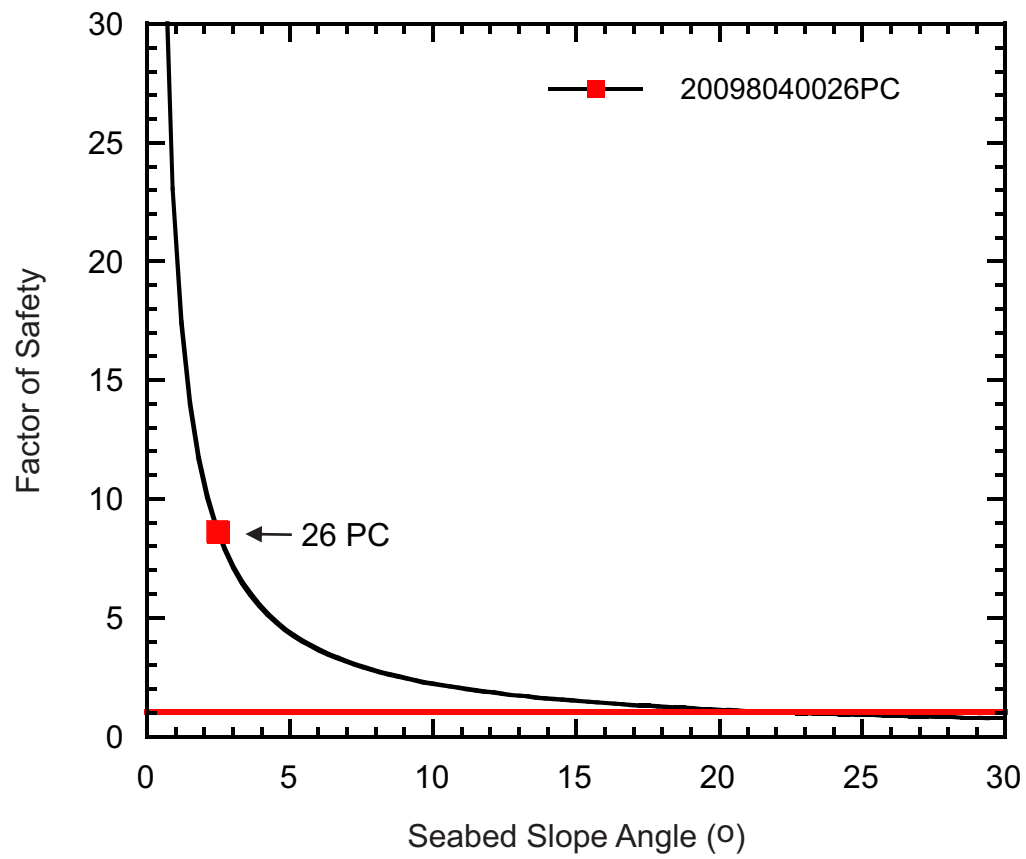Figure 9.68. Shear wave velocities at various confining pressures for piston core 20098040026.

Figure 9.69. FS at various slope angles for piston core 20098040026. The red square identifies the minimum FS for the present-day slope angle of the core site.
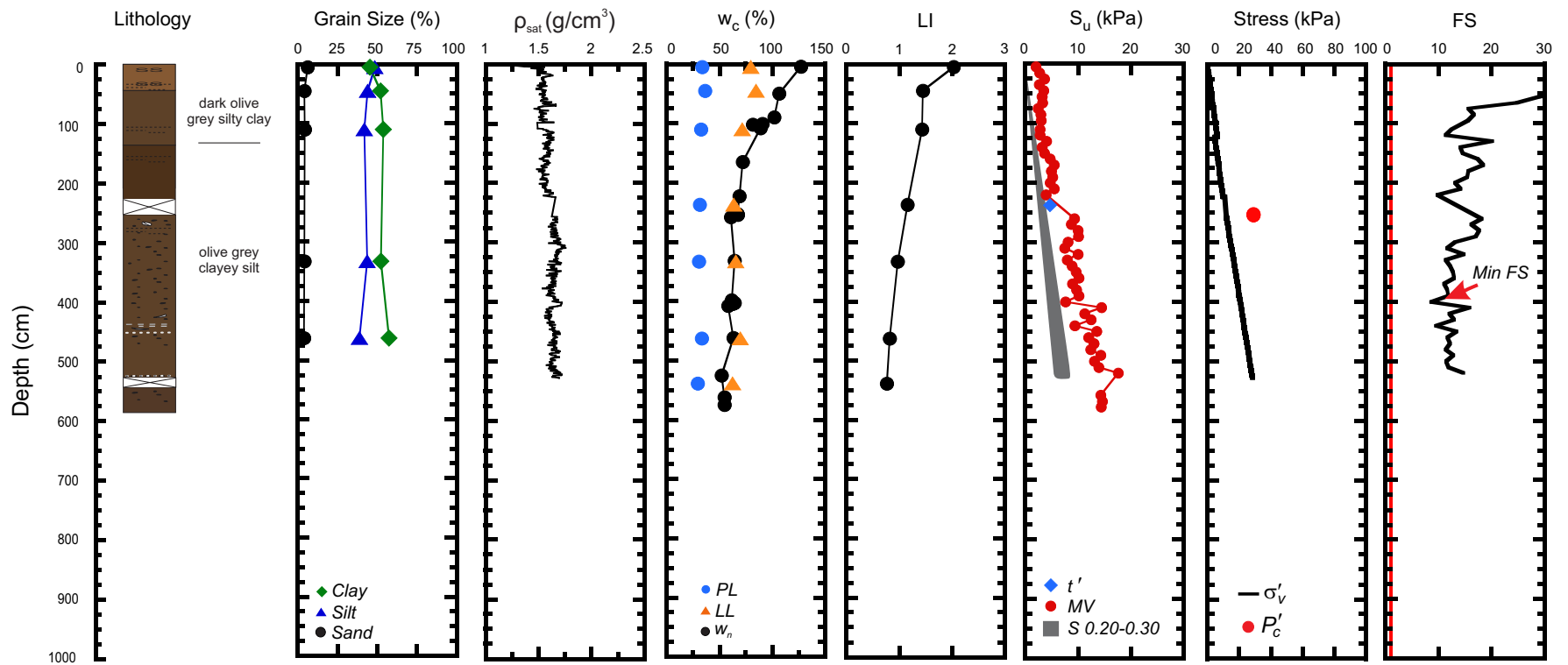
Figure 9.70. Geotechnical profile for core 20098040026 from Region 2. (ρ_{sat}= saturated bulk density, w_c = water content, w_n = natural in-situ water content, PL = plastic limit, LL = liquid limit, LI = liquidity index, S_u = undrained shear strength, MV = laboratory miniature vane shear strength, t' = maximum shear stress, S = shear strength calculated from the normalized strength ratio, σ'_v = effective overburden stress, P'_c = past maximum stress, FS = factor of safety).
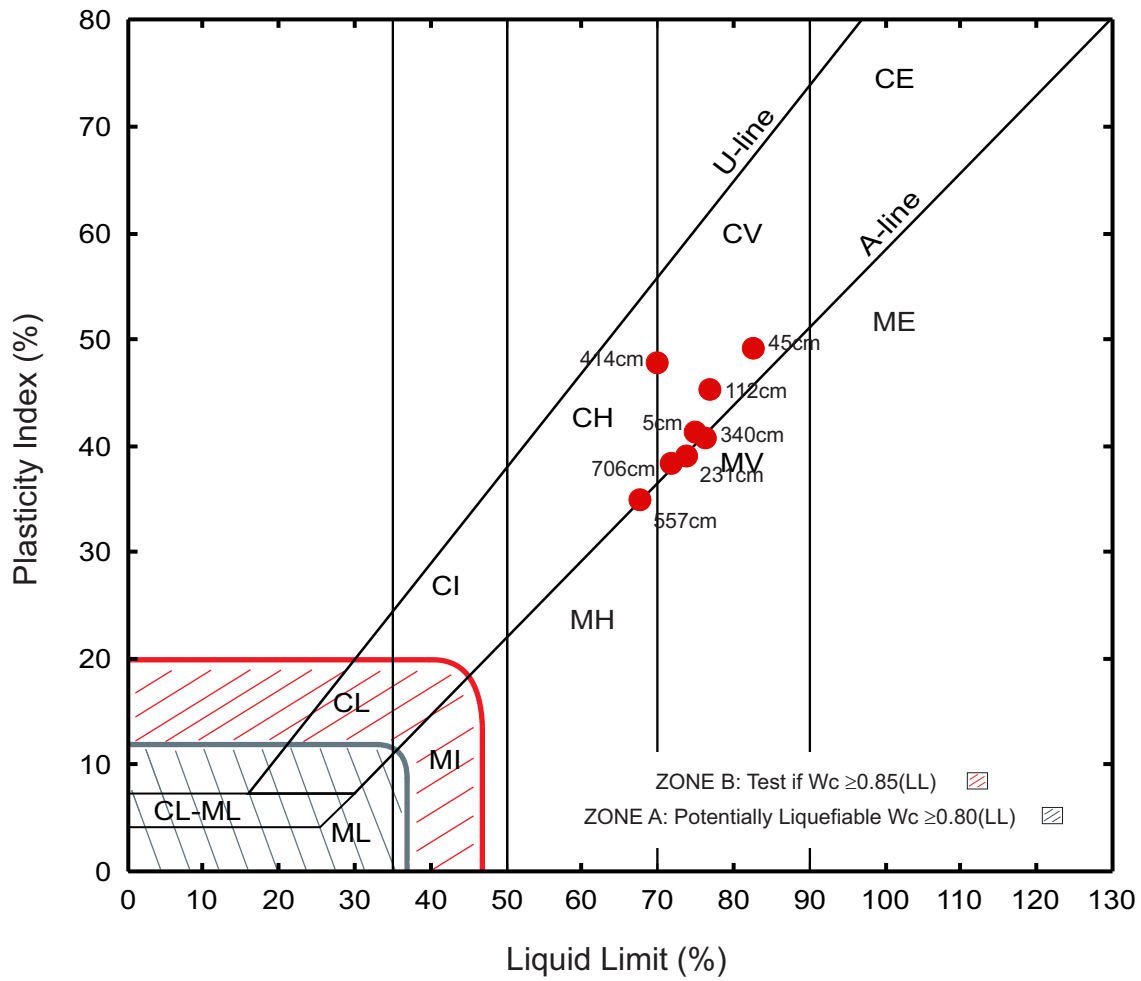
Figure 9.71. Plasticity chart showing Atterberg limit results of piston core 20098040036.
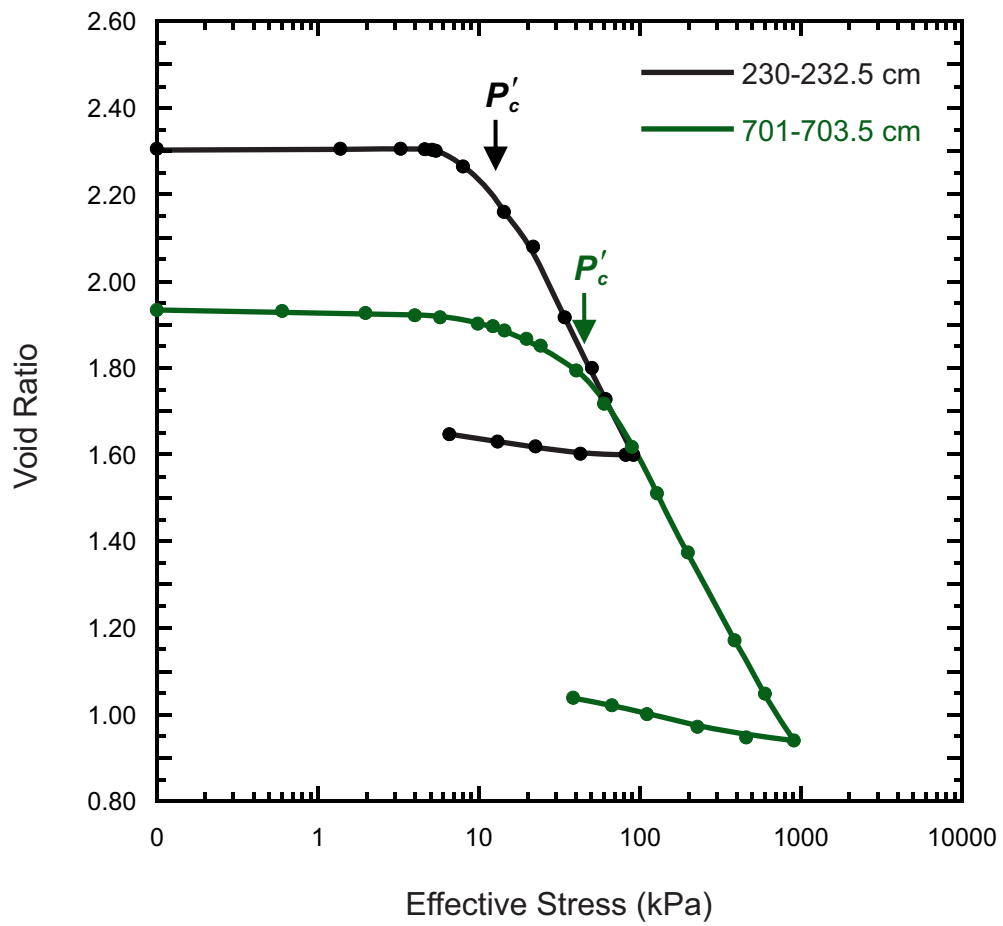
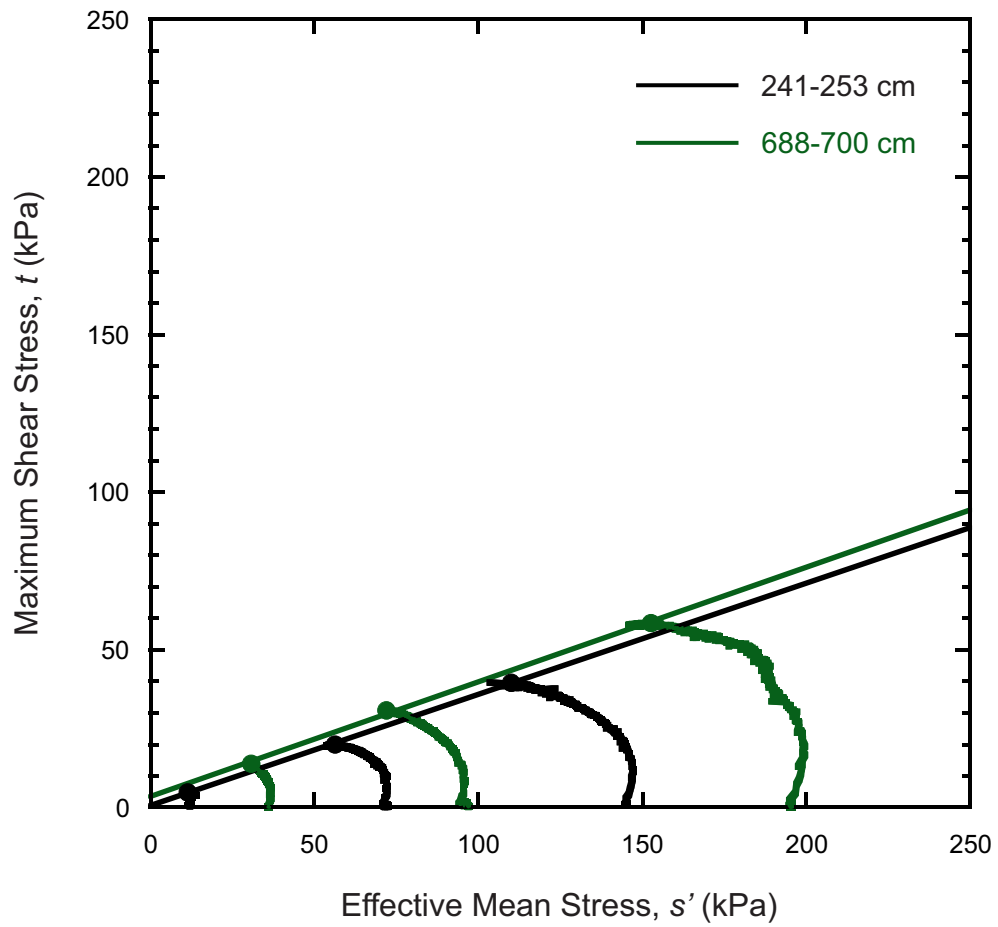Figure 9.72. Consolidation plot for piston core 20098040036.

Figure 9.73. Stress paths and failure envelopes from triaxial test results for piston core 20098040036.
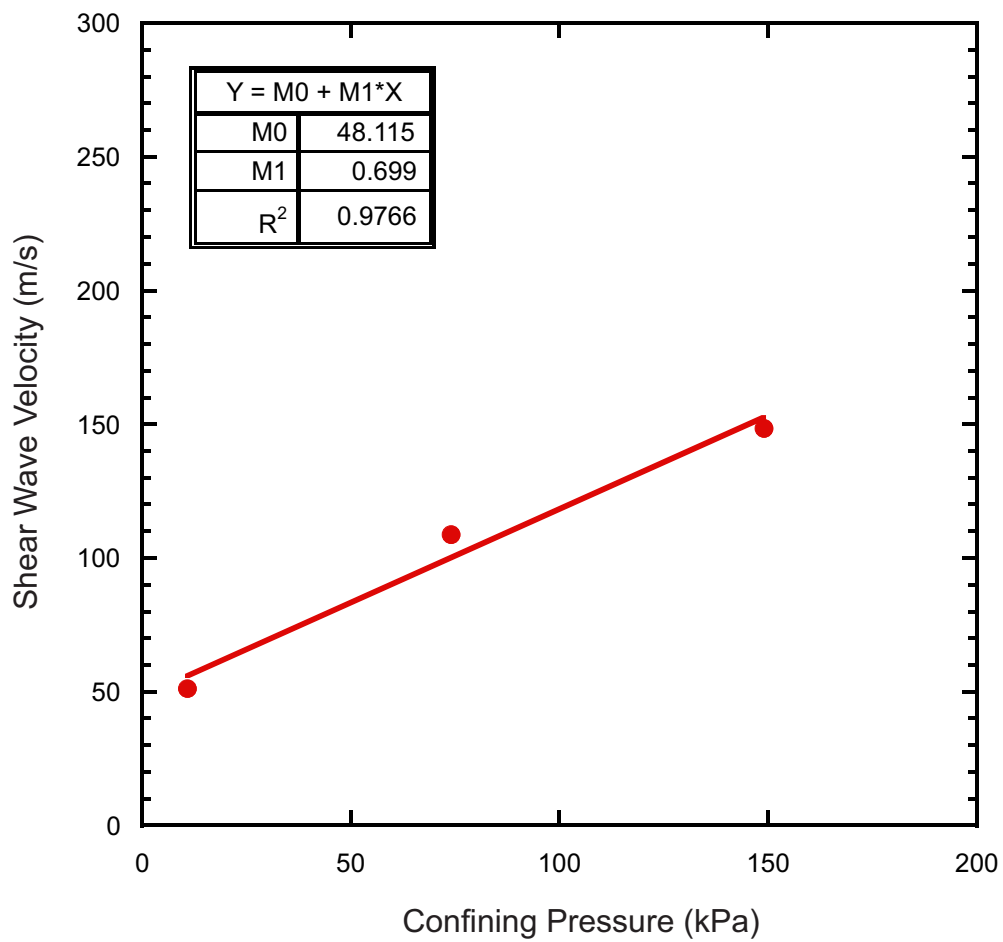
Figure 9.74a. Shear wave velocities at various confining pressures for piston core 20098040036 at core depth of 241-253cm.
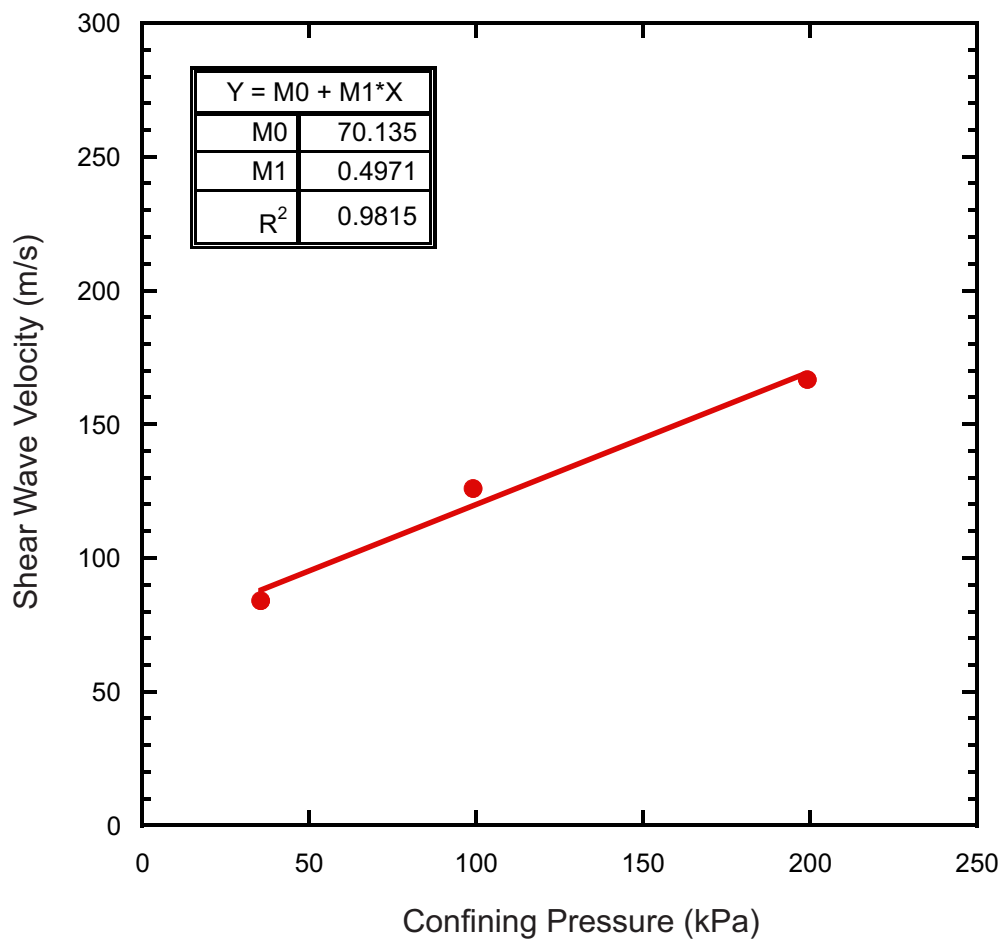
Figure 9.74b. Shear wave velocities at various confining pressures for piston core 20098040036 at core depth 688-700cm.
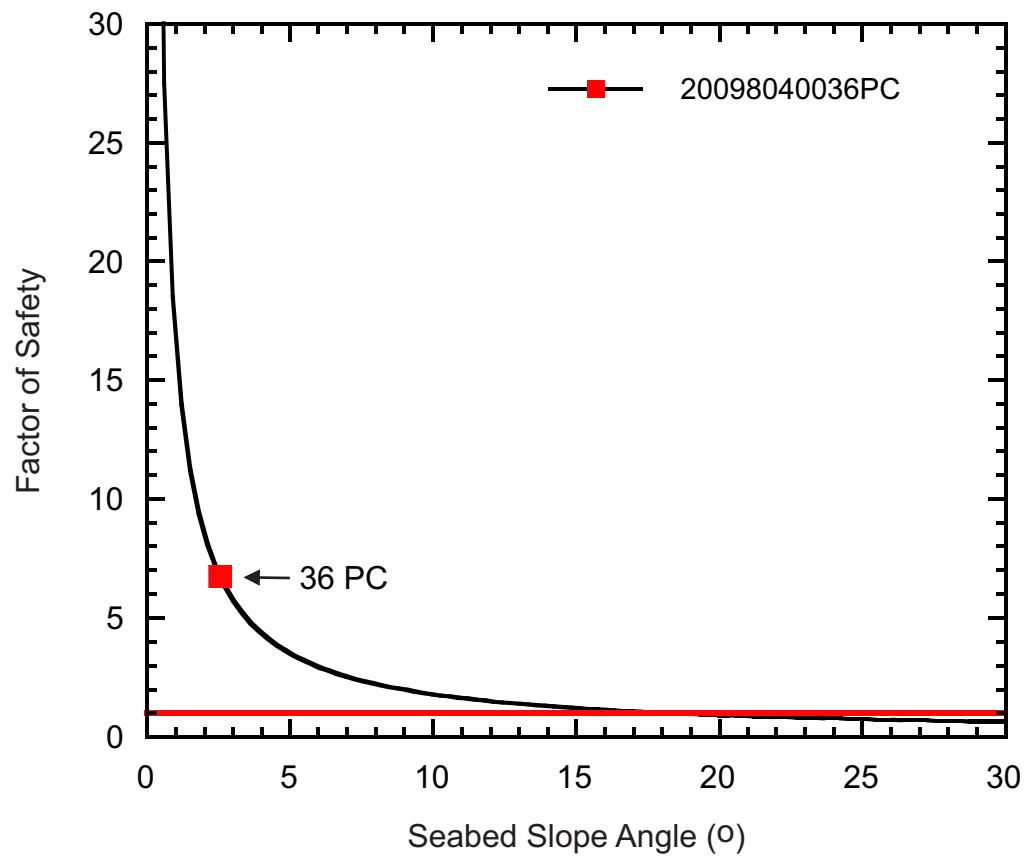
Figure 9.75. FS at various slope angles for piston core 20098040036. The red square identifies the minimum FS for the present-day slope angle of the core site.
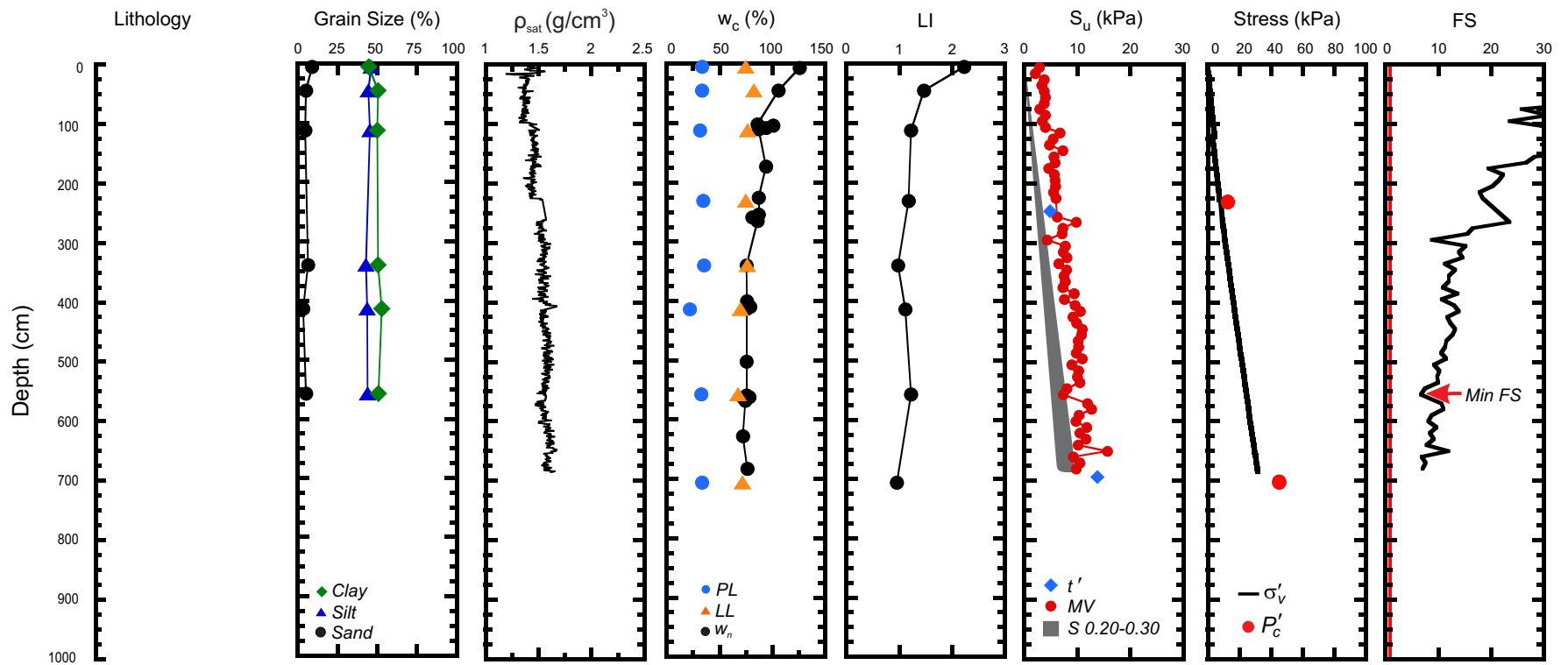
Figure 9.76. Geotechnical profile for core 20098040036 from Region 2. (ρ_{sat}= saturated bulk density, w_c = water content, w_n = natural in-situ water content, PL = plastic limit, LL = liquid limit, LI = liquidity index, S_u = undrained shear strength, MV = laboratory miniature vane shear strength, t' = maximum shear stress, S = shear strength calculated from the normalized strength ratio, σ'_v = effective overburden stress, P'_c = past maximum stress, FS = factor of safety).
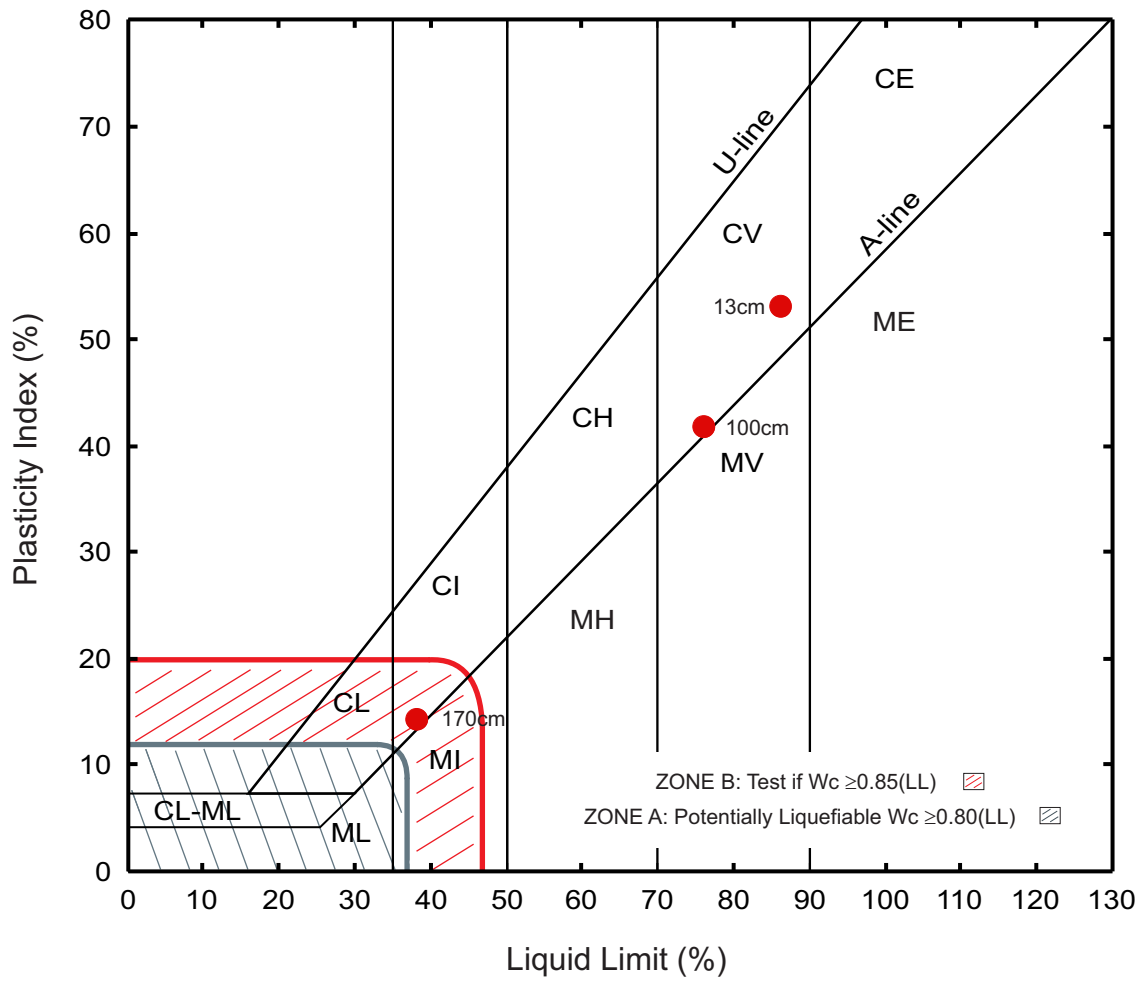
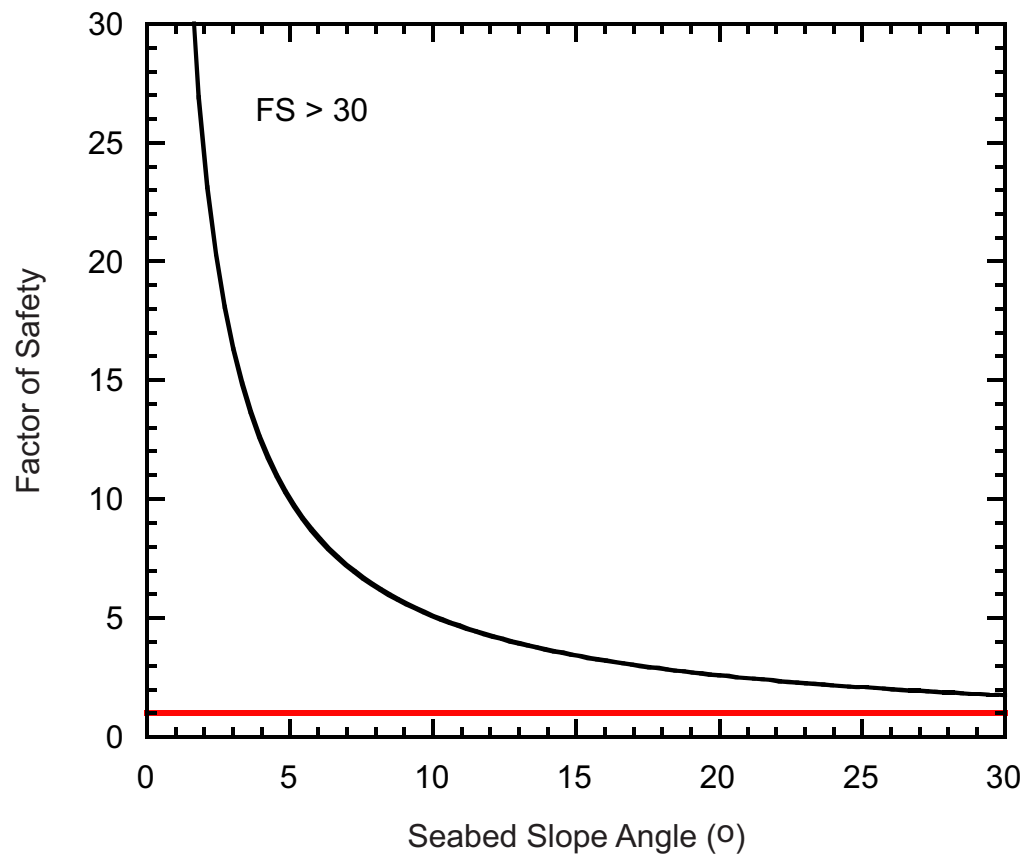Figure 9.77. Plasticity chart showing Atterberg limit results of piston core 20098040040.

Figure 9.78. FS at various slope angles for piston core 20098040040.The minimum FS for the present-day slope angle of the core site is > 30.
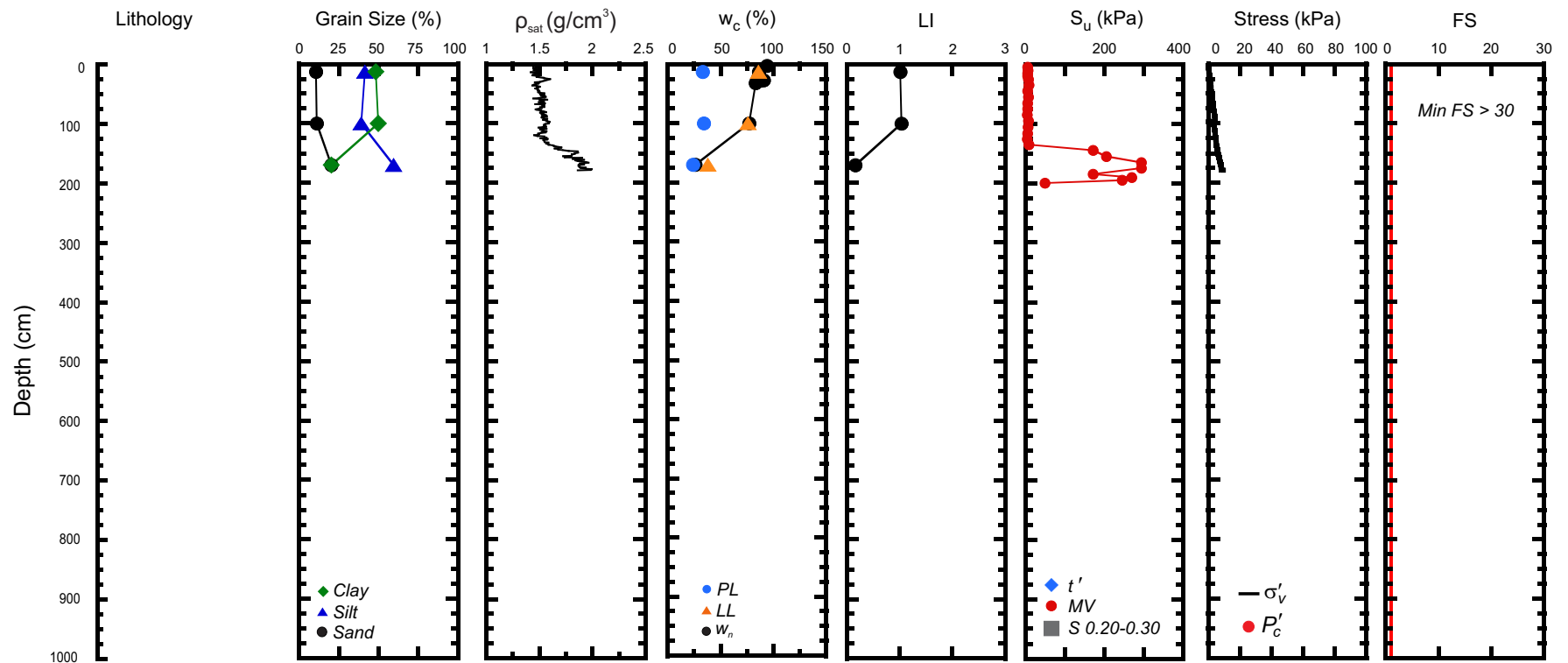
Figure 9.79. Geotechnical profile for core 20098040040 from Region 2. (ρ_{sat}= saturated bulk density, w_c = water content, w_n = natural in-situ water content, PL = plastic limit, LL = liquid limit, LI = liquidity index, S_u = undrained shear strength, MV = laboratory miniature vane shear strength, t' = maximum shear stress, S = shear strength calculated from the normalized strength ratio, σ'_v = effective overburden stress, P'_c = past maximum stress, FS = factor of safety).
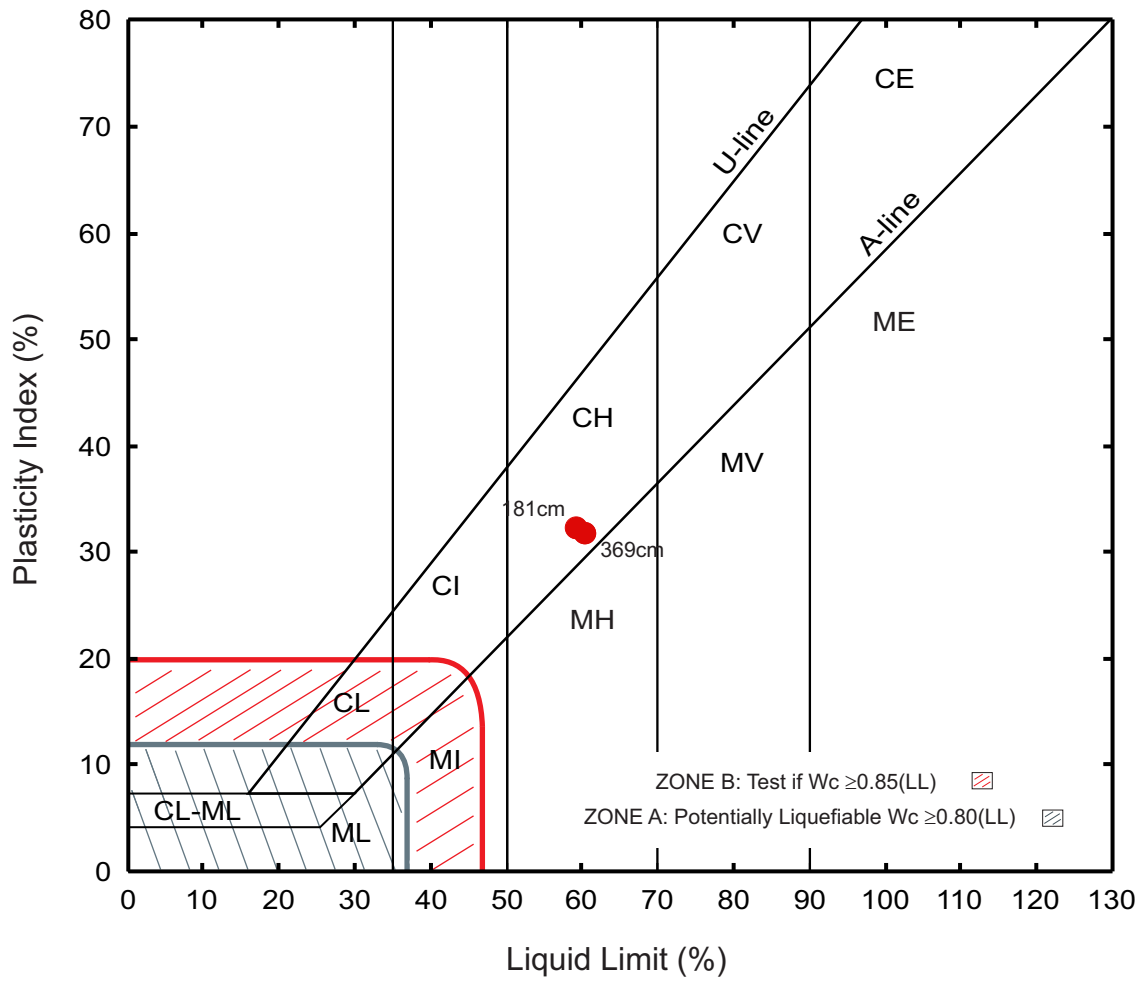
Figure 9.80. Plasticity chart showing Atterberg limit results of piston core 2012004PGC0025.
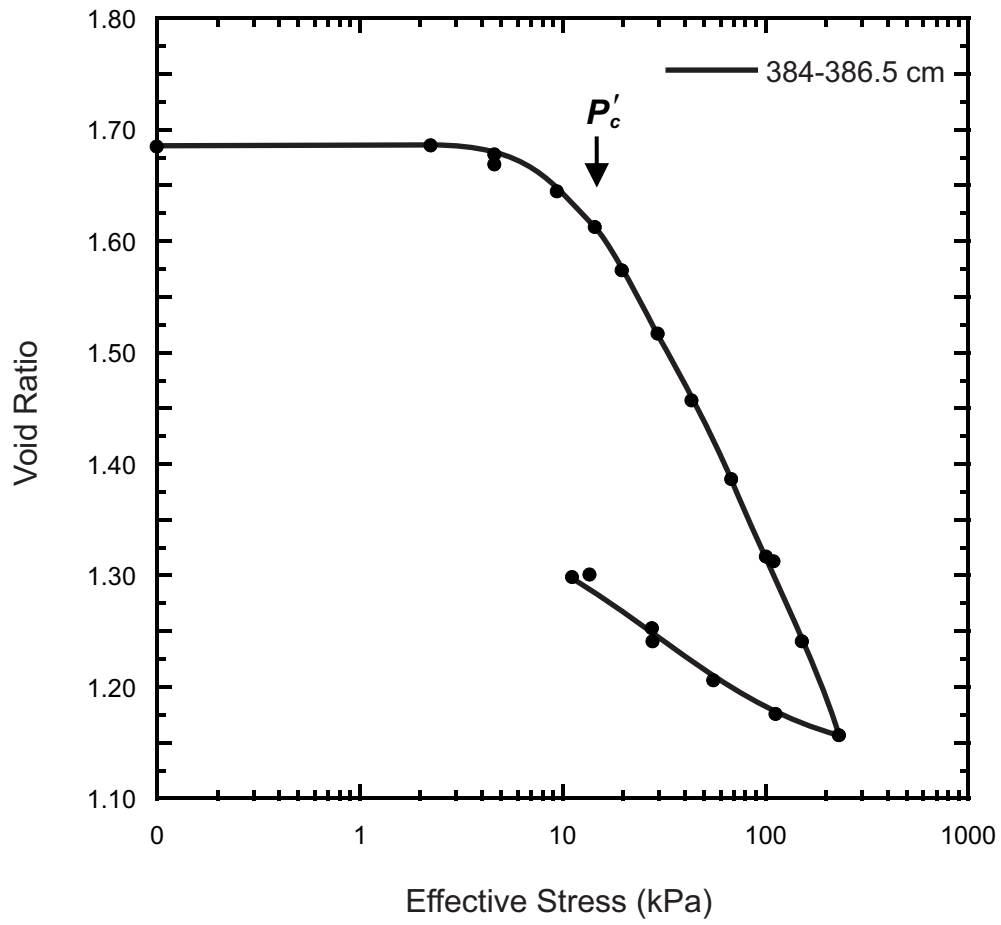
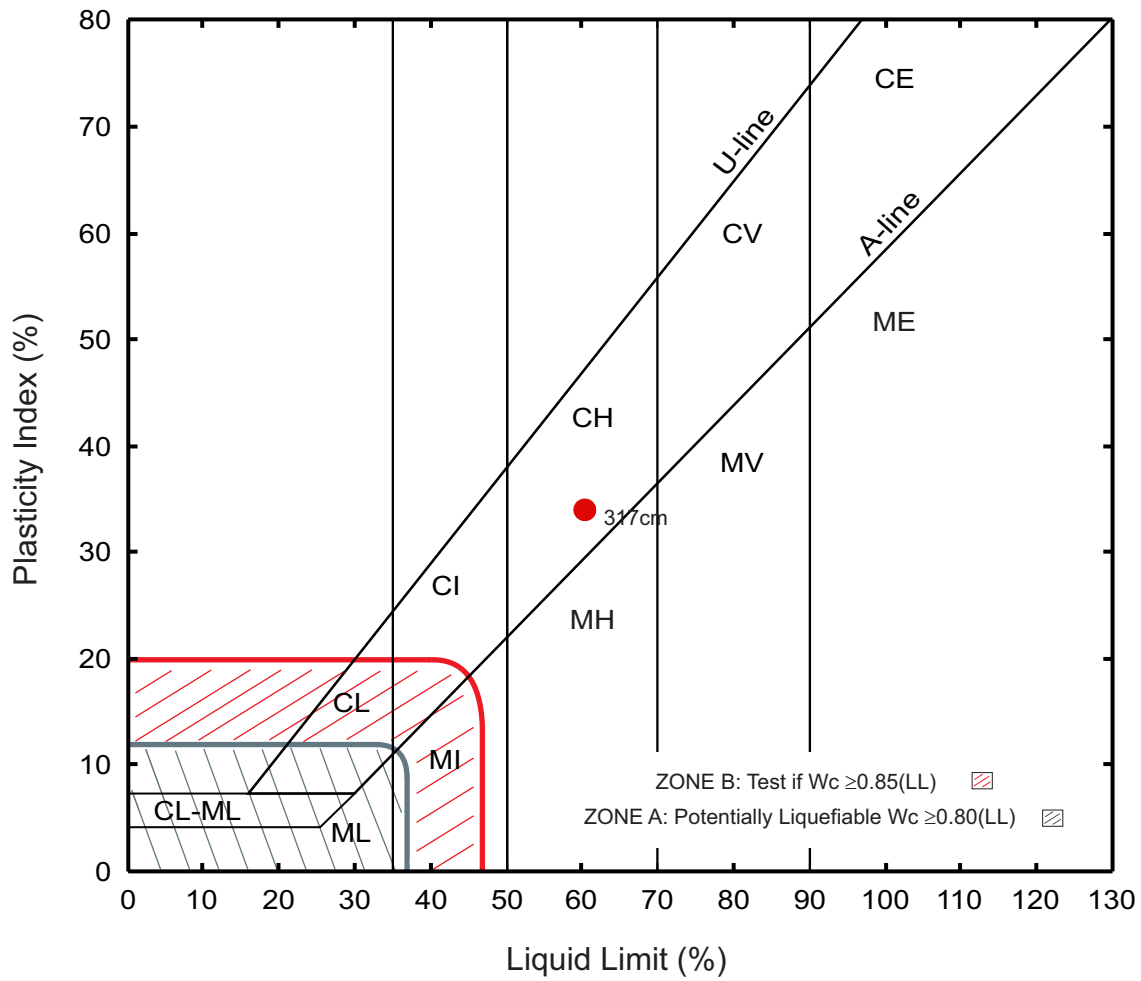Figure 9.81. Consolidation plot for piston core 2012004PGC0025.

Figure 9.82. Plasticity chart showing Atterberg limit results of piston core 2012004PGC0026.
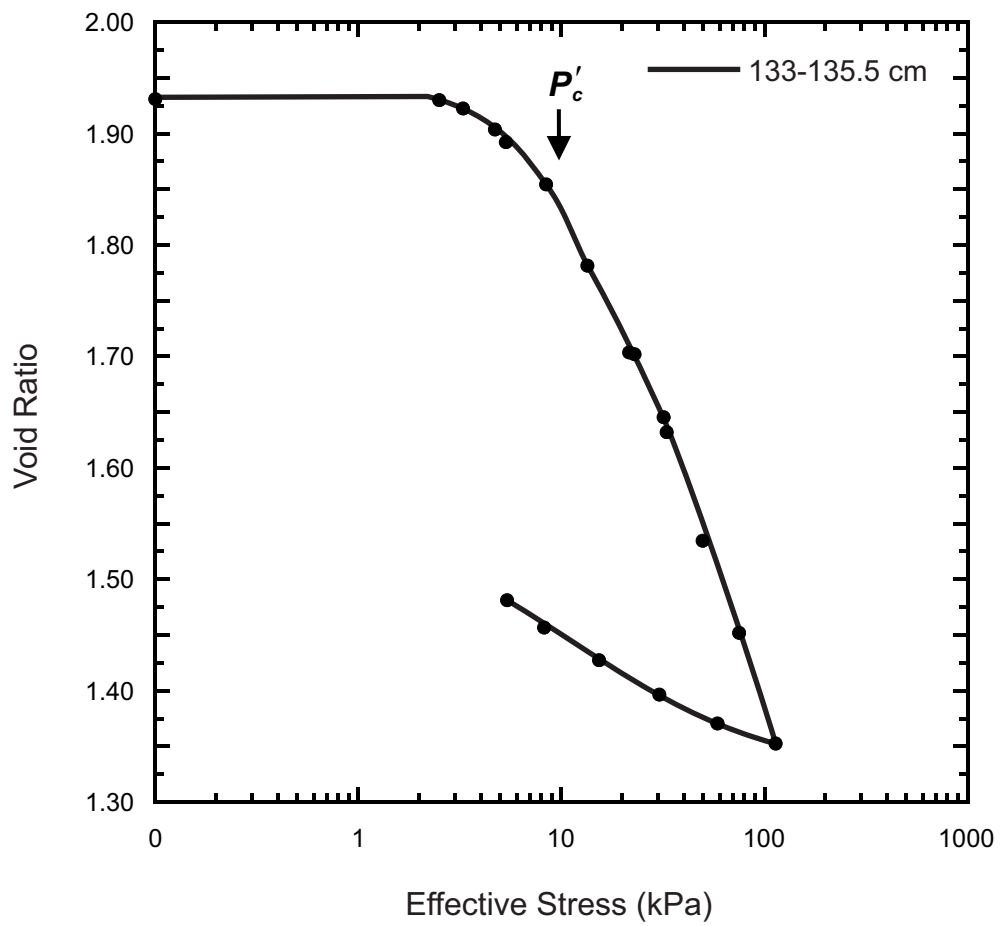
Figure 9.83a. Consolidation plot for piston core 2012004PGC0026 at a core depth of 133-135.5 cm.
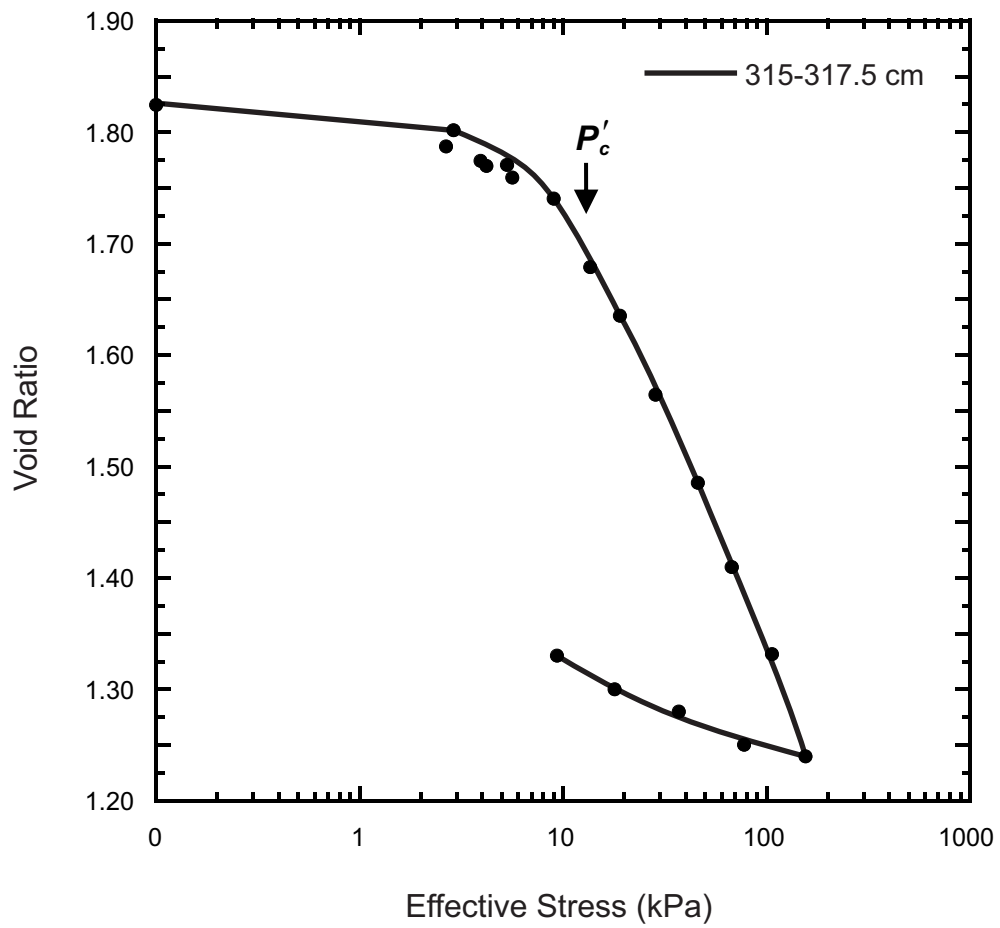
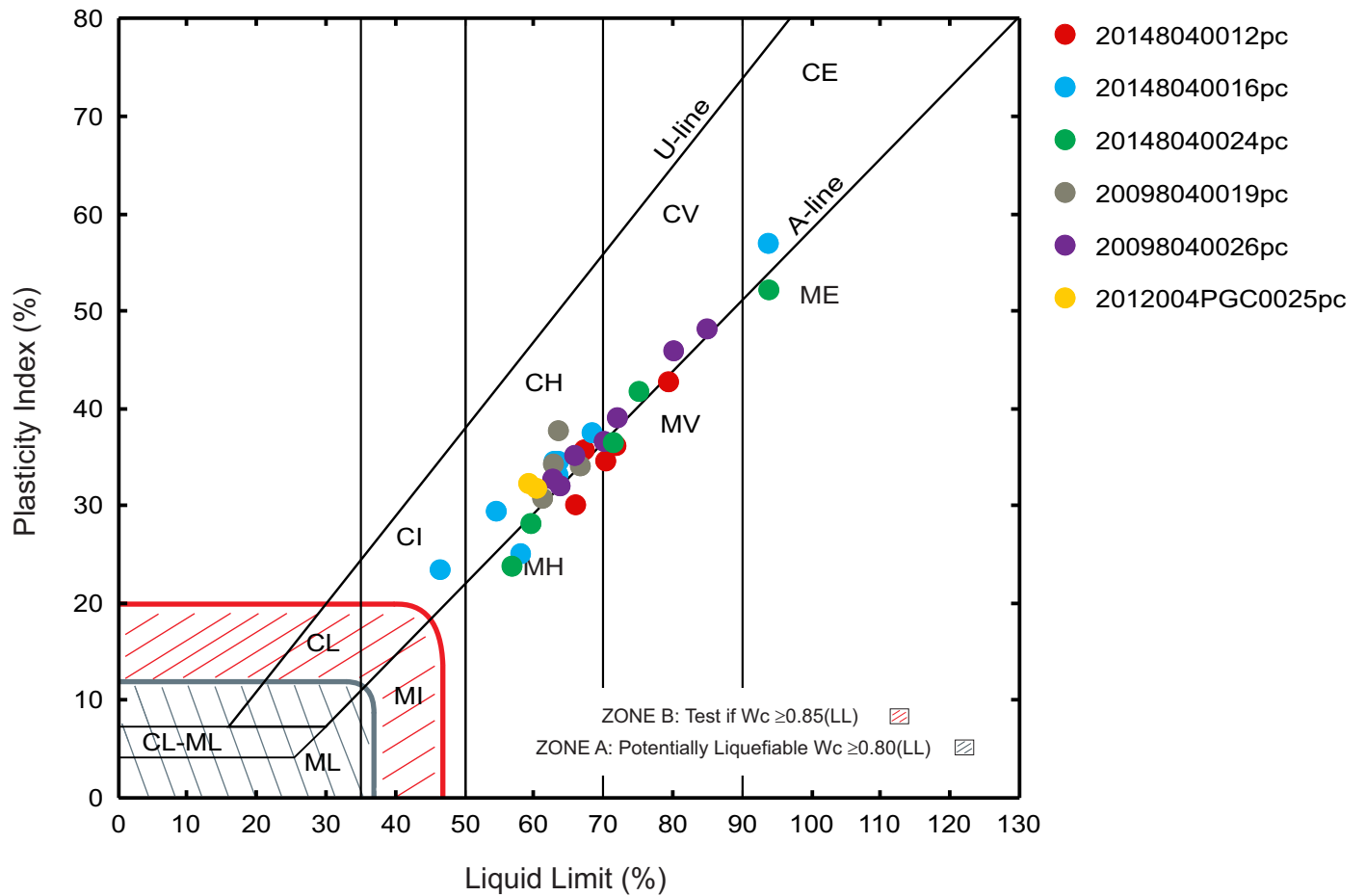Figure 9.83b. Consolidation plot for piston core 2012004PGC0026 at a core depth of 315-317.5 cm.

Figure 9.84a. Plasticity chart showing Atterberg limit results of cores in failed material in Region 2.
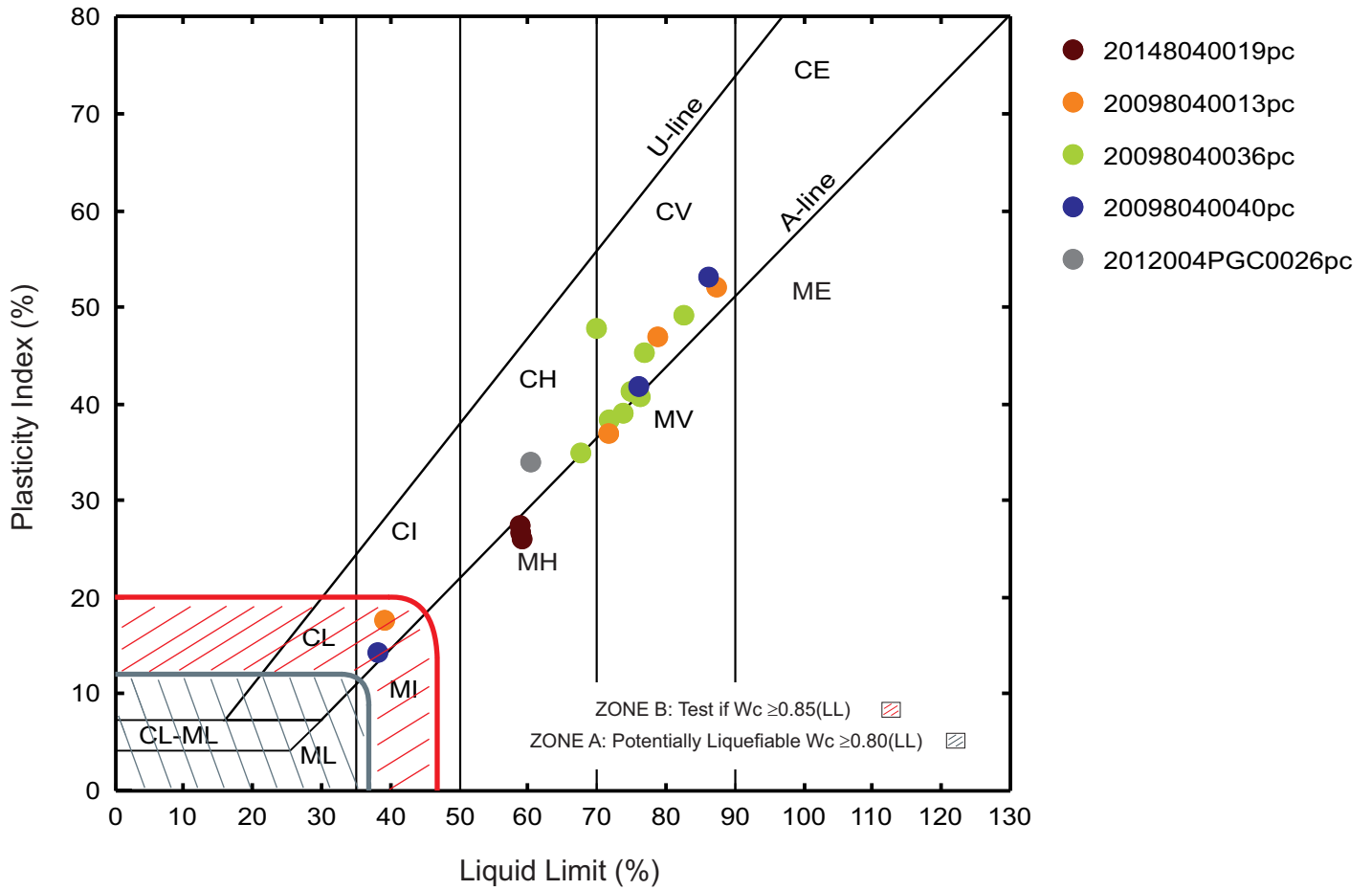
Figure 9.84b. Plasticity chart showing Atterberg limit results of cores in unfailed material in Region 2.
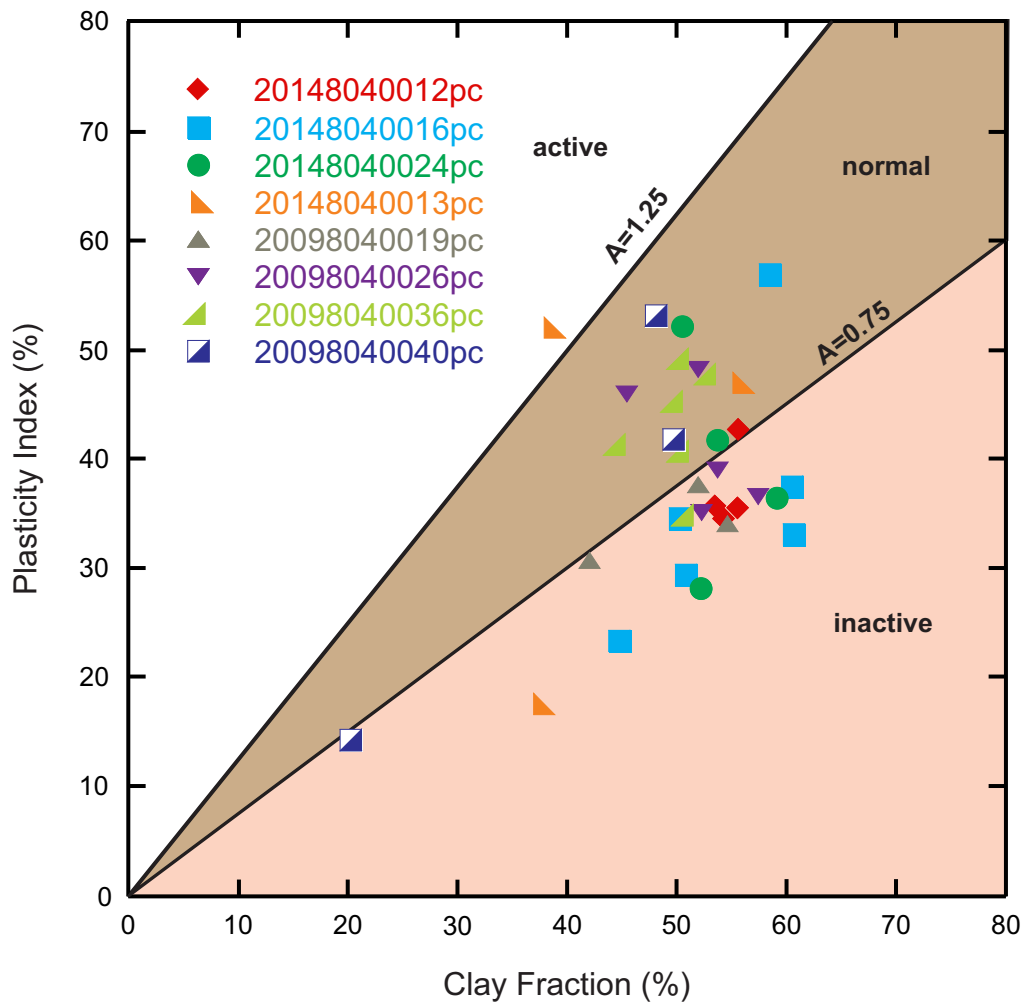
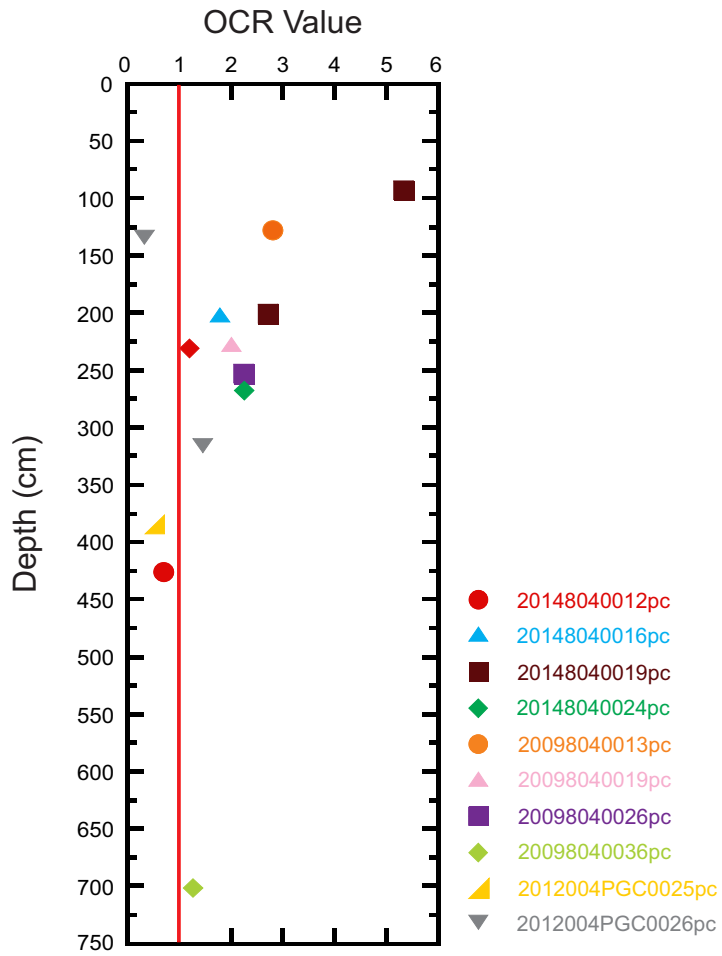Figure 9.85. Region 2 activity chart.

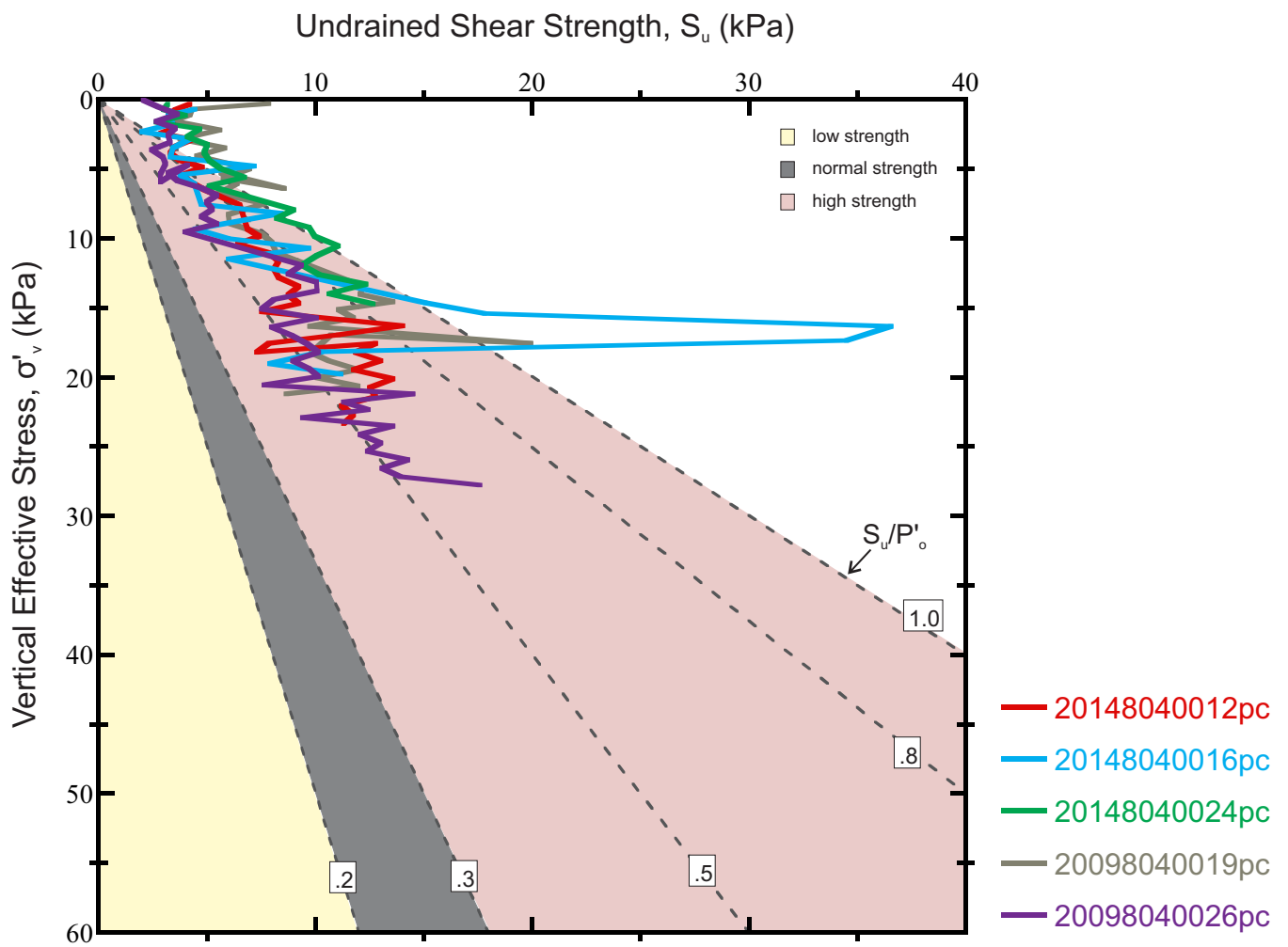Figure 9.86. OCR values with depth for consolidation tests in Region 2.

Figure 9.87a. Shear strength profiles with effective overburden pressure of cores in failed material in Region 2.
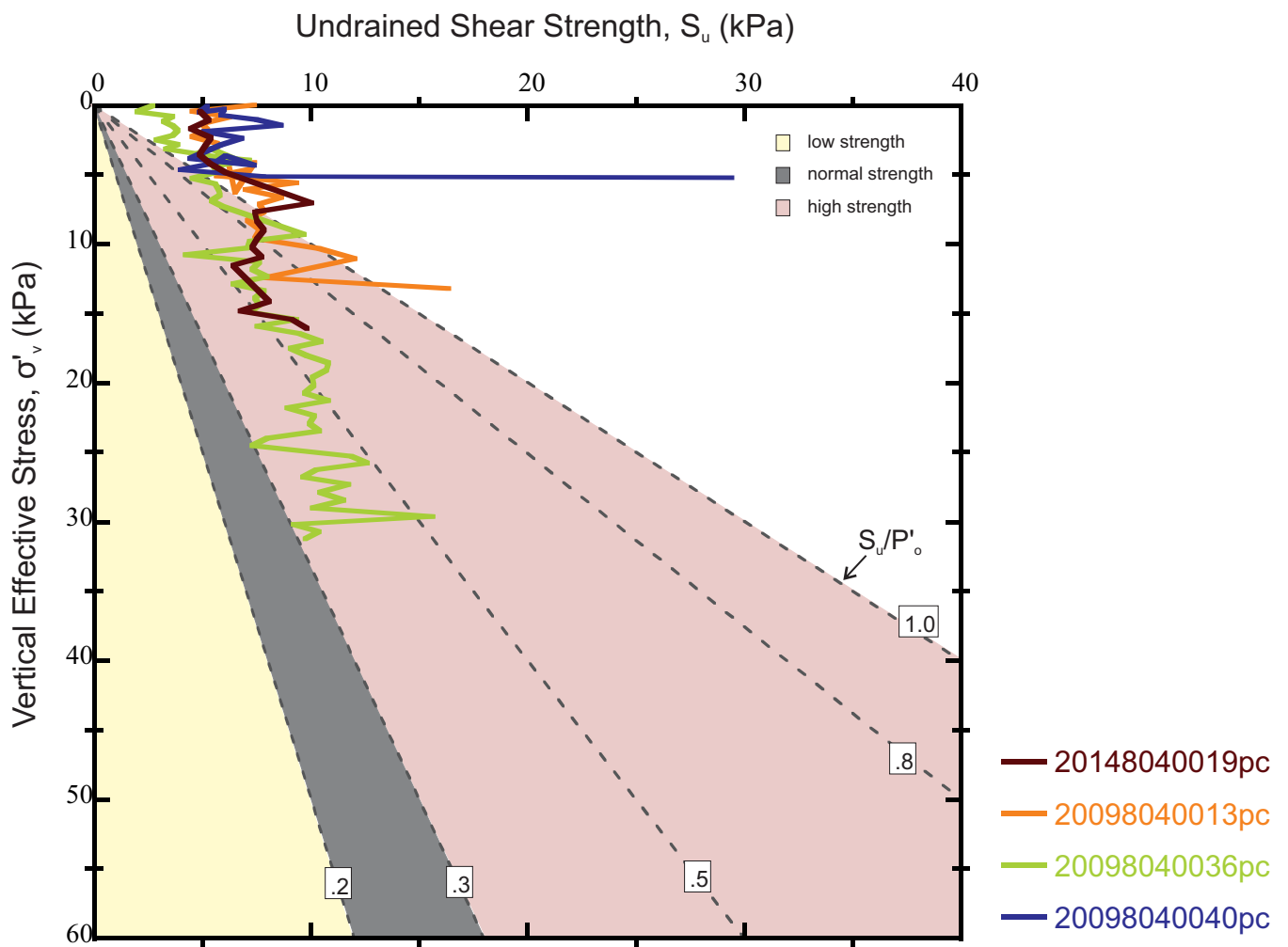
Figure 9.87b. Shear strength profiles with effective overburden pressure of cores in unfailed material in Region 2.
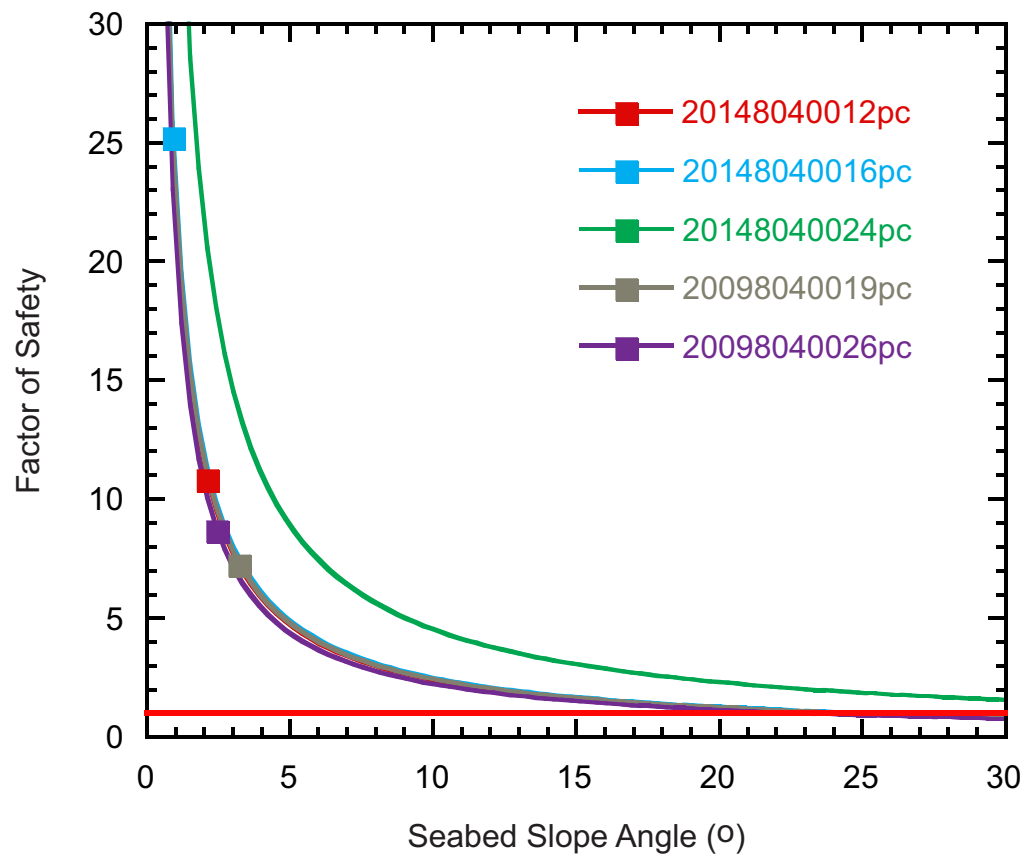
Figure 9.88a. FS at various slope angles for piston cores taken from failed material in Region 2.
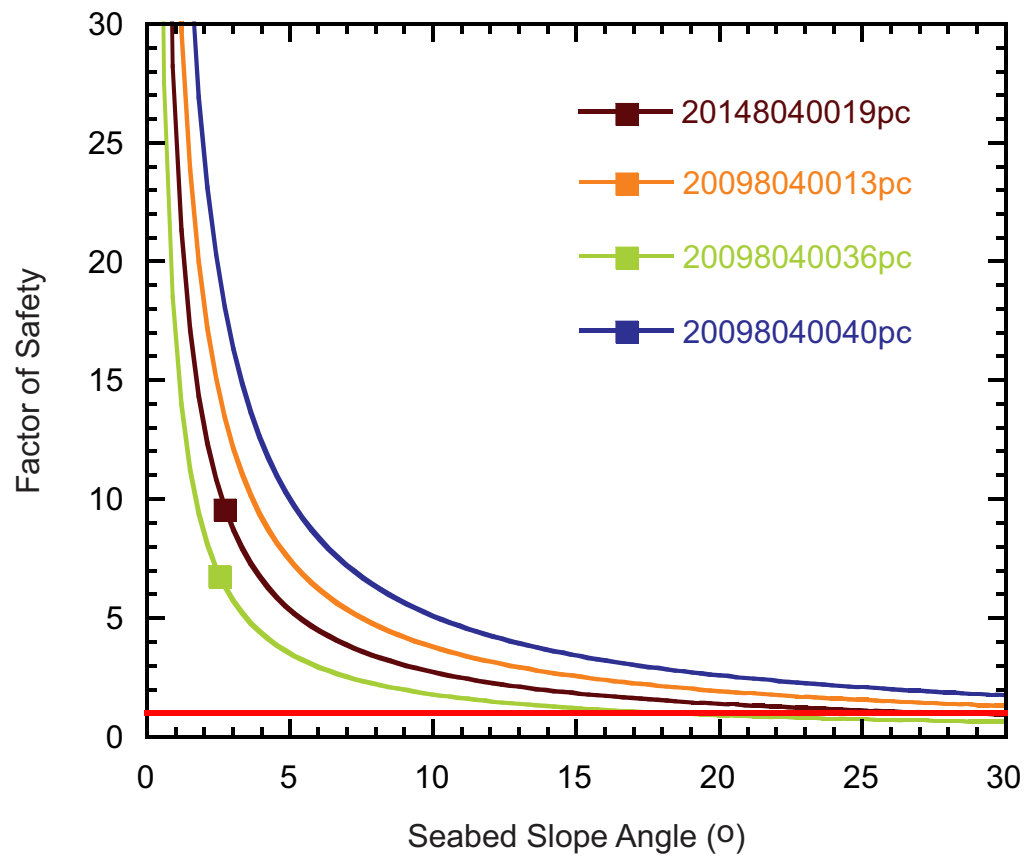
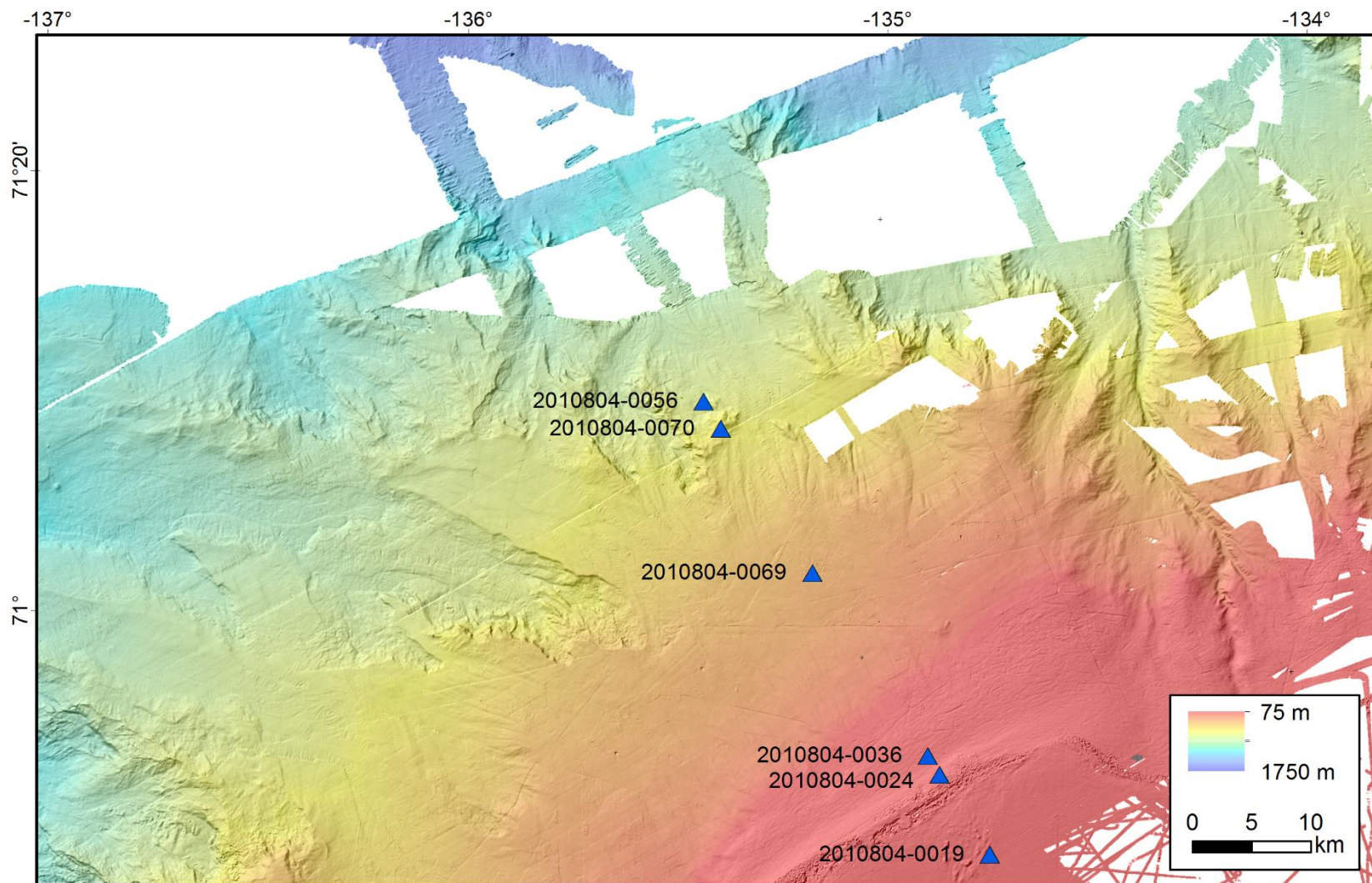Figure 9.88b. FS at various slope angles for piston cores taken from unfailed material in Region 2.

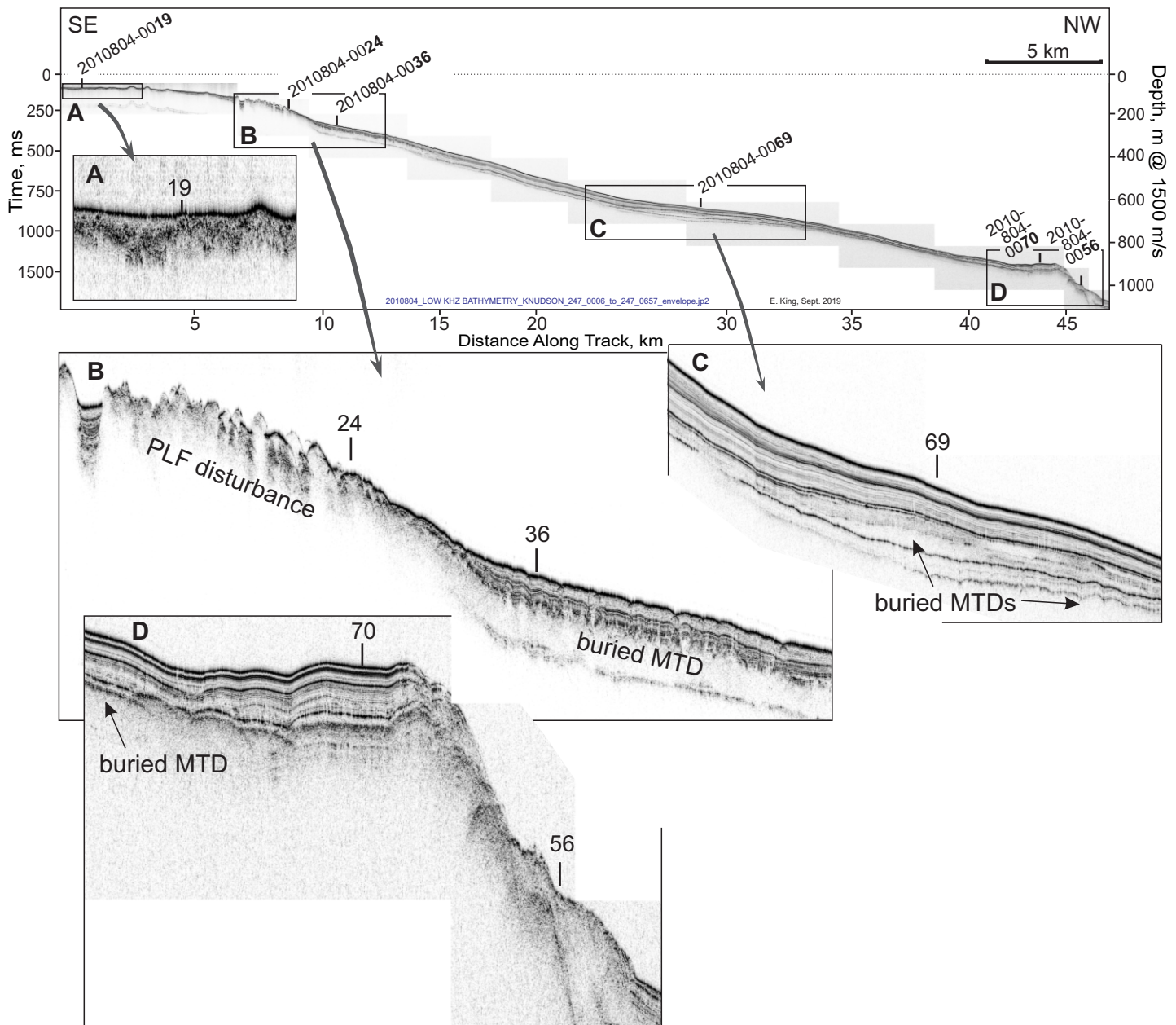Figure 9.89. Region 3 core locations on multi-beam ArcticNet bathymetry.

Figure 9.90. Sub-bottom profiler (3.5 kHz CHIRP) in the Pokak Area (Region 3), with core locations projected. Core 20108040019pc is located on the Beaufort Shelf and sampled late post-glacial mud derived mainly from the Mackenzie River-plume. Core 20108040024pc, is at the lower edge of seabed disturbance from the pingo-like features (PLF). Core 20108040036pc samples Holocene age muds transported over the shelf break. Cores 20108040069pc and 20108040070pc likely penetrate thin Holocene surficial muds (<2 m) and underlying glacimarine muds. Core 20108040056pc appears to have sampled mass transport material but the core structure and stratigraphy are intact (Lakeman et al. 2018), indicating it penetrated and an undisturbed flow block.
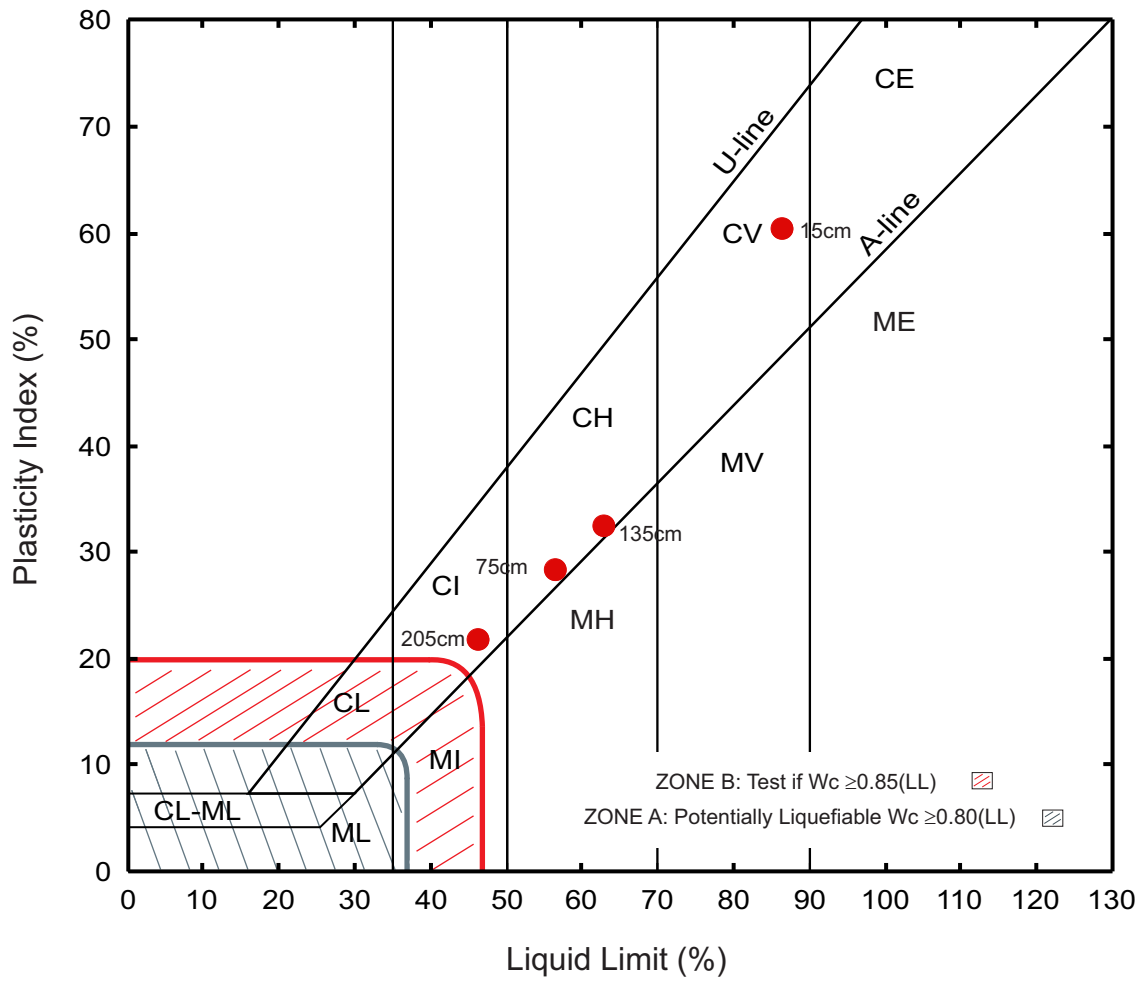
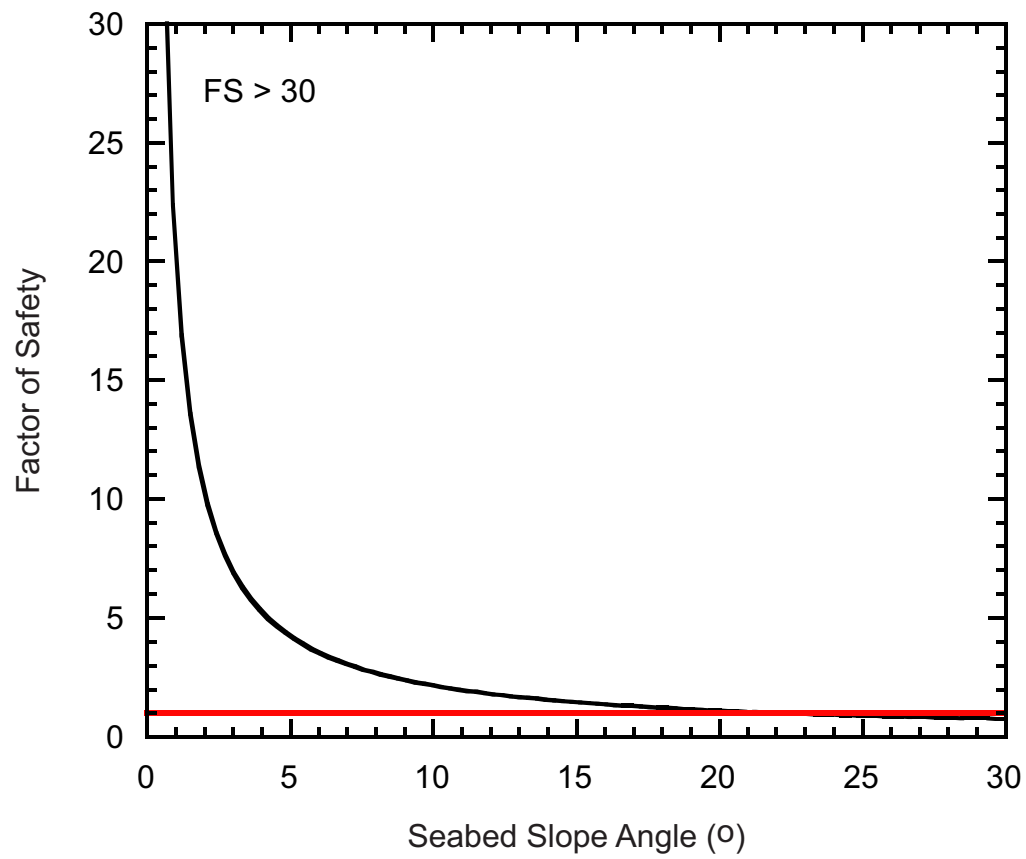Figure 9.91. Plasticity chart showing Atterberg limit results of piston core 20108040019.

Figure 9.92. FS at various slope angles for piston core 20108040019.The minimum FS for the present-day slope angle of the core site is > 30.
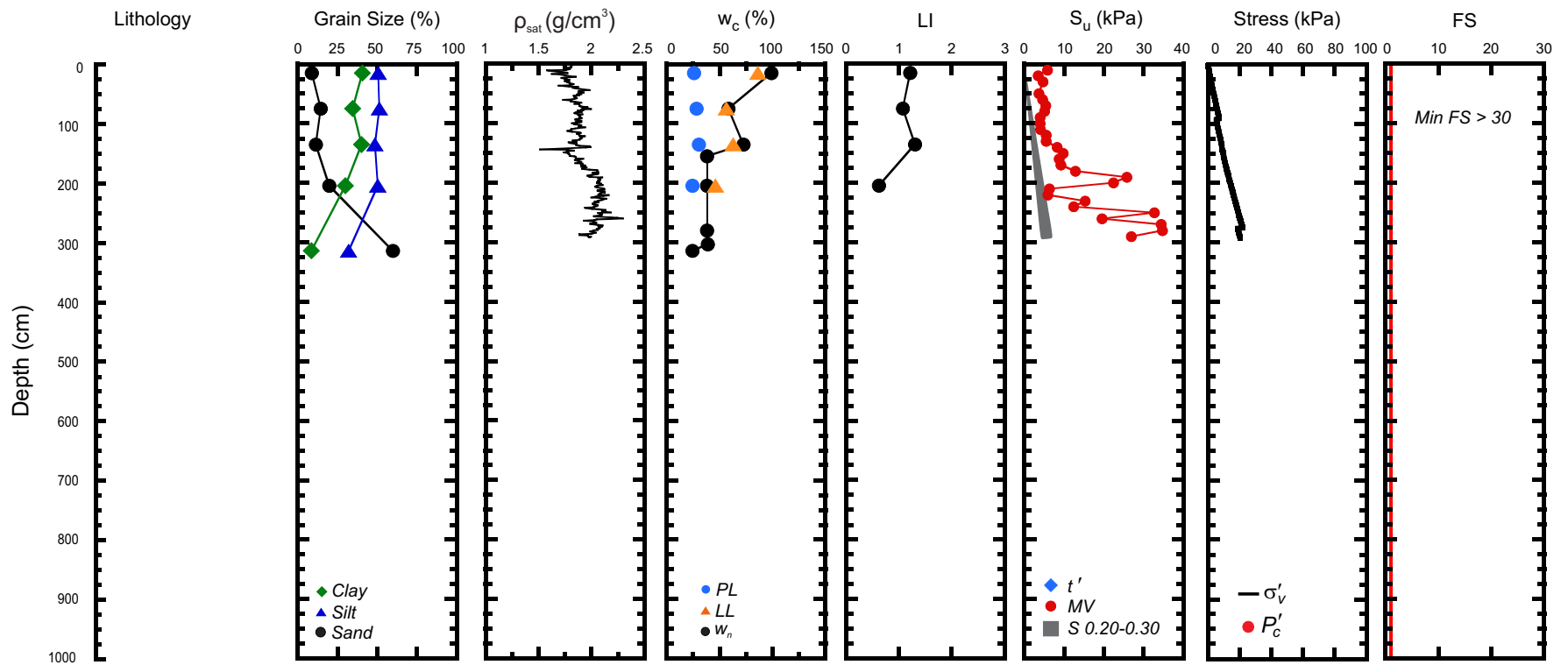
Figure 9.93. Geotechnical profile for core 20108040019 from the Beaufort Sea. (ρ_{sat}= saturated bulk density, w_c = water content, w_n = natural in-situ water content, PL = plastic limit, LL = liquid limit, LI = liquidity index, S_u = undrained shear strength, MV = laboratory miniature vane shear strength, t' = maximum shear stress, S = shear strength calculated from the normalized strength ratio, σ'_v = effective overburden stress, P'_c = past maximum stress, FS = factor of safety).
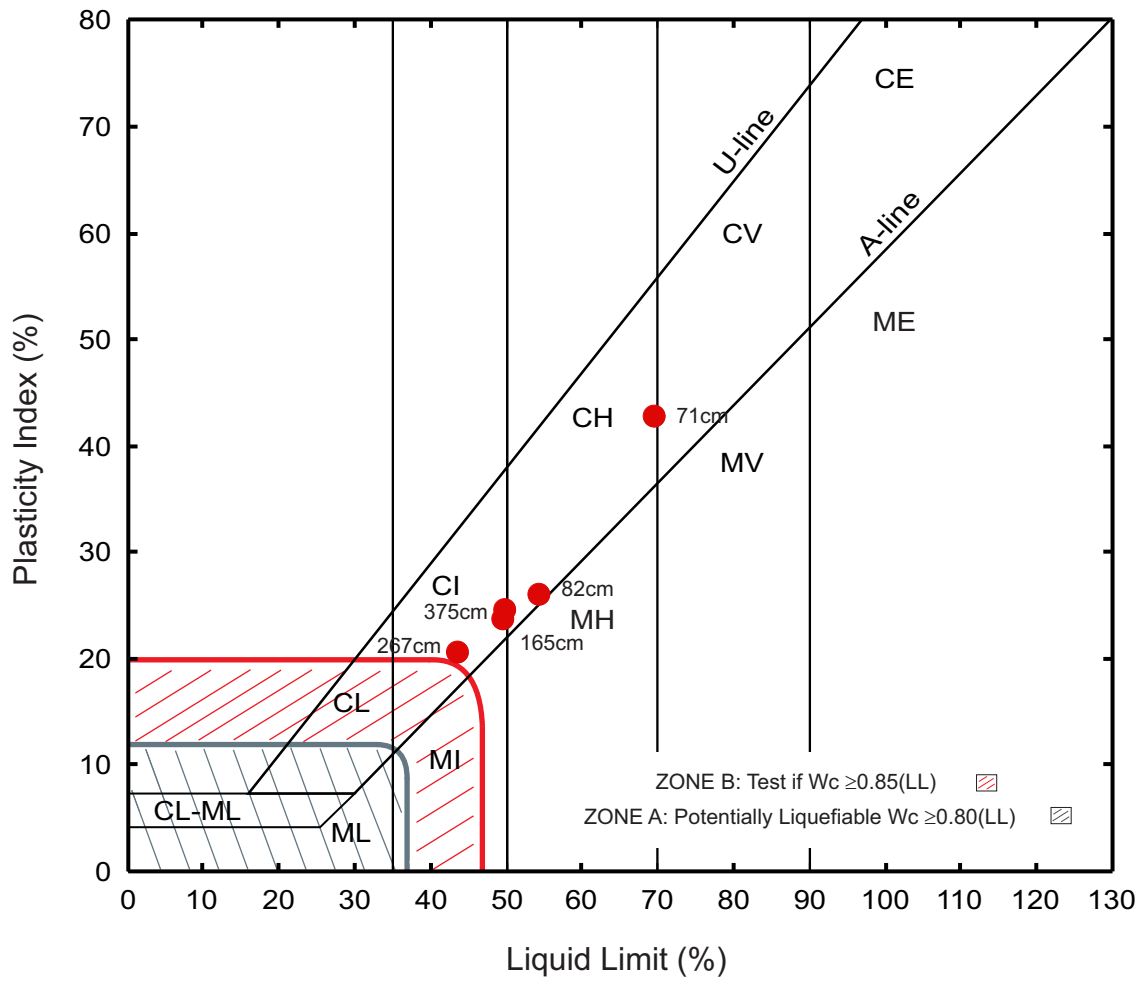
Figure 9.94. Plasticity chart showing Atterberg limit results of piston core 20108040024.
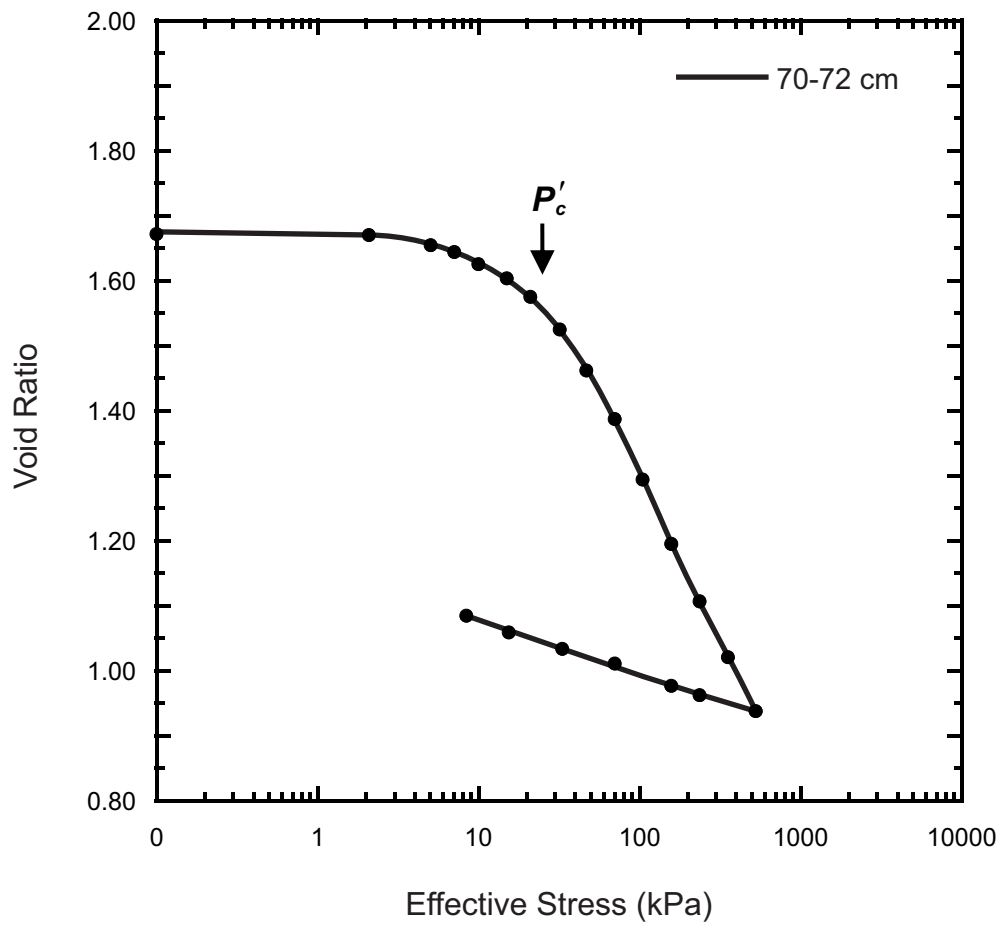
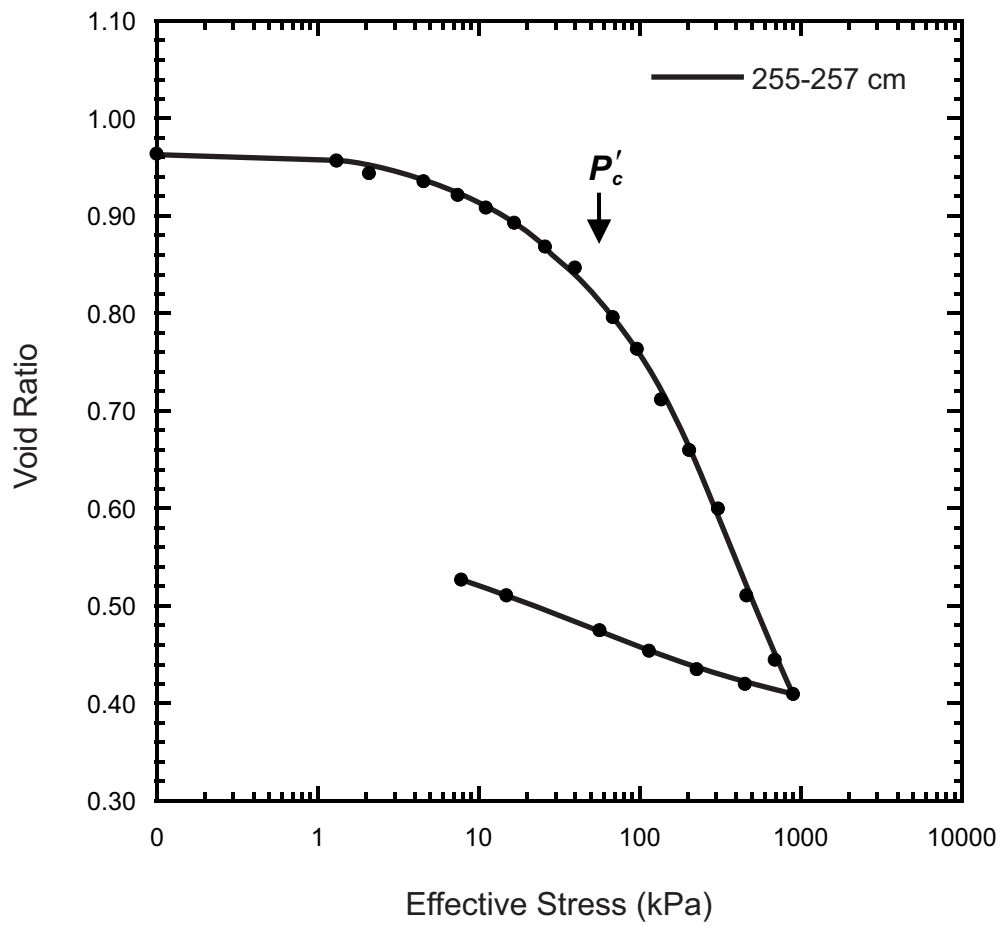Figure 9.95a. Consolidation plot for piston core 20108040024.

Figure 9.95b. Consolidation plot for piston core 20108040024.

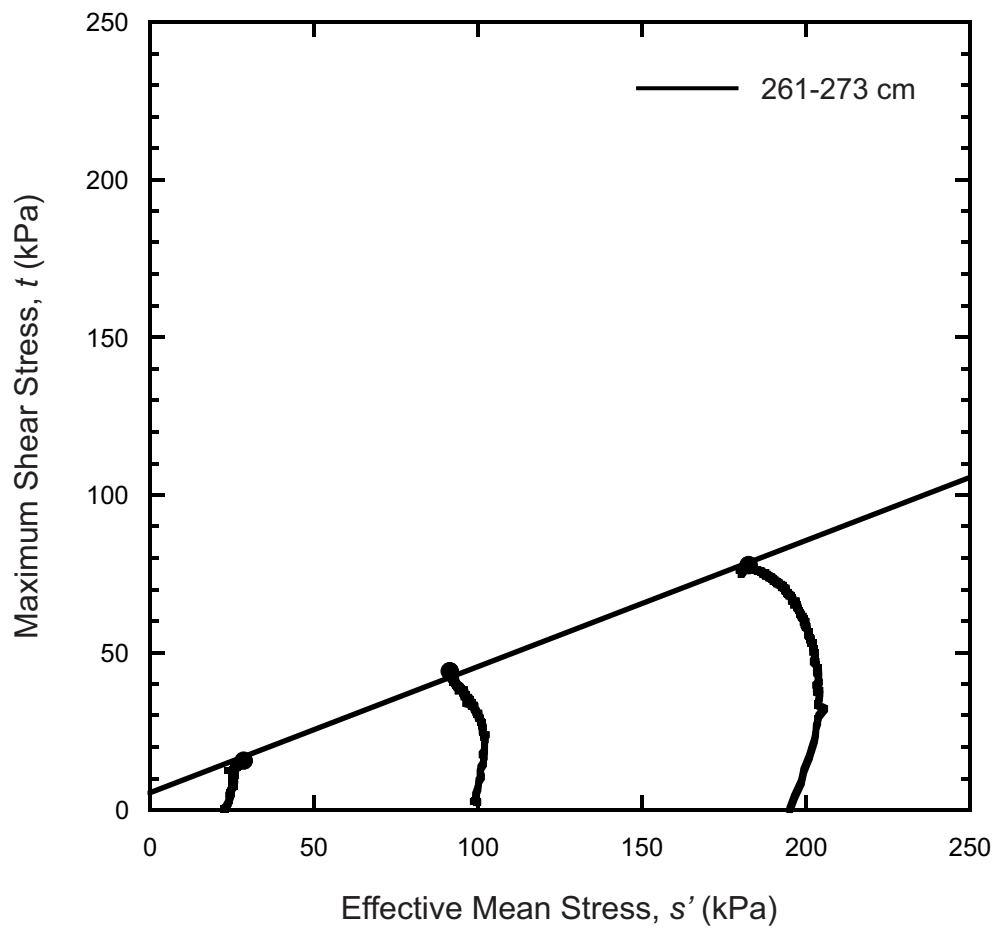Figure 9.96. Stress paths and failure envelopes from triaxial test results for piston core 20108040024.

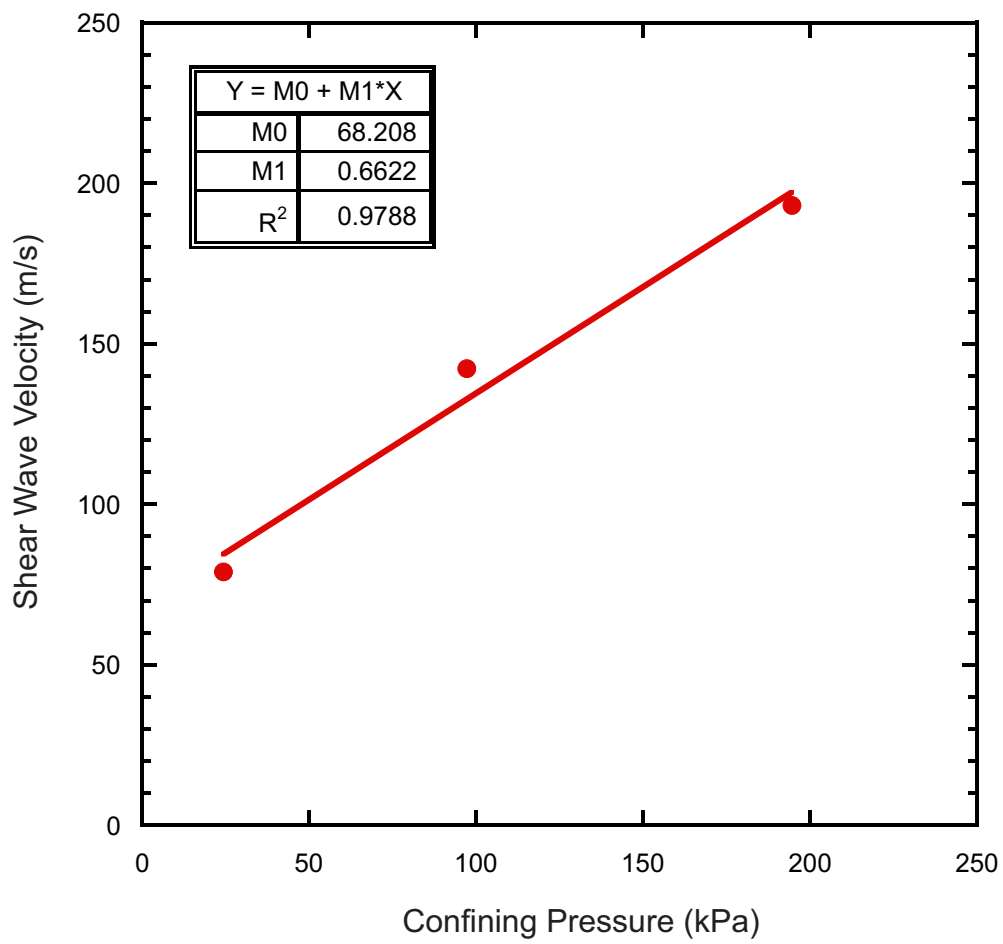| Y = M0 + M1*X	
M0	68.208
M1	0.6622
R^2	0.9788

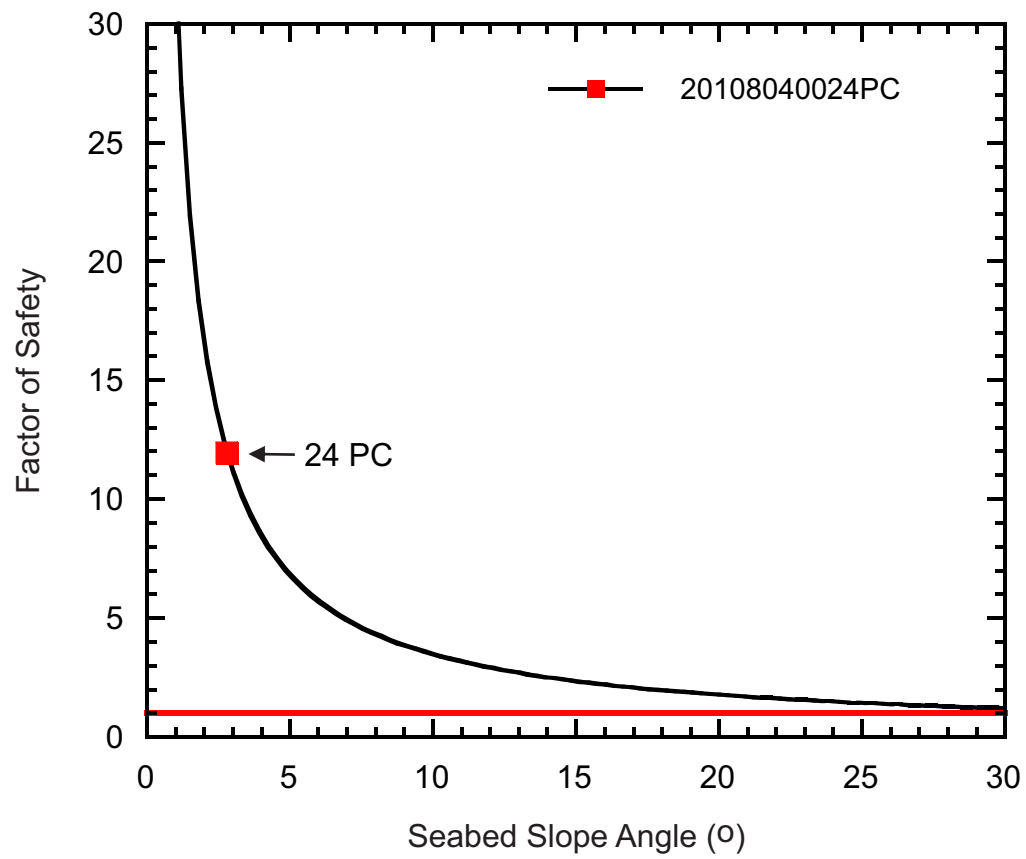Figure 9.97. Shear wave velocities at various confining pressures for piston core 20108040024.

Figure 9.98. FS at various slope angles for piston core 20108040024. The red square identifies the minimum FS for the present-day slope angle of the core site.
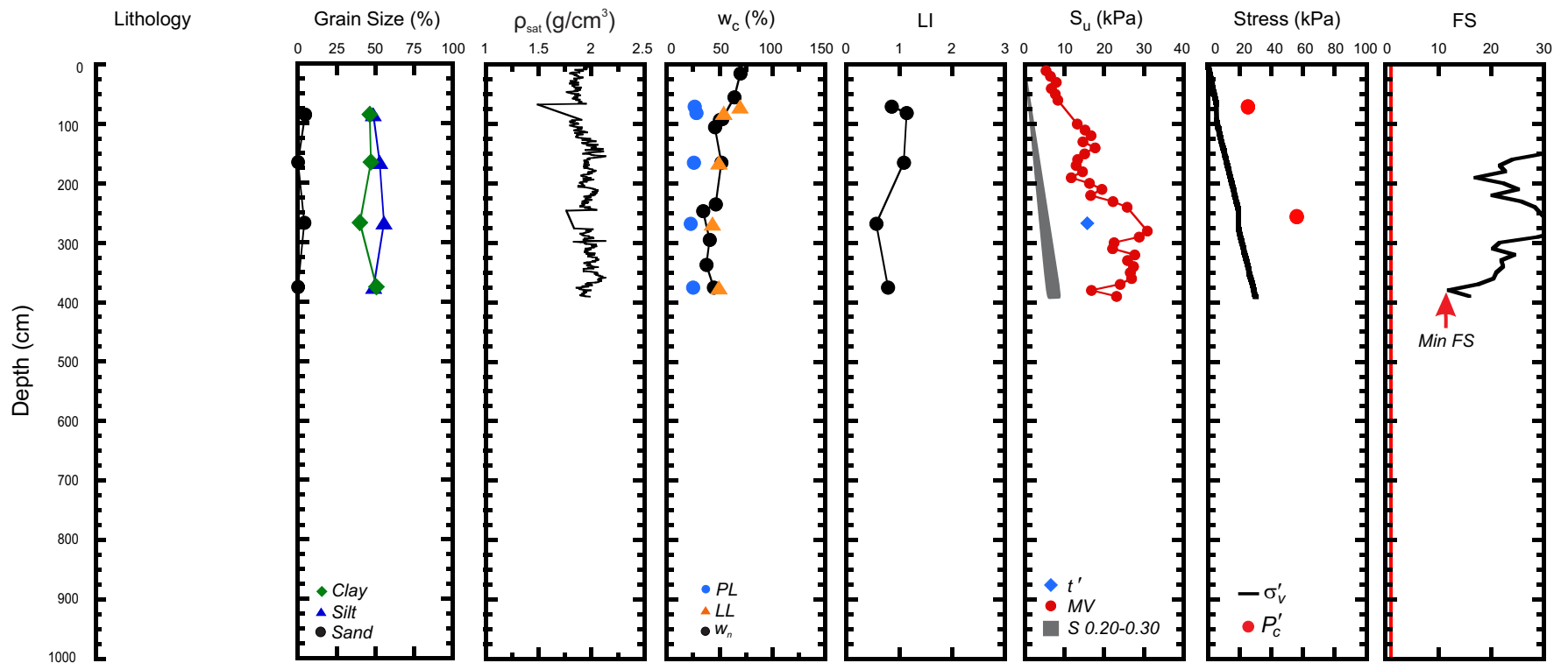
Figure 9.99. Geotechnical profile for core 20108040024 from Region 3. (ρ_{sat}= saturated bulk density, w_c = water content, w_n = natural in-situ water content, PL = plastic limit, LL = liquid limit, LI = liquidity index, S_u = undrained shear strength, MV = laboratory miniature vane shear strength, t' = maximum shear stress, S = shear strength calculated from the normalized strength ratio, σ'_v = effective overburden stress, P'_c = past maximum stress, FS = factor of safety).
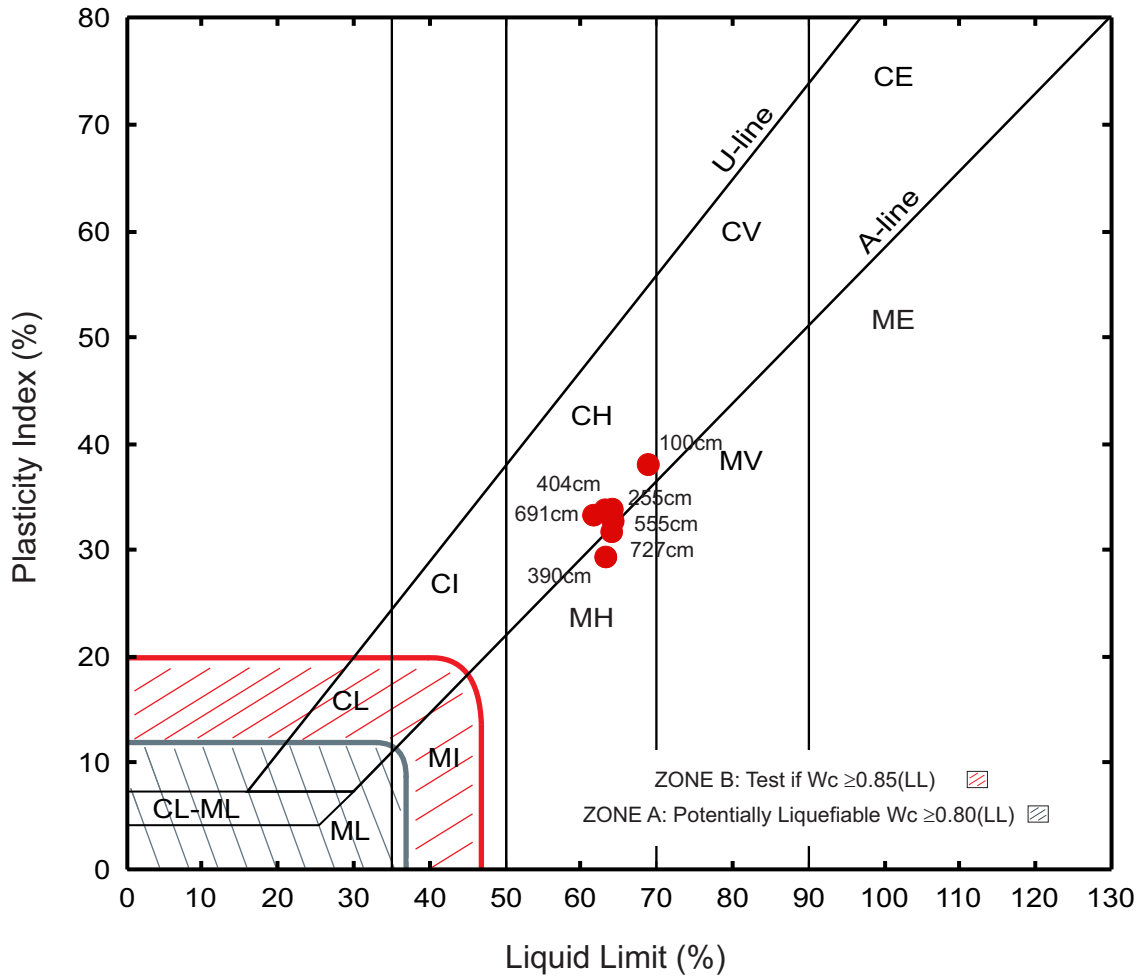
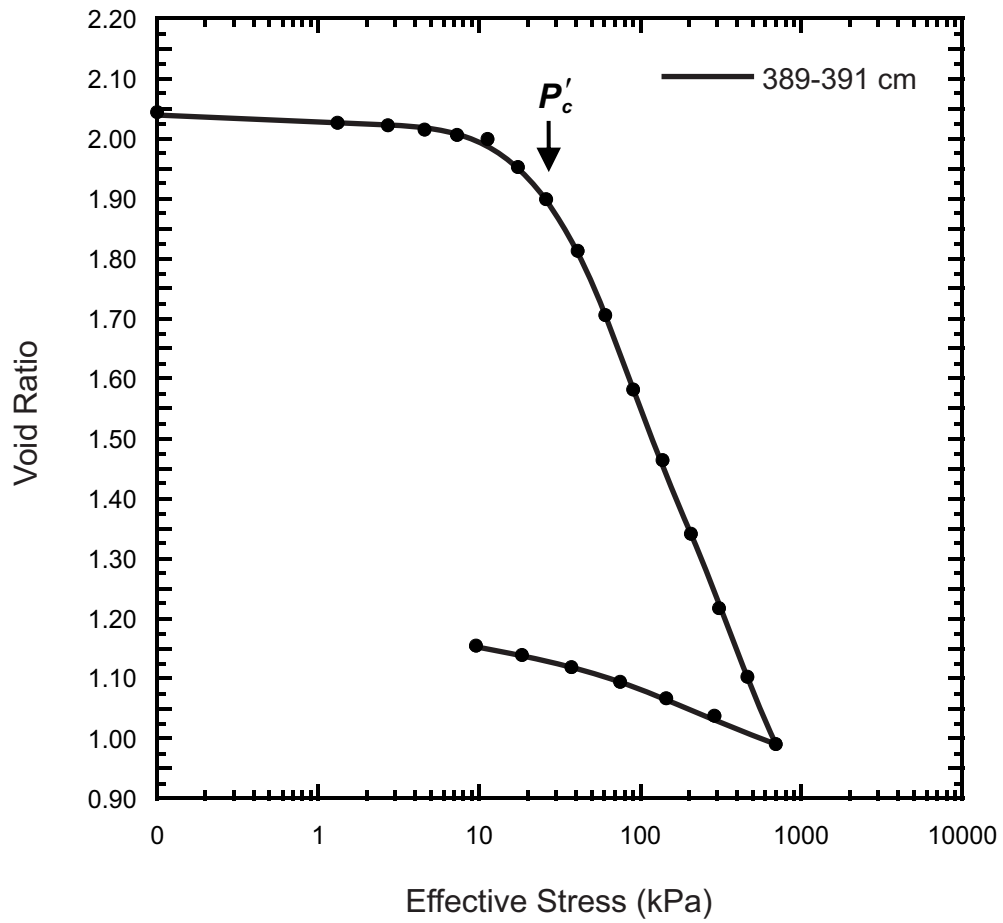Figure 9.100. Plasticity chart showing Atterberg limit results of piston core 20108040036pc.

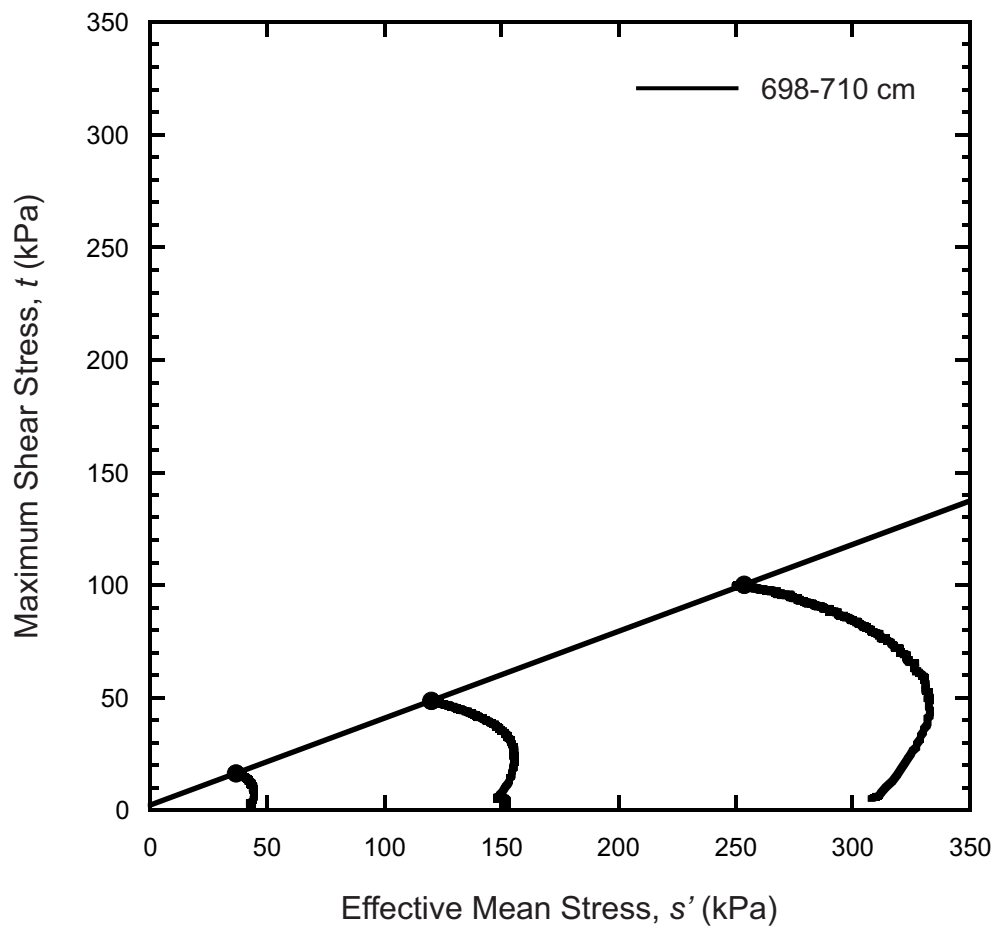Figure 9.101. Consolidation plot for piston core 20108040036.

Figure 9.102. Stress paths and failure envelopes from triaxial test results for piston core 20108040036.
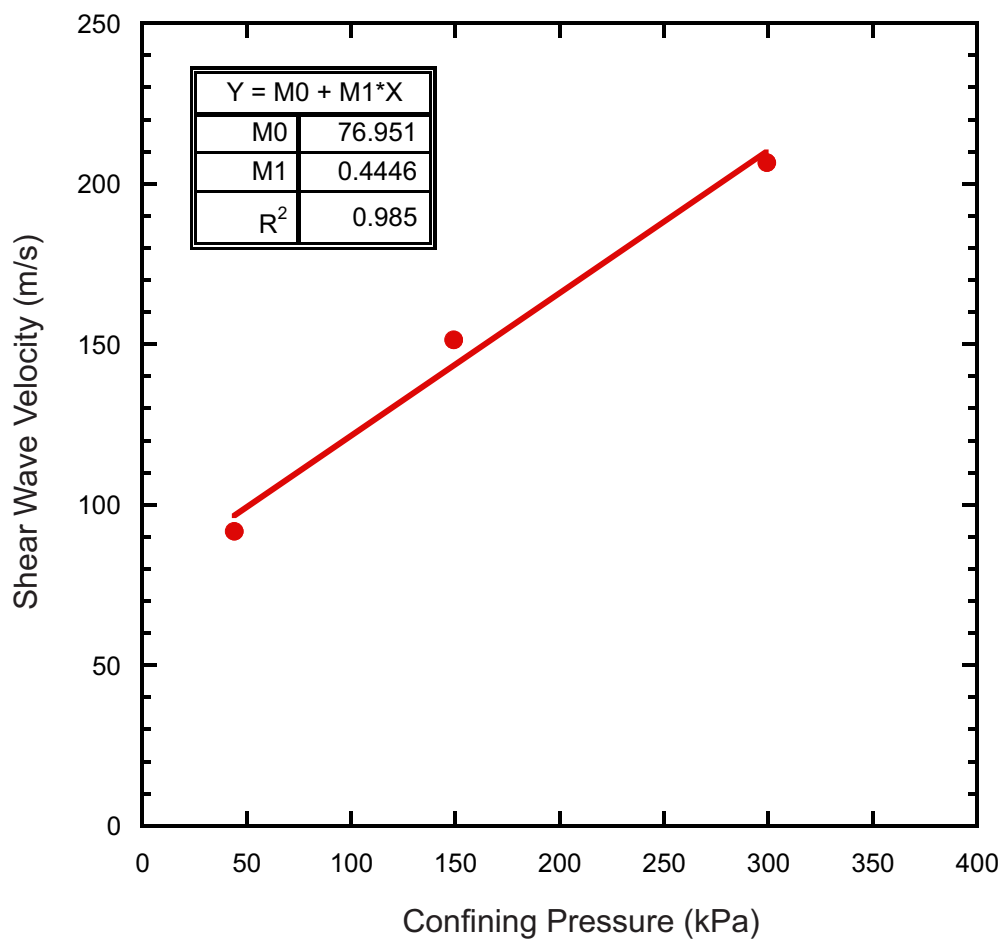
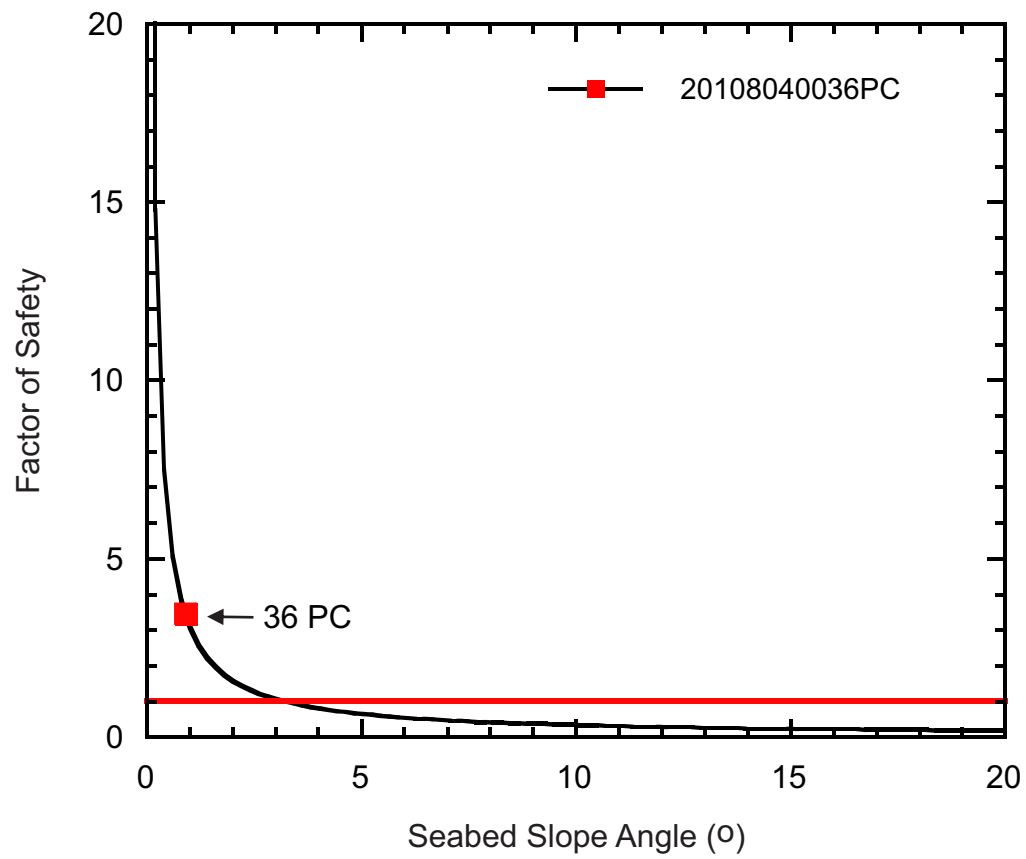Figure 9.103. Shear wave velocities at various confining pressures for piston core 20108040036.

Figure 9.104. FS at various slope angles for piston core 20108040036. The red square identifies the minimum FS for the present-day slope angle of the core site.
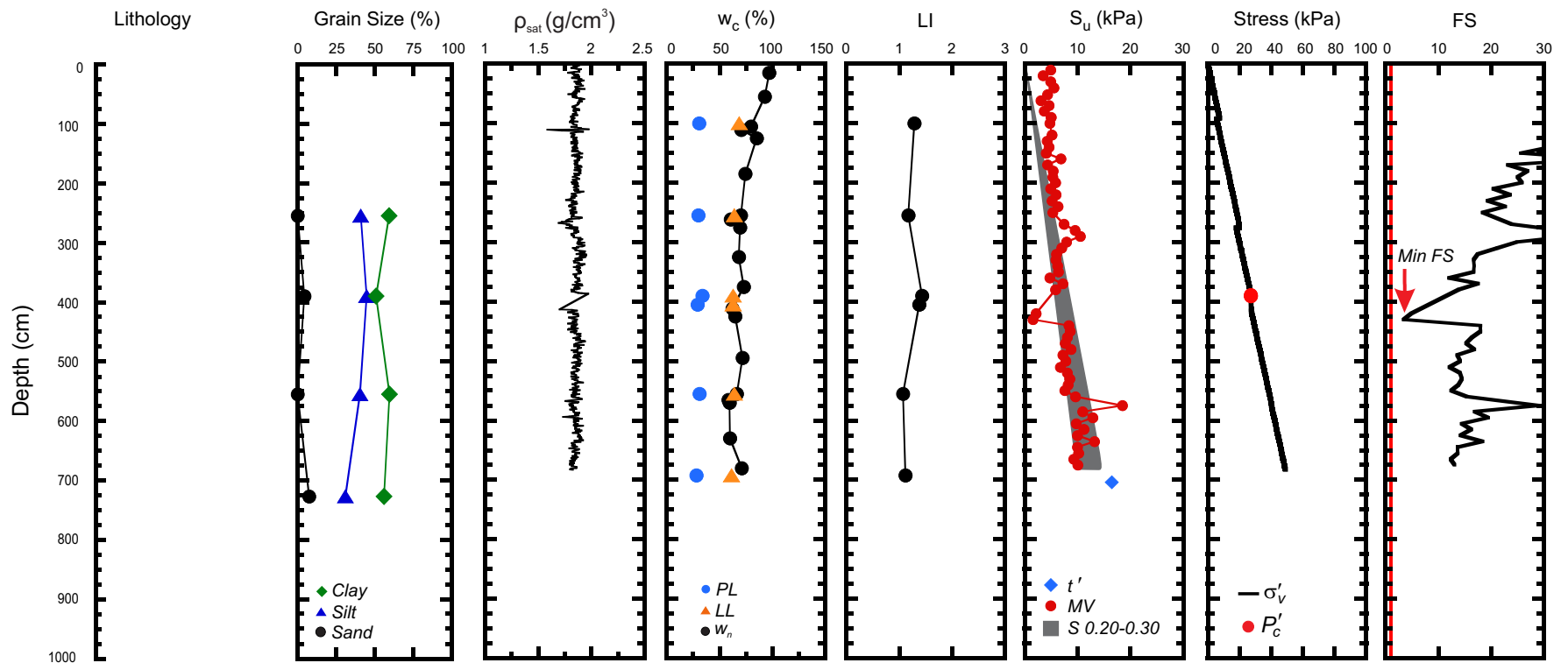
Figure 9.105. Geotechnical profile for core 20108040036 from Region 3. (ρ_{sat}= saturated bulk density, w_c = water content, w_n = natural in-situ water content, PL = plastic limit, LL = liquid limit, LI = liquidity index, S_u = undrained shear strength, MV = laboratory miniature vane shear strength, t' = maximum shear stress, S = shear strength calculated from the normalized strength ratio, σ'_v = effective overburden stress, P'_c = past maximum stress, FS = factor of safety).
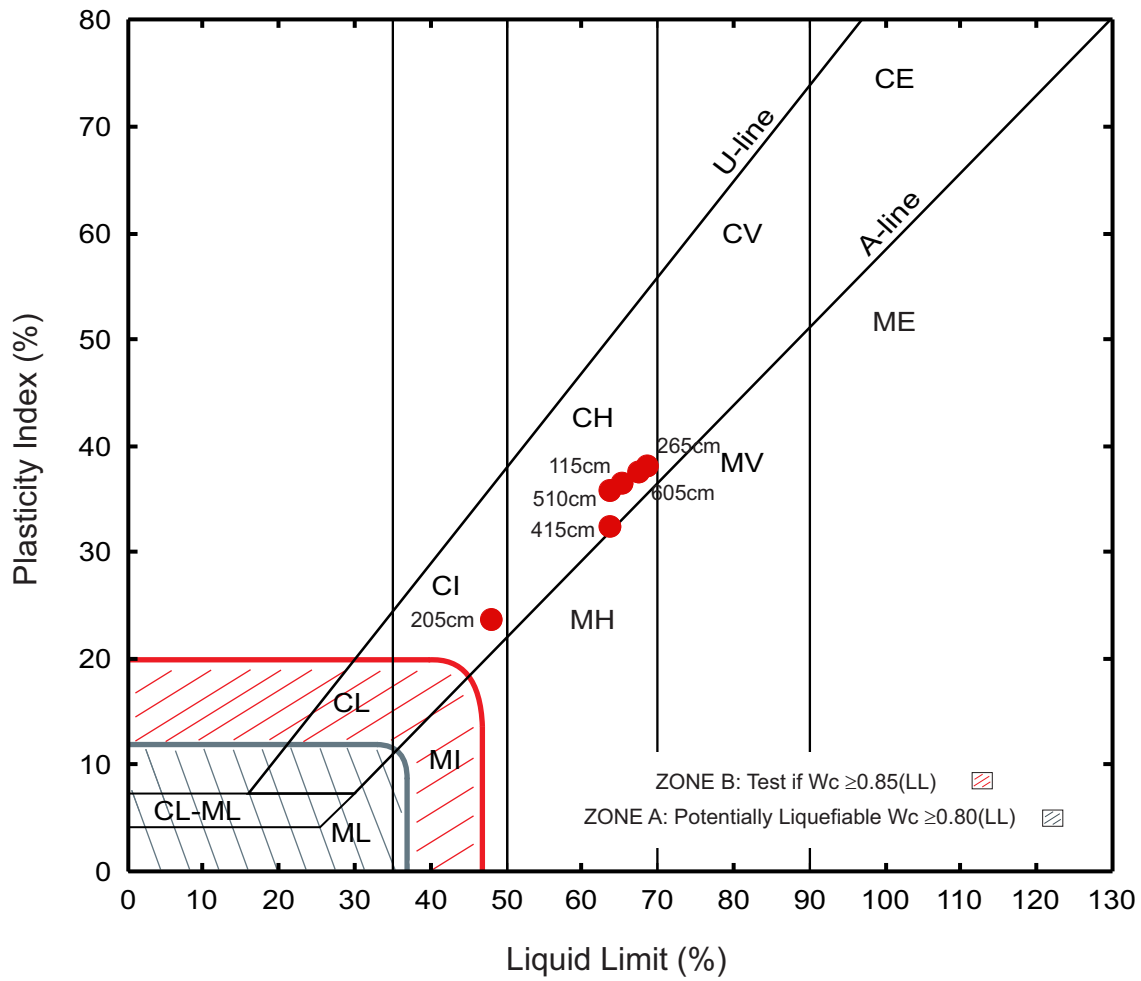
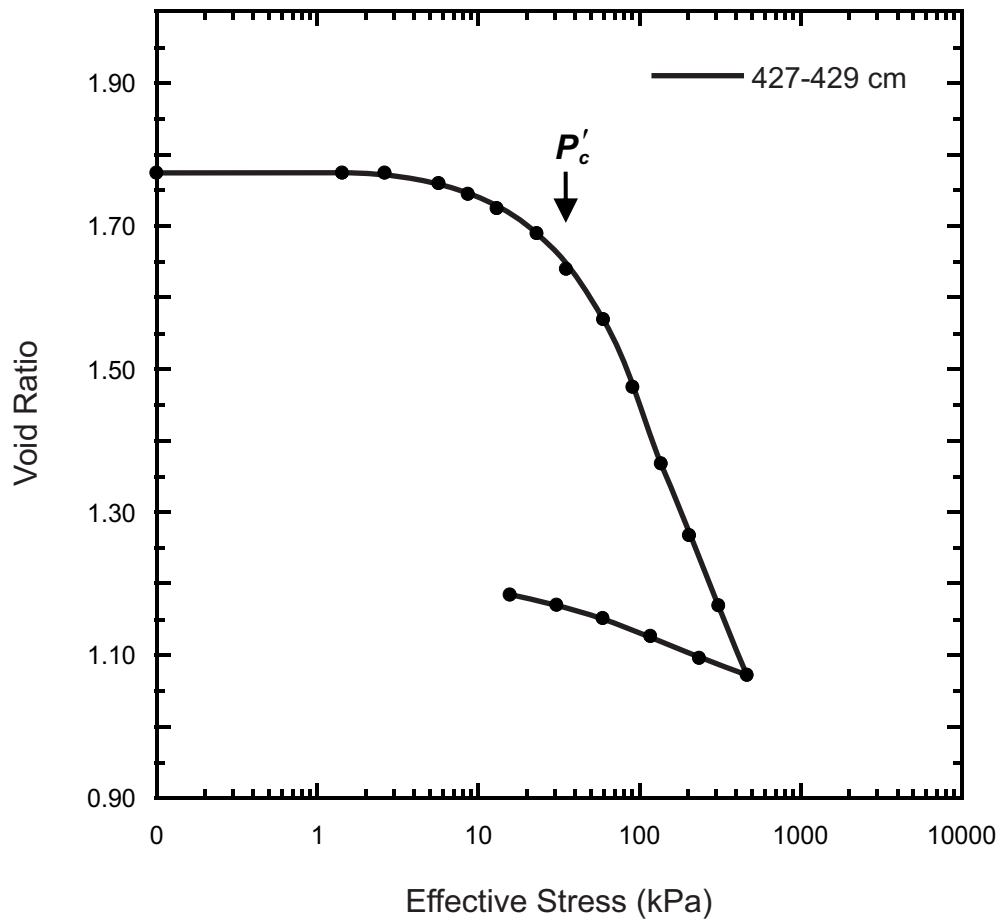Figure 9.106. Plasticity chart showing Atterberg limit results of piston core 20108040056.

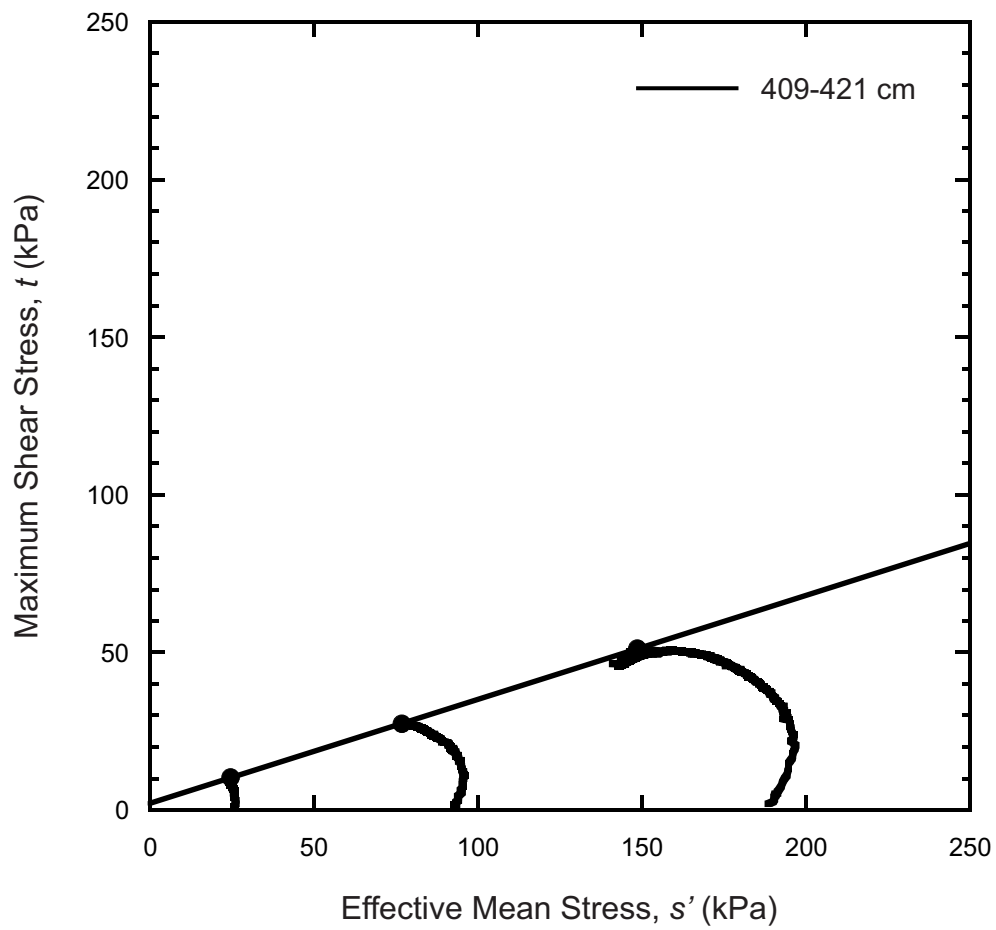Figure 9.107. Consolidation plot for piston core 20108040056.

Figure 9.108. Stress paths and failure envelopes from triaxial test results for piston core 20108040056.
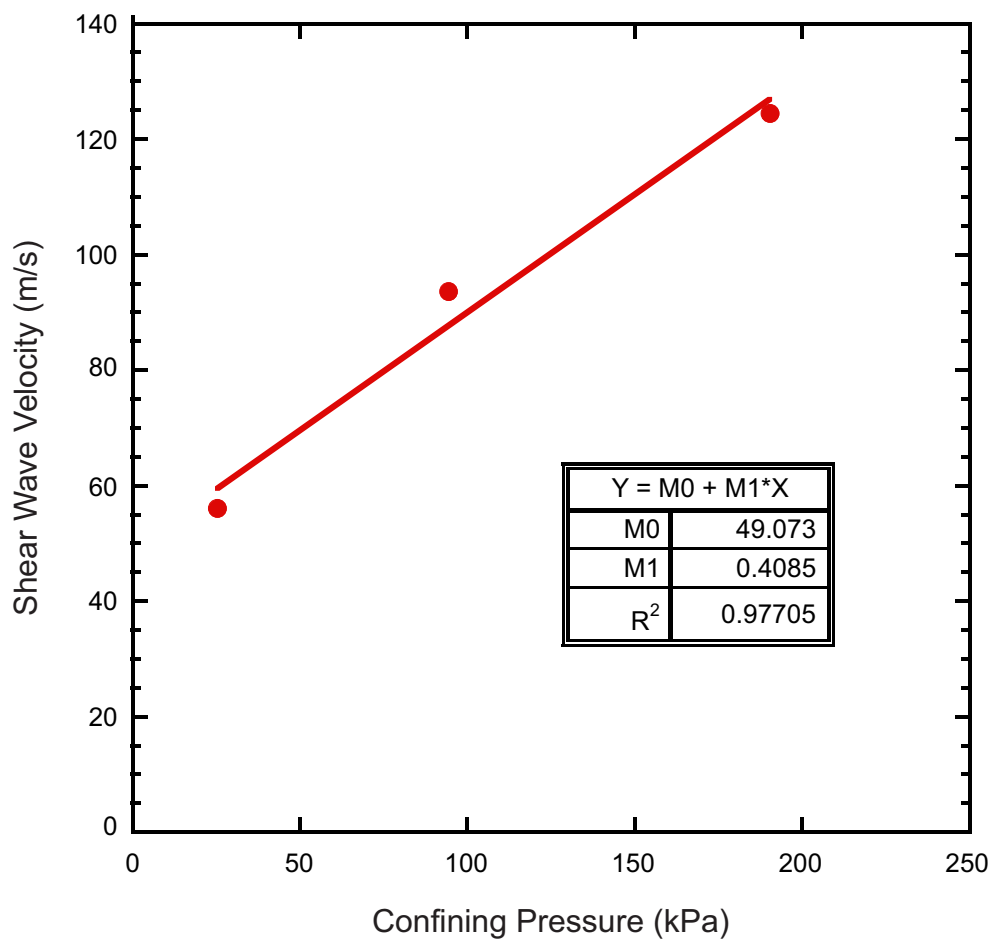
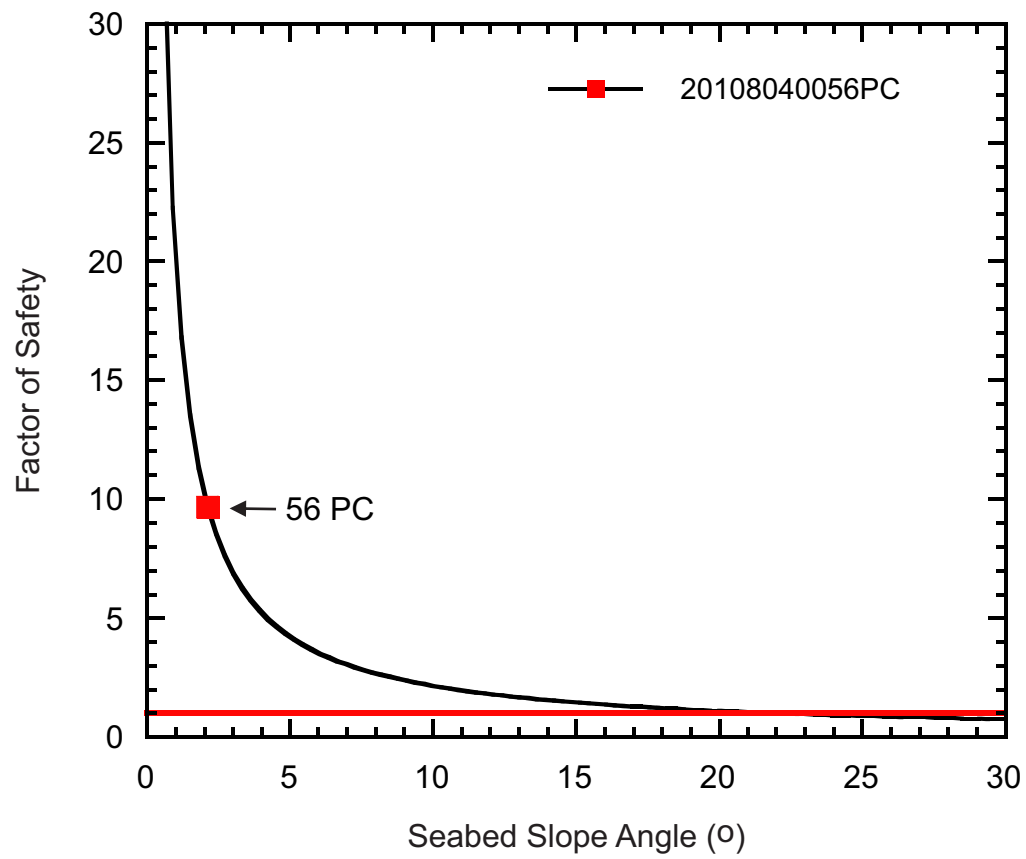Figure 9.109. Shear wave velocities at various confining pressures for piston core 20108040056.

Figure 9.110. FS at various slope angles for piston core 20108040056. The red square identifies the minimum FS for the present-day slope angle of the core site.

Figure 9.111. Geotechnical profile for core 20108040056 from Region 3. (ρ_{sat}= saturated bulk density, w_c = water content, w_n = natural in-situ water content, PL = plastic limit, LL = liquid limit, LI = liquidity index, S_u = undrained shear strength, MV = laboratory miniature vane shear strength, t' = maximum shear stress, S = shear strength calculated from the normalized strength ratio, σ'_v = effective overburden stress, P'_c = past maximum stress, FS = factor of safety).

Figure 9.112. Plasticity chart showing Atterberg limit results of piston core 20108040069.

Figure 9.113. Consolidation plot for piston core 20108040069.

Figure 9.114. Stress paths and failure envelopes from triaxial test results for piston core 20108040069.

Figure 9.115. FS at various slope angles for piston core 20108040069. The red square identifies the minimum FS for the present-day slope angle of the core site.
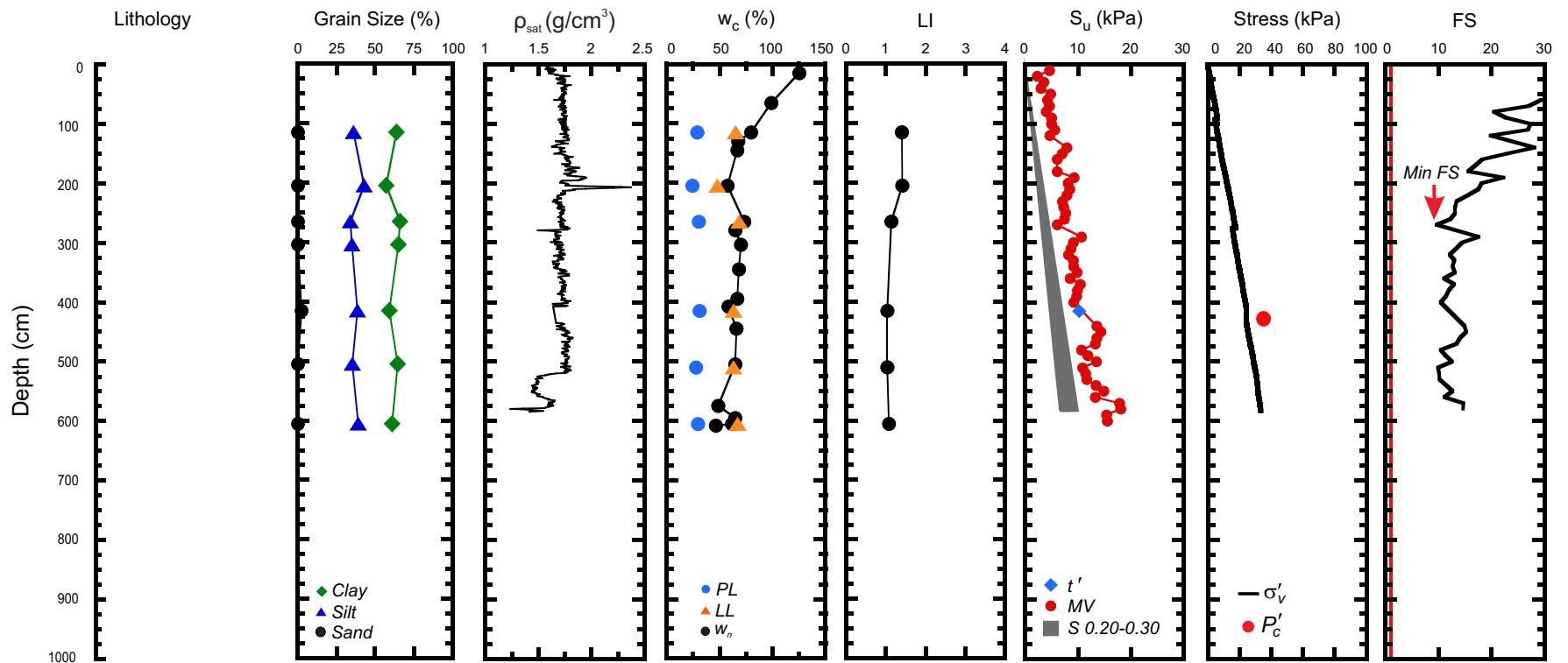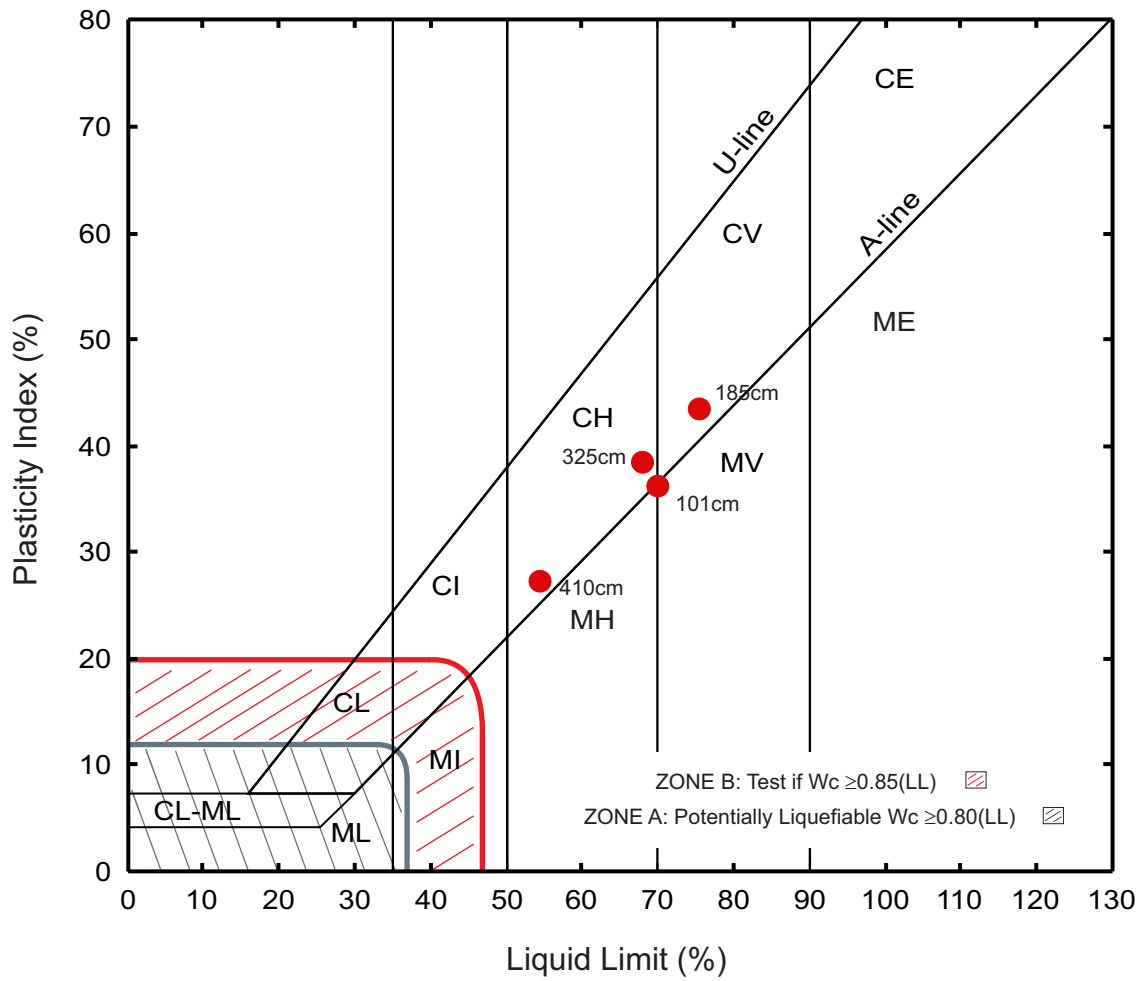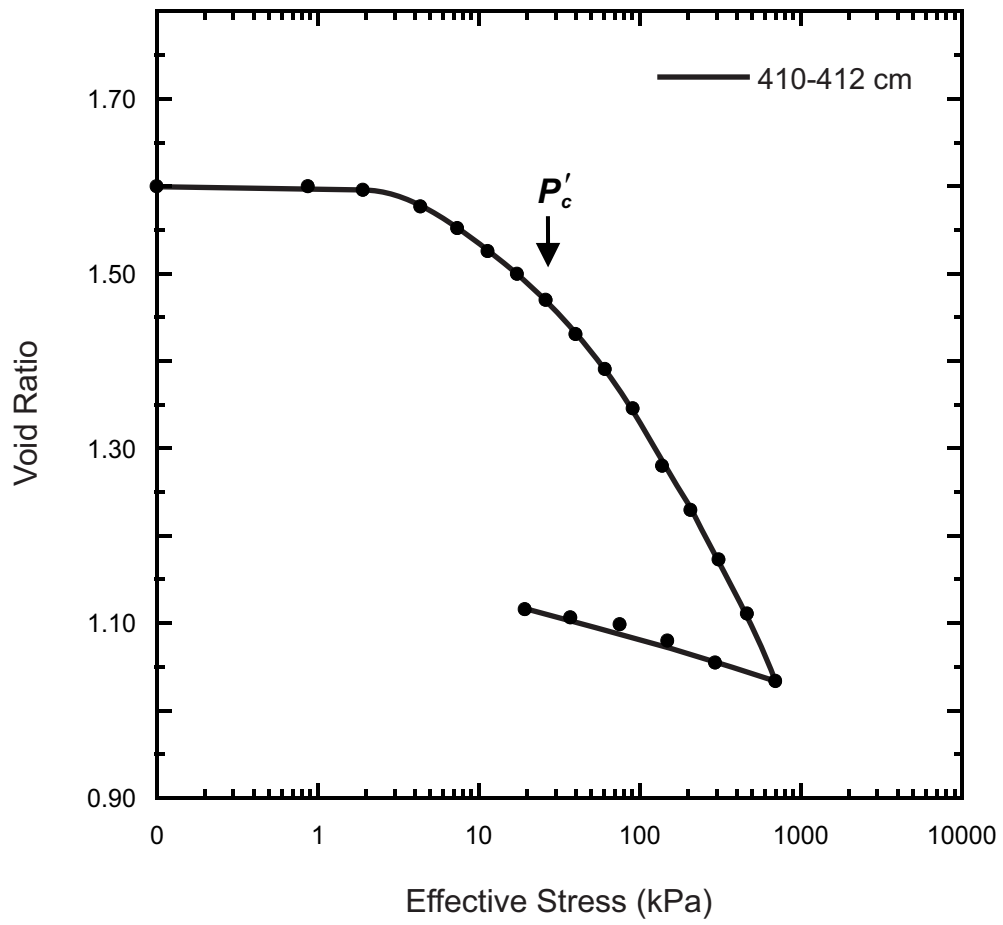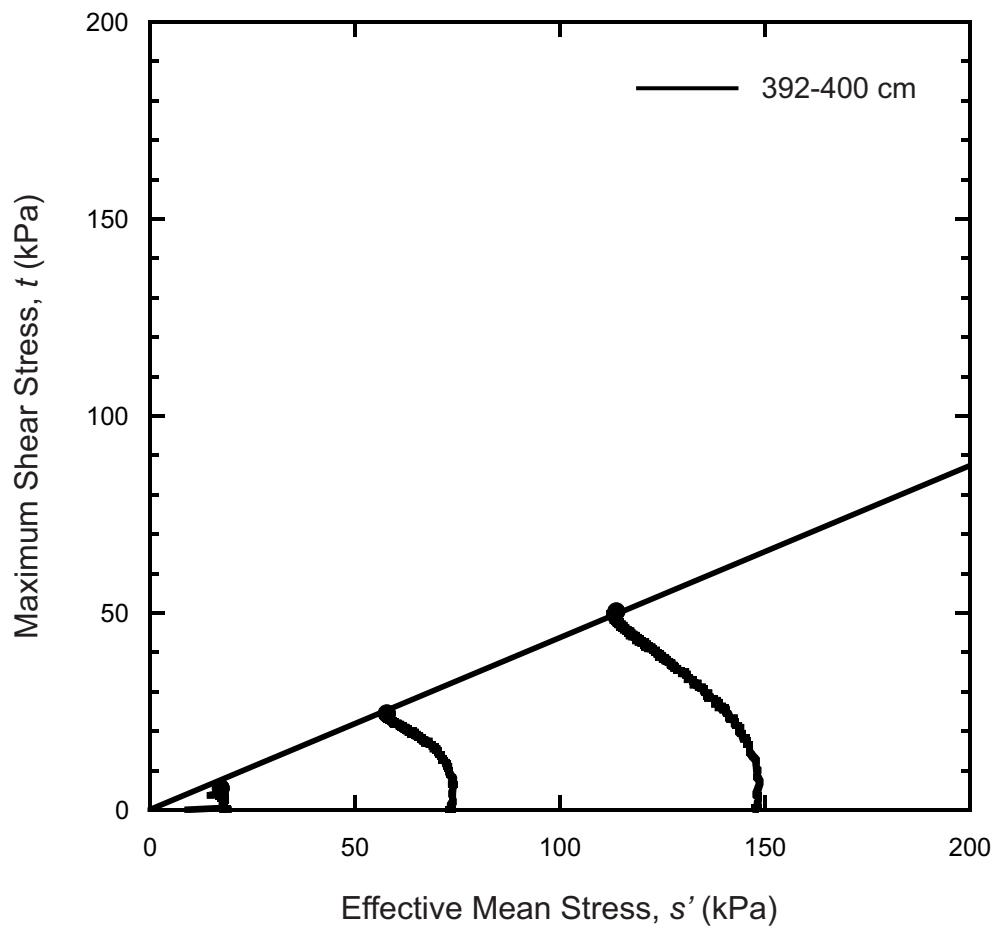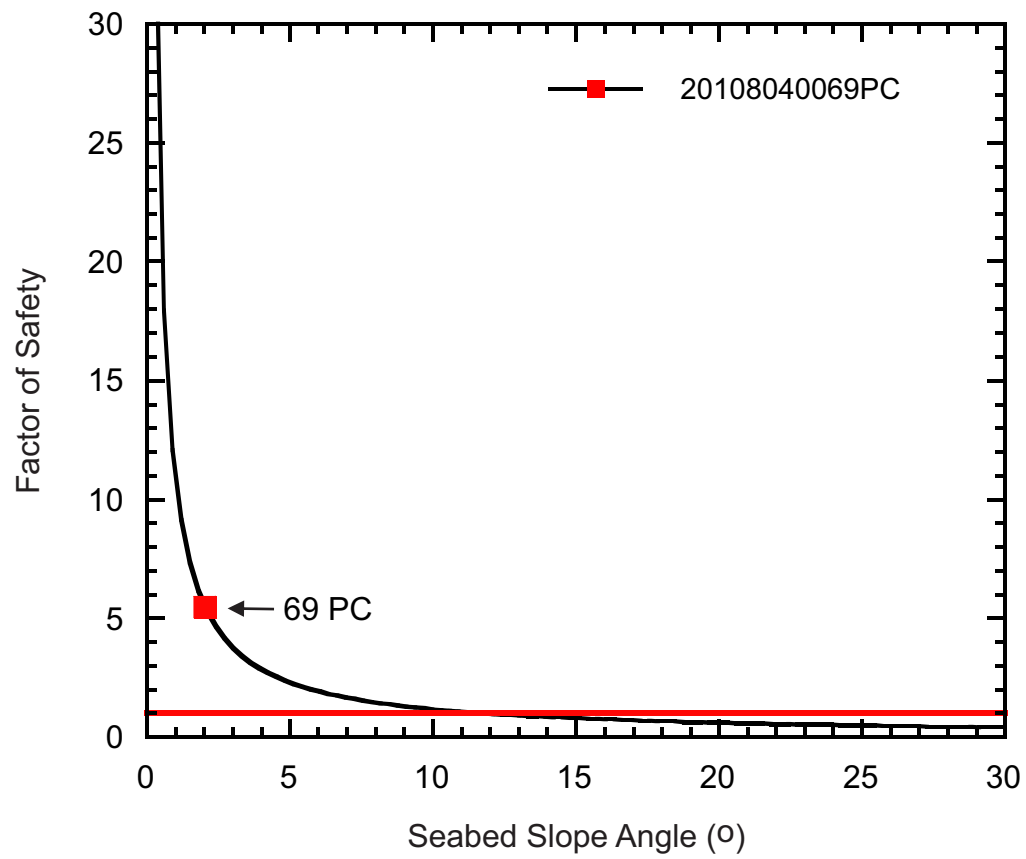
Figure 9.116. Geotechnical profile for core 20108040069 from Region 3. (ρ_{sat}= saturated bulk density, w_c = water content, w_n = natural in-situ water content, PL = plastic limit, LL = liquid limit, LI = liquidity index, S_u = undrained shear strength, MV = laboratory miniature vane shear strength, t' = maximum shear stress, S = shear strength calculated from the normalized strength ratio, σ'_v = effective overburden stress, P'_c = past maximum stress, FS = factor of safety).

Figure 9.117. Plasticity chart showing Atterberg limit results of piston core 20108040070.

Figure 9.118. Consolidation plot for piston core 20108040070.

Figure 9.119. Stress paths and failure envelopes from triaxial test results for piston core 20108040070.

Figure 9.120. FS at various slope angles for piston core 20108040070. The red square identifies the minimum FS for the present-day slope angle of the core site.
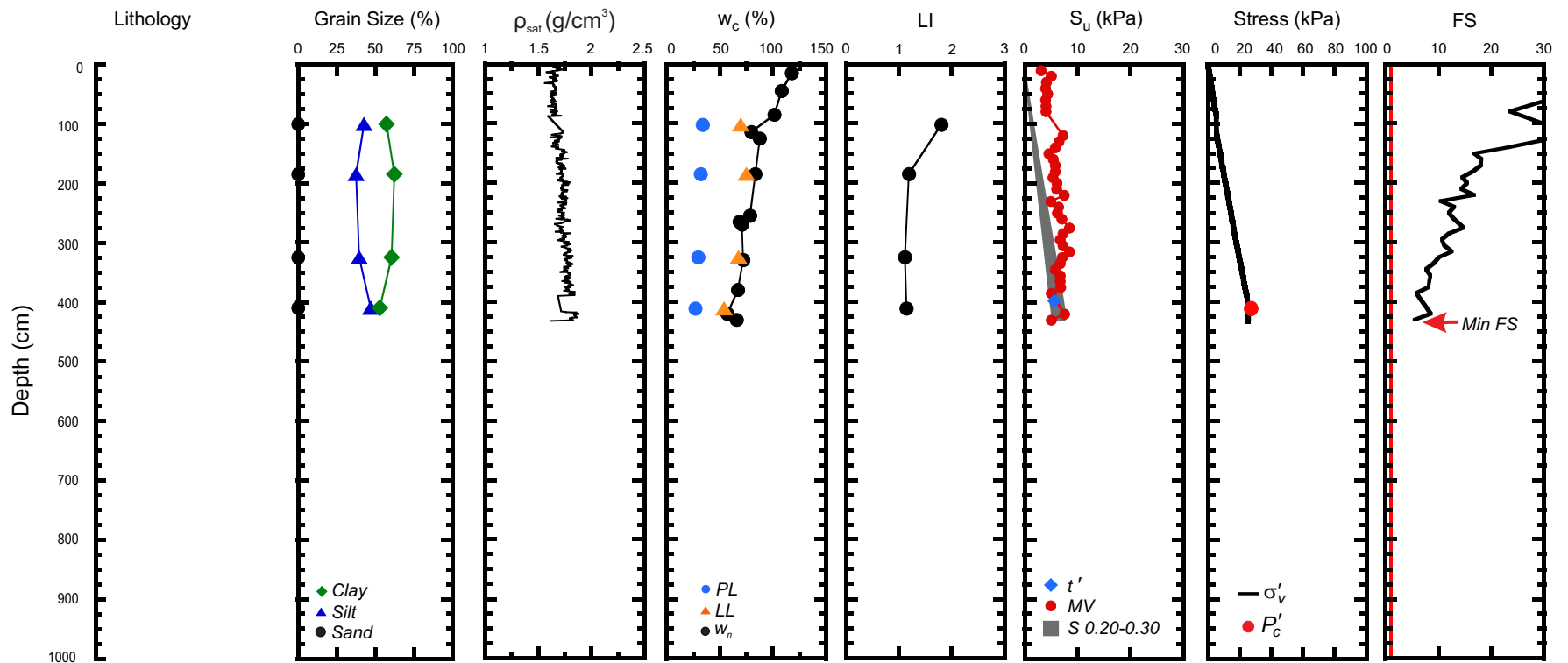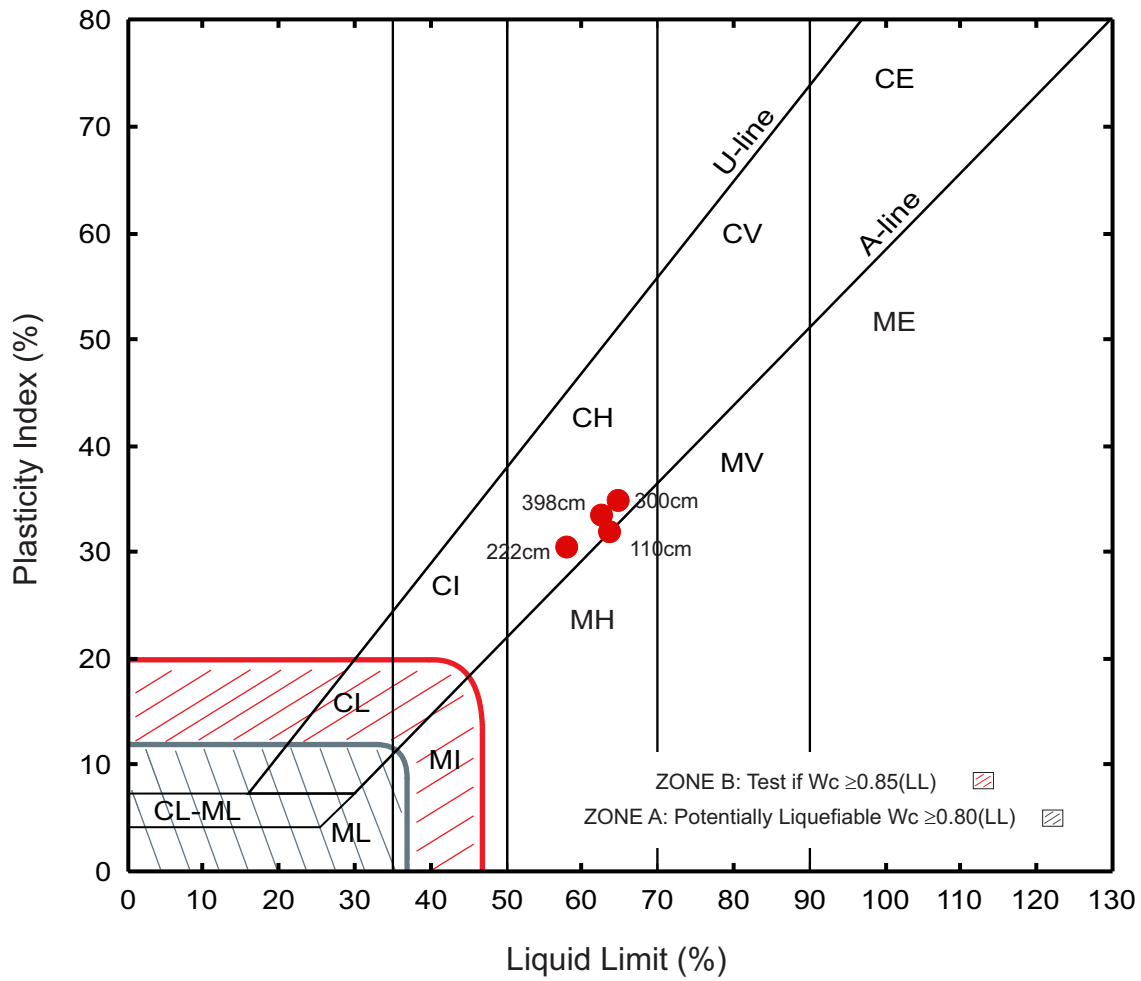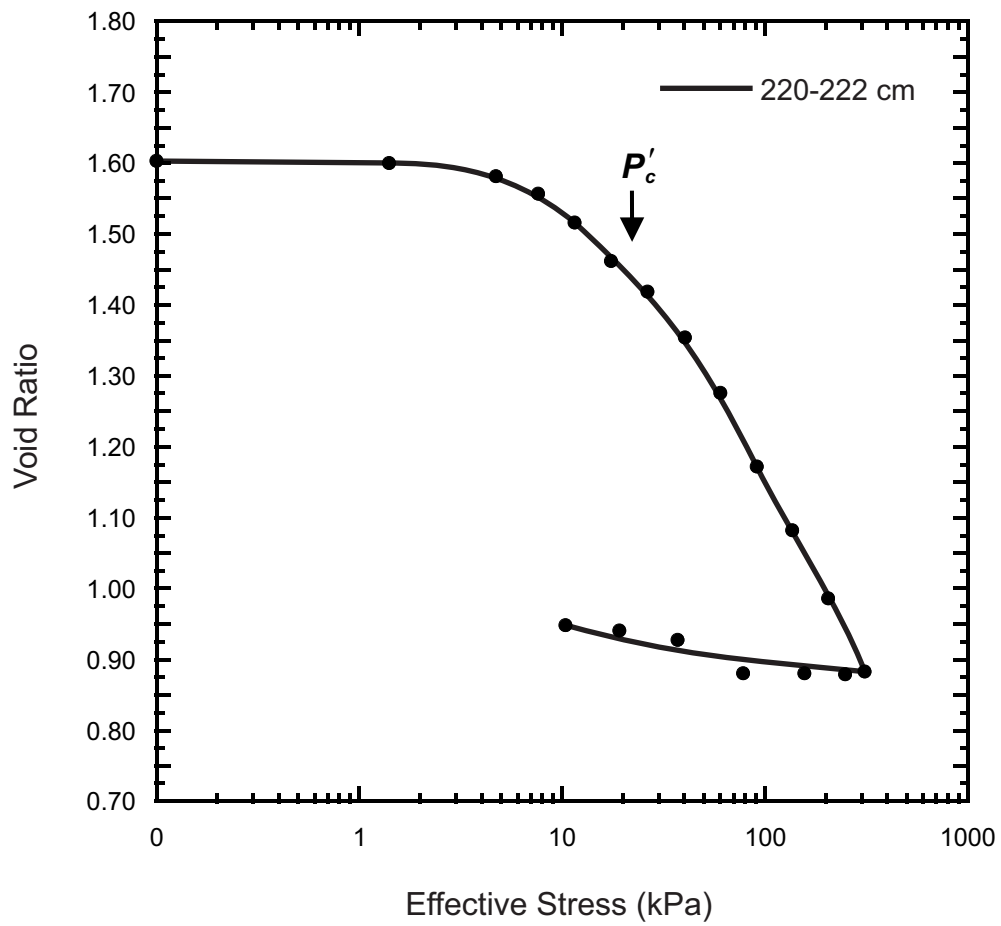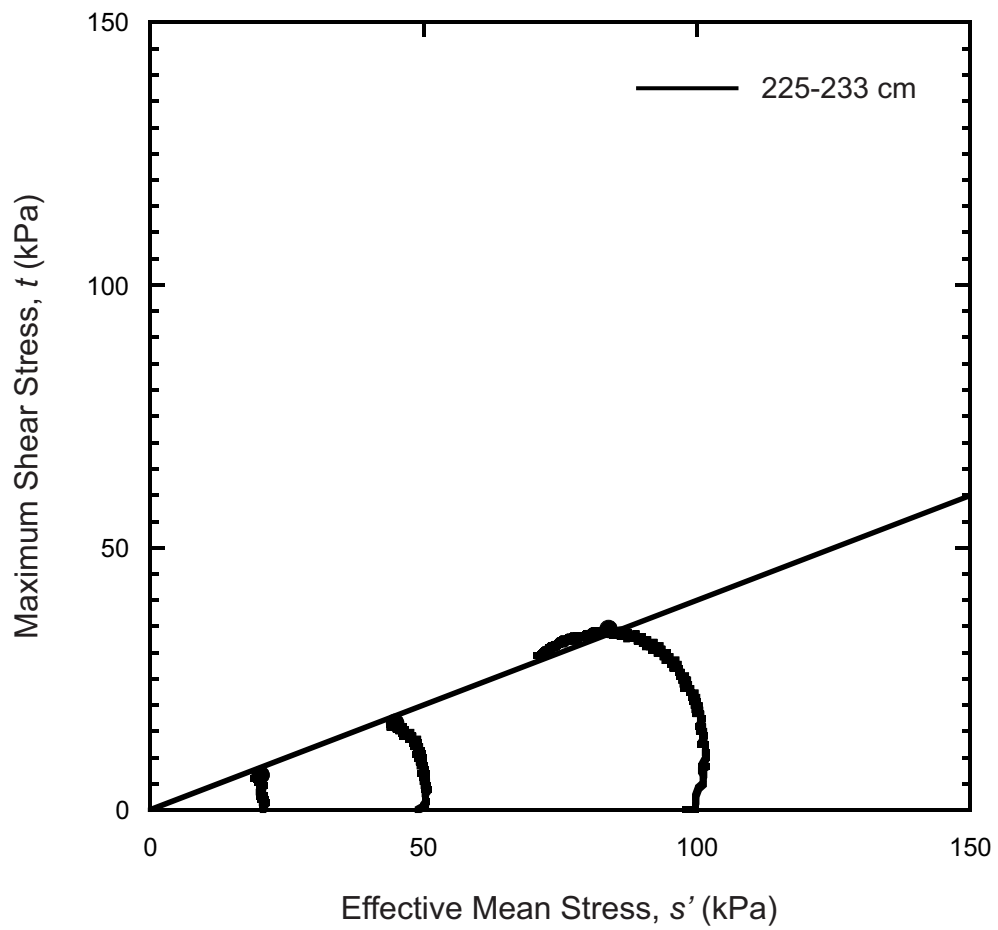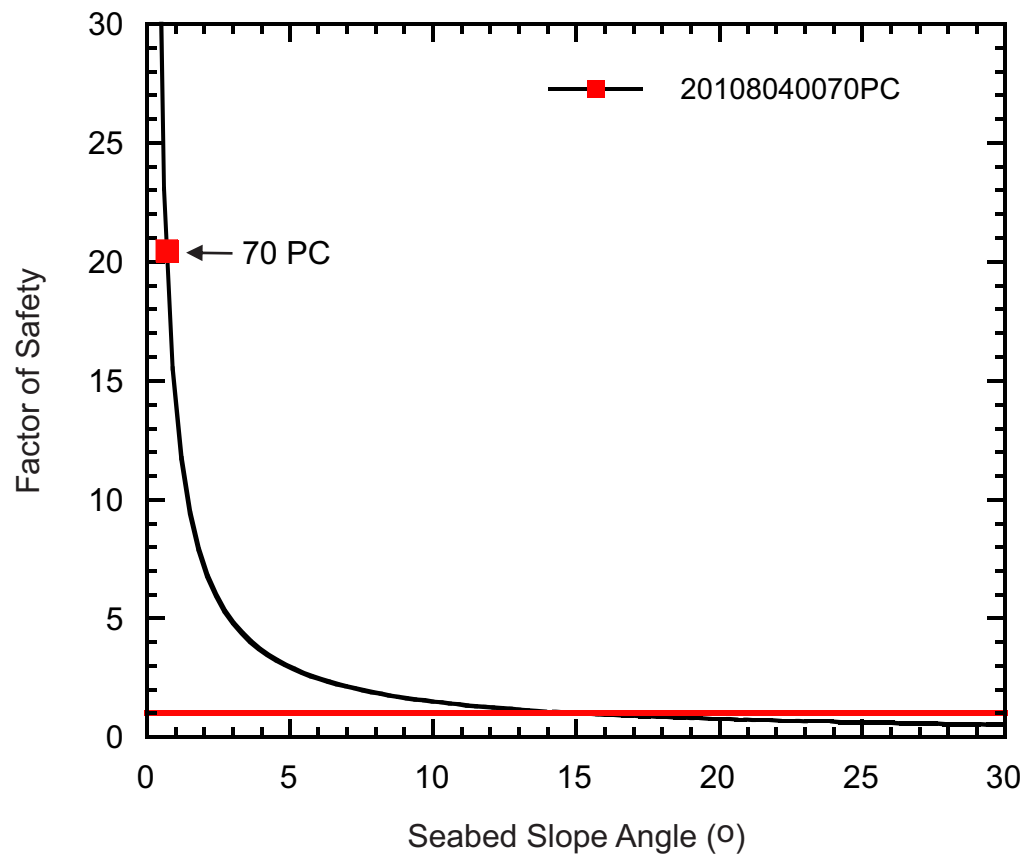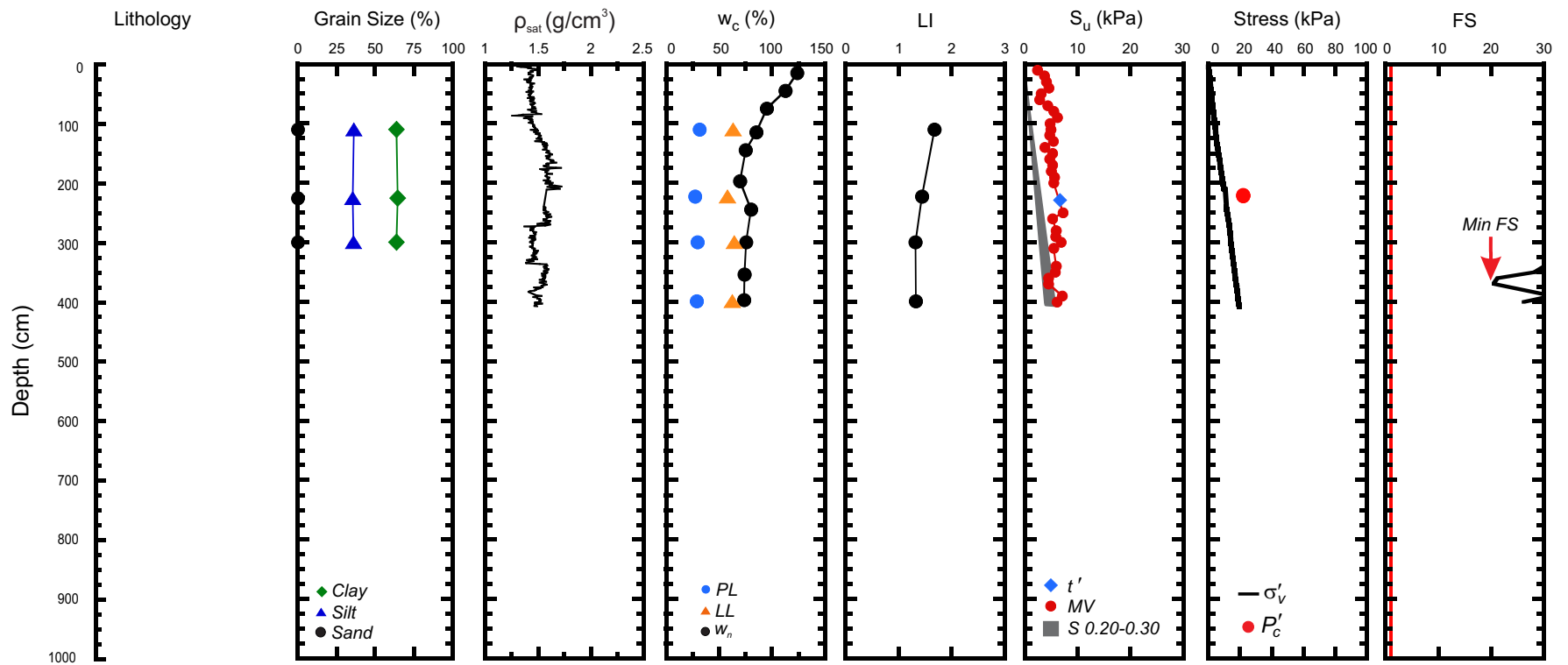
Figure 9.121. Geotechnical profile for core 20108040070 from Region 3. (ρ_{sat}= saturated bulk density, w_c = water content, w_n = natural in-situ water content, PL = plastic limit, LL = liquid limit, LI = liquidity index, S_u = undrained shear strength, MV = laboratory miniature vane shear strength, t' = maximum shear stress, S = shear strength calculated from the normalized strength ratio, σ'_v = effective overburden stress, P'_c = past maximum stress, FS = factor of safety).
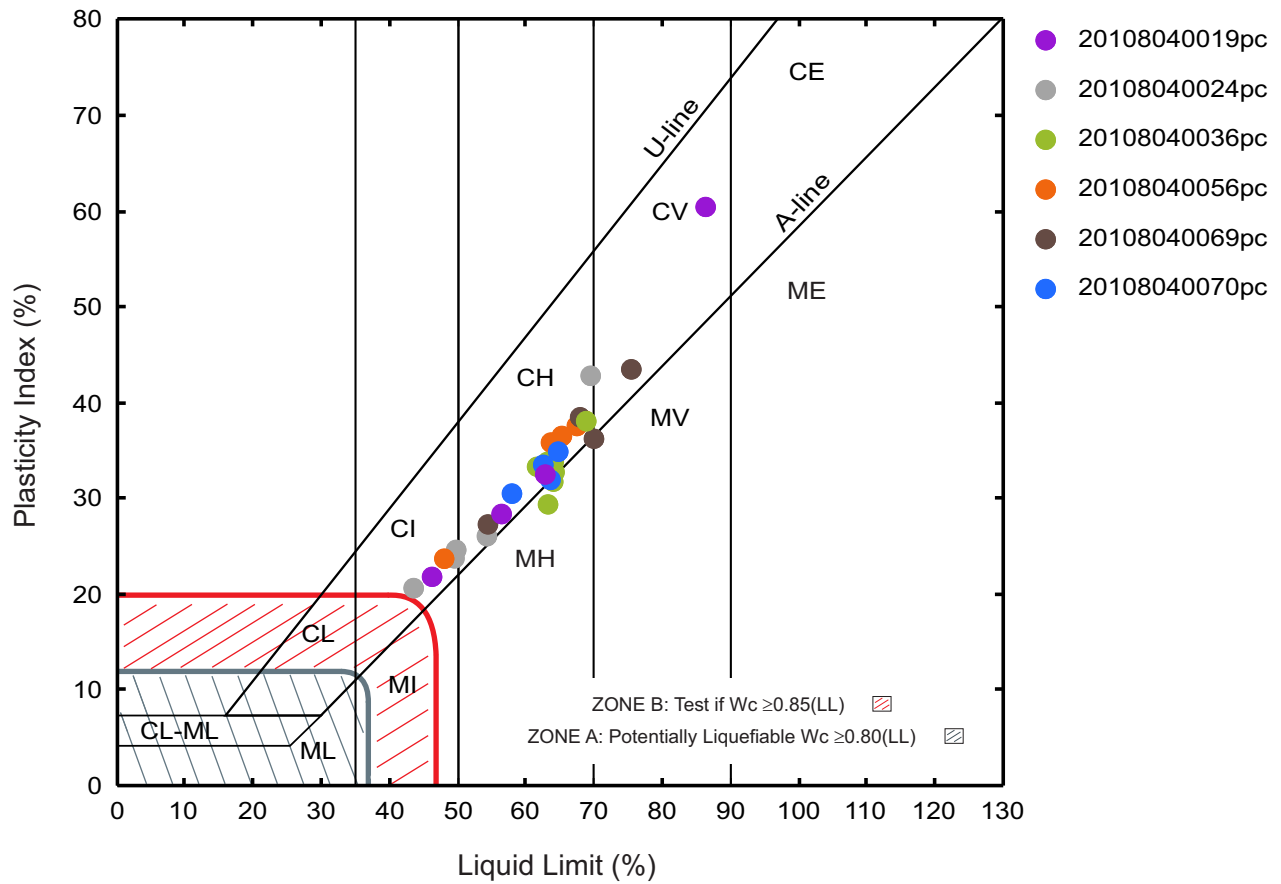
Figure 9.122. Plasticity chart showing Atterberg limit results of piston cores in Region 3.
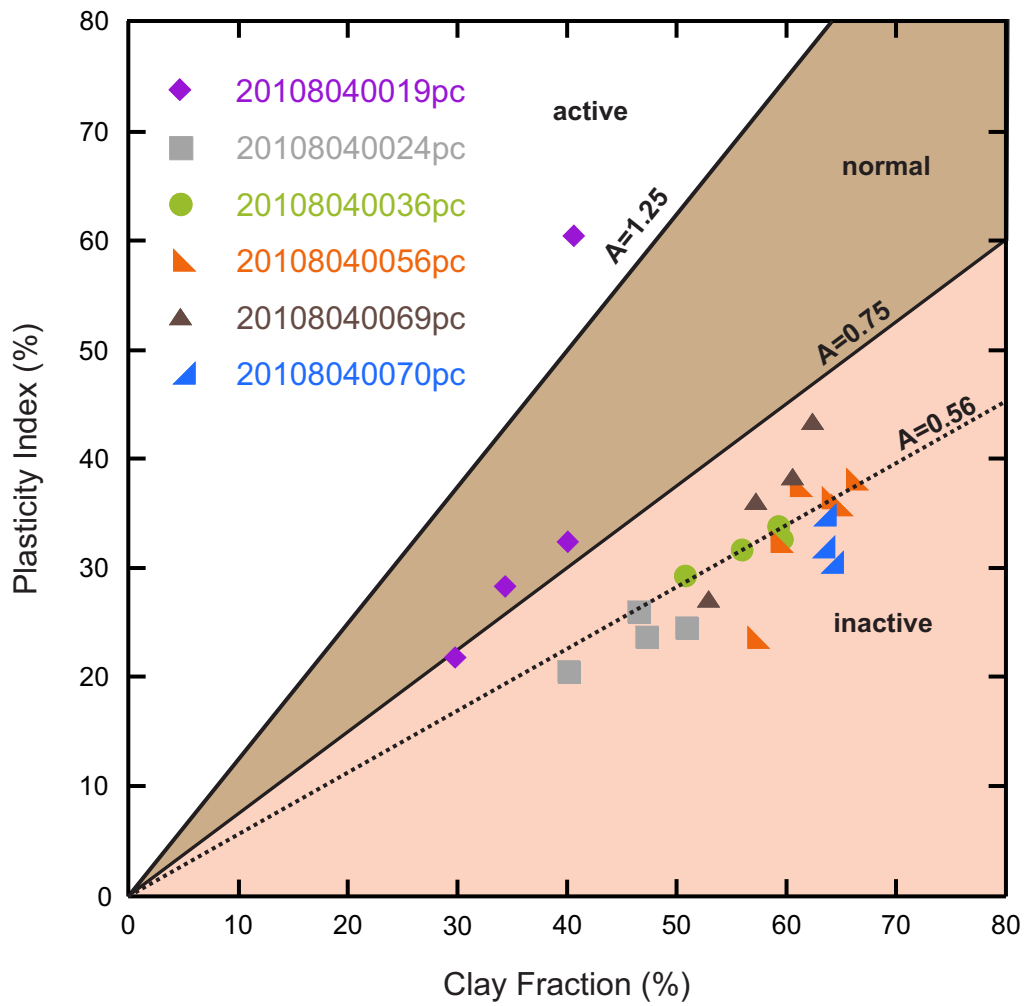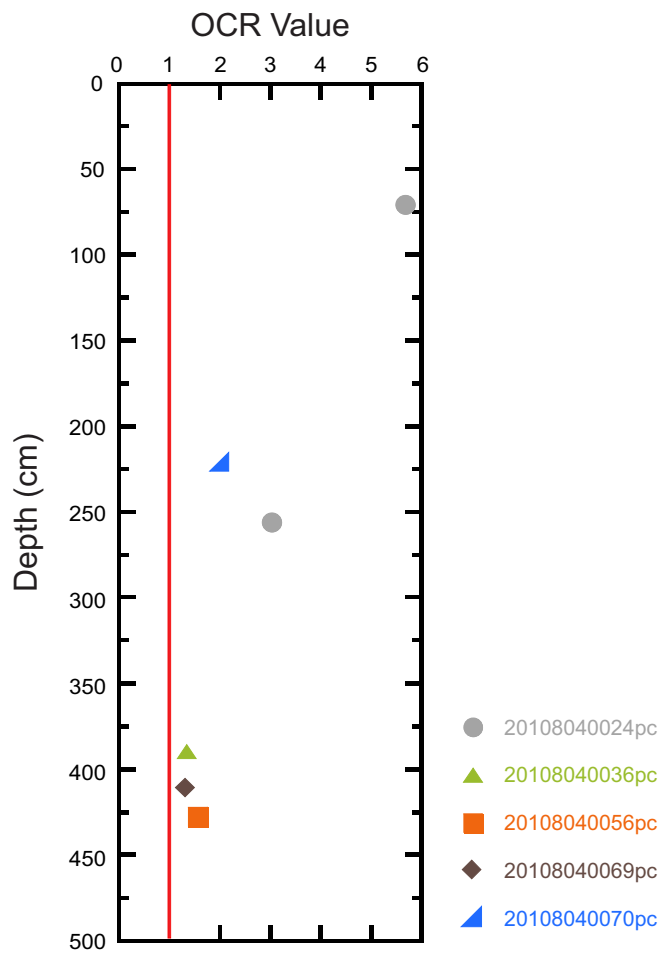
Figure 9.123. Region 3 activity chart.

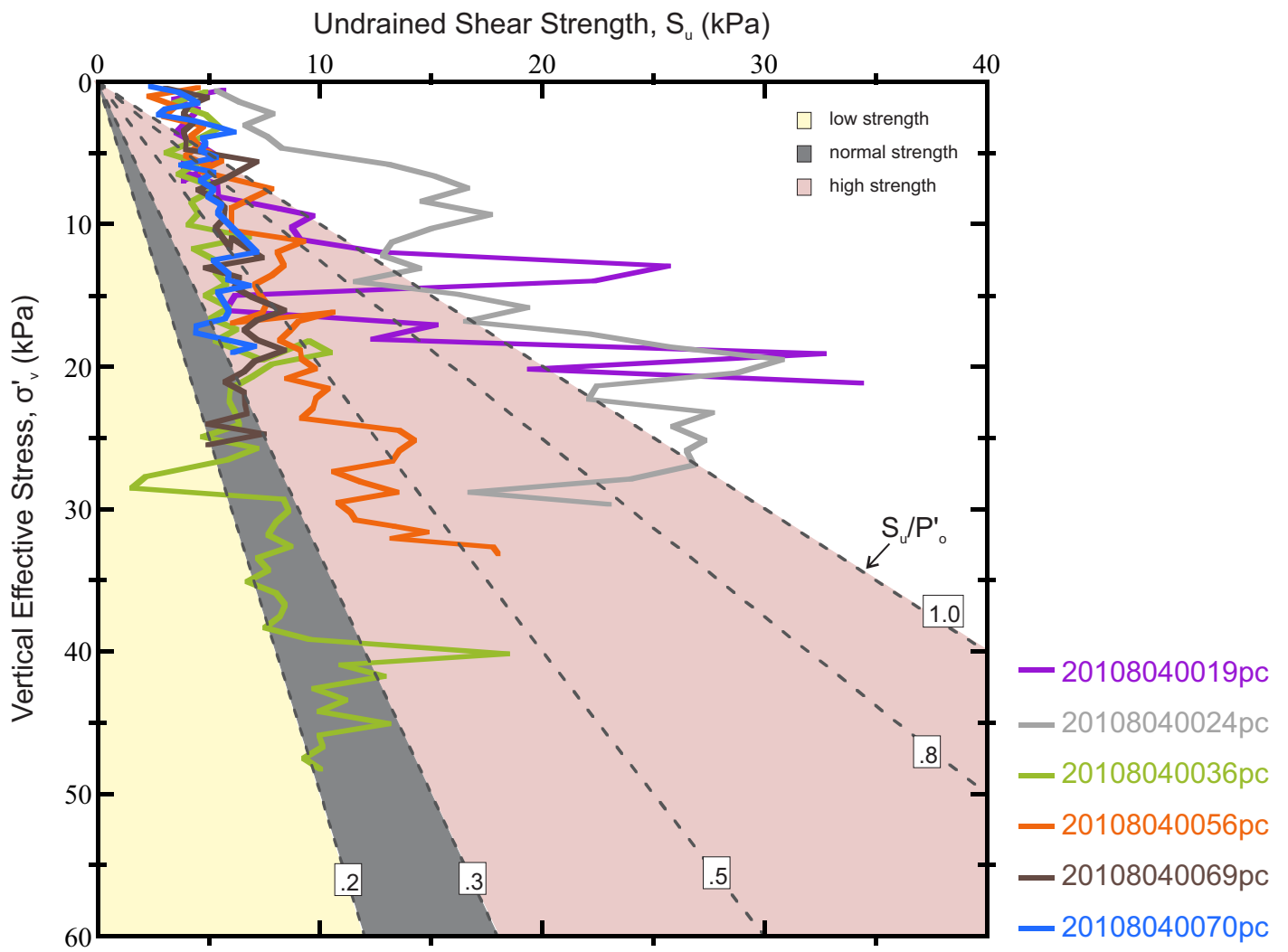Figure 9.124. OCR values with depth of consolidation tests in Region 3.

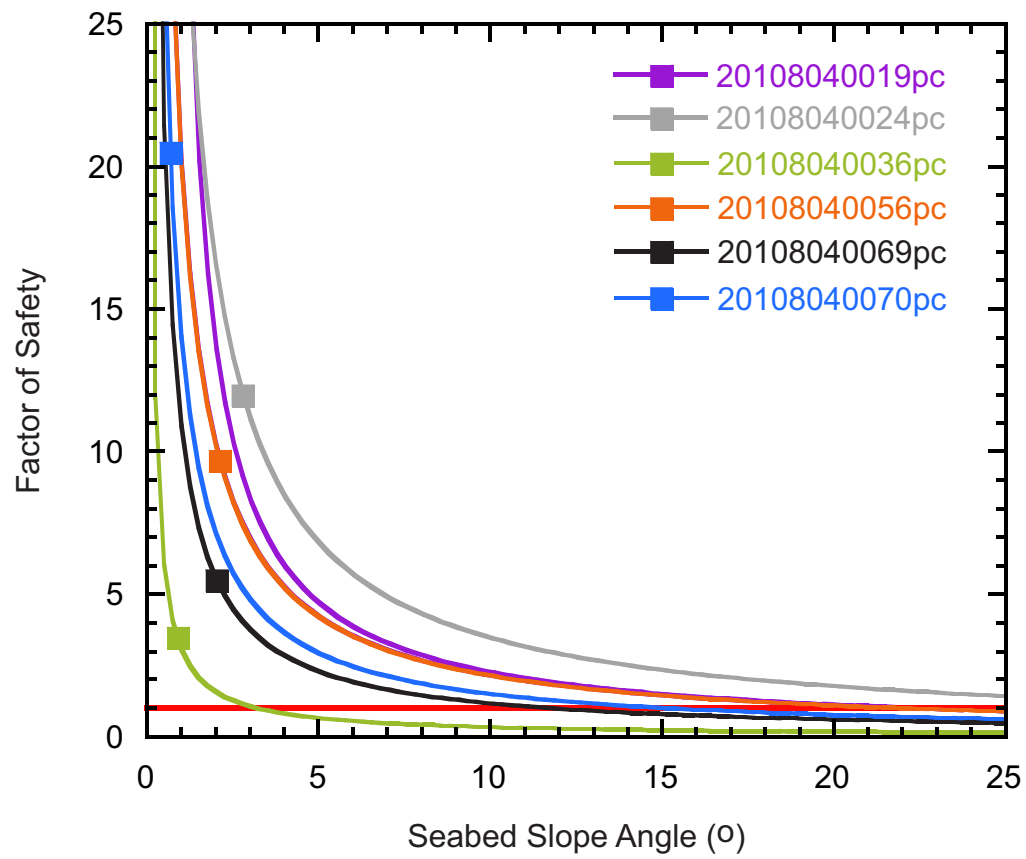Figure 9.125. Shear strength profiles with effective overburden pressure of cores in Region 3.

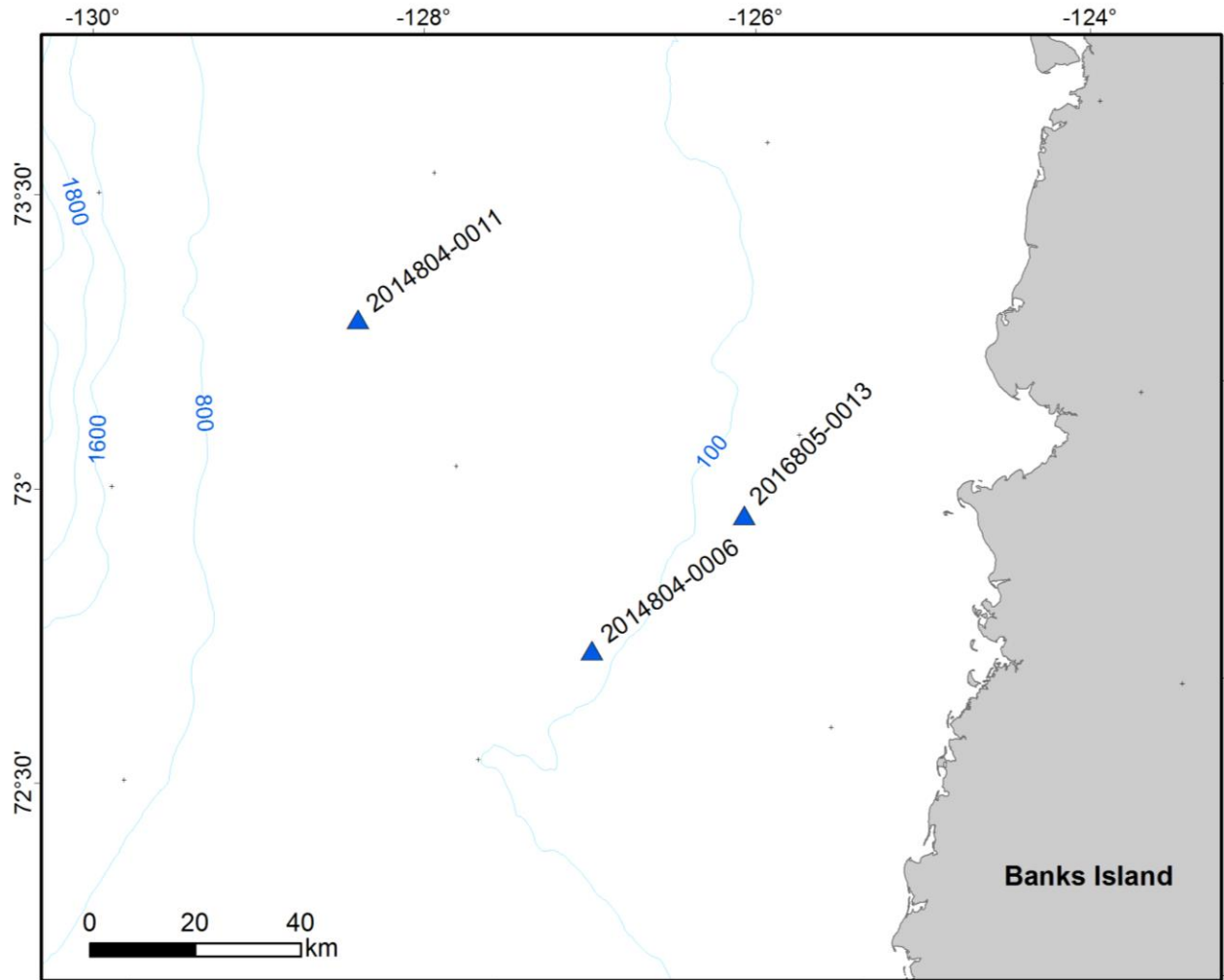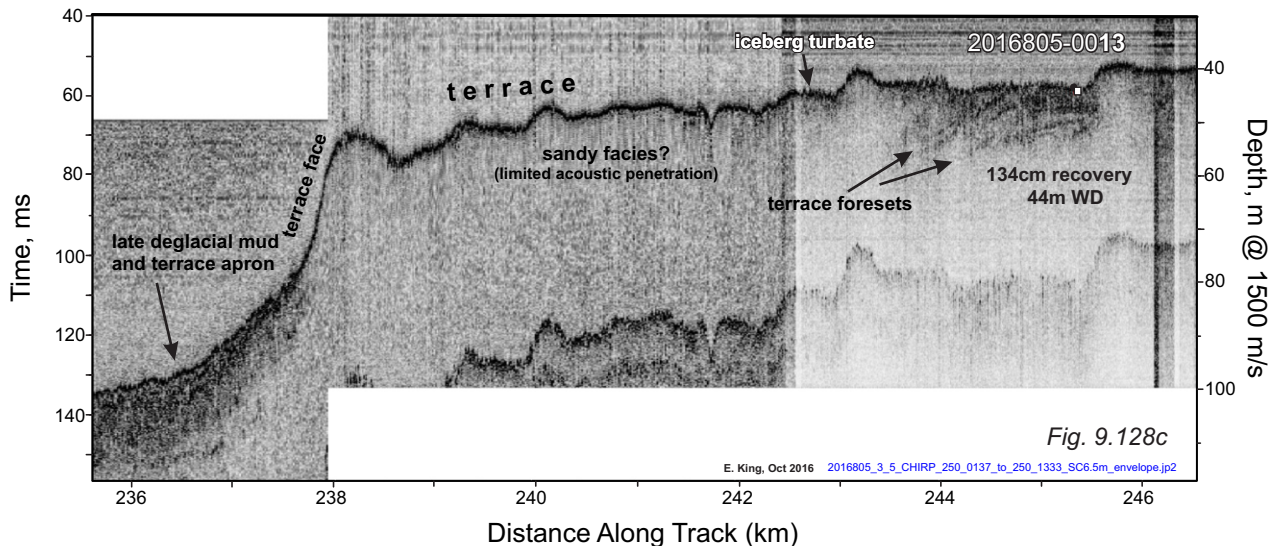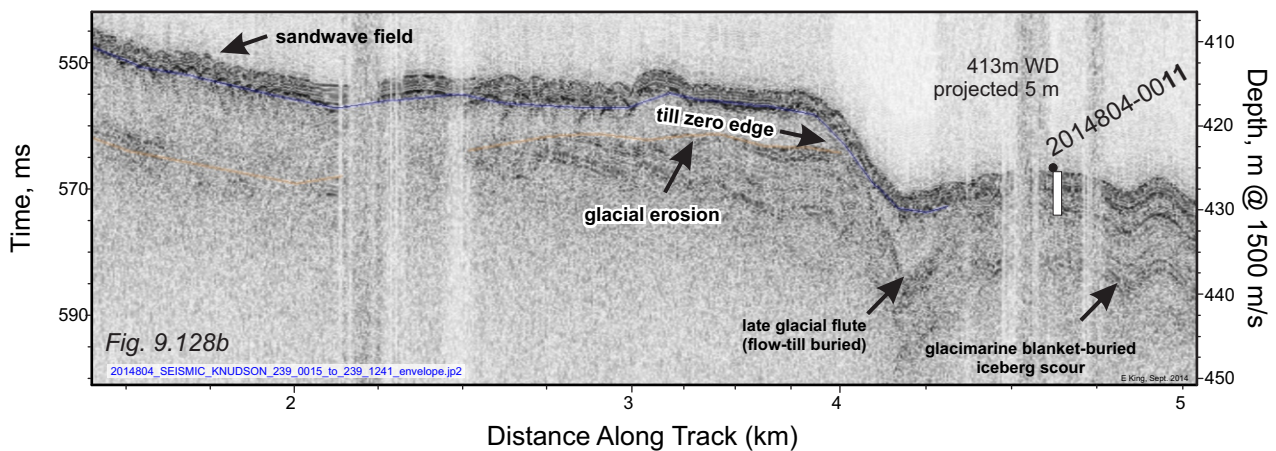Figure 9.126. FS at various slope angles for piston cores in Region 3.

Figure 9.127. Region 4 core locations with bathymetry lines.
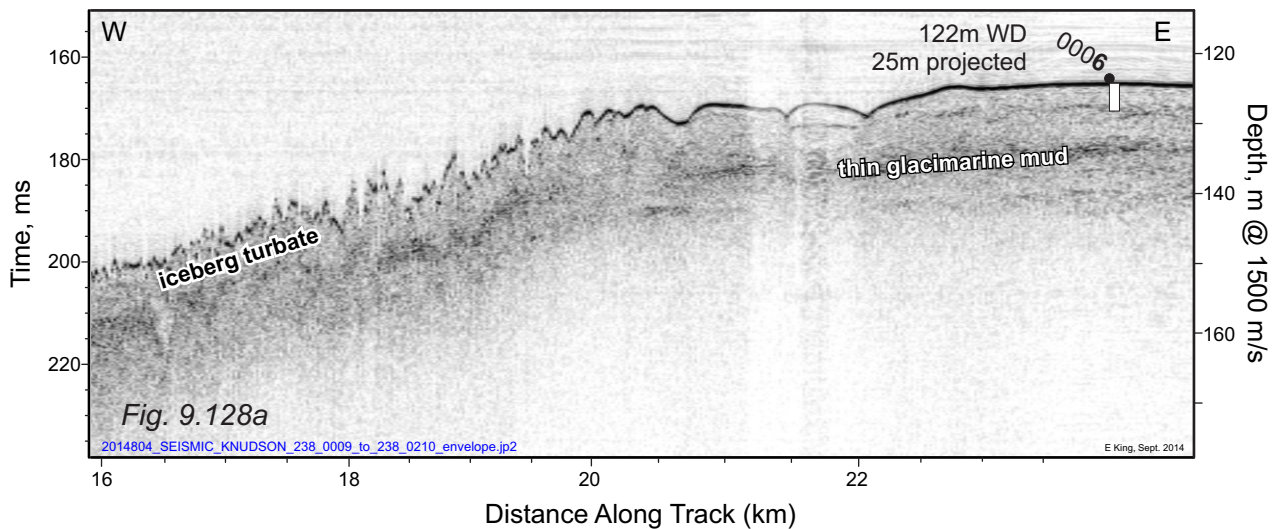
Figures 9.128. 3.5 kHz sub-bottom profile showing the acoustic stratigraphy and position of piston core sites in the Banks Island Area (Region 4). Core 2014804006pc, Fig. 9.128a, recovered silt and clay over a weakly stratified glacial diamict. Core 2014804011pc, Fig. 9.128b, contains a complex sequence of stratified glacimarine mud with ice rafted debris and a basal, partly stratified diamict. Core 20168050013pc, Fig 9.128c, is situated on the low-stand- related terrace which covers the entire inner shelf. The sample is from a shallow basin.

Figure 9.129. Plasticity chart showing Atterberg limit results of piston core 20148040006.

Figure 9.130. Consolidation plot for piston core 20148040006.

Figure 9.131. Stress paths and failure envelopes from triaxial test results for piston core 20148040006.
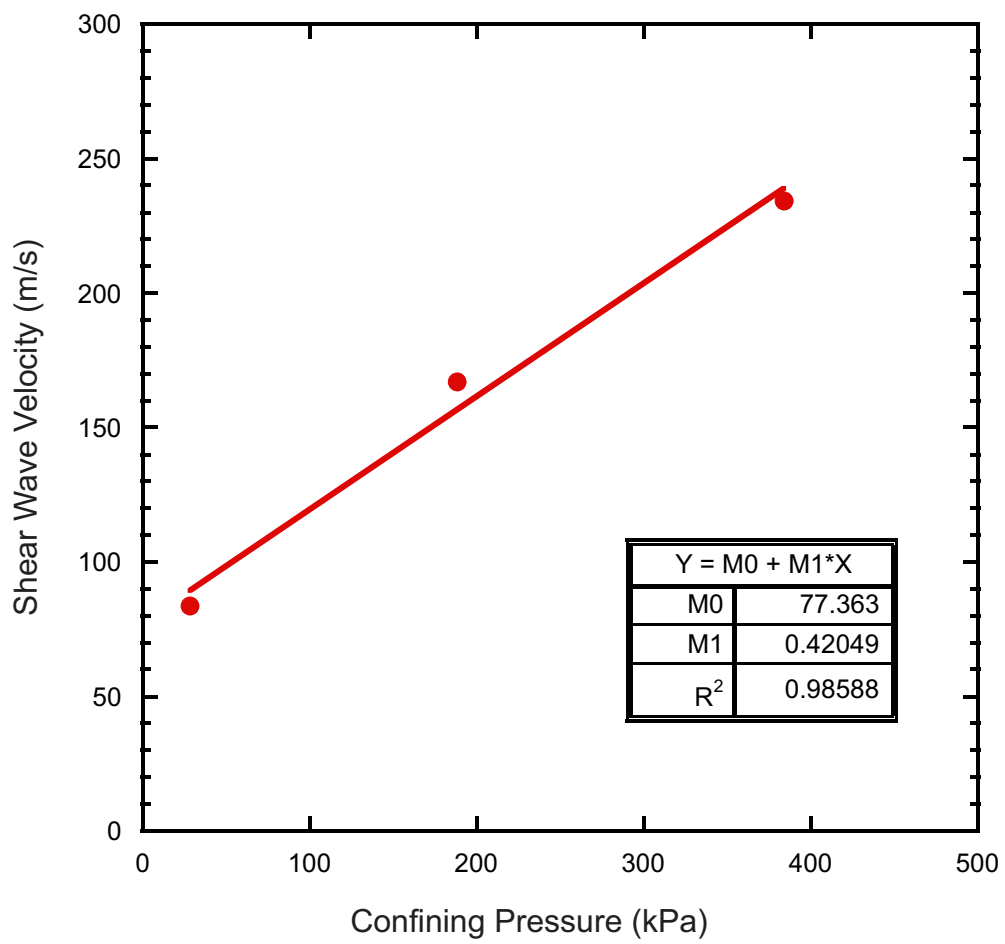
Figure 9.132. Shear wave velocities at various confining pressures for piston core 20148040006.
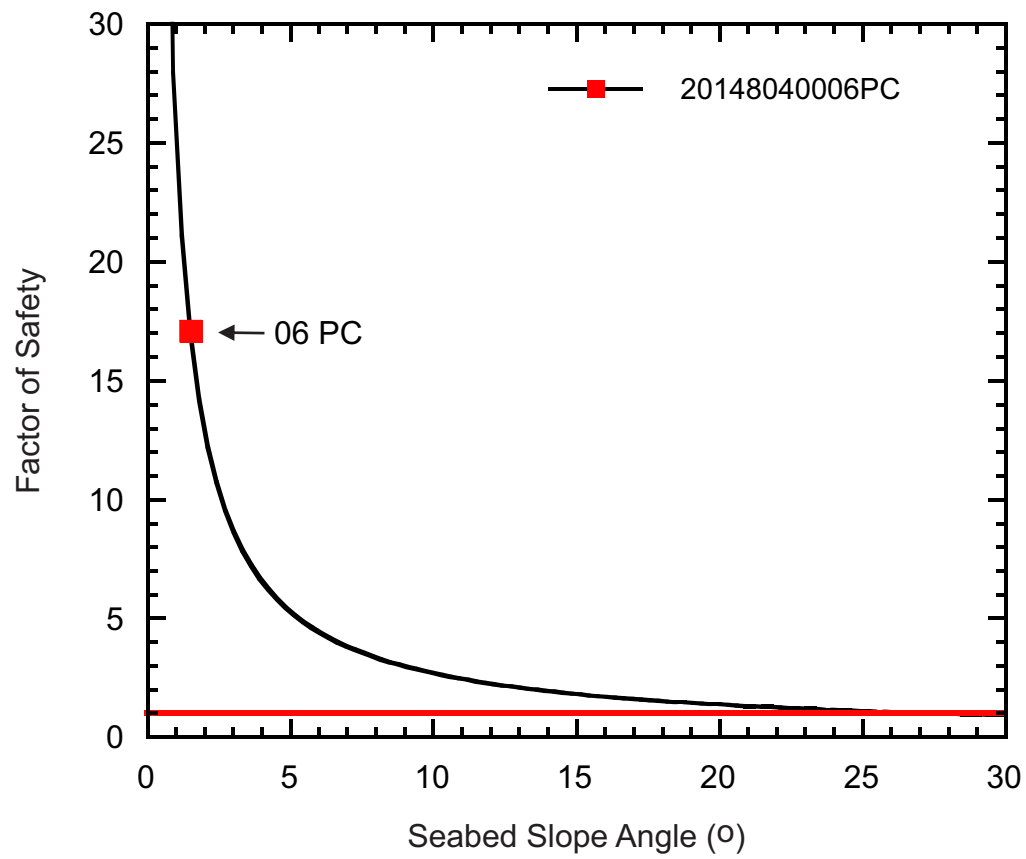
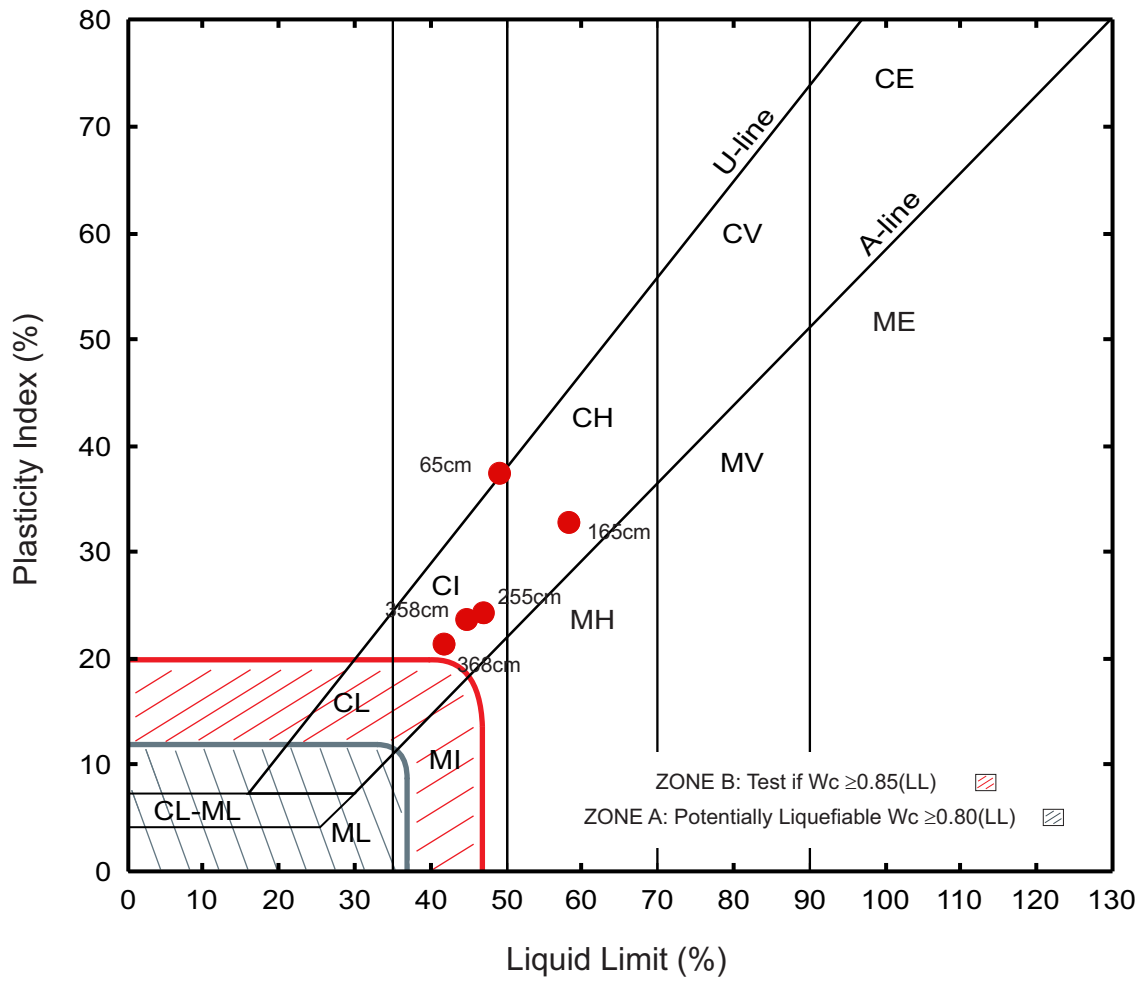Figure 9.133. FS at various slope angles for piston core 20148040006. The red square identifies the minimum FS for the present-day slope angle of the core site.

Figure 9.134. Geotechnical profile for core 20148040006 from the shelf west of Banks Island. (ρ_{sat} = saturated bulk density, w_c = water content, w_n = natural in-situ water content, PL = plastic limit, LL = liquid limit, LI = liquidity index, S_u = undrained shear strength, MV = laboratory miniature vane shear strength, t' = maximum shear stress, S = shear strength calculated from the normalized strength ratio, σ'_v = effective overburden stress, P'_c = past maximum stress, FS = factor of safety).

Figure 9.135. Plasticity chart showing Atterberg limit results of piston core 20148040011.
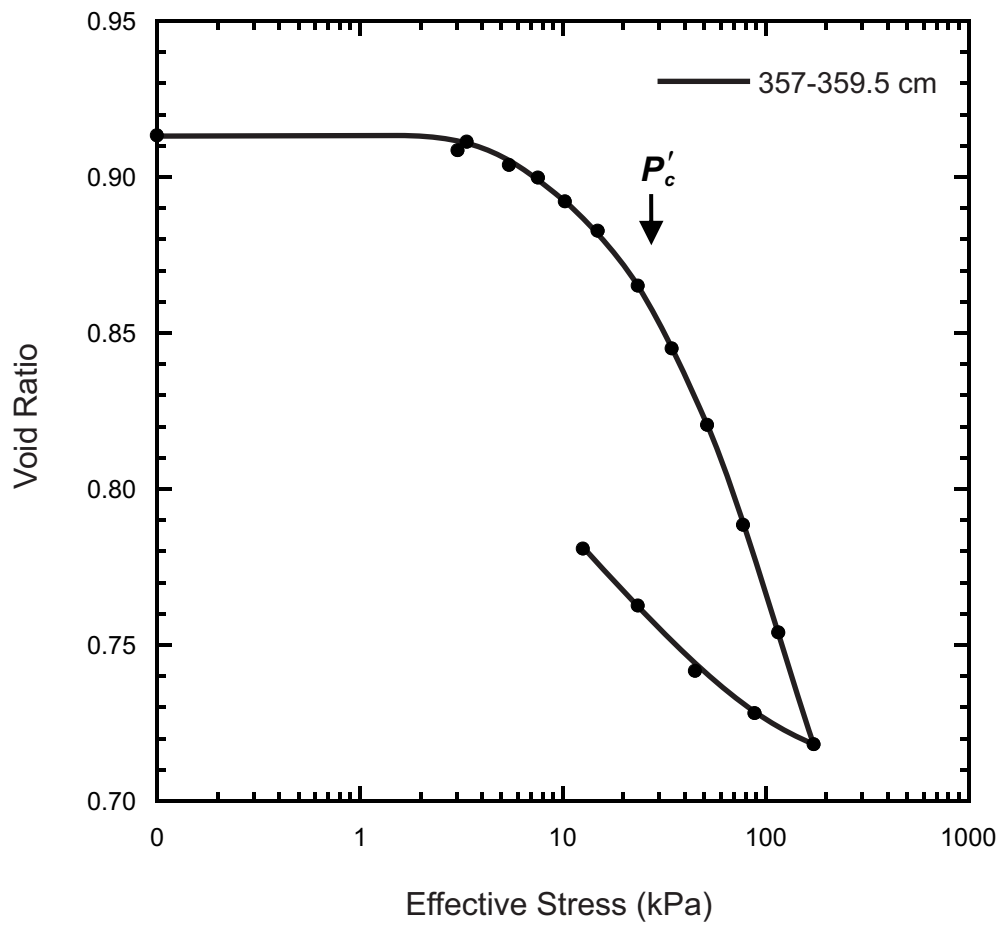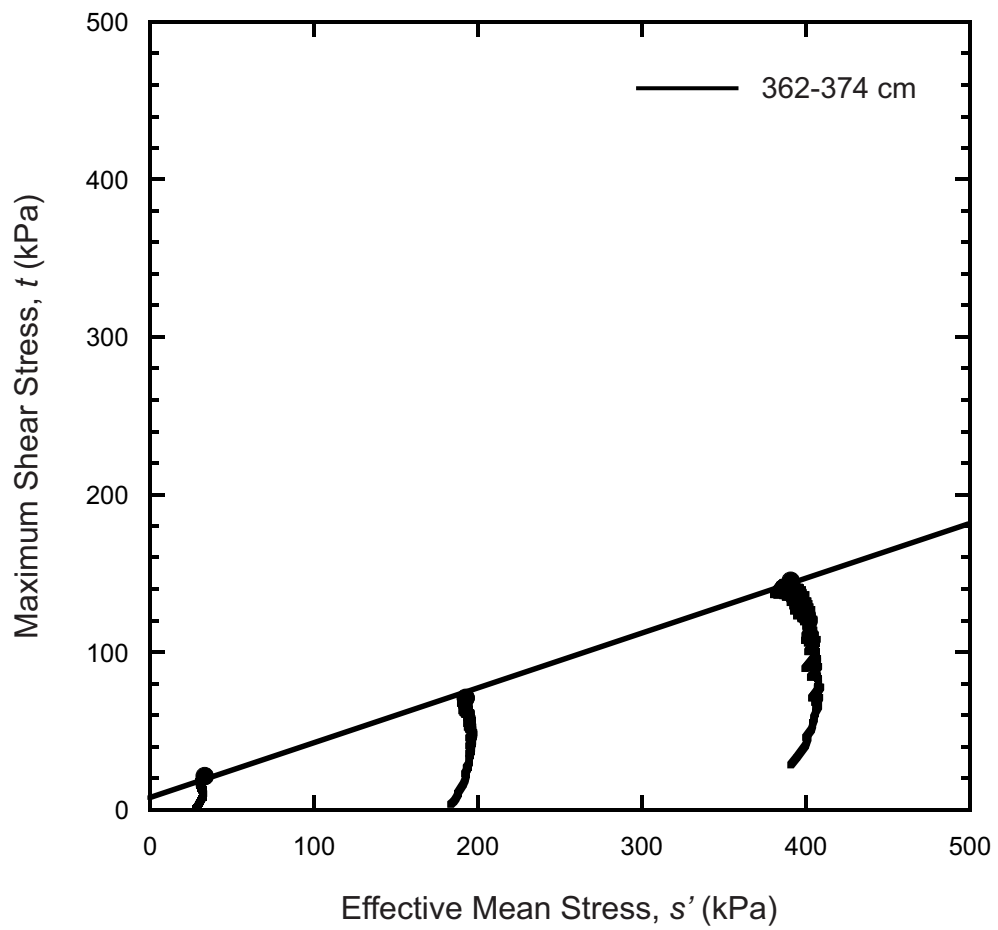
Figure 9.136. Consolidation plot for piston core 20148040011.

Figure 9.137. Stress paths and failure envelopes from triaxial test results for piston core 20148040011.

Figure 9.138. FS at various slope angles for piston core 20148040011. The minimum FS for the present-day slope angle of the core site is > 30.
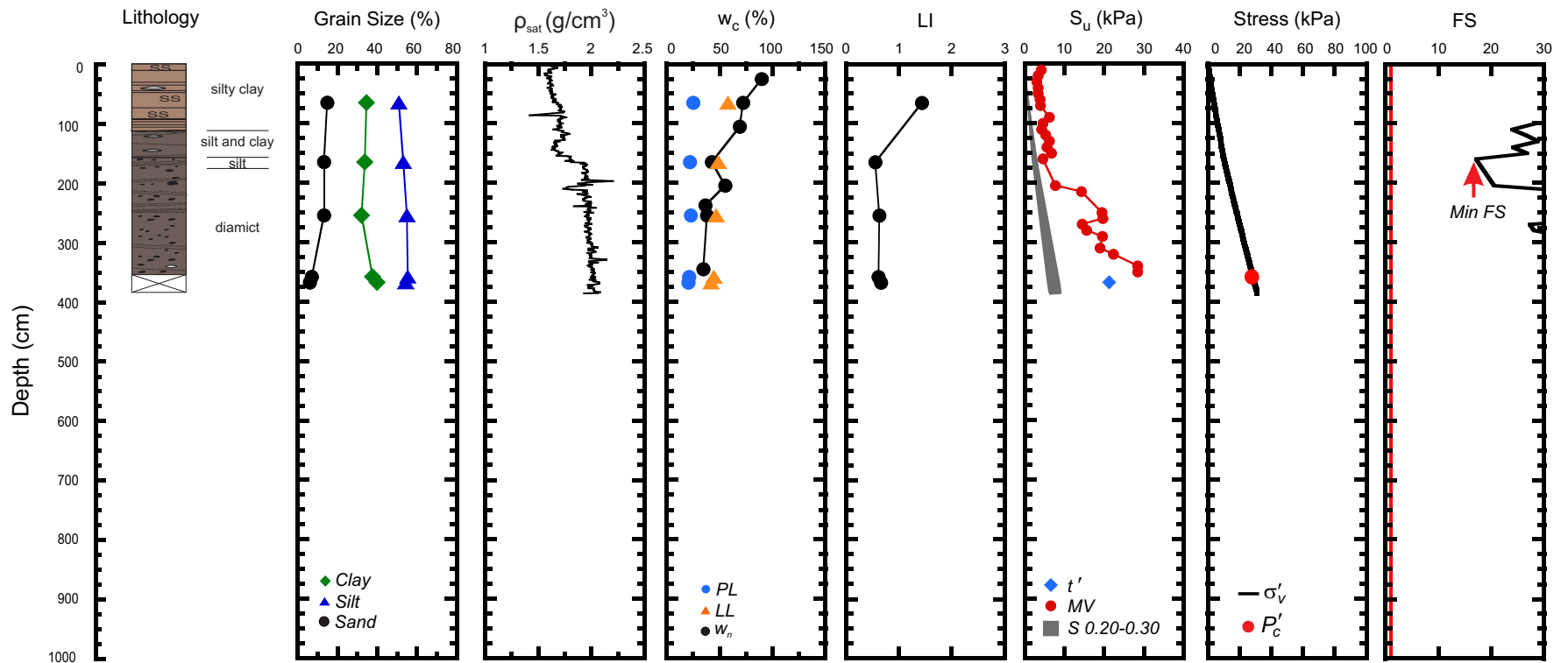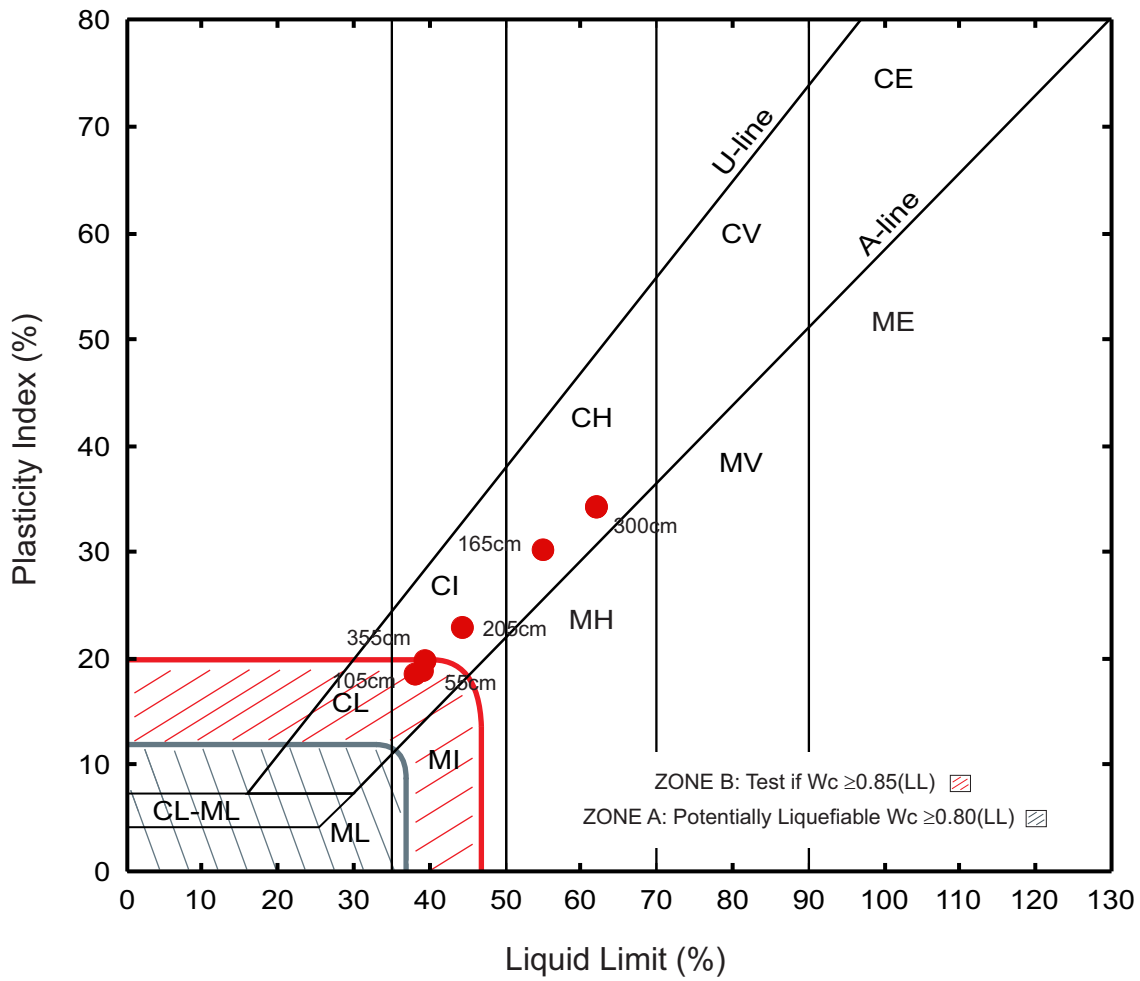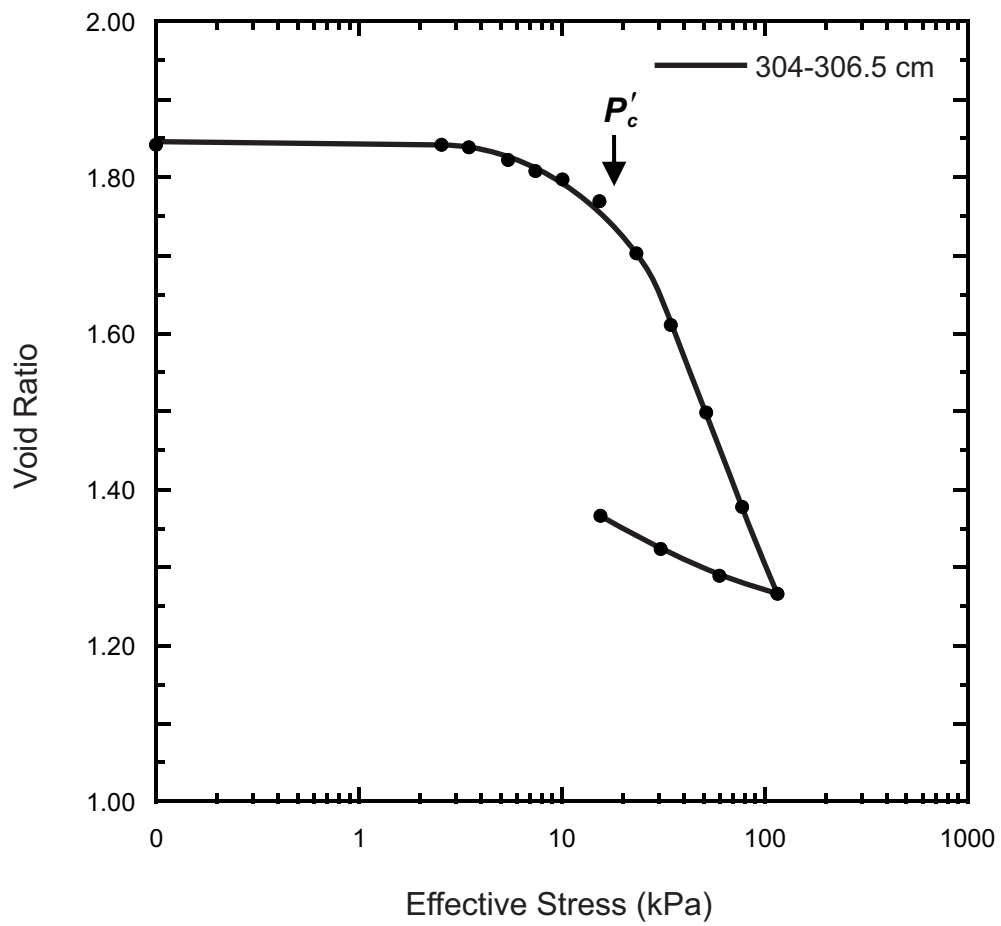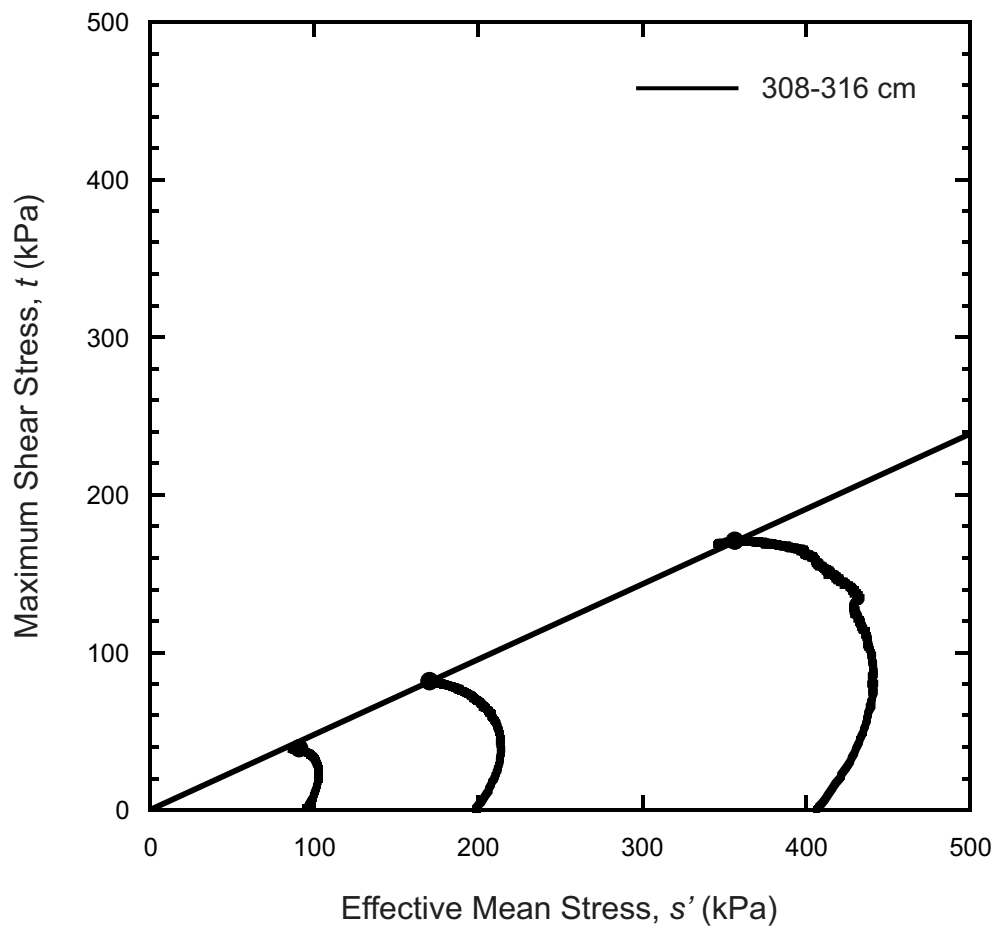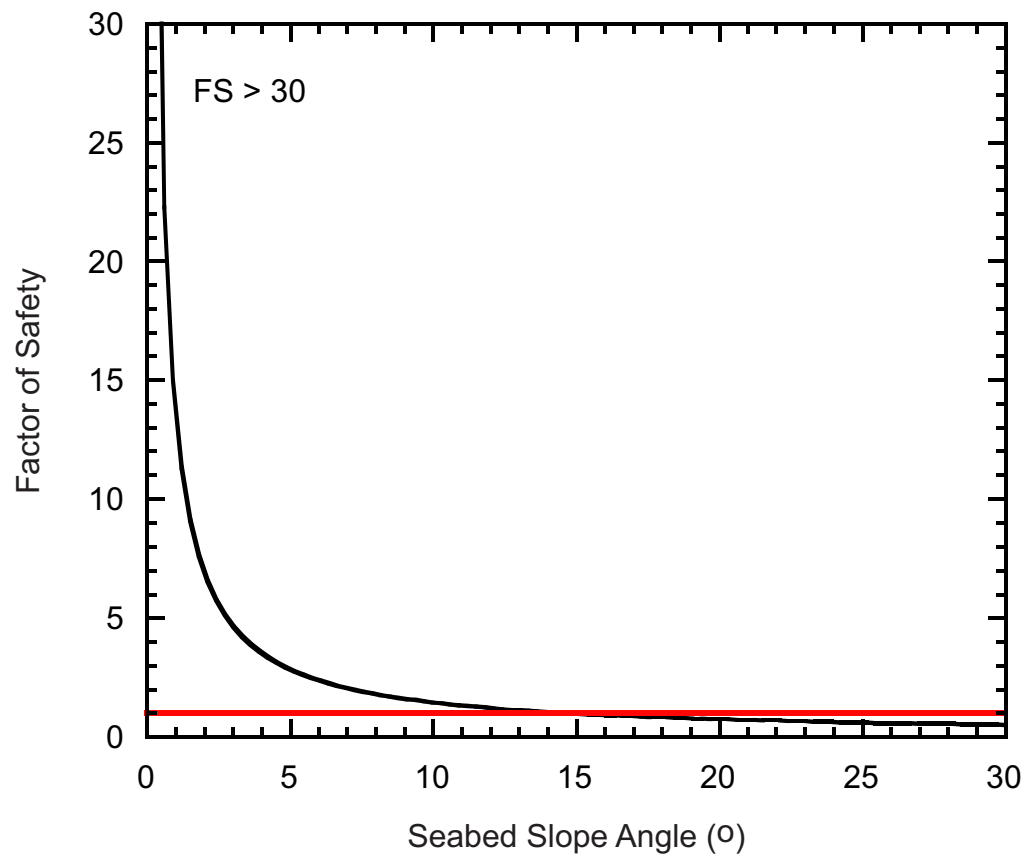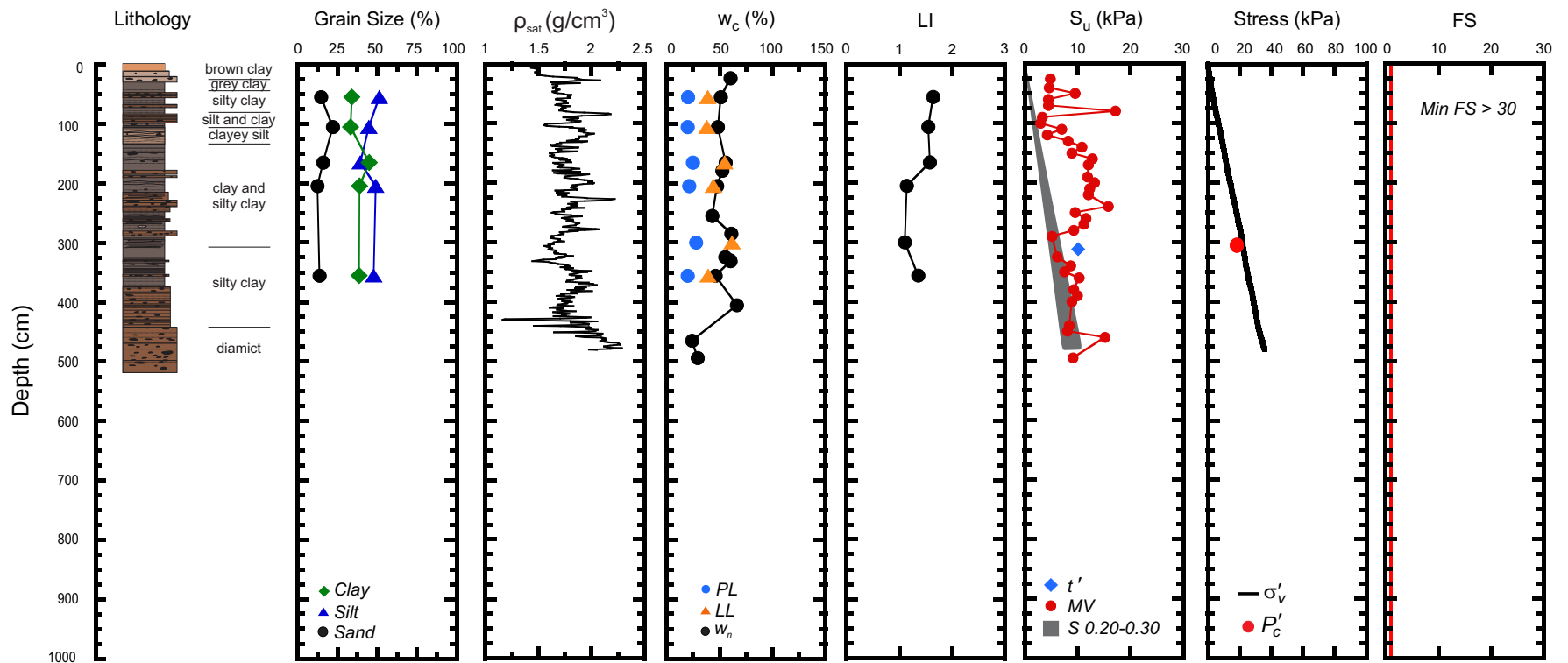
Figure 9.139. Geotechnical profile for core 20148040011 from the outer shelf West of Banks Island. (ρ_{sat}= saturated bulk density, w_c = water content, w_n = natural in-situ water content, PL = plastic limit, LL = liquid limit, LI = liquidity index, S_u = undrained shear strength, MV = laboratory miniature vane shear strength, t' = maximum shear stress, S = shear strength calculated from the normalized strength ratio, σ'_v = effective overburden stress, P'_c = past maximum stress, FS = factor of safety).

Figure 9.140. Plasticity chart showing Atterberg limit results of piston core 20168050013.

Figure 9.141. Consolidation plot for piston core 20168050013.
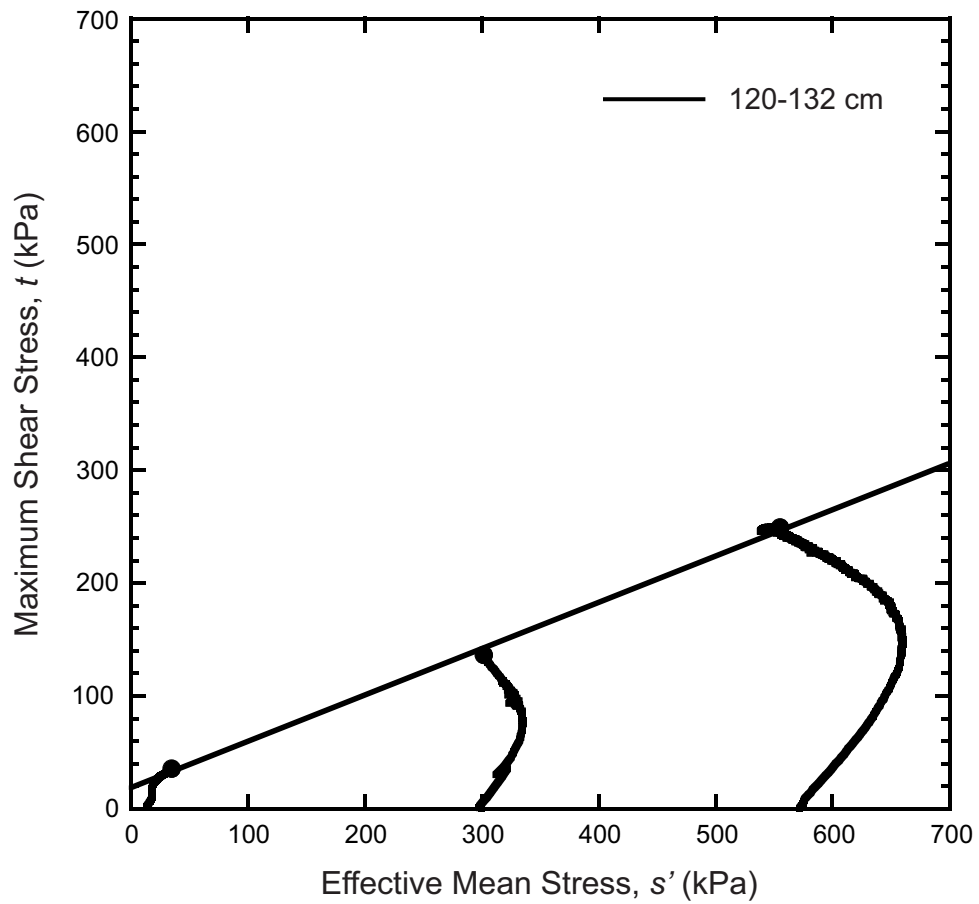
Figure 9.142. Stress paths and failure envelopes from triaxial test results for piston core 20168050013. Note the second shear stage was not included in the calculation of Mohr-Coulomb parameters.

Figure 9.143. Shear wave velocities at various confining pressures for piston core 20168050013.

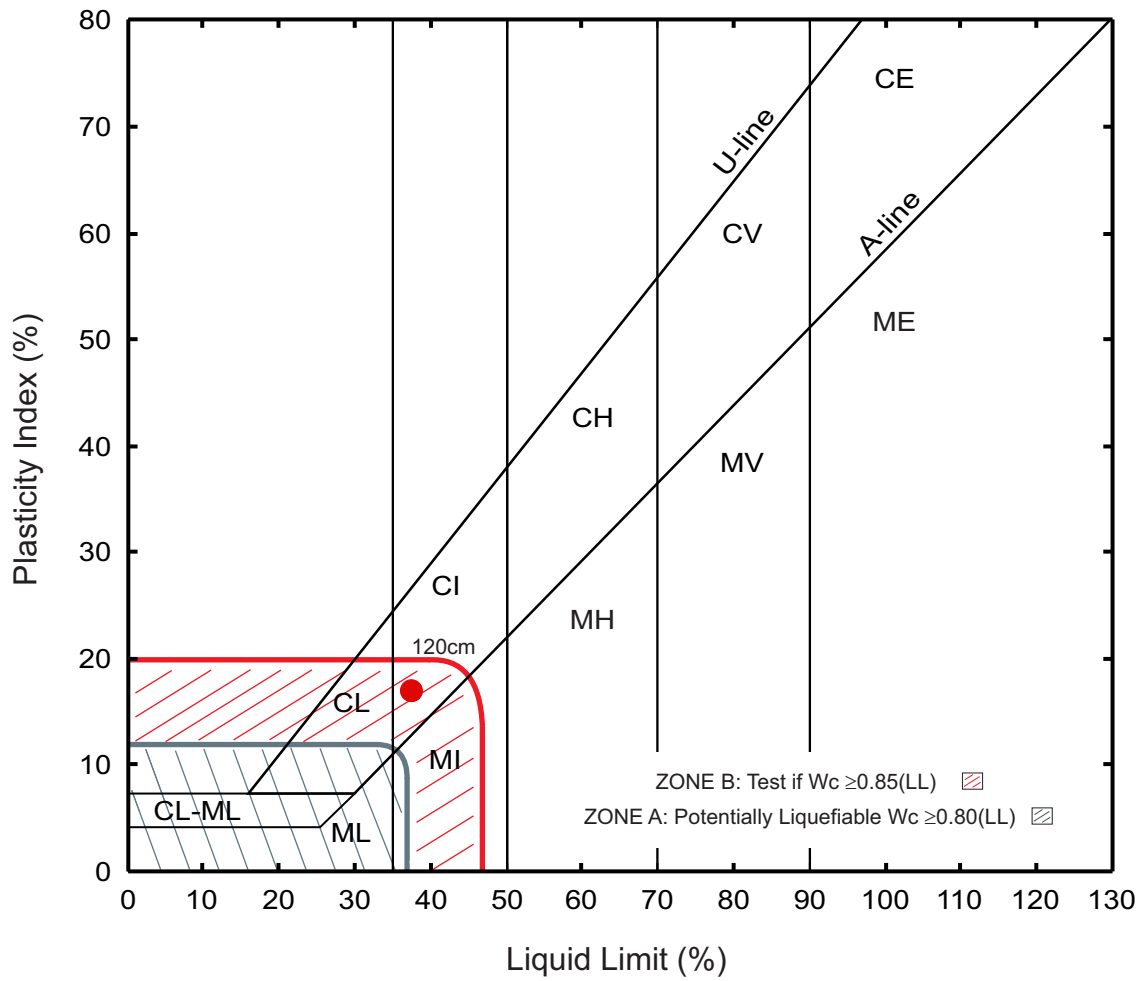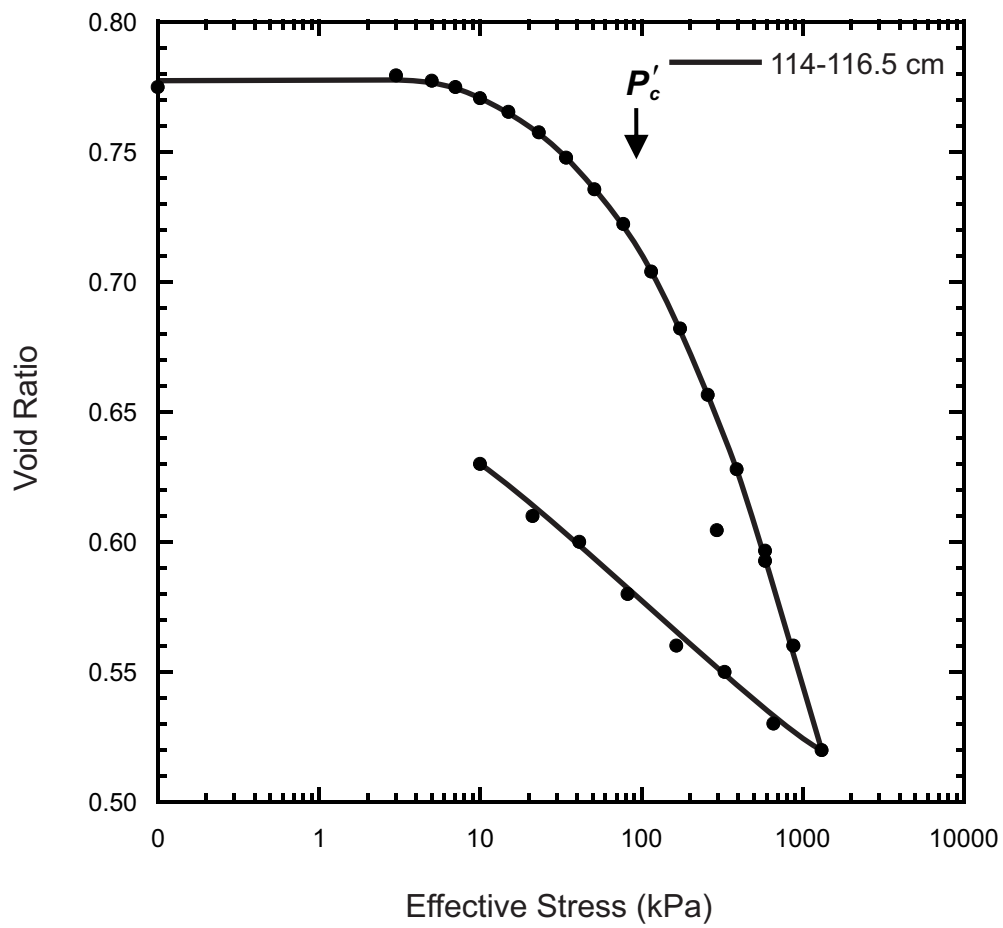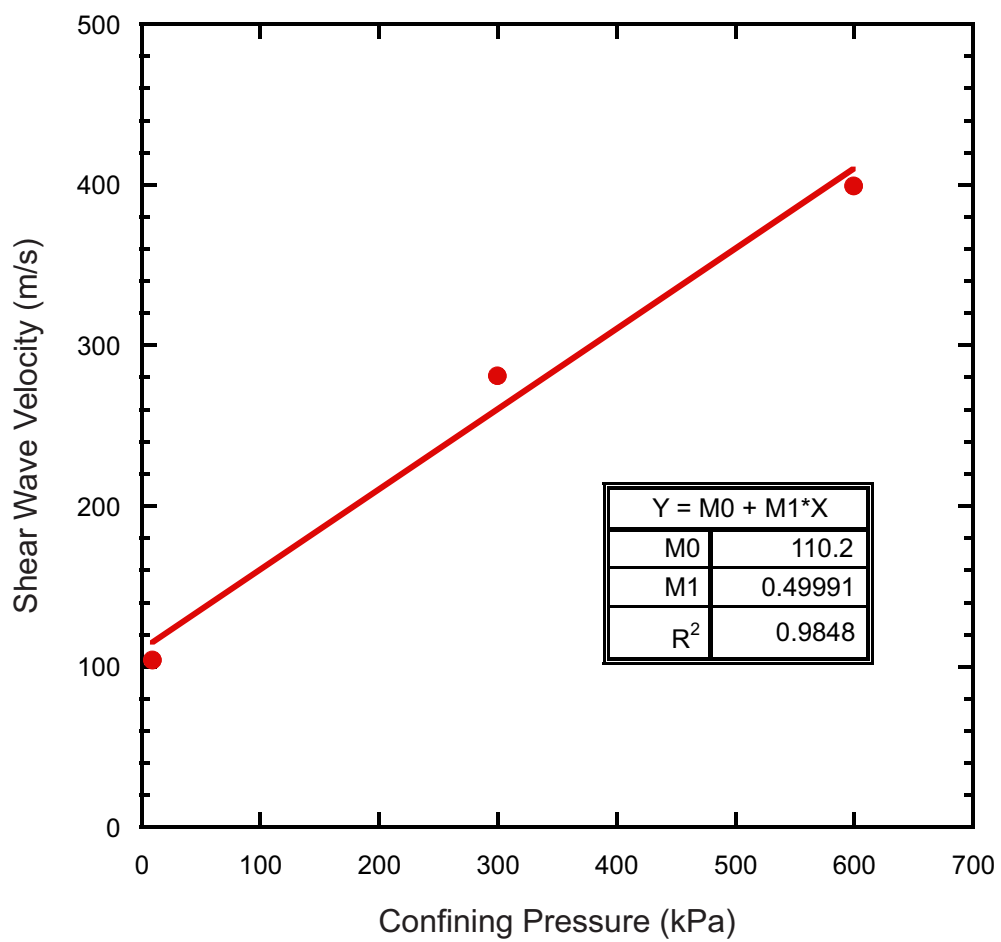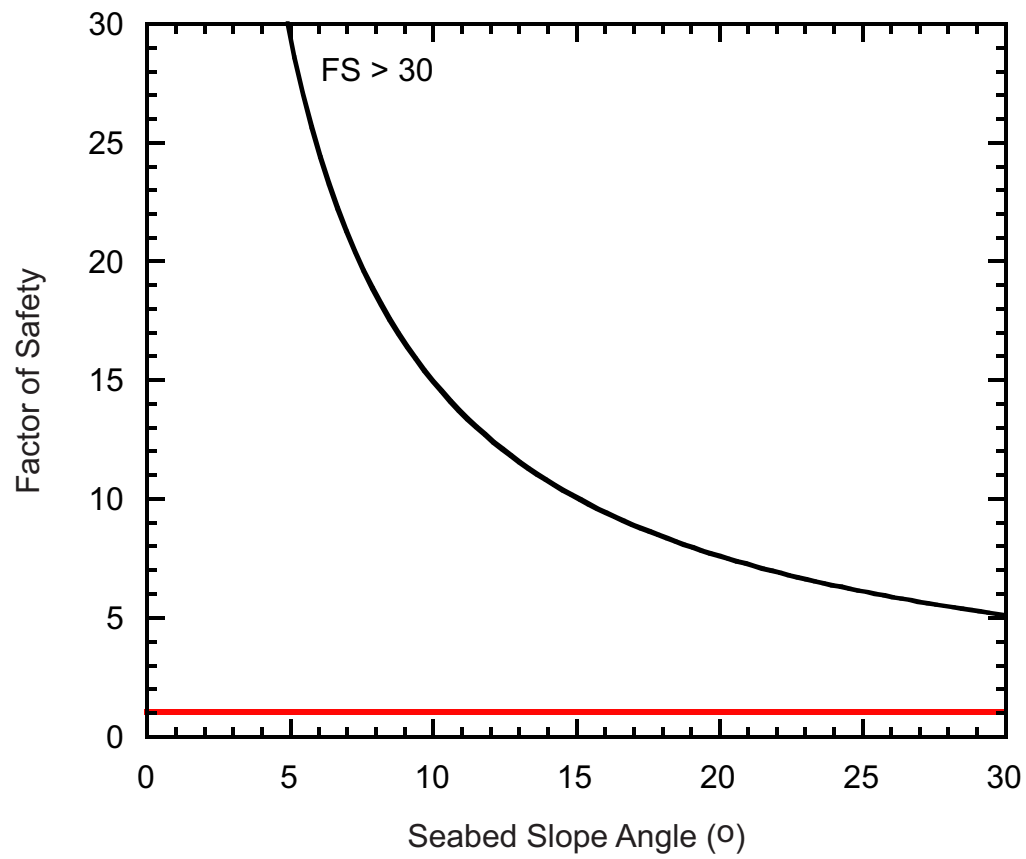Figure 9.144. FS at various slope angles for piston core 20168050013. The minimum FS for the present-day slope angle of the core site is > 30.
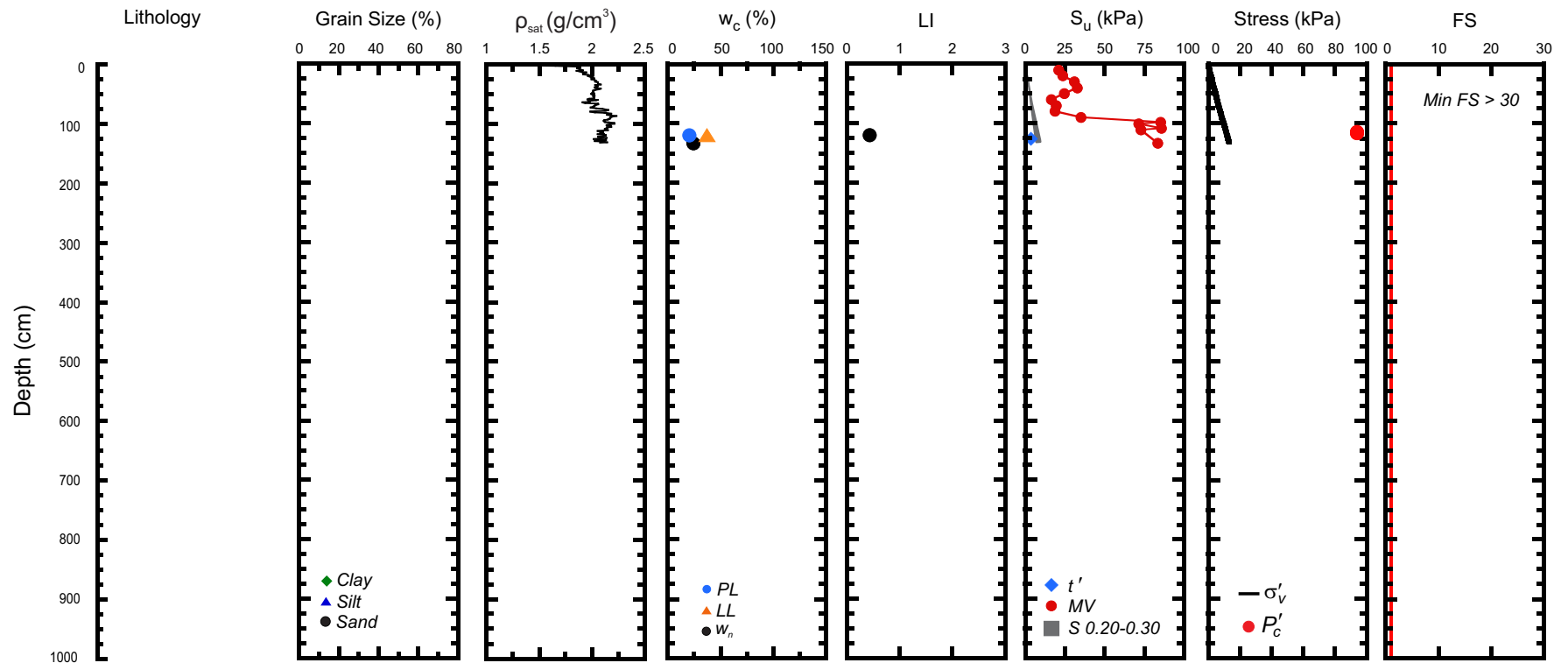
Figure 9.145. Geotechnical profile for core 20168050013 from the shelf west of Banks Island. (ρ_{sat}= saturated bulk density, w_c = water content, w_n = natural in-situ water content, PL = plastic limit, LL = liquid limit, LI = liquidity index, S_u = undrained shear strength, MV = laboratory miniature vane shear strength, t' = maximum shear stress, S = shear strength calculated from the normalized strength ratio, σ'_v = effective overburden stress, P'_c = past maximum stress, FS = factor of safety).

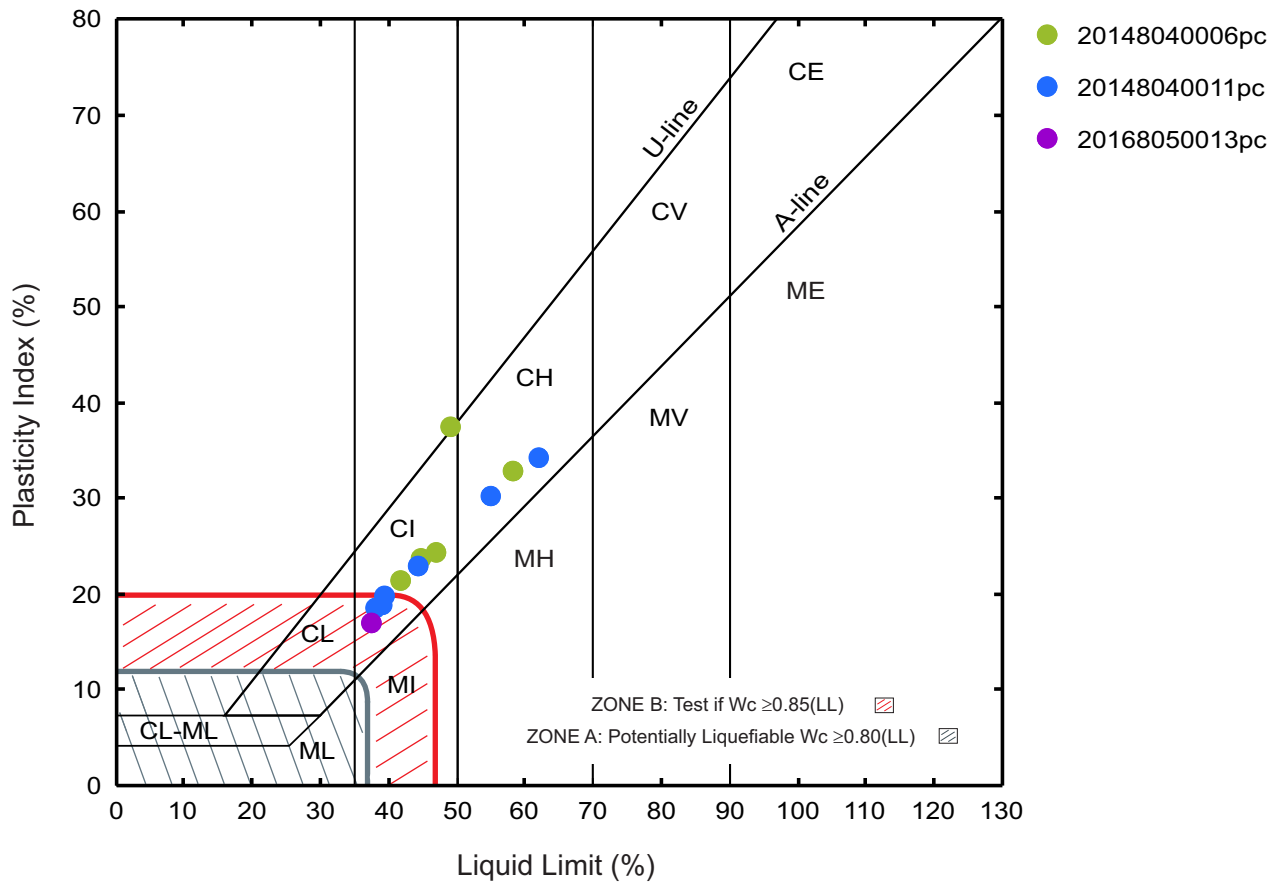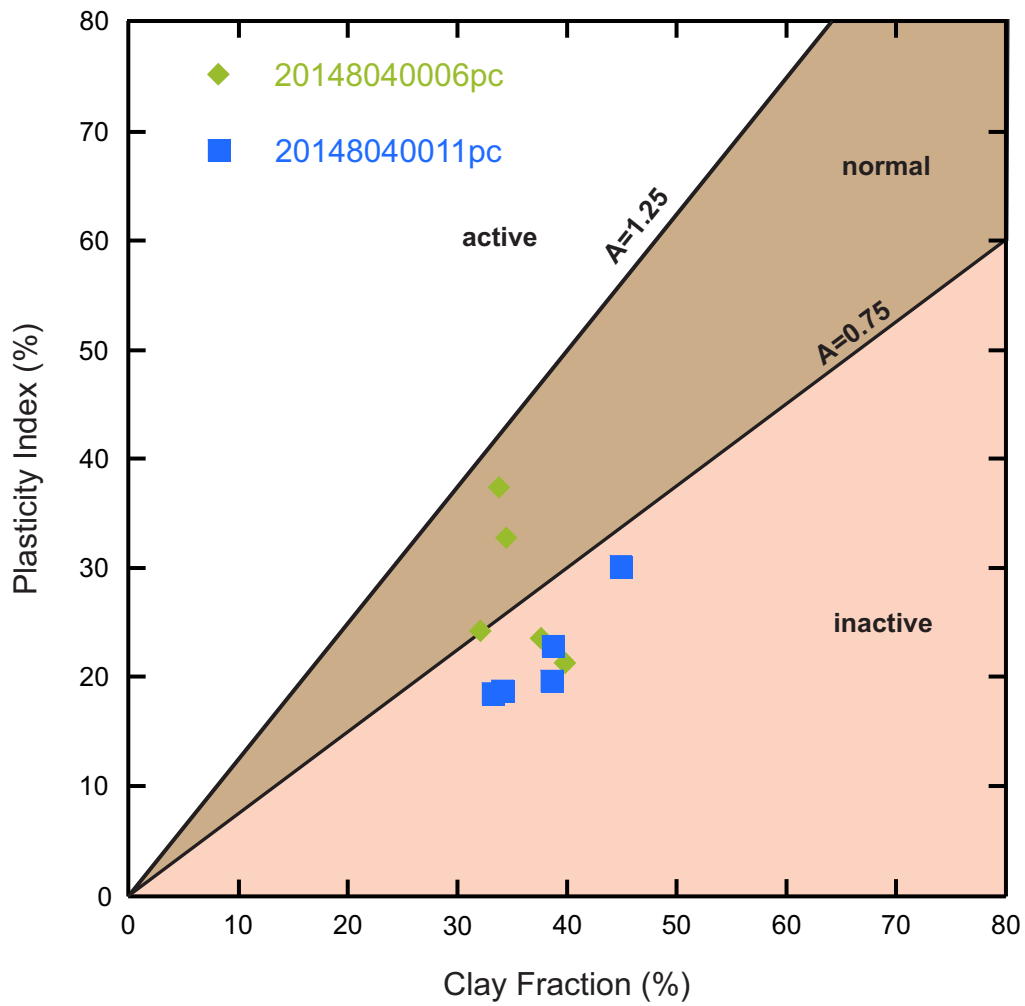Figure 9.146. Plasticity chart showing Atterberg limit results of cores in Region 4.

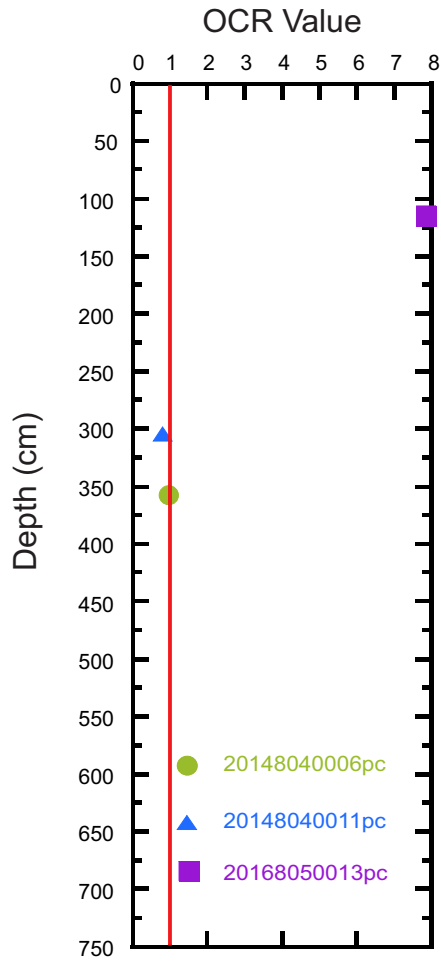Figure 9.147. Region 4 activity chart.

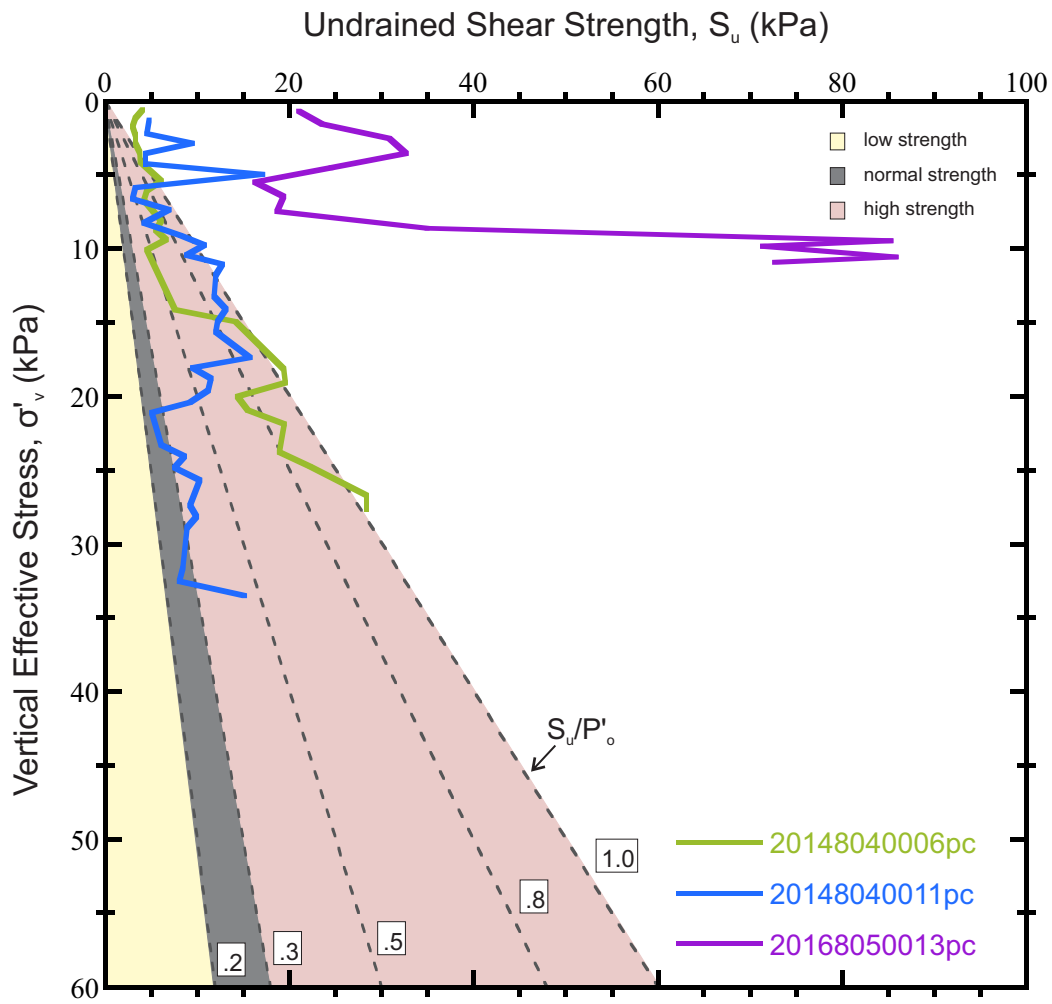Figure 9.148. OCR values with depth for consolidation tests in Region 4.

Figure 9.149. Shear strength profiles with effective overburden pressure of cores in Region 4.
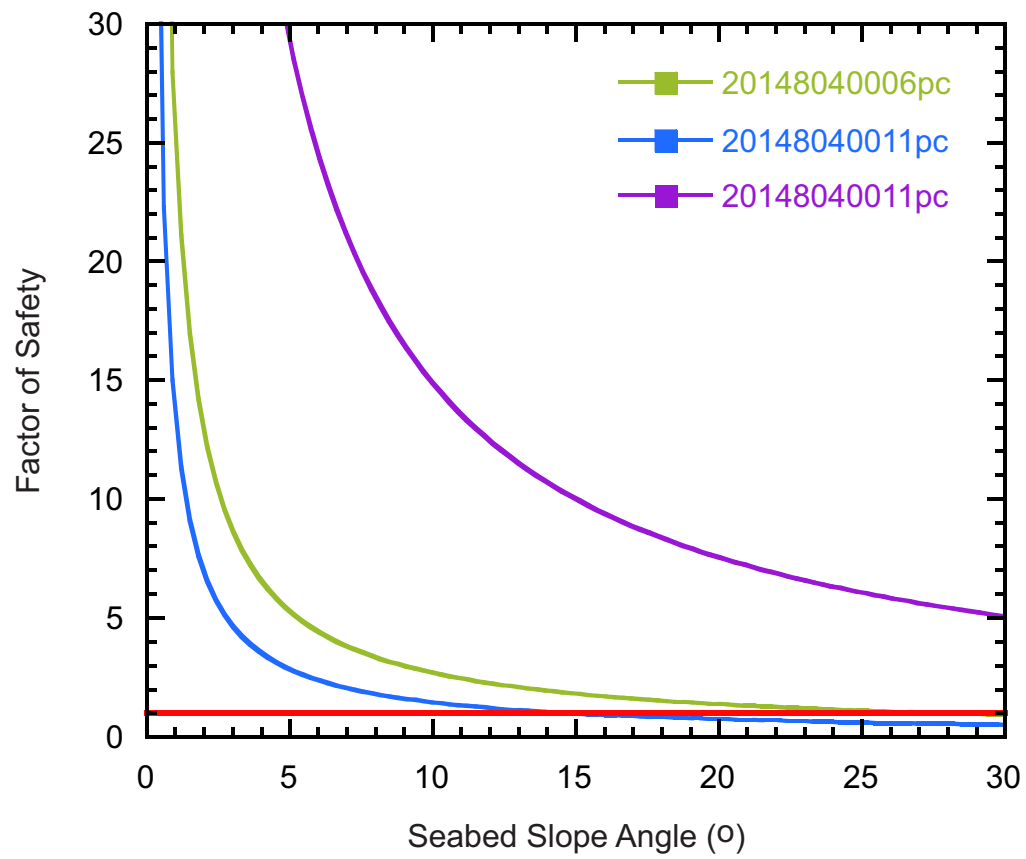
Figure 9.150. FS at various slope angles for piston cores in Region 4.
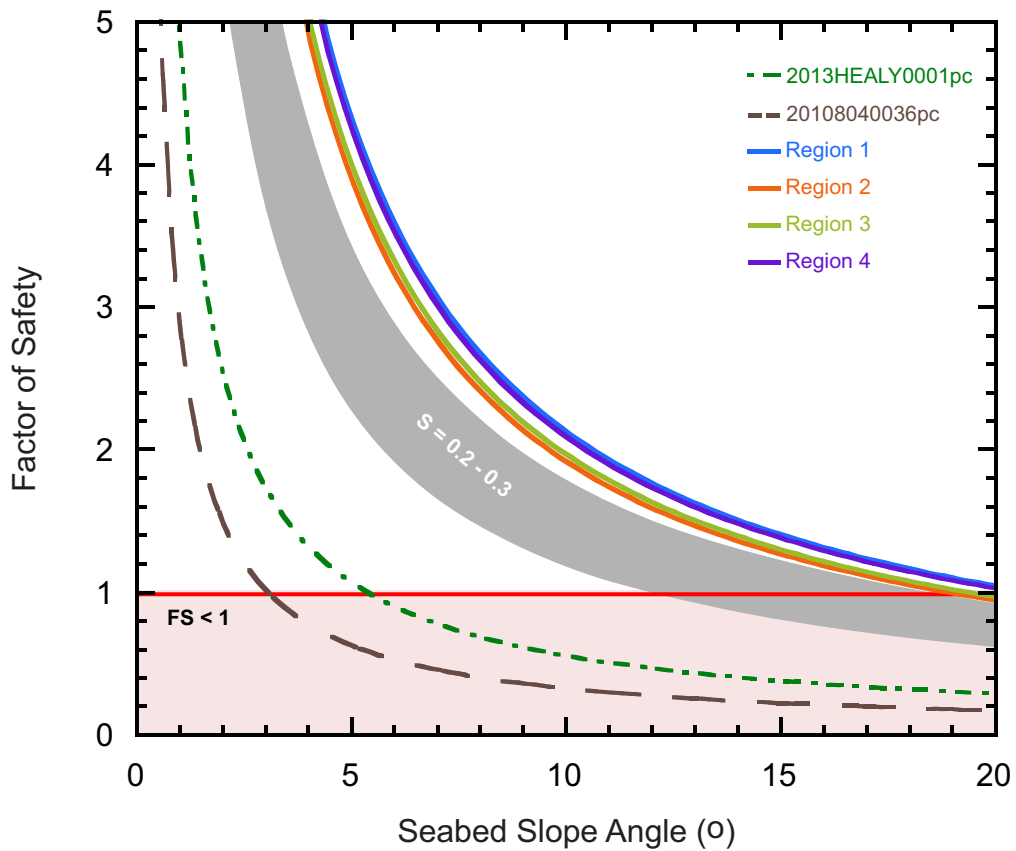
Figure 10.1. Slope stability analysis under gravitational loading using total and (TSA) and effective stress analysis (ESA). *FS* is calculated using the minimum ϕ' for each region to estimate S_u at various slope angles (*soils lines*). 2) *FS* calculated for sediment were S_u/ϕ' 0.2 and 0.3 (*grey-shaded area*). *FS* is calculated using MV measurements for cores 2013HEALY0001pc & 20108040036pc. The red-shaded area indicates where the slope becomes unstable (*FS* < 1).

Figure 10.2. Location map of all regions with historical earthquakes epicenters.

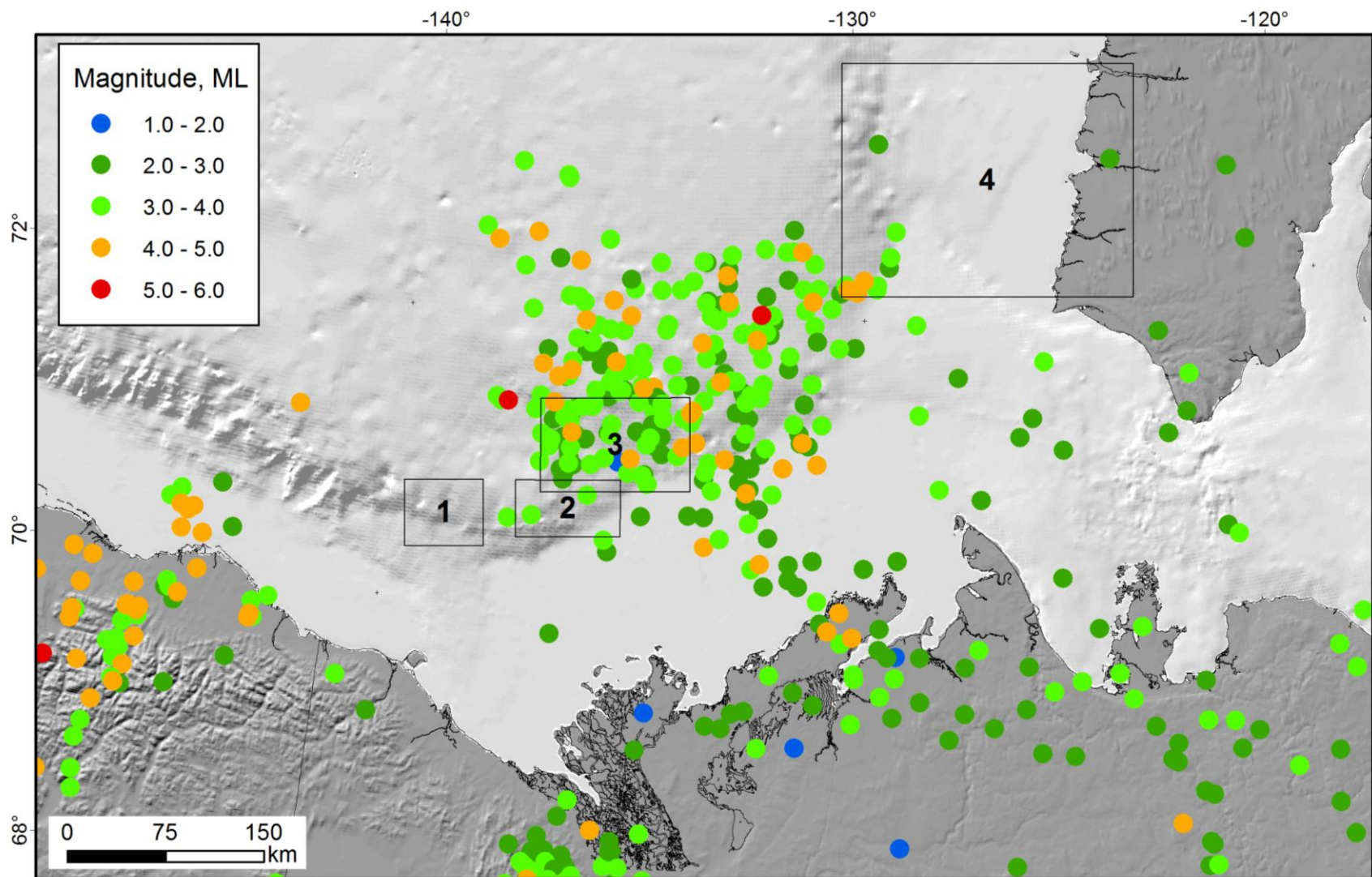Figure 10.3a. Calculated distance from fault capable of triggering slope failures in Region 1, as a function of slope angle and earthquake moment magnitude. Parameters used (average): V_{s30} = 126.4 m/s, S = 0.26, γ'/γ = 0.36, GMPEs of Boore et al (1997).

Figure 10.3b. Calculated distance from fault capable of triggering slope failures in Region 1, as a function of slope angle and earthquake moment magnitude. Parameters used (maximun): V_{s30} = 147.2 m/s, S = 0.28, γ'/γ = 0.38, GMPEs of Boore et al (1997).
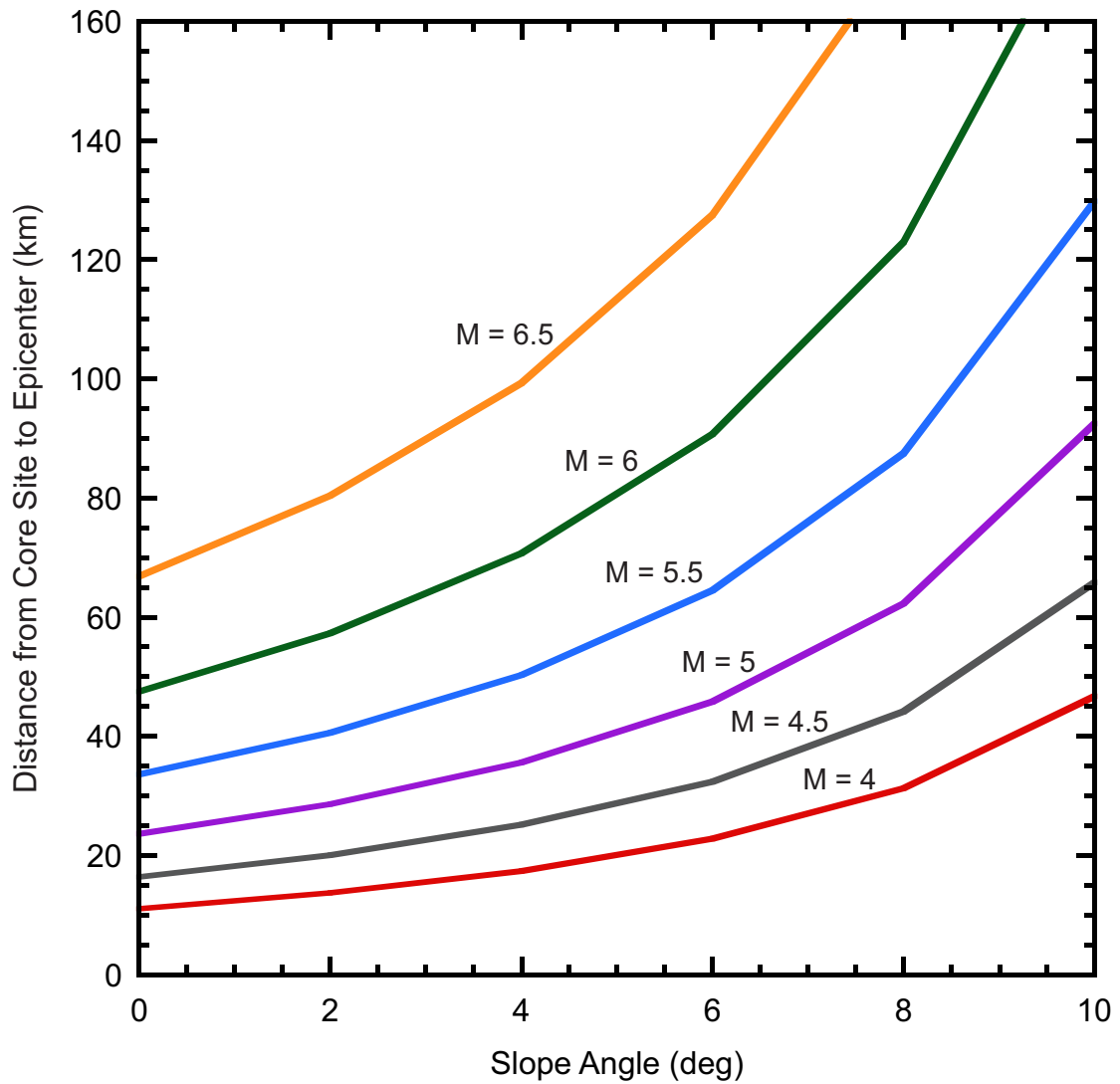
Figure 10.3c. Calculated distance from fault capable of triggering slope failures in Region 1, as a function of slope angle and earthquake moment magnitude. Parameters used (minimum): V_{s30} = 105.5 m/s, S = 0.23, γ'/γ = 0.34, GMPEs of Boore et al (1997).
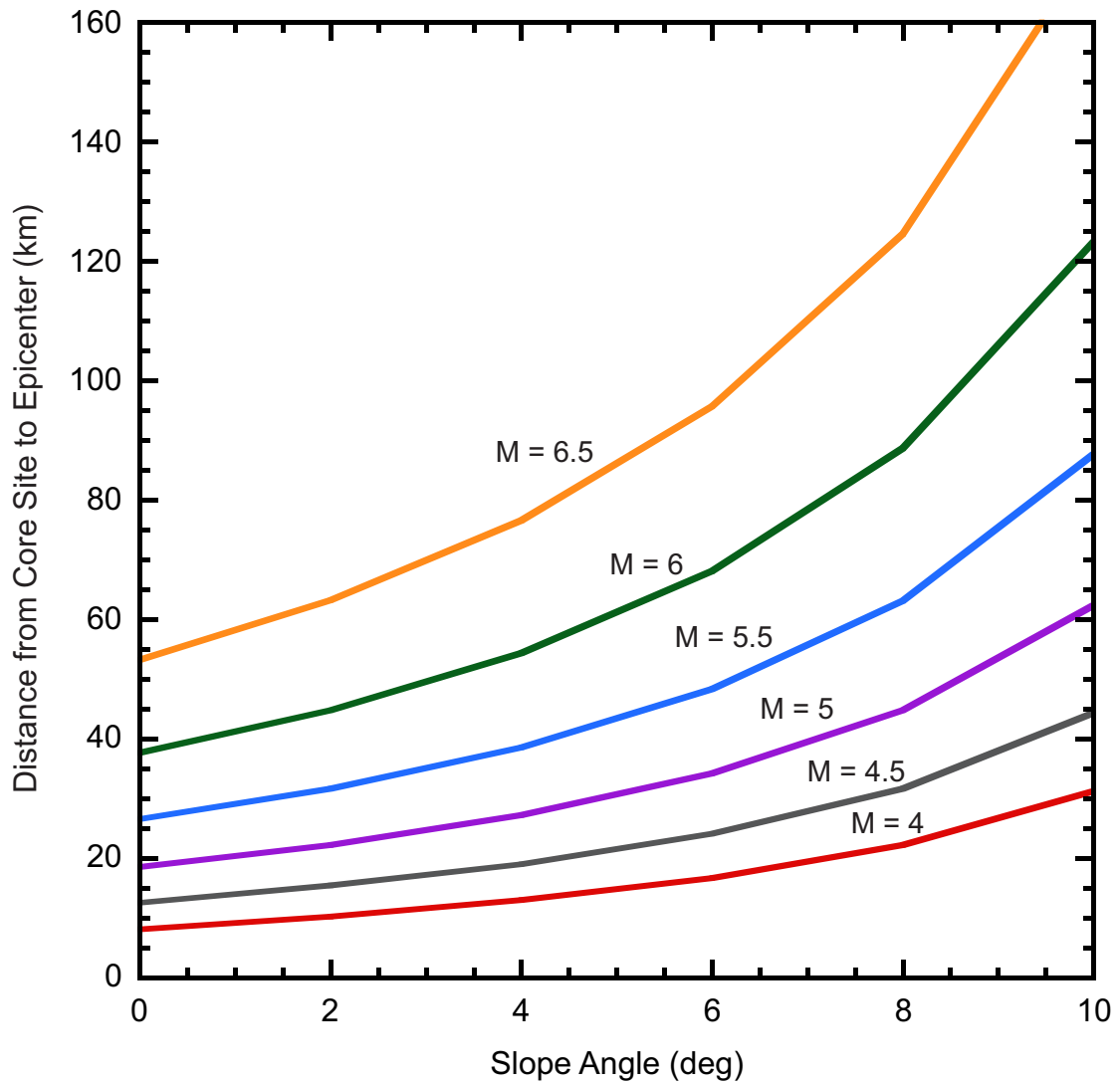
Figure 10.4a. Calculated distance from fault capable of triggering slope failures in Region 2, as a function of slope angle and earthquake moment magnitude. Parameters used (average): $V_{s30} = 124.3$ m/s, $S = 0.26$, $\gamma'/\gamma = 0.37$, GMPEs of Boore et al (1997).
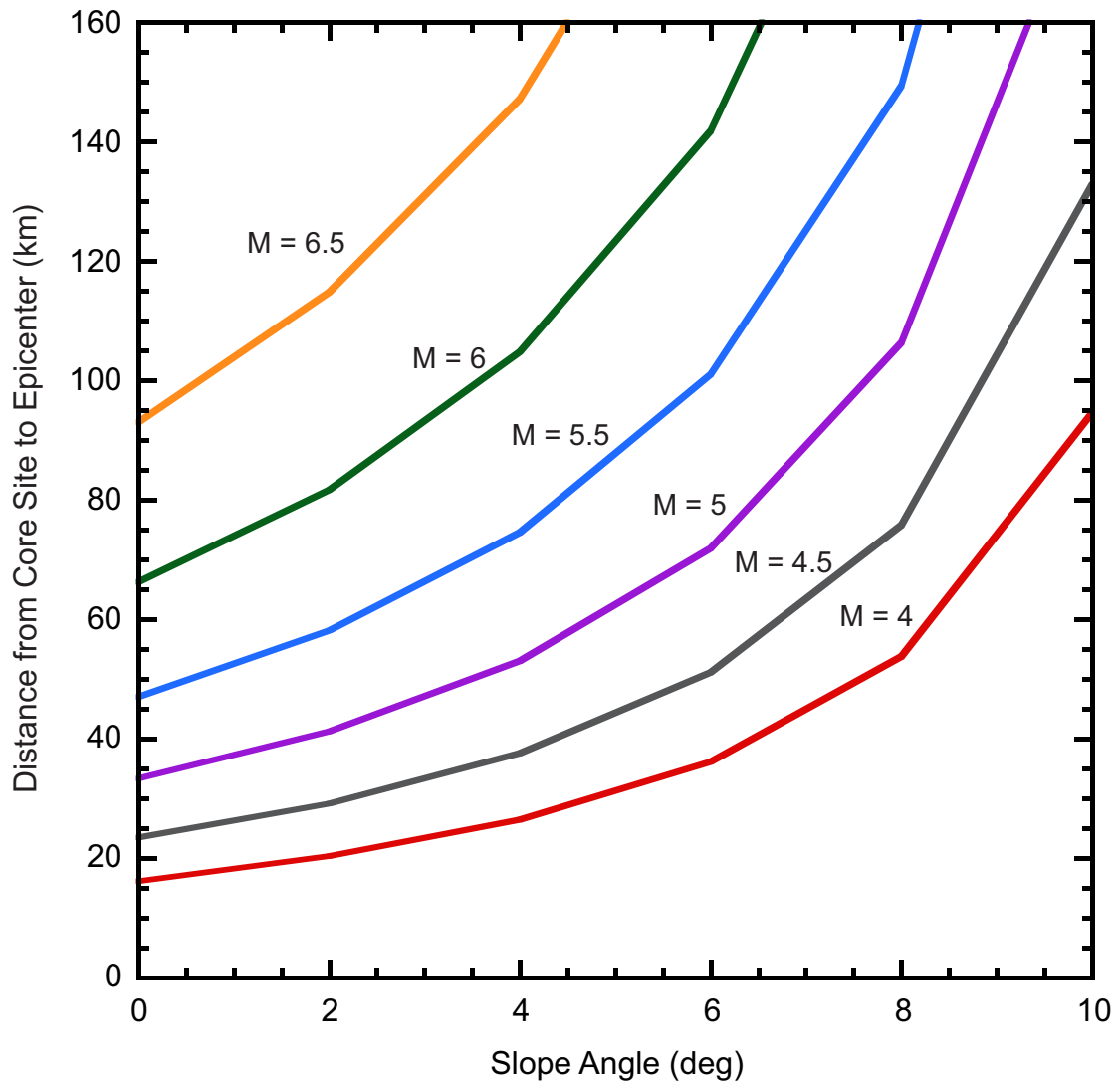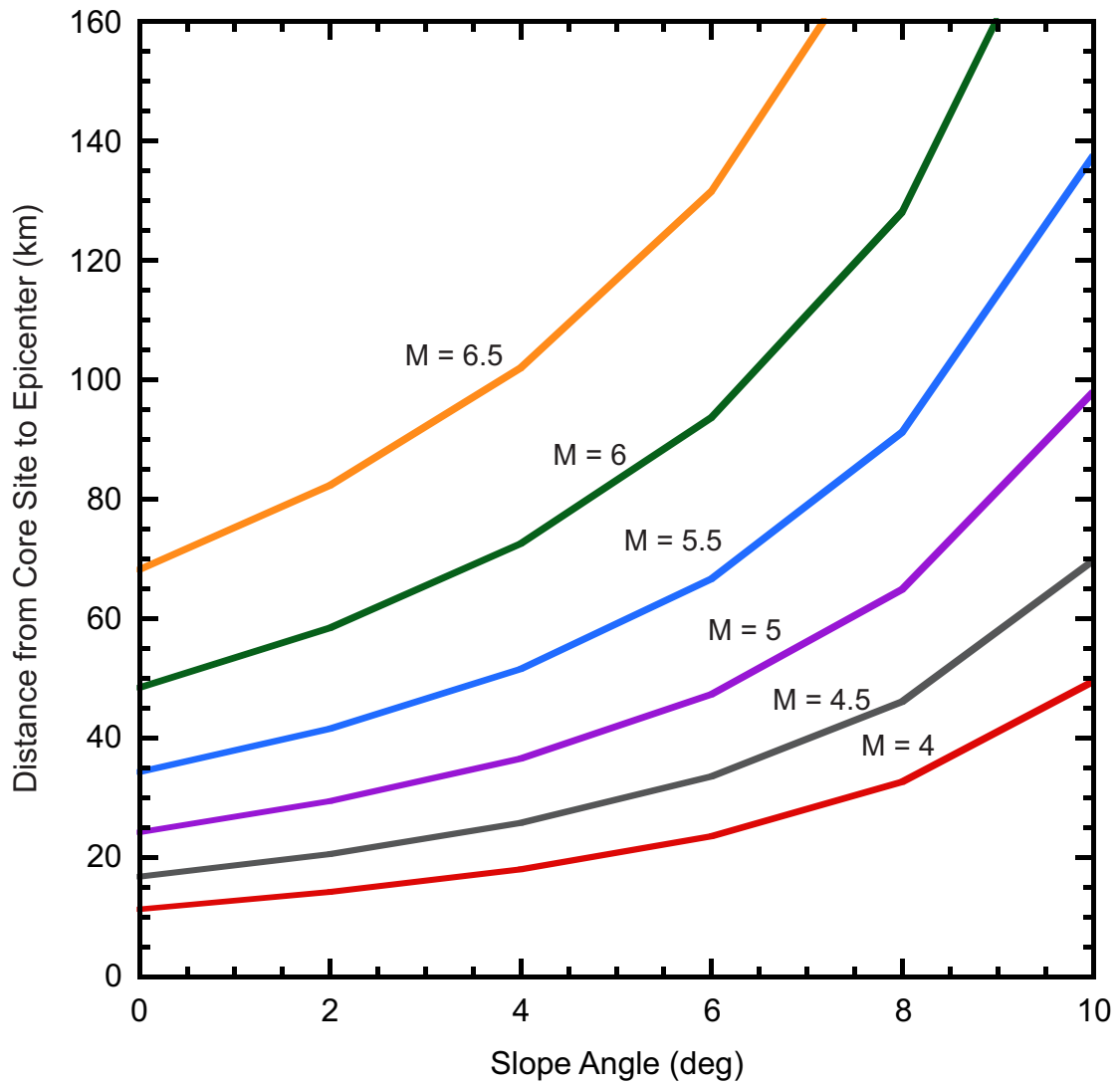
Figure 10.4b. Calculated distance from fault capable of triggering slope failures in Region 2, as a function of slope angle and earthquake moment magnitude. Parameters used (maximum): V_{s30} = 185.8 m/s, S = 0.29, γ'/γ = 0.41, GMPEs of Boore et al (1997).

Figure 10.4c. Calculated maximum distance from fault capable of triggering slope failures in Region 2, as a function of slope angle and earthquake moment magnitude. Parameters used (minimum): V_{s30} = 101.5 m/s, S = 0.22, γ'/γ = 0.32, GMPEs of Boore et al (1997).
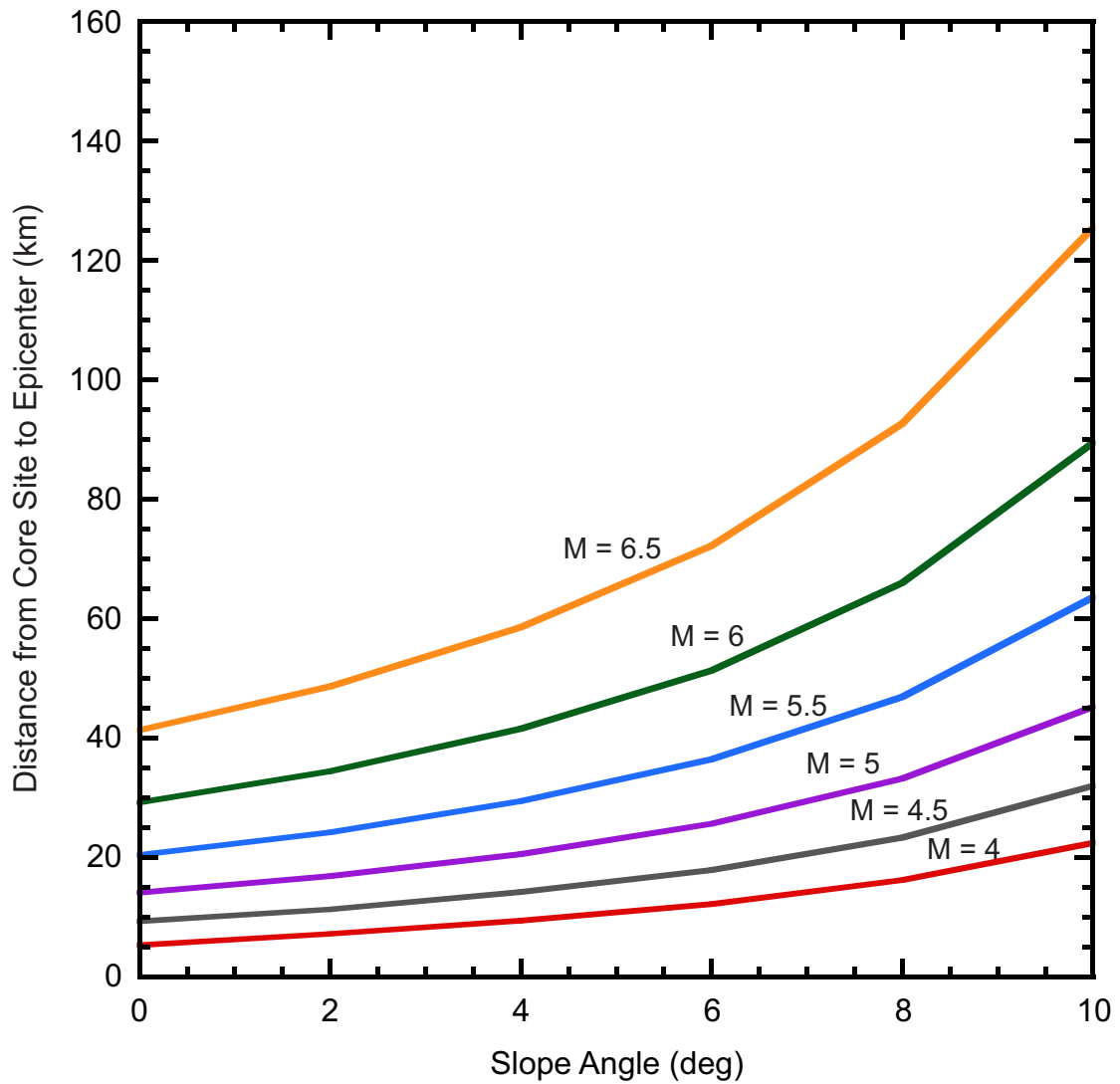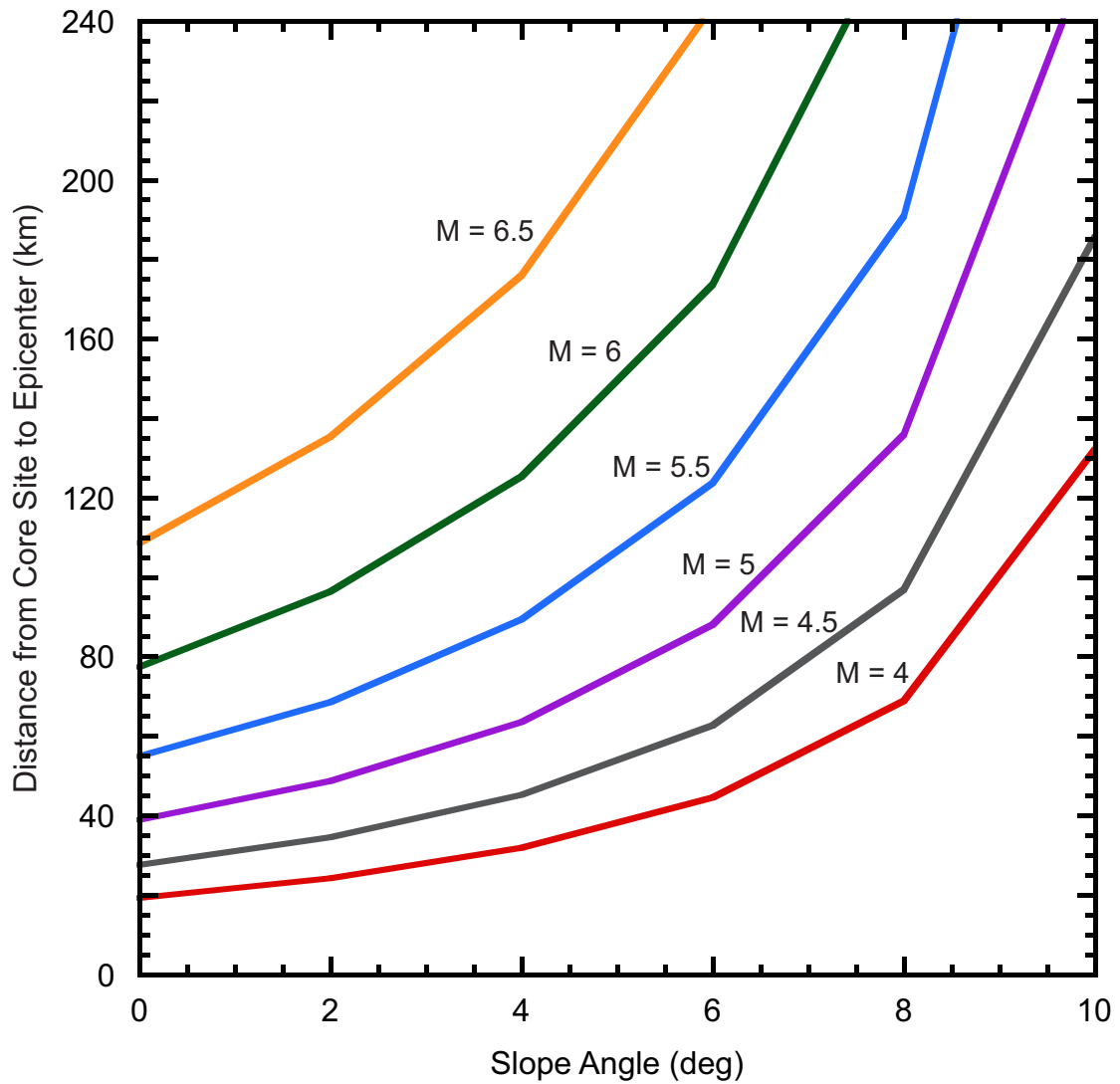
Figure 10.5a. Calculated distance from fault capable of triggering slope failures in Region 3, as a function of slope angle and earthquake moment magnitude. Parameters used (average): V_{s30} = 189.0 m/s, S = 0.27, γ'/γ = 0.42, GMPEs of Boore et al (1997).
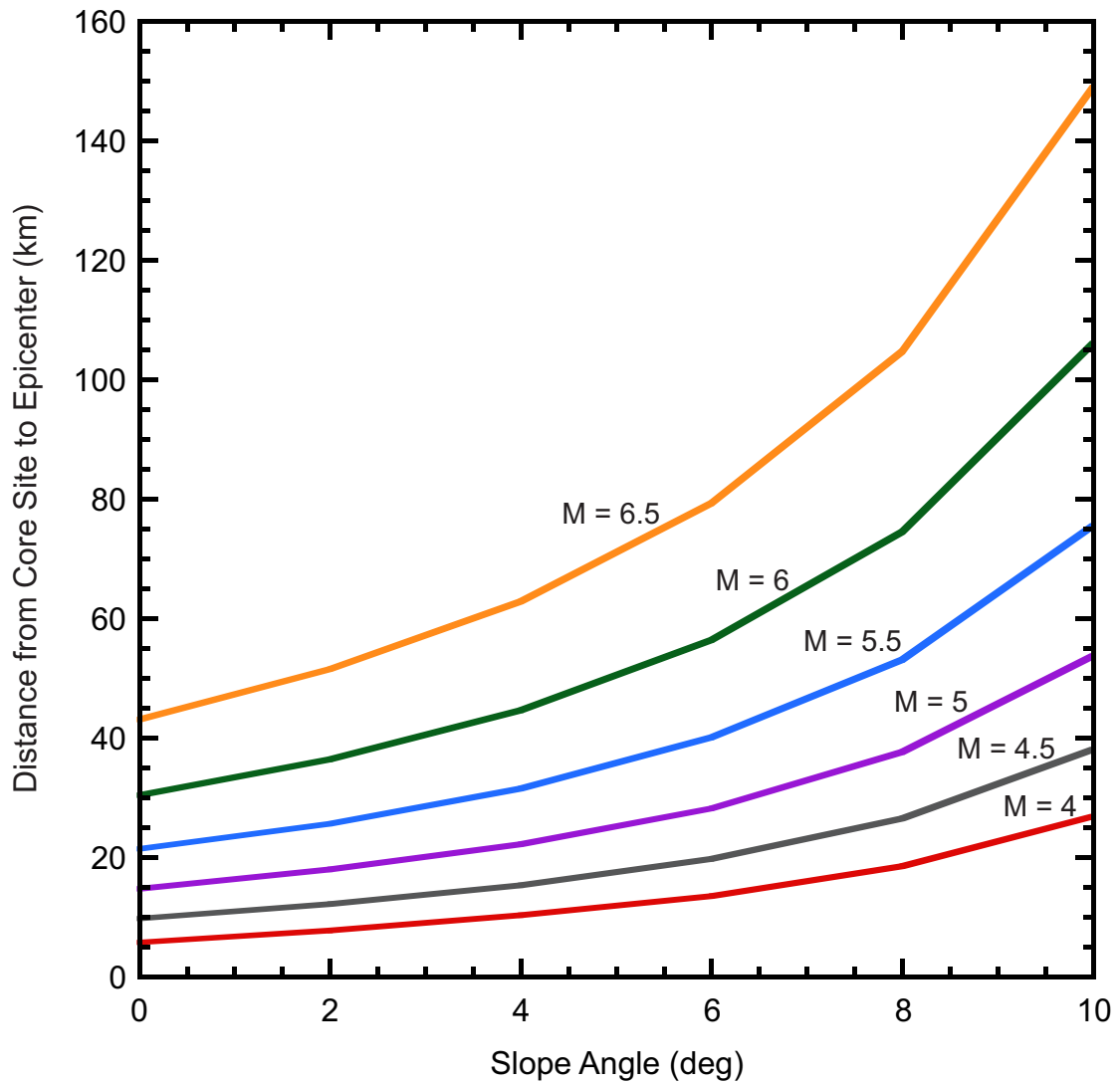
Figure 10.5b. Calculated distance from fault capable of triggering slope failures in Region 3, as a function of slope angle and earthquake moment magnitude. Parameters used (maximum): $V_{s30} = 227.2$ m/s, $S = 0.34$, $\gamma'/\gamma = 0.47$, GMPEs of Boore et al (1997).
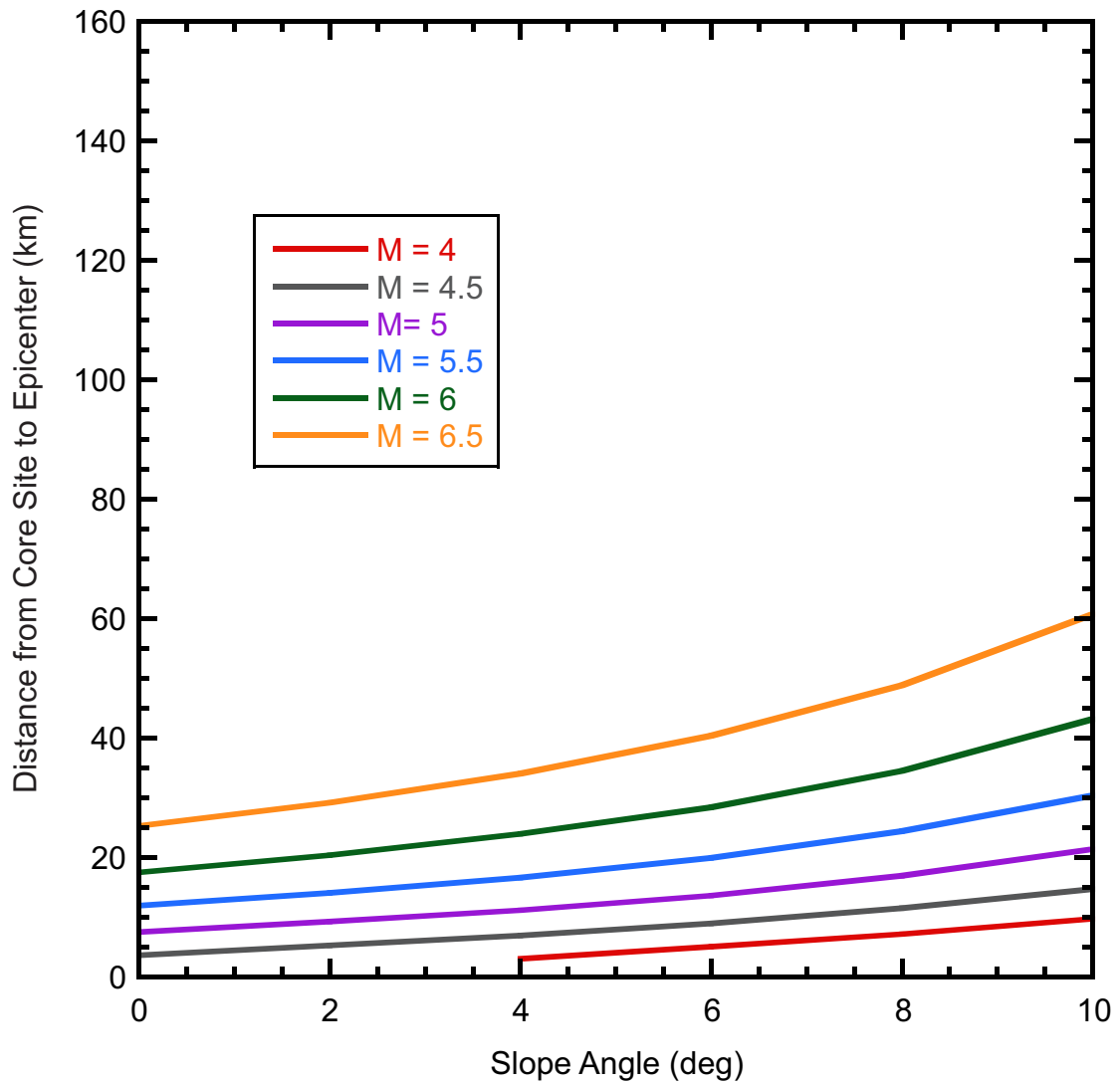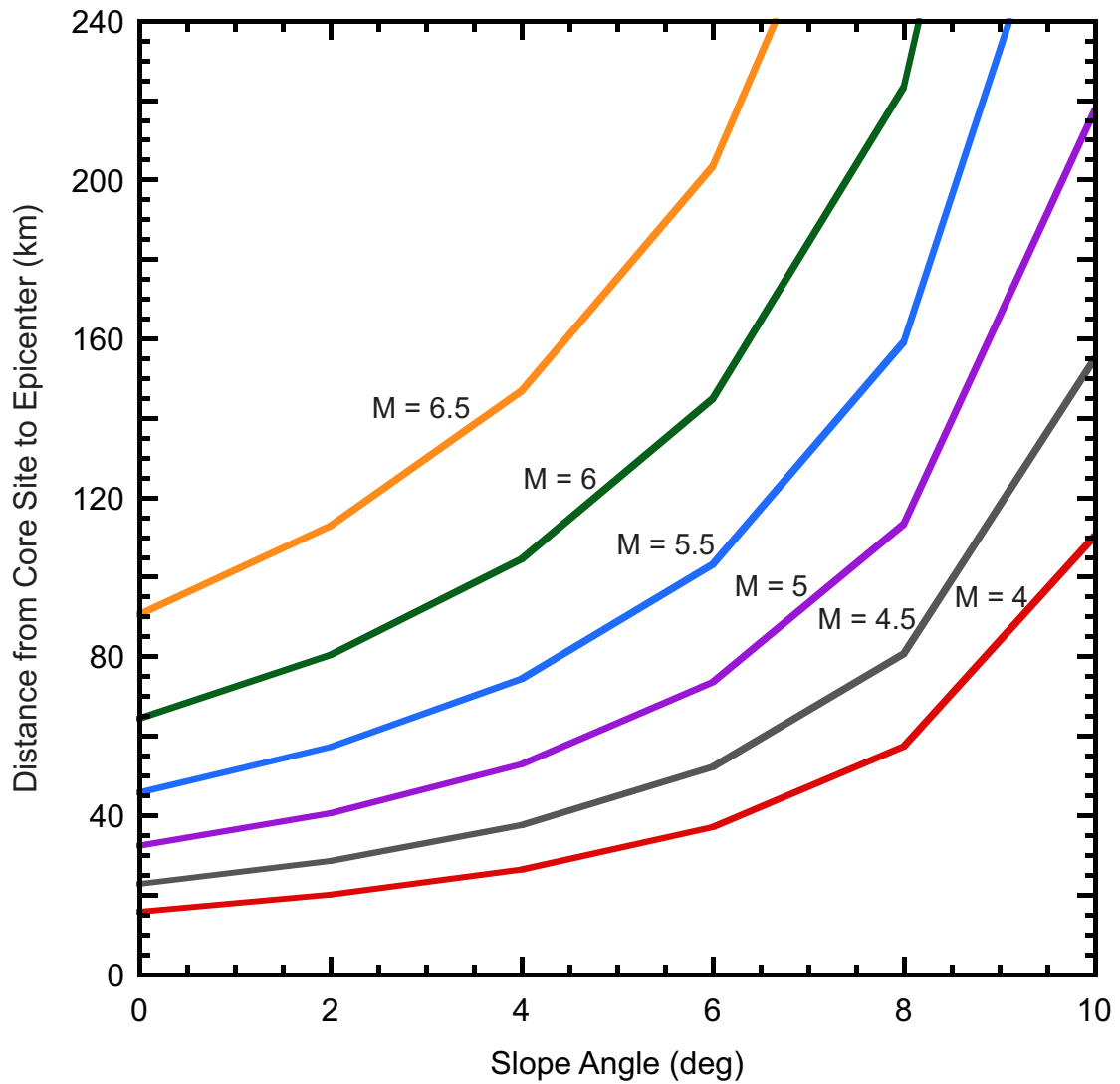
Figure 10.5c. Calculated distance from fault capable of triggering slope failures in Region 3, as a function of slope angle and earthquake moment magnitude. Parameters used (minimum): $V_{s30} = 148.3$ m/s, $S = 0.22$, $\gamma'/\gamma = 0..32$, GMPEs of Boore et al (1997).
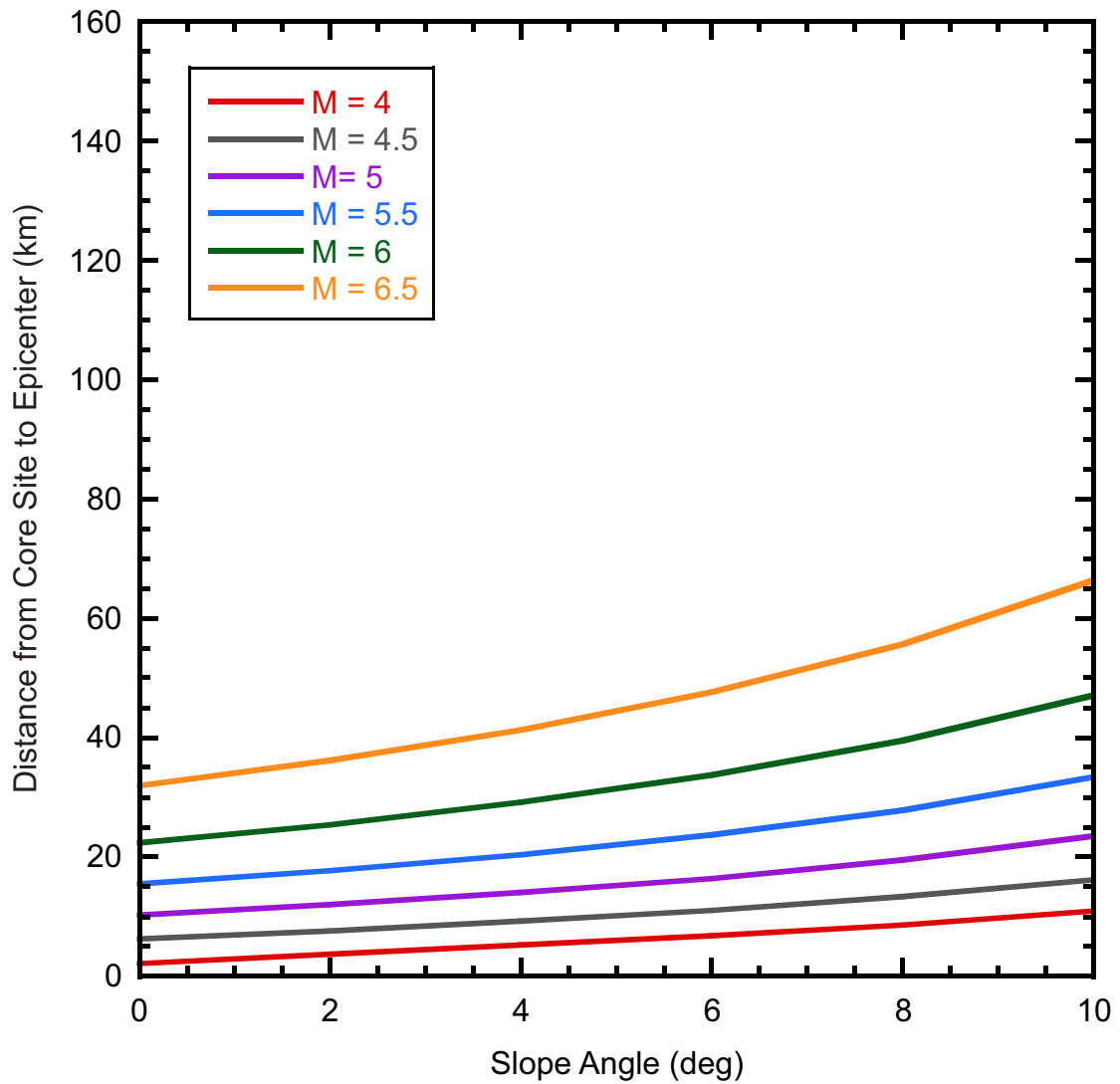
Figure 10.6a. Calculated distance from fault capable of triggering slope failures in Region 4, as a function of slope angle and earthquake moment magnitude. Parameters used (average): $V_{s30} = 134.7$ m/s, $S = 0.35$, $\gamma'/\gamma = 0.45$, GMPEs of Boore et al (1997).
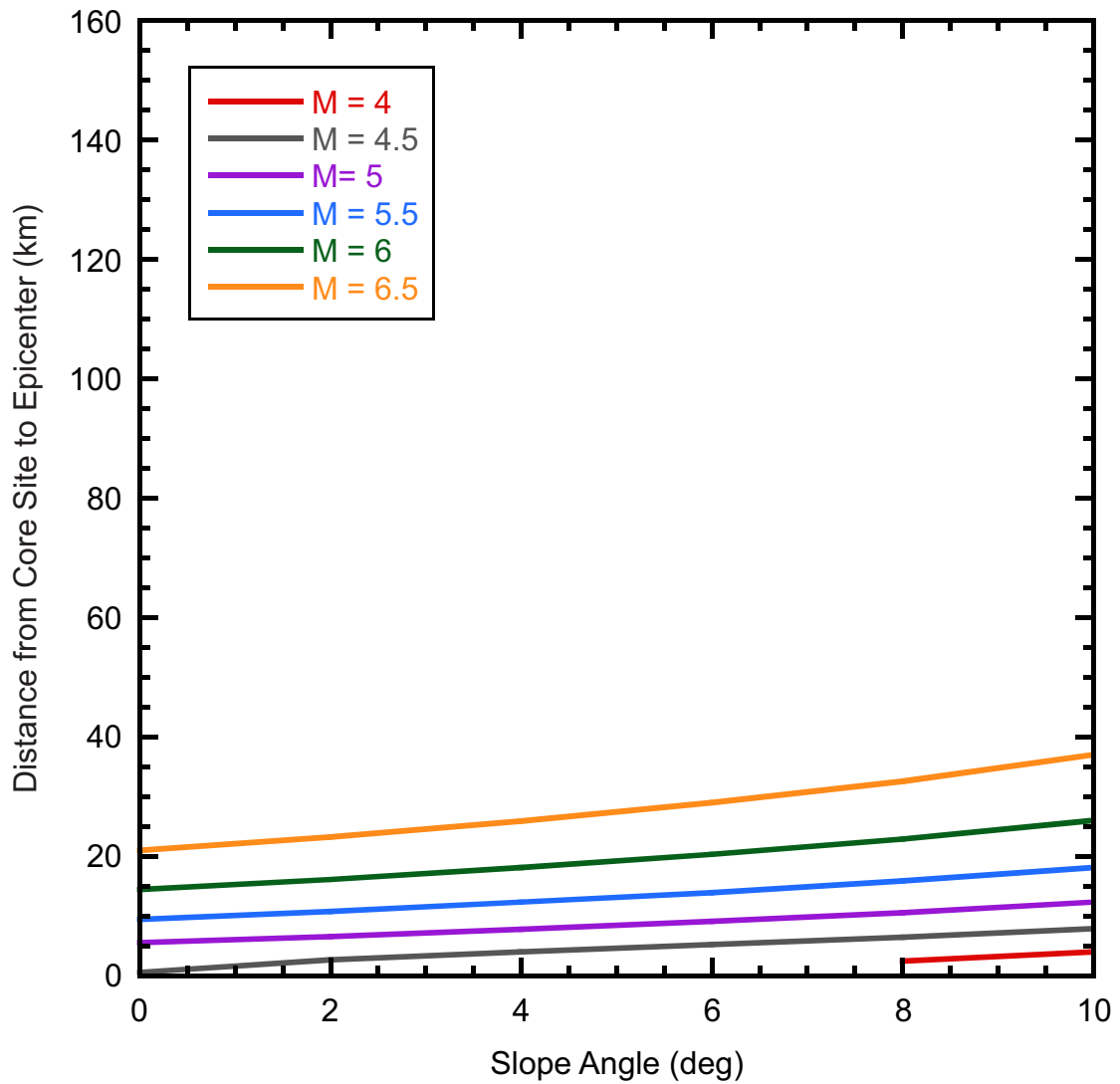
Figure 10.6b. Calculated distance from fault capable of triggering slope failures in Region 4, as a function of slope angle and earthquake moment magnitude. Parameters used (maximum): V_{s30} = 154.2 m/s, S = 0.38, γ'/γ = 0.5, GMPEs of Boore et al (1997).
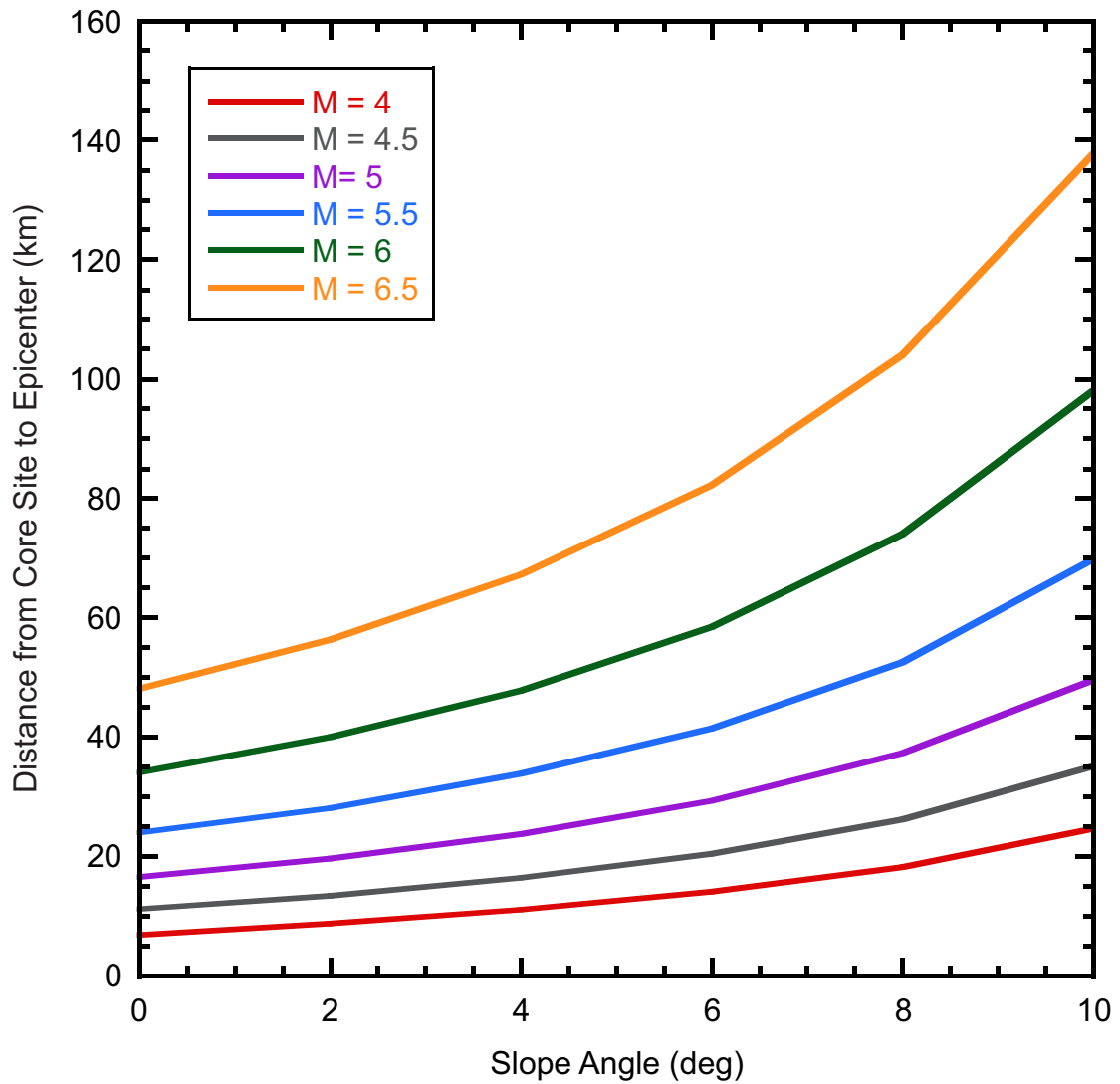
Figure 10.6c. Calculated distance from fault capable of triggering slope failures in Region 4, as a function of slope angle and earthquake moment magnitude. Parameters used (minimum): V_{s30} = 115.2 m/s, S = 0.30, γ'/γ = 0.42, GMPEs of Boore et al (1997).
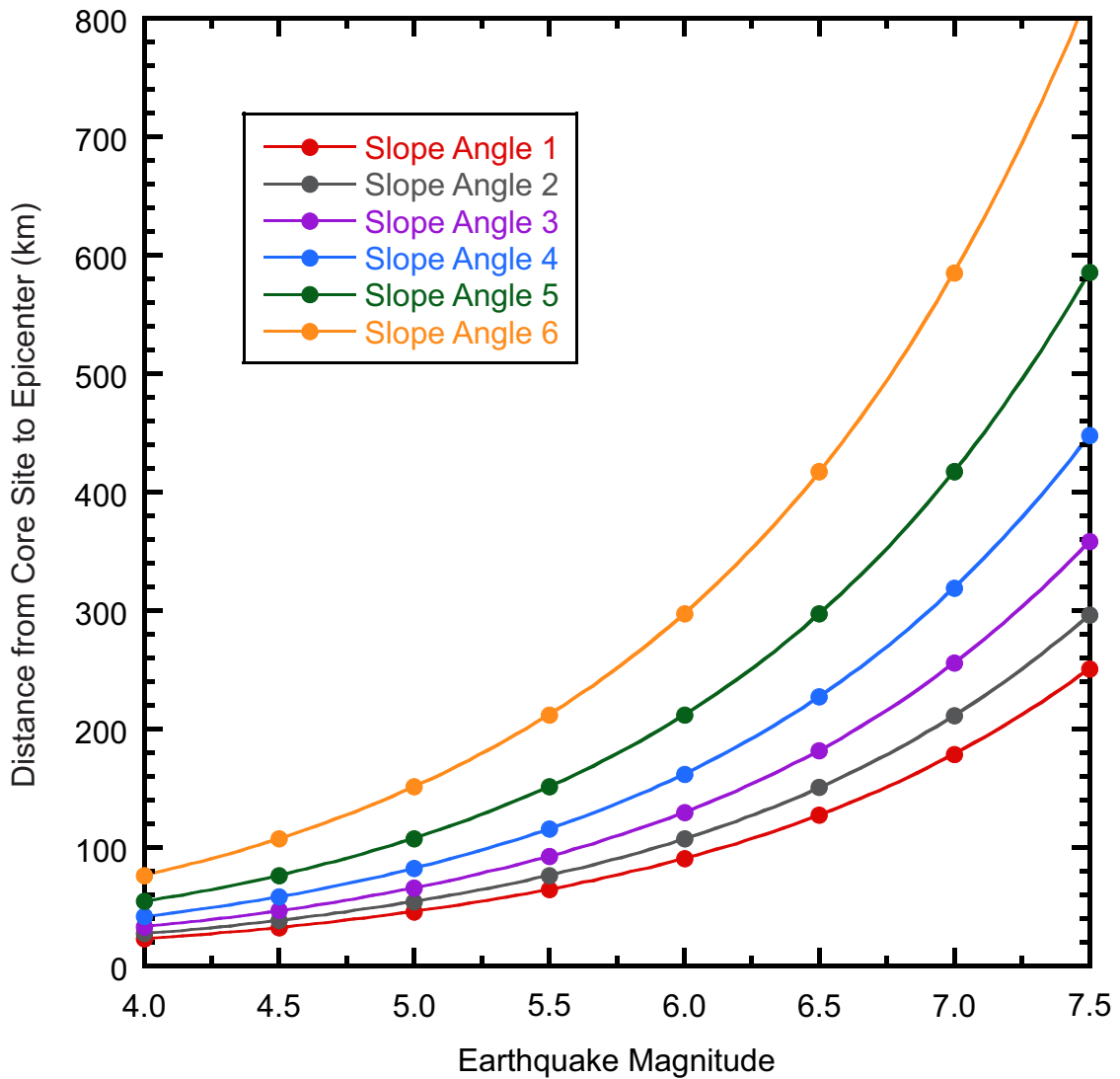
Figure 10.7 Calculated distance from fault capable of triggering slope failures for core site 2013Healy0001pc,as a function of earthquake moment magnitude and slope. Parameters used were: V_{s30} = 147.24 m/s, S = 0.16, γ'/γ = 0.38, GMPEs of Boore et al (1997).
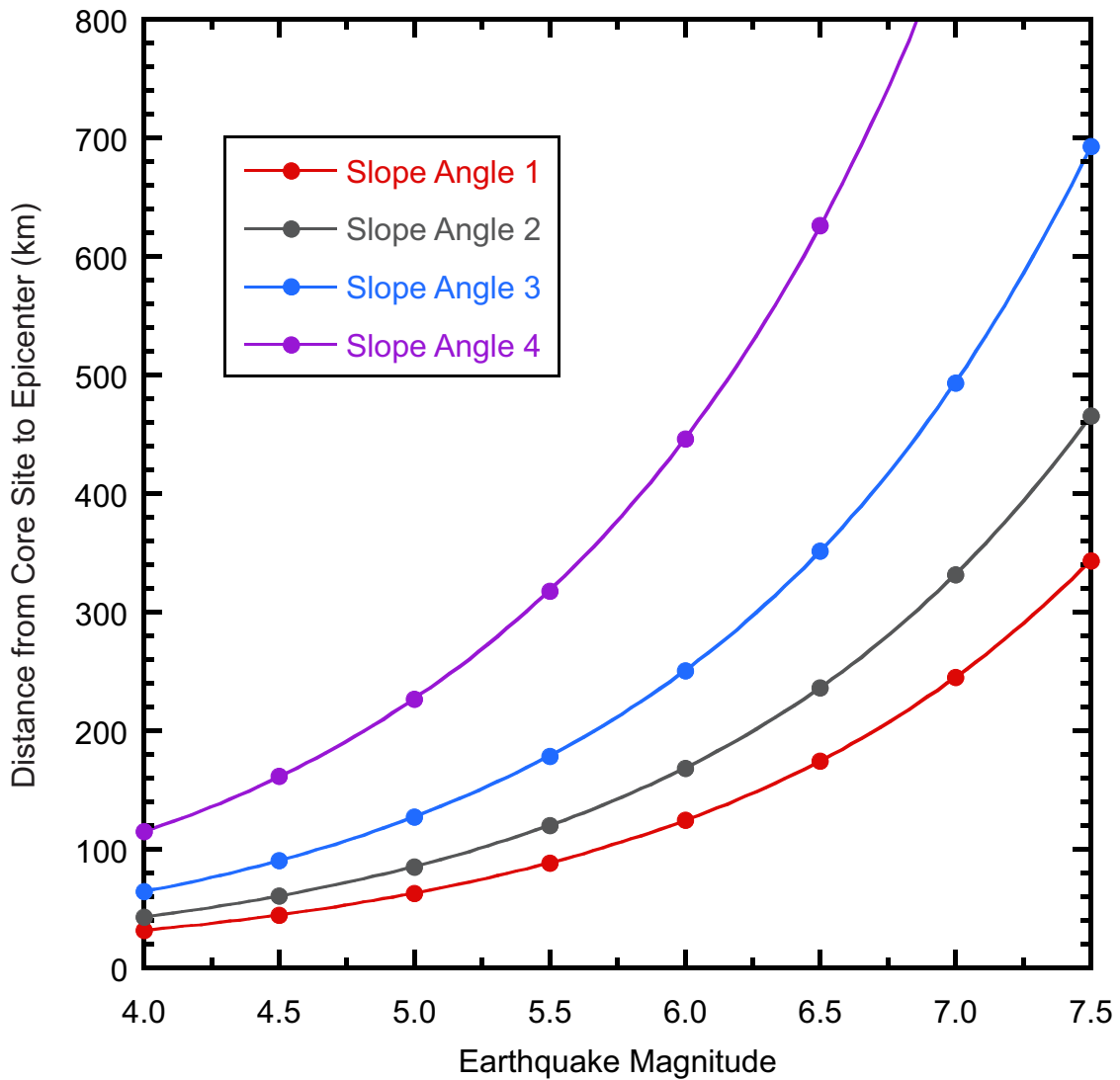
Figure 10.8 Calculated distance from fault capable of triggering slope failures for core site 20108040036pc,as a function of earthquake moment magnitude and slope. Parameters used were: V_{s30} = 210.31 m/s, S = 0.10, γ'/γ = 0.45, GMPEs of Boore et al (1997).
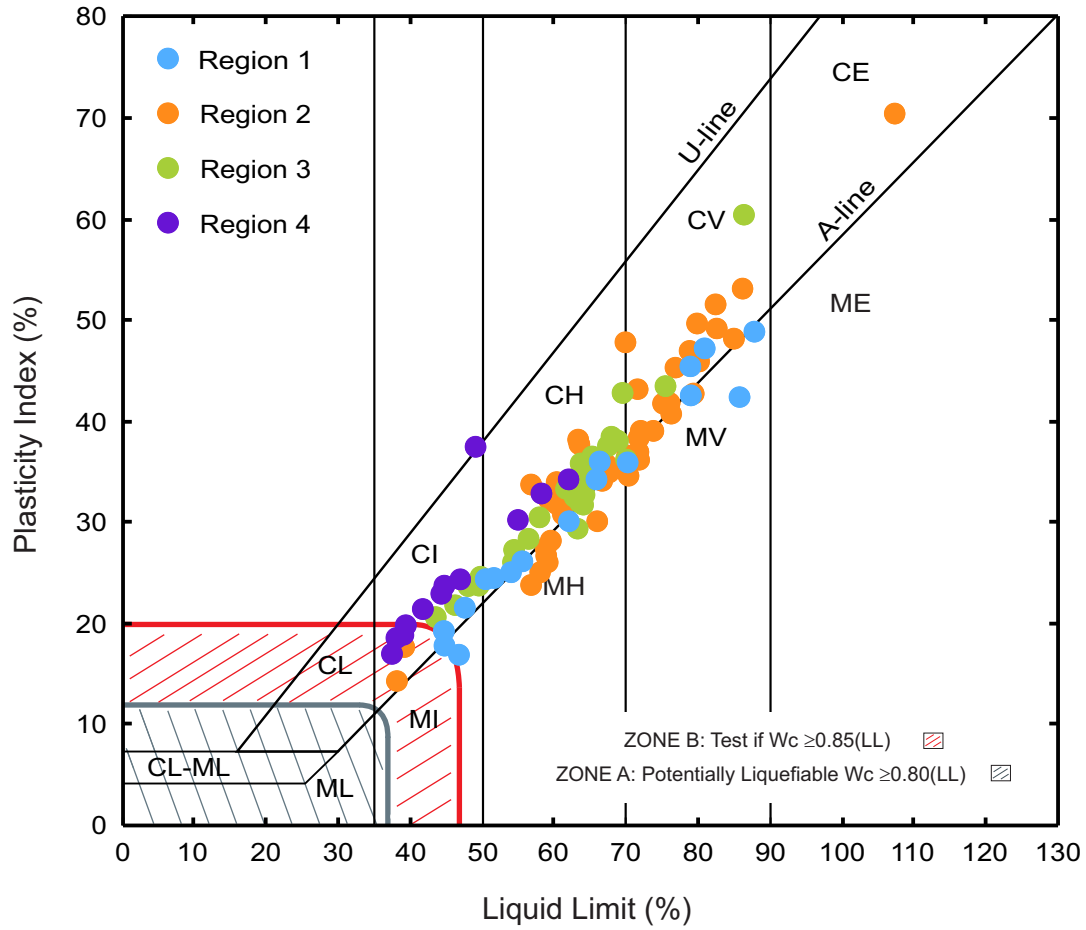
Figure 11.1. Plasticity chart showing Atterberg limit results of all cores in study area separated into regions.
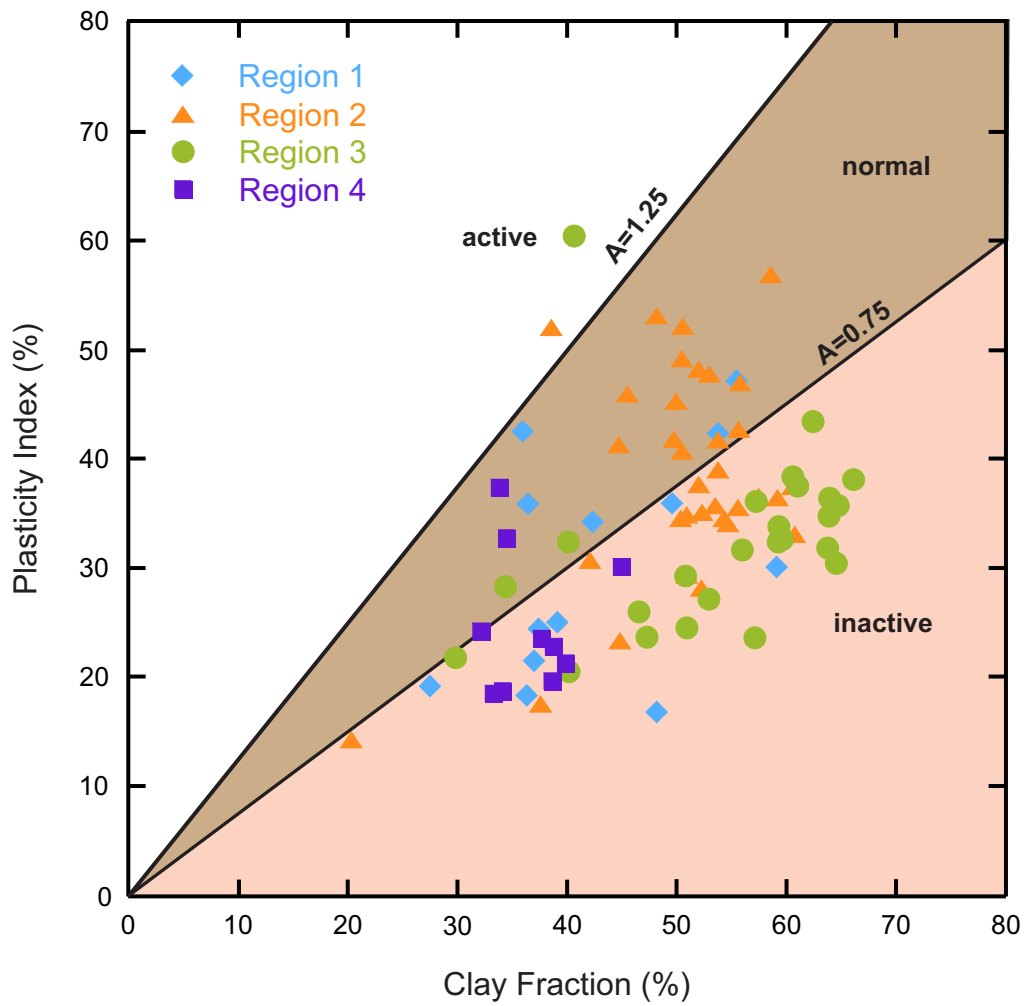
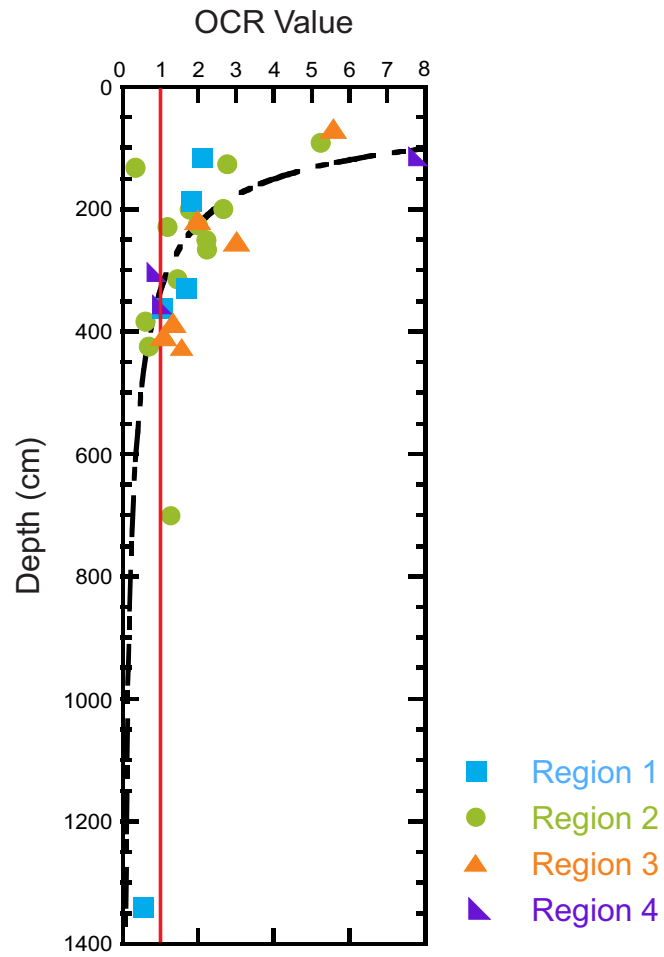Figure 11.2. Activity of all cores in study area separated into regions.

Figure 11.3. OCR values with depth of all cores in study area separated into regions.